TOWARDS GENERALIZED CHARACTERIZATION OF EXOPLANET ATMOSPHERES WITH TRANSIT SPECTROSCOPY

LUIS CARLOS WELBANKS CAMARENA

Supervisor: Prof. Nikku Madhusudhan

Institute of Astronomy
University of Cambridge

This thesis is submitted for the degree of
Doctor of Philosophy

Churchill College

July 8th, 2021

DECLARATION

This thesis is the result of my own work and includes nothing which is the outcome of work done in collaboration except as declared in the Preface and specified in the text. I further state that no substantial part of my thesis has already been submitted, or, is being concurrently submitted for any such degree, diploma or other qualification at the University of Cambridge or any other University or similar institution except as declared in the Preface and specified in the text. It does not exceed the prescribed word limit for the relevant Degree Committee. The work in this dissertation was performed under the supervision of Prof. Nikku Madhusudhan, who also contributed to the published manuscripts upon which this thesis is based.

- Cross sections in this work: The cross sections employed in this work were calculated by Dr. Siddharth Gandhi, except for the H_2 broadened Na and K cross sections which I computed. Additional cross sections such as O_2-O_2, CO_2-CO_2, and N_2-N_2 collision induced absorption were initially computed by Anjali Piette and later verified and reproduced by me.

- Retrieval frameworks: The retrieval framework employed in Chapters 2, 3, 6, and 7 was adapted by me from the frameworks AURA (Pinhas et al., 2018) and HyDRA (Gandhi & Madhusudhan, 2018), developed in Prof. Nikku Madhusudhan's research group. Aurora, the framework presented in Chapter 4 and used in Chapter 5, builds upon AURA (Pinhas et al., 2018). As explained in Chapter 4, Aurora keeps part of the essential infrastructure of AURA, such as the numerical model for calculating radiative transfer in a transmission geometry, the methods for interpolating opacities into a given temperature grid (also adapted after HyDRA, Gandhi & Madhusudhan 2018), and the methods for binning down a spectrum to the resolution of the input observations. Then, I implemented new functionalities and enhanced the framework as further described in Chapter 4.

- Chapter 1: Some figures have been adapted or taken from published works. The attributions of these figures have been specified in their captions.

- Chapter 2: The contents of this chapter are based on the published work of Welbanks & Madhusudhan (2019). Anjali Piette provided additional input for producing Figure 18.
- Chapter 3: The contents of this chapter are based on the published work of Welbanks et al. (2019). The tables and information necessary to compute the H_2-broadened Na and K cross sections was provided by Dr. Nicole F. Allard, Dr. Ivan Hubeny, and Dr. Fernand Spiegelman. Dr. Kaisey Mandel contributed to helpful discussions about statistical tests on the mass-metallicity relation.
- Chapters 4 and 5: The contents of these chapters are based on the published work of Welbanks & Madhusudhan (2021). Aurora, the retrieval framework introduced and implemented in these chapters, is the result of refactoring AURA (Pinhas et al., 2018). I then added key features to the retrieval framework as described in Chapter 4. Dr. Siddharth Gandhi and Dr. Arazi Pinhas provided help with the AURA and HyDRA retrieval codes which are the progenitors of Aurora and through various helpful discussions. Peter McGill contributed to this work through helpful conversations about Gaussian Processes and their implementation. Matthew Nixon provided additional input for producing Figure 35.
- Chapters 6 and 7: The contents of Chapter 6 are based on the published work of Chen et al. (2018); von Essen et al. (2019) and Chen et al. (2020). Then, the contents of Chapter 7 are based on the published work of Madhusudhan et al. (2020); Colón et al. (2020) and Sheppard et al. (2021). The data analysis and reduction that produced the spectra interpreted in these chapters was conducted by the co-authors in the respective published works. These co-authors additionally contributed to the text and figure preparation for the manuscripts from which this chapter is based.

I thank Amanda Smith for designing the graphic shown in the title page of this dissertation. This dissertation contains fewer than 60,000 words including summary, tables, footnotes and appendices, but excluding table of contents, photographs, diagrams, figure captions, list of figures, bibliography and acknowledgments.

Cambridge, UK, July 2021

Luis Carlos Welbanks
Camarena

TOWARDS GENERALIZED CHARACTERIZATION OF EXOPLANET ATMOSPHERES WITH TRANSIT SPECTROSCOPY

LUIS CARLOS WELBANKS CAMARENA

The field of exoplanetary sciences has grown from an era of detection to one of characterization. To date, over 4000 exoplanets have been discovered and over 50 of them have been observed with primary transit spectroscopy methods. The current population of characterized exoplanets spans a wide range of parameter space; from ultra-hot Jupiters with atmospheric temperatures beyond 3000 K, to temperate mini Neptunes that may host water in their atmospheres. Upcoming observational facilities in the next two decades will deliver exquisite spectra of exoplanet atmospheres at wavelengths never probed before, with unprecedented precision, and at much higher resolution than currently possible, effectively expanding the number of exoplanets with observed spectra. Nonetheless, an increasingly diverse planet population and higher fidelity data necessarily demand more flexible, complex, and generalized modeling frameworks.

In this thesis, we present our work on atmospheric retrievals of exoplanets, focusing on investigating the robustness of the model assumptions inevitably employed to infer basic planetary conditions, compositional trends across the exoplanet mass range, and considerations for next-generation generalized retrieval frameworks. First, we present our systematic investigation of degeneracies between different model considerations in retrievals of transmission spectra and the observations that can resolve them. This study used a combination of Bayesian atmospheric retrievals and a range of common model assumptions, focusing on H_2-rich atmospheres. We find that a combination of models including variable cloud coverage, prominent opacity sources, and high-precision optical and infrared spectra with current facilities enable constraints on cloud/haze properties and chemical abundances.

Second, we apply our atmospheric retrieval framework to a large sample of 19 exoplanets ranging from cool mini-Neptunes to hot Jupiters. This effort constitutes the largest (i.e., broad wavelength coverage, multiple chemical species, mini-Neptunes to Jupiter sized planets) homogeneous chemical abundance survey for transiting exoplanets to date. We

find a mass–metallicity trend of increasing H_2O abundances with decreasing mass, significantly lower than the mass–metallicity relation for carbon in the solar system giant planets and similar predictions for exoplanets. On the other hand, the Na and K mass–metallicity trends are generally consistent with the solar system metallicity trend. We argue that the trends observed in this sample suggest different formation pathways for these close-in exoplanets compared to the long-period solar system giants.

Third, we introduce Aurora, a next-generation retrieval framework for the characterization of H-rich and H-poor atmospheres. Here, we build upon state-of-the-art architectures and incorporate the following key advancements (a) a generalized compositional retrieval allowing for H-rich and H-poor atmospheres, (b) a generalized prescription for inhomogeneous clouds/hazes, (c) multiple Bayesian inference algorithms for high-dimensional retrievals, (d) modular considerations for refraction, forward scattering, and Mie scattering, and (e) noise modeling functionalities. We then carry out an investigation of the current and future chemical composition constraints for exoplanet atmospheres using this new retrieval framework. We estimate the abundance constraints achievable for hot Jupiters, mini Neptunes, and rocky exoplanets with current and upcoming observational facilities.

Lastly, we present our contribution to recent studies characterizing exoplanet atmospheres using ground and space based facilities. We perform atmospheric retrievals on a diverse population of exoplanets from ultra-hot Jupiters to temperate mini Neptunes. Among the planets studied are WASP-127b, WASP-33b, WASP-21b, K2-18b, KELT-11b, and HAT-P-41b. Our results add to the vast chemical inventory of atomic and molecular species found in exoplanet atmospheres. Moreover, our analyses unveil some of the challenges when interpreting high-precision spectroscopic data and possible instrument systematics. The atmospheric reconnaissance presented in this work explores some of the considerations needed for generalized characterization of exoplanet atmospheres with upcoming ground-based and space-based facilities.

We conclude this dissertation by summarizing our findings and their implications to the broader field of exoplanet characterization. We discuss some of the outstanding questions from our research and the prospect of future modeling and retrieval approaches to robustly characterize exoplanet atmospheres. The lessons from this work highlight that, although the inferences derived from observations are strongly influenced by model assumptions, the use of physically motivated models with

minimal assumptions, and broadband transmission spectra with current and future facilities can provide plausible estimates for the atmospheric properties for planets outside our solar system.

Dedicated to the loving memory of Nelson Welbanks Cozzulo.

1928 – 2020

ACKNOWLEDGEMENTS

I consider myself extremely lucky and blessed to have the opportunity to write these words and this dissertation. I deeply thank Nature for all the lessons it has shared with me, for its care, love, and for the opportunity to be here.

I am forever grateful to my supervisor Prof. Nikku Madhusudhan for his passionate and selfless support. From before I had the fortune to become his student, Prof. Nikku Madhusudhan started seeding his wisdom, humor, kindness, and view of the landscape of life in me. As his student, he continued to inspire me to become a better scientist and human-being. I am thankful for his unwavering support. At my best and at my worst he has been there to listen, troubleshoot, and give hope. I am indebted with him for introducing me to the field of exoplanets, an action that has changed my life. This dissertation would not have been possible without him.

It is common place to say that it takes a village to raise a child. Whether the child is this dissertation or the journey to get here, I am extremely grateful for the collective support from so many of my peers, colleagues, and friends. I would like to thank Dr. Siddharth Gandhi and Dr. Arazi Pinhas for receiving me with open arms here in Cambridge. Their advise, friendship, and willingness to teach me have deeply touched me. Likewise, I would like to sincerely thank my colleagues and friends at Prof. Nikku Madhusudhan's research group. Anjali Piette, Matthew Nixon, Adam Langeveld, Samuel Cabot, and Savvas Constantinou are more than just my 'academic siblings', they are my friends. Their attentive ear, their supportive company, and their empathy throughout this journey has made me grateful for our shared academic experience. I thank them for all their kindness.

I would like to sincerely express my gratitude to the collaborators who made much of the work in this dissertation possible. I would like to thank Dr. Guo Chen, Dr. Enric Pallé, Dr. Carolina von Essen, Dr. Knicole Colón, Dr. Laura Kreidberg, Dr. Avi Mandell, Dr. Drake Deming, and Kyle Sheppard for sharing with me their exquisite observations and providing a glimpse into the hard-work that these entail. As well, I would like to express my deep gratitude to Dr. Nicole Allard, Dr. Ivan Hubeny, Dr. Fernand Spiegelman, Dr. Thierry Leininger, and Dr. Michael Line for sharing their technical and theoretical expertise. Additionally, I am

grateful for the helpful discussions and meaningful insights provided by Dr. Kaisey Mandel, Dr. Richard Booth, and Jeffrey Salmond. All together, their contributions have made of my work more robust and complete. I am grateful for their advise, leadership, and hard work.

I would be remiss if I were not to thank my friends outside the exoplanet community, as their support through this journey has been key to my well-being. I thank Peter McGill, Dylan Gaffney, Sophie Koudmani, Antranik Sefilian, Michael Pashkevich, Dr. Gyuchul Myeong, Amy Rankine, Andrea Kusec, Daniel Rothchild, among many others who I am extremely fortunate to call my friends, for listening to me, providing sound advice, and offering an opportunity to call Cambridge home for the last four years. Likewise, I would like to thank Dr. Graham Farmelo for his mentorship and friendship during the last four years. I must acknowledge that part of this work was performed during the COVID-19 pandemic. There have been countless people, many of them unaware of their contribution, who allowed me to continue and finish this work; I thank them for their inestimable support. I express my sincere gratitude to the Institute of Astronomy, Churchill College, and the Gates Cambridge Trust for enabling the right environment for my academic growth. My deepest apologies if I have missed someone.

I would like to thank my friends and family for all their love and support throughout this endeavor. My mother Nelly, my grandparents, Darlene and Les Bachewich, I thank them for supporting me and believing in me. I would like to especially thank my father, Luis. I simply do not have the words to express how much I appreciate all he has done for me. There has not been a single day in the last 10 years, since I left home for the first time, that he has not been there by my side. I owe most of who I am today, to him.

To conclude, I would like to share a brief story. While producing some of the work in this dissertation, I had the opportunity to read a book by John Aitchison. It was in his work that I found a sentiment that completely resonated with me and made me wish I had thought of it first, as it describes my absolute appreciation for Stephanie Bachewich. Stephanie, you have been a constant among many variables. Thank you for always being there for me, believing in me, and being my best friend.

PUBLICATIONS

Some ideas and figures have appeared previously in the following publications:

- Welbanks & Madhusudhan (2019)
- Welbanks, Madhusudhan, Allard, Hubeny, Spiegelman & Leininger (2019)
- Welbanks & Madhusudhan (2021)
- Chen et al., (2018)
- von Essen, Mallonn, Welbanks, Madhusudhan, Pinhas, Bouy & Weis Hansen (2019)
- Chen, Casasayas-Barris, Pallé, Welbanks, Madhusudhan, Luque & Murgas (2020)
- Madhusudhan, Nixon, Welbanks, Piette & Booth (2020)
- Colón et al., (2020)
- Sheppard et al., (2021)

CONTENTS

LIST OF FIGURES

LIST OF TABLES

Part I

TOWARDS GENERALIZED CHARACTERIZATION OF EXOPLANET ATMOSPHERES WITH TRANSIT SPECTROSCOPY

1

INTRODUCTION

Our understanding of the universe took a gigantic leap forward almost three decades ago, when we confirmed the existence of other worlds beyond the boundaries of our solar system. What was previously confined to the realm of our imagination and theoretical astrophysics was suddenly accessible to our senses. These planets orbiting other stars challenged from the get go any preconceptions about how planets form, where they form, and what they should be made of. Since then, we have been incessantly working to keep up with the crescendo of wonders Nature has been letting us contemplate. The discovery and characterization of these other worlds, so called exoplanets, has offered us a new window to explore the cosmos. By looking at these other worlds, not only do we learn about the vast diversity of environments out there, but also about the remarkable place our home planet occupies in the universe.

We understand the nature of exoplanets by becoming aware of their existence and measuring, directly or indirectly, the light they radiate, reflect, or absorb. With this information, we can deduce the natural properties of these worlds, from the outer layers of their atmospheres to their interiors. Additionally, by studying several of these exoplanets and comparing their properties to other bodies, including those in our own solar system, we can deduct their possible origins and fates. Together, this accumulation of knowledge will lead us to a better understanding of planet composition, planet formation and evolution, and even the prospect for other habitable planets. This area of scientific inquiry known as exoplanetary science has therefore emerged as a prosperous frontier in science. The rapid technological and scientific advancements witnessed in exoplanetary science has made my generation[1] the first to grow up knowing about the existence of alien worlds.

However, thirty years in, this story is just in its opening chapters. Recent and upcoming surveys such as TESS, CHEOPS, PLATO, and complementary ground-based surveys promise to find hundreds, if not thousands, of additional exoplanets. Accompanying these detection efforts, the imminent launch of the James Webb Space Telescope (JWST), and the series of Extremely Large Telescopes (ELTs) planned to emerge in this

1 Besides this use of the first person singular, the rest of this work uses the first person plural for stylistic consistency.

new decade, will offer us detailed information about the composition of these planets at a rate never experienced before. As such, we stand at the dawn of what promises to be yet another revolution. Inspired by this outstanding opportunity, we can embark on a reconnaissance mission to prepare our tools and models for the upcoming transformation of the field.

1.1 DETECTION METHODS

At the time of writing this thesis, 4384 exoplanets have been confirmed detections according to the NASA Exoplanet Archive (Akeson et al., 2013). Figure 1 illustrates the cumulative number of discovered exoplanets as a function of time, highlighting some of the milestones in the field. From planets around pulsars (e.g., PSR B1257+12, Wolszczan & Frail, 1992) and substellar objects previously thought to be exoplanets (e.g., HD114762b, Latham et al., 1989) to the first planet around a sun-like star (e.g., 51 Pegasi b, Mayor & Queloz, 1995) and the well studied directly imaged systems (e.g., HR 8799, Marois et al., 2008), the vast number of discovered exoplanets has provided us a wide phase space of planetary conditions to study. Below, we briefly summarize the different methods used to detect exoplanets.

The first step in our quest to understand exoplanets is to detect them. Intuition dictates that the easiest way to do so is by looking directly at them, just like we see stars in the sky. This method is called direct imaging and is conceptually straightforward. In direct imaging the effort is focused on detecting photons coming directly from an exoplanet. The problem here is that by being close to another source of photons which is many times brighter (i.e., their host star) it is challenging to detect the photons directly from a fainter source (i.e., the planet). This is cleverly overcome by nulling out the starlight using a coronograph. Directly imaging an Earth-like exoplanet in the visible requires a contrast of $\sim 10^{-10}$ (Liu et al., 2015), while current technology is capable of detecting contrasts of $\sim 10^{-5}$–10^{-7} (e.g., Ren et al., 2012; Schneider et al., 2014). Consequently, current technology limits the applicability of this technique to young, massive, or bright planets that are far from their host stars, with observations in the near-infrared (e.g., Kalas et al., 2008; Marois et al., 2008). Through this method, we measure the thermal emission from the planet which has two possible sources: light reflected from the host star (extrinsic) and thermal emission from the planet (intrinsic). With a relatively small number of planets found using this technique to

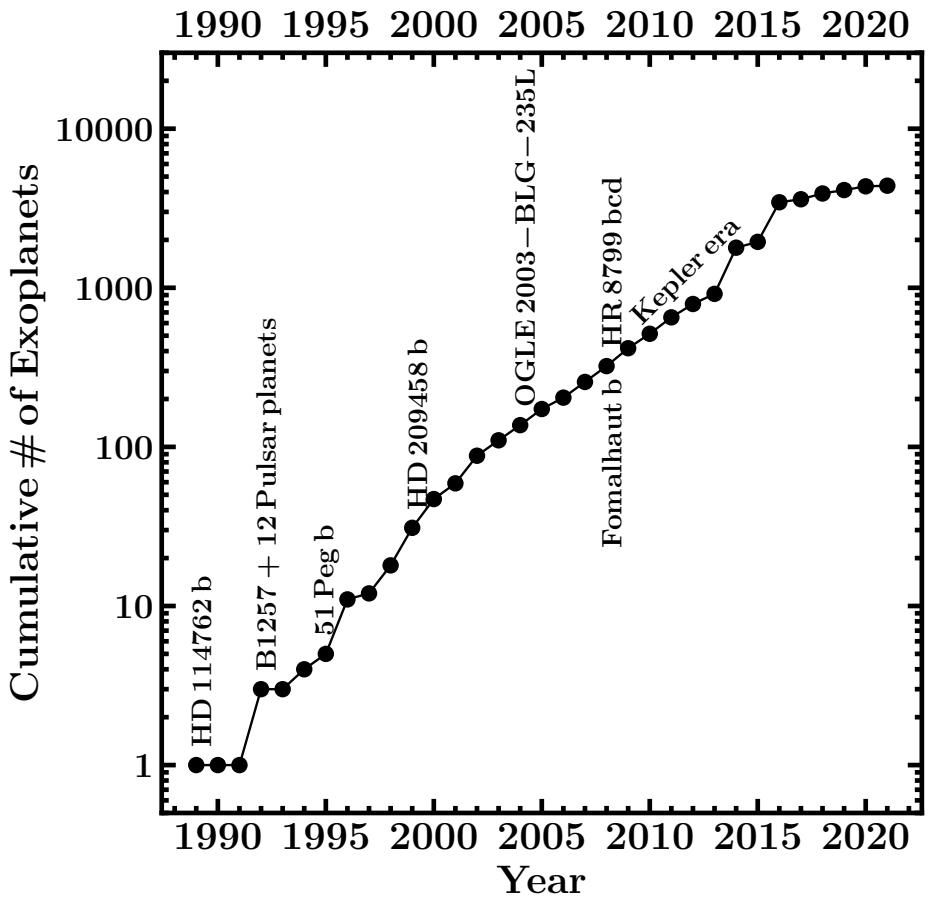

Figure 1 Cumulative number of exoplanets as a function of time with data from the NASA Exoplanet Archive. At the time of writing this work, 4384 exoplanets have been confirmed. The plot additionally shows some exemplary discoveries: a stellar/substellar object previously thought to be the first discovered exoplanet (HD114762b, Latham et al., 1989), the discovery of planets around a pulsar (PSR B1257+12, Wolszczan & Frail, 1992), the first exoplanet orbiting a main-sequence star (51 Pegasi b, Mayor & Queloz, 1995), the first transiting exoplanet (HD 209458 b, Charbonneau et al., 2000; Henry et al., 2000), the first exoplanet discovered by gravitational microlensing (OGLE-2003-BLG-235L b, Bond et al., 2004), and the first multiplanetary system directly imaged (HR 8799, Marois et al., 2008). Additionally, the plot shows the lifetime of the Kepler/K2 mission (2009-2018) responsible for finding over two thousand exoplanets (Borucki, 2018). This plot is adapted from the Mamajek's Law plot by Christine Corbett Moran, Deputy Manager for the NASA Exoplanet Exploration Program.

date (e.g., Marois et al., 2008; Lagrange et al., 2010; Marois et al., 2010), the prospect of the field is to develop better tools, including space-based coronographs, and some day produce an image of an Earth-like planet (e.g., Kaltenegger, 2017; Checlair et al., 2021; Wagner et al., 2021). This

method, as its name suggests, is a direct method for detecting exoplanets. However, it is through indirect methods that most exoplanets have been detected.

The first exoplanet orbiting a sun-like star, 51 Pegasi b (Mayor & Queloz, 1995), was detected by means of an indirect method known as the radial velocity method. This detection technique, also known as the Doppler technique, works on the basis of measuring the gravitationally-induced oscillation of a host star due to its orbiting planets. This is done by measuring the Doppler shift of the stellar absorption lines as the planet-star pair orbit their common center of mass. The heavier and closer the planet is to its host star, the larger the amplitude of the oscillation, and the easier it is to detect. This rationale explains why the majority of the planets discovered by this method are massive Jupiter-like planets, orbiting their host stars at very short separations. Detecting 51 Pegasi b required measuring a radial velocity of ~ 59 m s^{-1}, and was achieved with a precision of ~ 13 m s^{-1} (Mayor & Queloz, 1995). Since then, pioneering technology has allowed for measuring radial velocities of a few meters per second with precisions of ~ 1 m s^{-1}(e.g., Mayor et al., 2003; Anglada-Escudé et al., 2016; Fischer et al., 2016). These remarkable advancements have allowed the field to detect exoplanets with masses similar to Earths' orbiting small M dwarfs (e.g., Anglada-Escudé et al., 2016). However, detecting an Earth like planet around a Sun like star will require measuring velocities of roughly 10 cm s^{-1} (Jurgenson et al., 2016; Fischer et al., 2016). This goal, while currently beyond our technical capabilities, promises to be possible with upcoming facilities (e.g., Plavchan et al., 2015; Jurgenson et al., 2016; Fischer et al., 2016). From this method not only can we infer the presence of a planet, but we can also get an estimate for the minimum mass the planet must have.

Then, there is an indirect method that has proven to be the most successful in providing us information about exoplanets and their atmospheres, the transit method. To understand the transit method, we need to consider a specific configuration illustrated in Figure 2. Begin by imagining the line of sight between an observer and a planetary system. If the alignment of the system with respect to the observer is close to edge on, we can expect that any planets orbiting the star will eventually and periodically eclipse their host star. As a planet passes in front of its host star (i.e., transits the host star) the amount of light the observer receives from the host star will decrease. This decrease in the measured stellar flux allows us to infer the presence of a planet, its radius, and orbital inclination.

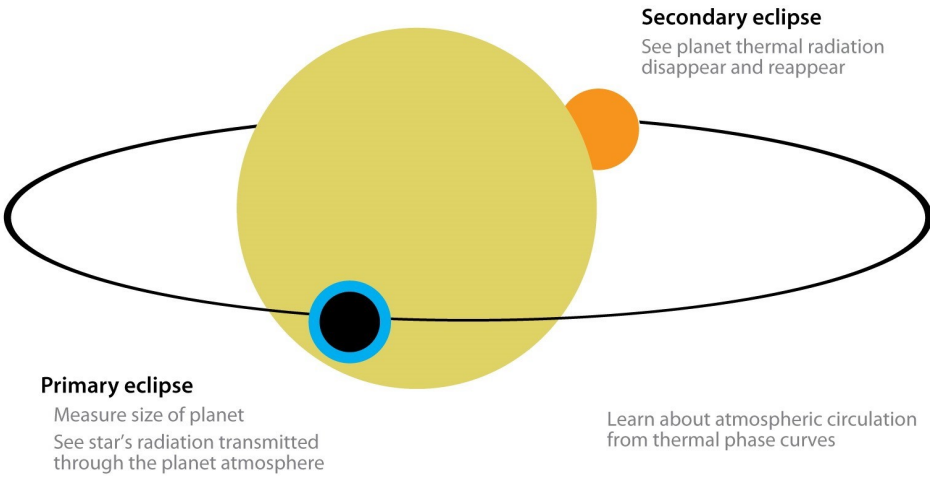

Figure 2 Schematic of a transiting planet. The planet orbits its host star (yellow circle). When the planet transits in front of the star we call this primary eclipse, whereas when the planet passes behind the star we call this secondary eclipse. Figure obtained from Seager & Deming (2010).

For this method to be successful, a series of advantageous scenarios must occur. First, the closer the planet is to its host star, the probability of transit becomes higher. Second, the bigger the planet, the bigger the transit depth. Consequently, this method has been particularly successful at detecting many massive exoplanets with sizes comparable to Jupiter. Moreover, many of these Jupiter sized planets are highly irradiated since they orbit their host stars at semi-major axes < 0.5 au (see e.g., Figure 3). These close-in, highly irradiated, Jupiter sized planets are commonly referred to as hot Jupiters. While this technique has been mostly successful in detecting hot gas giants, recent technological advancements and survey efforts have made it possible to detect planets smaller than Neptune orbiting sun like stars, and Earth-sized exoplanets orbiting smaller M-Dwarfs (e.g., Pollacco et al., 2006; Gillon et al., 2012, 2016; Daylan et al., 2021).

The transit depth is proportional to the projected areas between planet and star. A Jupiter sized planet around a sun-like star will have a transit depth of $(R_p/R_{star})^2 \sim 1\%$.

For completeness, it is important to mention that other detection methods have been ingeniously devised. Some of these include gravitational microlensing, and transit timing variations. In a nutshell, gravitational microlensing refers to the deflection of light from a distant star, e.g., source, due to the presence of a massive object, a 'lens', in between the source star and the observer (Gould, 2001). For the purposes of exoplanet detection, the massive object is a planet-star system. By using our understanding of how light bends as dictated by the principles of general relativity, we can derive some knowledge about the planet-star system and infer the presence of an exoplanet. On the other hand, detect-

ing a planet by transit timing variations refers to inferring the presence of a previously unknown planet due to changes in the timing of transits of a known exoplanet (Agol et al., 2005). The gravitational interaction between a previously unknown body and the known exoplanet will result in changes to its expected transit time. Specialized reviews of these and other detection methods are available in Gaudi (2012); Wright & Gaudi (2013) and Fischer et al. (2014).

1.2 A BRIEF OVERVIEW OF EXOPLANET DIVERSITY

Mercury: 0.06 $M_\oplus$, 0.38 $R_\oplus$
Venus: 0.82 $M_\oplus$, 0.95 $R_\oplus$
Earth: 1.00 $M_\oplus$, 1.00 $R_\oplus$
Mars: 0.11 $M_\oplus$, 0.53 $R_\oplus$
Jupiter: 317.83 $M_\oplus$, 11.21 $R_\oplus$
Saturn: 95.16 $M_\oplus$, 9.45 $R_\oplus$
Uranus: 14.54 $M_\oplus$, 4.01 $R_\oplus$
Neptune: 17.15 $M_\oplus$, 3.88 $R_\oplus$

The last 30 years have witnessed an exponential growth in the sheer number of exoplanets known to humankind. Since the detection of the first exoplanet orbiting a sun like star (Mayor & Queloz, 1995), more than 4200 exoplanets have been confirmed to date, with the majority of them being larger than Earth (e.g., Borucki et al., 2011; Howard et al., 2012; Petigura et al., 2013; Fulton et al., 2017, see also Figures 3 and 4). The surprising range of phase space covered by these newly discovered exoplanets made it clear that the distinct classification resulting from our own solar system was insufficient. From a solar system perspective, three main planetary classifications arise. First, we have the small close-in rocky planets (i.e., Mercury, Venus, Earth, and Mars) with masses close to Earth (e.g., $\lesssim 1 M_\oplus$). Second, we have the more distant, massive gas giants (i.e., Jupiter and Saturn) with masses $\gtrsim 100 M_\oplus$. Finally, furthest out, we have the ice giants (i.e., Uranus and Neptune) with masses $\sim 14\times$ and $\sim 17\times$, respectively, that of Earth. This classification in terms of orbital separation and mass, falls short when trying to comprehend the exoplanet diversity.

Figures 3 and 4 show the diversity in exoplanetary radius, orbital distances, period, and planetary mass for the 4384 exoplanets discovered at the time of writing this work. Inspecting the population of discovered exoplanets it becomes evident that, unlike the solar system, the population of known exoplanets is continuous. Mass analogues of Jupiter, Saturn, Uranus, and Neptune are abundant, although their orbits are closer than that of Mercury around the Sun. Similarly, many planets with radii between that of Earth and Neptune (i.e., super-Earths and mini Neptunes) have been discovered. Planets like these, which fall between the rocky planets and ice giants, do not have a direct analogue in our solar system.

The considerable number of planets known to date has been largely possible thanks to survey missions such as the Kepler/K2 space mis-

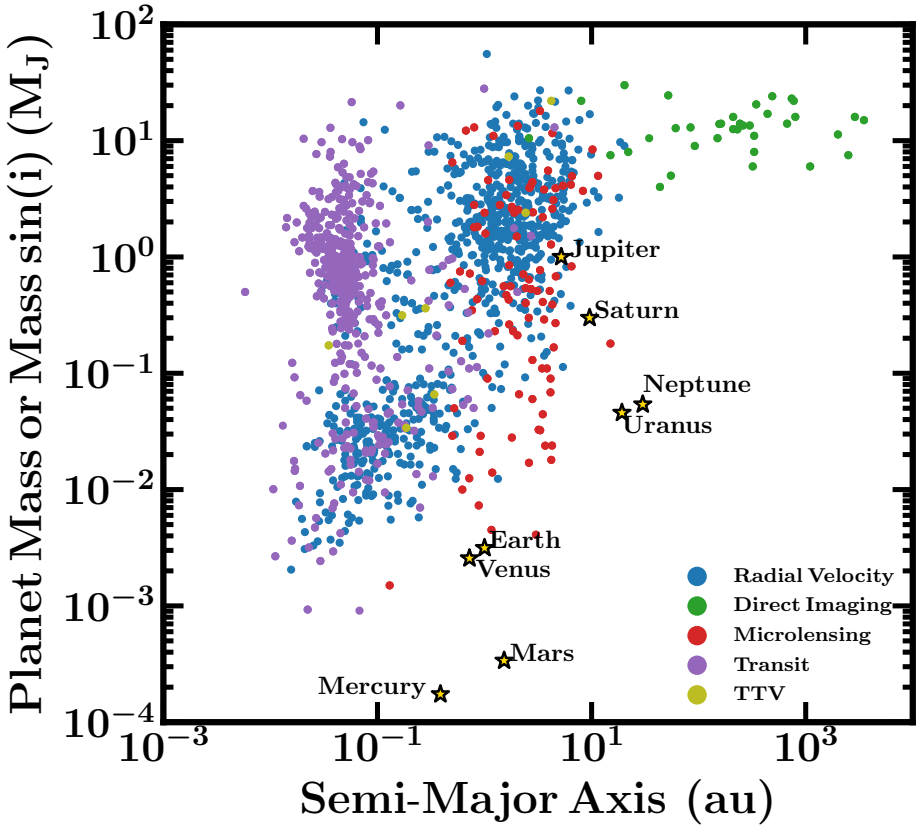

Figure 3 Mass vs. semi-major axis distribution for confirmed exoplanets, color coded by detection method. Planets without a known mass but an estimate for their minimum mass (mass sin(i)) are included. Solar system planets are shown for comparison using gold stars. Data obtained from the NASA Exoplanet Archive.

sions, which are solely responsible for discovering almost half of the planets known to date (Borucki, 2018). This large number of known exoplanets has allowed us to start deriving some knowledge about the occurrence of exoplanets and their properties (see e.g., reviews by Howard, 2013; Fischer et al., 2014; Winn & Fabrycky, 2015; Désert et al., 2015; Winn, 2018). So far, we know that most stars in our galaxy have planets (e.g., Howard et al., 2012; Fressin et al., 2013; Winn & Fabrycky, 2015; Zhu et al., 2018). Additionally, the most common type of planet is small sized planets with radii somewhere between that of Earth and Neptune (Fressin et al., 2013; Winn & Fabrycky, 2015). Many of these low-mass exoplanets orbit M-dwarf hosts (Dressing & Charbonneau, 2015; Mulders et al., 2015). The internal structure of this type of planet remains not known; they could have rocky or icy interiors (e.g., Valencia et al., 2013). Similarly, a detailed inventory of their atmospheric composition remains elusive from mass and radius measurements alone.

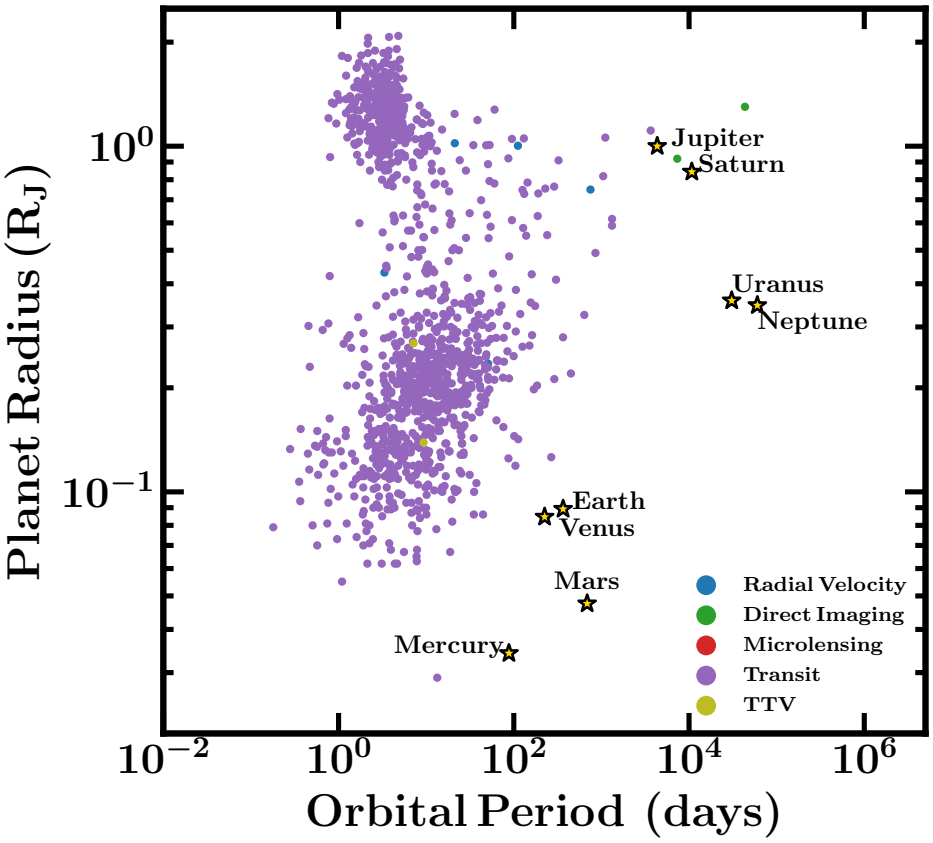

Figure 4 Radius vs. orbital period distribution for confirmed exoplanets, color coded by detection method. Solar system planets are shown for comparison using gold stars. Data obtained from the NASA Exoplanet Archive.

This recently found exoplanetary diversity has opened up several questions about planet formation and classification. As a consequence, the scope of exoplanetary science has grown from detection to detailed characterization of exoplanets. Our scientific goals now include obtaining a better understanding of the internal composition of exoplanets and that of their atmospheres, deciphering the formation and migration histories of these worlds, and exploring the complex physical processes they undergo. The key to solving many of these mysteries resides in observations of their atmospheres.

1.3 ATMOSPHERIC OBSERVATIONS AND CHARACTERIZATION

In order to fully understand the nature of an exoplanet, we must turn to its atmosphere. Observations of exoplanetary atmospheres enable inferences about the presence of chemical species in the form of gases, condensates, and small-sized particles. Additionally, these observations can

inform our understanding of the thermal structure of the atmosphere and the dynamical processes occurring in it (e.g., the presence of winds and circulation between the day side and night side of the planet). The characterization of exoplanet atmospheres allows us to explore a rich family of processes occurring on the planet, and even obtain hints of the planet's formation and migration history.

Detecting the presence of an exoplanet atmosphere is much more challenging than detecting the presence of the planet itself, requiring a sensitivity orders of magnitude better. However, several techniques have been successful in characterizing the atmospheres of exoplanets. These techniques rely on detecting the thermal emission of the planet, variations in the planet-to-star flux ratio, or the ratio between the planetary and stellar radii. Below we discuss some of the methods by which we detect and characterize exoplanet atmospheres.

1.3.1 *Transit Spectroscopy*

As explained in Section 1.1, transiting exoplanets are those that pass in front of their host stars as viewed by an observer. In this configuration, it is possible to detect exoplanets by observing the decrease in stellar flux due to the transiting planet. This quantity, as previously mentioned, is called transit depth. The transit depth or occultation (Δ) refers to the fractional flux deficit from the light curve (e.g., the brightness of the planet-star system as a function of time, see Figure 5), and is proportional to the projected area between the planet and the star (Seager, 2010; Sing, 2018)

$$\frac{\Delta f}{f} = \Delta \simeq \left(\frac{R_p}{R_{star}}\right)^2, \tag{1}$$

where the approximate equality corresponds to the case of an exoplanet without an atmosphere. It is from the equation above that our previous estimate of a transit depth of $\sim 1\%$ for a Jupiter sized planet around a sun like star, in Section 1.1, comes from. However, detecting the fractional flux deficit due to the presence of an exoplanet atmosphere requires detecting a much smaller signal.

When a planet with an atmosphere passes in front of its host star, a small fraction of the star light will be filtered through the planet's atmosphere. Depending on its composition, the atmosphere will be opaque or transparent at some wavelengths. This effect will make the planet

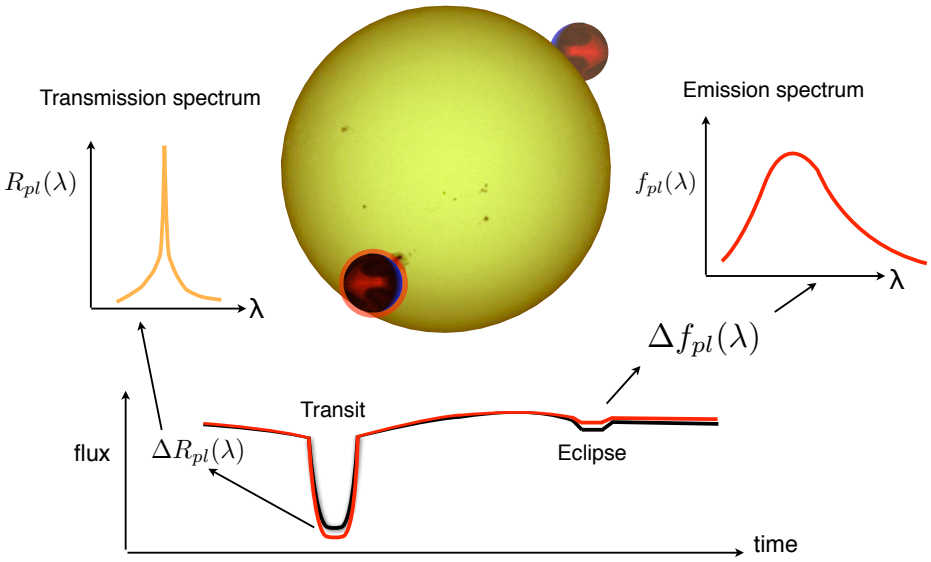

Figure 5 Atmospheric characterization of exoplanets in a transiting geometry. During a planetary orbit, it is possible to monitor the planet-star system light curve (bottom of the schematic). When the planet transits the star (i.e., primary eclipse) and when the planet is occulted by the star (i.e., secondary eclipse) there is a drop in the measured flux from the light curve. When the change in transit depth as a function of wavelength is measured, we obtain a transmission spectrum (top left). On the other hand, when the change in eclipse depth is measured as a function of wavelength we obtain a thermal emission spectrum (top right). Figure adapted from Sing (2018).

seem to be larger or smaller at different wavelengths, and the transit depth will respectively change. This apparent change in transit depth is what encodes information about the chemical composition of the planet atmosphere (Seager, 2010).

We can amend equation 1 to account for the presence of an opaque atmosphere of height A as

$$\Delta = \left(\frac{R_p + A}{R_{star}}\right)^2 \approx \frac{R_p^2 + 2R_pA}{R_{star}^2}, \tag{2}$$

assuming the height of the atmosphere is much smaller than the planetary radius (i.e., $A << R_p$). The height of the atmosphere is usually compared to the atmospheric scale height (H) as these quantities are proportional for a haze-free atmosphere (i.e., $A \propto H$, Madhusudhan et al., 2014a). The scale height is given by

$$H = \frac{kT}{\mu g}, \tag{3}$$

where k is the Boltzmann constant, T is the temperature of the planet's atmosphere, μ is the mean molecular weight, and g is the surface gravity of the planet (Seager, 2010). The size of an opaque atmosphere (e.g., the absorbing annulus of the planet's atmosphere) can be approximated as 5–10 scale heights above the planet's radius (Madhusudhan et al., 2014a). Then, we can estimate the corresponding change in transit depth due to an exoplanet atmosphere as

$$\delta \simeq \left(\frac{R_p + 5H}{R_{star}}\right)^2 - \left(\frac{R_p}{R_{star}}\right)^2. \tag{4}$$

Take for instance the prototypical hot Jupiter HD 209458 b ($R_p = 1.36\ R_J$, $g = 9.4\ m\ s^{-2}$, $T = 1450$ K, $R_{star} = 1.155\ R_\odot$, Torres et al., 2008; Sing et al., 2016) and assume a mean molecular weight of $\mu = 2.3$ atomic mass units (i.e., a H-rich atmosphere). For such conditions we obtain a scale height of $H = 558$ km and, assuming 5 scale heights as shown in equation 4, an atmospheric height of $A \sim 2790$ km. This means that the nominal transit depth of $\sim 1.5\%$ would increase by $\sim 0.085\%$ at the wavelengths with strong atmospheric absorption (i.e., where the atmosphere is opaque). These numbers exemplify the challenge of atmospheric characterization; detecting the atmosphere of an exoplanet requires a precision at least an order of magnitude higher than that required to detect a planet.

Inspecting equation 4 allows us to understand why most atmospheric detections of transiting exoplanets correspond to hot gas giants. Atmospheres with large scale heights are the easiest to characterize. Therefore, planets with high temperatures (i.e., highly irradiated, short period planets), low mean molecular weights (i.e., gas giants with H-rich atmospheres), and/or weak surface gravity have large scale heights and are prime targets for atmospheric characterization with the transit technique.

The opacity of the atmosphere is a wavelength dependent quantity. This means that by measuring the chromatic (i.e., wavelength dependent) change in transit depth, we are measuring the spectrum of the exoplanet atmosphere. We call this technique primary transit spectroscopy, and we call the chromatic change in transit depth a transmission spectrum. A transmission spectrum is essentially an absorption spectrum in

which we can identify the signatures of different atoms and molecules in the atmosphere of the exoplanet by their absorption of the stellar light (Seager & Sasselov, 2000).

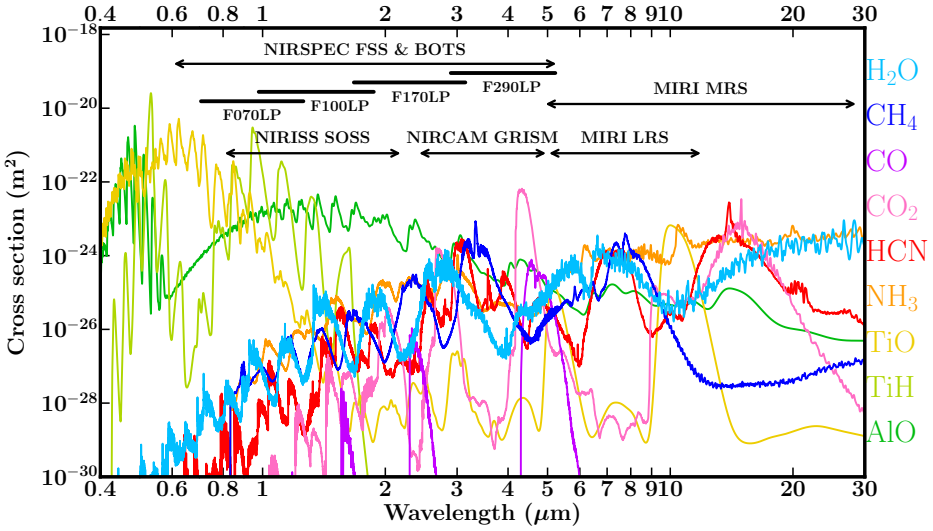

Figure 6 Molecular cross sections for some of the species expected in exoplanet atmospheres (e.g., Madhusudhan, 2012, 2019). The cross sections are shown from the optical to mid-infrared wavelengths. The top of the figure shows the spectral range covered by different instruments on board the upcoming JWST. The cross sections are shown for a temperature of 1400 K and a pressure of 1 bar.

The absorption signatures of different chemical species can be inferred by means of their cross sections. Figure 6 shows the cross sections of some of the chemical species expected in the atmospheres of exoplanets (e.g., Madhusudhan, 2012, 2019) in the optical and mid-infrared wavelengths. If these chemical species are present in an exoplanet atmosphere, their spectral features will be embedded in the planet's transmission spectrum. Provided the observations are of sufficient spectral coverage, resolution, and signal-to-noise, by measuring the wavelength dependent variations in the transit depth we can constrain the presence of the spectroscopically active species in a planet's atmosphere.

Moreover, transmission spectroscopy is useful to identify other processes that result in variations to chromatic transit depth. A particular example of such chromatic variations is the presence of hazes, small sized particles, that scatter light at characteristic frequencies and result in spectral signatures that resemble Rayleigh scattering (e.g., Hubbard et al., 2001; Sudarsky et al., 2003; Lecavelier Des Etangs et al., 2008). Additionally, transmission spectroscopy can be useful to identify the presence of condensate clouds that absorb light at all frequencies (e.g., gray

clouds) and mask or mute other spectral features (e.g., Seager & Sasselov, 2000; Hubbard et al., 2001). Finally, due to the temperature dependence of both the cross sections and the scale height, we can make initial inferences about the atmospheric temperature of the planet (Seager & Sasselov, 2000).

Transmission spectra of exoplanets are nowadays routinely obtained in the optical and near-infrared using ground-based facilities such as the Very Large Telescope VLT (e.g., Nikolov et al., 2016; Sedaghati et al., 2017), Magellan (e.g., Rackham et al., 2017; Espinoza et al., 2019), and the Gran Telescopio Canarias (e.g., Chen et al., 2017; Murgas et al., 2020), and space observatories such as the Hubble Space Telescope (HST) (e.g., Charbonneau et al., 2002; Désert et al., 2008; Deming et al., 2013; Mandell et al., 2013; McCullough et al., 2014; Kreidberg et al., 2014b; Sing et al., 2016; Spake et al., 2018; Wakeford et al., 2020). In the optical, we expect to find signatures of atomic species such as sodium and potassium (e.g., Seager & Sasselov, 2000; Sudarsky et al., 2003). On the other hand, the near-infrared gives us sensitivity to species with signatures between $\sim$ 1–10 μm such as H_2O, CH_4, CO, and CO_2 (e.g., Seager & Sasselov, 2000; Hubbard et al., 2001; Sudarsky et al., 2003; Madhusudhan et al., 2014a, see also Figure 6). Indeed, it was observing in the optical with the Space Telescope Imaging Spectrograph (STIS) that the first detection of an exoplanet atmosphere and sodium absorption was observed by Charbonneau et al. (2002) in the canonical hot Jupiter HD 209458 b. Since then, we have obtained transmission spectra of $\sim$ 50 exoplanets (Zhang, 2020), and over a dozen chemical species have been identified in $\sim$ 30 of these worlds (Madhusudhan, 2019).

One of the advantages of transit spectroscopy is that it is not limited to observations of primary transits only. Besides probing the atmosphere of an exoplanet at the day-night terminator with primary transit observations, it is also possible to probe the day side of the planet using secondary transit observations. A secondary transit, or secondary eclipse, refers to the moment when the planet passes behind the star and the thermal emission of the planet is blocked. By measuring the wavelength-dependent decrease in light when the planet crosses behind the star we can obtain what is known as an emission spectrum.

The fractional flux deficit at secondary transit (see e.g, Figure 5) allows us to effectively separate the light from the planet from that of the star. This quantity, also referred to as eclipse depth, is proportional to the planet-to-star flux ratio,

$$\frac{\Delta f}{f} = \left(\frac{F_p}{F_{star}}\right)\left(\frac{R_p}{R_{star}}\right)^2, \tag{5}$$

where F_p and F_{star} are the planetary and stellar surface flux, respectively (Seager, 2010; Sing, 2018). We may approximate the star and planet fluxes with their black body fluxes $\pi B(T, \lambda)$, where $B(T, \lambda)$ is the Planck function for a given temperature T and wavelength λ. Then, the wavelength dependent eclipse depth can be approximated as

$$\frac{\Delta f}{f} = \frac{B(T_p, \lambda)R_p^2}{B(T_{star}, \lambda)R_{star}^2}. \tag{6}$$

The planet-to-star flux contrast for an Earth twin orbiting a Sun-like star in the visible is 10^{-10} (Seager & Deming, 2010).

As it can be inferred from equation 6, the eclipse depth of a planet is largest when the planetary temperature is high. Therefore, hot Jupiters which are heated by their host stars to temperatures > 1000 K are prime targets for this characterization method. For instance, taking the above system parameters for the canonical hot Jupiter HD 209458b ($R_p = 1.36\ R_J$, $T = 1450$ K, $R_{star} = 1.155\ R_\odot$, Torres et al., 2008; Sing et al., 2016), an effective temperature of 6065 K for the host star (Torres et al., 2008), and Equation 6, we can estimate the planet-to-star flux ratio in the visible wavelengths (0.38–0.75 μm) to range from $\sim 10^{-11}$ to $\sim 10^{-7}$. On the other hand, the planet-to-star flux ratio for the same system in the near-infrared, near the 3.6 μm Spitzer photometric channel, is $\sim 10^{-3}$. This estimated planet-to-star flux ratio of 0.1% is an order of magnitude smaller than the estimated planet-to-star radius ratio of 1% for the primary transit of the same system. These order of magnitude estimates help explain why the majority of these eclipse observations have been done in the infrared.

Unlike transmission spectra, which probe the properties of the atmosphere at the day-night terminator, emission spectra provide us information about the properties at the day side of the planet. In this configuration, we are sensitive to both spectral emission features and absorption emission features. For instance, rising temperatures in the planet atmosphere create the conditions for hot atmospheric gas to lie above cooler atmospheric gas, resulting in spectral emission features. On the other hand, if the temperature of the atmosphere decreases with higher altitudes, cold gas will overlay hot gas and spectral absorption features will result. Lastly, if the atmosphere is isothermal the spectrum will lack any spectral features. The ability to probe both emission and absorption

spectral features allows us to probe the temperature of the atmosphere at different regions. At wavelengths in which the atmosphere is relatively transparent, we probe the atmospheric temperature deeper than in the opaque regions of the atmosphere. This strong connection between the presence of spectral features and temperature gradients makes emission spectroscopy an outstanding tool for rigorously constraining the temperature profile and chemical composition of exoplanet atmospheres.

As with transmission spectra, technological advancements such as the Wide Field Camera 3 (WFC3) on board HST have enabled strong constraints on the composition and temperature structure of the day side of multiple exoplanets (e.g., Kreidberg et al., 2014b; Line et al., 2016; Evans et al., 2016; Arcangeli et al., 2018). One of the first emission spectra came from Knutson et al. (2008) who used the photometric channels of the Infrared Array Camera (IRAC) on the Spitzer Space Telescope to characterize HD 209458 b. Since then, observations from space with Spitzer and HST (e.g., Blecic et al., 2014; O'Rourke et al., 2014; Kammer et al., 2015; Mansfield et al., 2018; Baxter et al., 2020), and ground-based facilities such as the VLT, the Canada-France-Hawaii Telescope (CFHT), Magellan, among others (e.g., Sing & López-Morales, 2009; Wang et al., 2013; Clark et al., 2018), have enabled observations of $\sim$ 30 exoplanets (Zhang, 2020), with at least 5 different chemical species detected in over half a dozen planets (Madhusudhan, 2019).

1.3.2 *Other Atmospheric Characterization Methods*

Besides the transit technique discussed above, other methods allow for the atmospheric characterization of exoplanets by observing their thermal emission. These methods include thermal emission phase curves and direct imaging. Additionally, measurements of the Doppler shift of the radiation emitted or absorbed by a planet's atmosphere can been performed via what is known as high resolution Doppler spectroscopy. These three methods, briefly discussed below, are not limited to transiting exoplanets.

Planets at semimajor axes $\lesssim$ 0.05 au (i.e., few day periods) are expected to be tidally locked (Seager, 2010).

The majority of the planets accessible for atmospheric characterization have short periods (see e.g., Figure 4) and are tidally locked. As such, most of these exoplanets have hotter and brighter day sides compared to their cooler and dimmer night sides. By observing a planet throughout its orbit, we can access the change in the system brightness during a full orbit. The amplitude of this almost sinusoidal change can tell us about the temperature gradient between the day side and night side (Seager,

2010). By observing a phase curve, we are able to obtain a longitudinal map of the planet's temperature (e.g., Knutson et al., 2007; Cowan & Agol, 2008, 2011; Stevenson et al., 2014, 2017; Bell et al., 2021). While this method is easy to picture for a transiting planet, it has been successfully applied to non-transiting exoplanets (e.g., Crossfield et al., 2010).

Phase curve observations allow measurements of the atmospheric properties as a function of orbital phase (e.g., Stevenson et al., 2014). For example, these observations allow for the identification of the hottest and coldest regions of the atmosphere. If these regions lie on the substellar and antistellar points, we could infer the absence of strong winds in the exoplanet atmosphere. On the other hand, if the hottest region of the atmosphere has been shifted away from the center of the day side of the planet, we may infer the presence of strong winds and learn about the dynamics of the atmosphere (e.g., Showman & Guillot, 2002; Zhang et al., 2018). Furthermore, if these are wavelength dependent phase curves, we could map the planetary emission spectrum as a function of longitude (e.g., Knutson et al., 2009; Stevenson et al., 2014), and constrain the chemical composition including the presence of clouds at different longitudes (e.g., Demory et al., 2013; Parmentier et al., 2016). Parmentier & Crossfield (2018) present a detailed review of phase curve observations.

Although so far we have spoken mainly about planets in very close orbits, we can also characterize exoplanet atmospheres on wider orbits. For planets that are well separated from their host star, far enough so that they can be spatially resolved by our telescopes, we can in principle obtain a spectrum of their thermal emission. This technique is known as direct imaging spectroscopy and is conceptually straightforward. Direct imaging spectroscopy favors observations of very bright planets distant from their host star, and as such has been mostly applied to young systems with planets emitting the residual heat from their formation (Madhusudhan et al., 2014a). Therefore, direct imaging spectroscopy provides us a complementary window into the formation and migration pathways of exoplanets.

Direct imaging spectroscopy requires high-contrast instruments on large-aperture telescopes. As a consequence, this technique has been limited to ground-based facilities such as Keck, Gemini, Subaru, and VLT. While far fewer exoplanets have been characterized using direct imaging spectroscopy, those characterized by this method generally have spectra at higher resolution and/or precisions by virtue of the state-of-the-art facilities used for this purpose (e.g., Rajan et al., 2017; Konopacky et al.,

2013; Greenbaum et al., 2018). A detailed review of photometric and spectroscopic observations of directly imaged planets is presented in Biller & Bonnefoy (2018).

Lastly, there is high resolution Doppler spectroscopy. This method has been recently applied to a wide variety of exoplanets (e.g., Snellen et al., 2008; Brogi et al., 2012, 2014; Birkby et al., 2017; Hoeijmakers et al., 2018; Giacobbe et al., 2021), and has resulted in the detection of multiple chemical species, including ionic species, in over a dozen planets (e.g., Birkby, 2018; Madhusudhan, 2019). This method corresponds to observing the high resolution ($R \sim 10^5$) spectra of the planet-star system. The resulting spectra will contain information on both the planet and the star. However, as the planet orbits the star, the planetary spectral lines will undergo a Doppler shift due to the radial velocity of the planet (Birkby, 2018). By observing the Doppler shift of these spectral lines, we can constrain the chemical species present in the exoplanet atmosphere.

High resolution Doppler spectroscopy facilities include Subaru, VLT, NASA Infrared Telescope Facility, CFHT, Gemini, Keck, the Telescopio Nazionale Galileo, among others.

High resolution Doppler spectroscopy can resolve the broadening of spectral features and precisely measure wavelength shifts in absorption lines that arise from changes in the radial component of the planet's orbital velocity. This additional information can be used to derive constrains on the dynamical processes, such as the presence of winds, on exoplanet atmospheres (e.g., Snellen et al., 2010; Showman et al., 2013; Zhang et al., 2017). Furthermore, high resolution Doppler spectroscopy can be applied to non-transiting exoplanets. This has made possible detecting numerous chemical species in exoplanets that would not be accessible by means of the transit technique. Some exemplary cases include the detection of CO in τ Boötis b (Brogi et al., 2012) and H_2O in 51 Pegasi b (Birkby et al., 2017).

1.4 ATMOSPHERIC MODELING

The last couple decades witnessed a revolution in our understanding of exoplanets and the nature of their atmospheres. Since the detection of an atmosphere in the first transiting exoplanet (Charbonneau et al., 2002), spectroscopic observations of exoplanet atmospheres have provided meaningful insights into the composition and structure of these worlds. A key aspect of the interpretation of these observations is their confrontation to theoretical expectations in the form of theoretical models. Atmospheric models are routinely utilized to explain the observations of an exoplanet atmosphere, provide a fit to them, and explore the relevant physical processes that may occur in these alien worlds.

Two complementary modeling paradigms have emerged to interpret exoplanet atmospheres, forward and inverse models. Below we present an overview of these complementary techniques, and refer the reader to appropriate reviews for a more targeted perspective (Marley & Robinson, 2015; Heng & Showman, 2015; Fortney, 2018; Heng & Marley, 2018; Madhusudhan, 2018).

1.4.1 *Forward Models*

Forward models, also referred to as self-consistent models, produce a synthetic atmospheric spectrum for a given set of assumptions. As the name suggests, we establish a series of assumptions and 'move forward' to produce a spectrum which, if desired, can be compared to observations. A key aspect of these models resides in their assumptions, which aim to incorporate physical and chemical processes in a self-consistent way. This modeling paradigm is advantageous for predicting the spectroscopic signatures of a given atmospheric property (e.g., determining the observable signatures of a process of interest in order to plan for observations), presumptive understanding of atmospheric processes under varied conditions, and preparatory data interpretation.

The complexity and assumptions in these models is varied. Model complexity ranges from one-dimensional atmospheres (e.g., Seager & Sasselov, 1998; Hubeny et al., 2003; Fortney et al., 2005, 2008; Burrows et al., 2008; Mollière et al., 2015; Gandhi & Madhusudhan, 2017; Goyal et al., 2018) to full three-dimensional general circulation models (GCMs, e.g., Showman & Guillot, 2002; Showman et al., 2009; Cho et al., 2003; Dobbs-Dixon & Lin, 2008; Kataria et al., 2013; Mayne et al., 2014). Typical model assumptions include adopting certain elemental compositions (e.g., solar abundances), radiative-convective equilibrium, and thermochemical equilibrium. Models use the assumption of thermo-chemical equilibrium to determine the chemical compositions for an assumed temperature, pressure, and elemental abundance. The assumption of radiative-convective equilibrium would allow for computing a pressure-temperature profile that is consistent with the atmospheric chemistry. The treatment of these assumptions is varied in the literature with varying degrees of flexibility and complexity. In depth reviews of these frameworks and their assumptions are available in Hubeny (2017); Gandhi & Madhusudhan (2017) and Zhang (2020).

Sophisticated physical processes have been modeled on more complex, three-dimensional, GCMs. These models can be used to compute

and predict the chemical composition, temperature structure, dynamical processes (e.g., winds), and cloud formation on exoplanet atmospheres as a function of latitude and longitude. These outputs can be then 'post-processed' to generate a synthetic spectrum. The use of these more intricate models has been instrumental to predict and understand equatorial jets in strongly irradiated Jupiters (e.g., Showman & Guillot, 2002; Kataria et al., 2016), the formation of condensates (e.g., Parmentier et al., 2018; Roman & Rauscher, 2019), and phase curve observations (e.g., Showman et al., 2008; Lines et al., 2018). The complexity of these models makes them computationally expensive, an important limitation when trying to explore a wide range of physical properties. We refer the reader to Heng & Showman (2015) and Zhang (2020) for further reviews on these methods.

1.4.2 *Inverse Models*

A key approach employed to infer atmospheric properties from spectra are inference methods known in the exoplanetary literature as retrieval methods or inverse models. These inverse models are used to derive the atmospheric properties of an exoplanet by coupling an atmospheric model with a statistical inference algorithm. They are referred to as inverse models because, given an observed spectrum, a retrieval aims to disentangle the physical properties of the exoplanet atmosphere, e.g., it works its way back from a set of observations. Applying retrievals on reliable data sets allows for constraints on the chemical composition, pressure and temperature structure, and the presence of clouds and hazes in a planetary atmosphere (e.g., Madhusudhan & Seager, 2011; Madhusudhan et al., 2014b; Kreidberg et al., 2014b, 2015; Nikolov et al., 2018; Wakeford et al., 2018; Barstow et al., 2017; Pinhas et al., 2019). The application of this powerful framework to exoplanet transmission spectra has undoubtedly changed the way in which we interpret these observations (e.g., Madhusudhan & Seager, 2009; Line et al., 2012; Kreidberg et al., 2014b, 2015). Their flexibility and statistical rigor permit the data to drive the inferred solutions.

The advent of retrievals was motivated by what is known as the 'degeneracy problem' (see e.g., Madhusudhan & Seager, 2009). While a model spectrum can in principle provide a reasonable fit to an observed spectrum by means of some goodness of fit metric (e.g., χ^2), it is not possible to know from this model alone if it represents the best solution or the only solution for the data. Using single forward models to derive

any inferences from a data set can leave vast areas of parameter space unexplored and unconsidered, resulting in ignorance about any possible parameter degeneracies and little statistical rigor when claiming any detections or parameter constraints. The retrieval method offers a solution to this problem by fitting an atmospheric model to a data set using a statistical inference framework and providing model parameter estimates and their associated uncertainties.

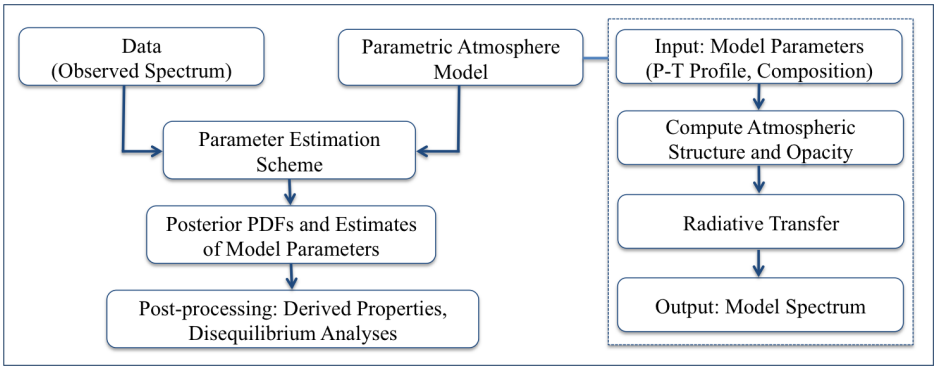

Figure 7 Schematic of an inverse model framework, also known as retrieval. An atmospheric retrieval framework combines an atmospheric forward model model with a parameter estimation scheme to derive statistical inferences on the model parameters from an observed spectrum (data). The typical considerations (e.g., components) of a parametric atmospheric model are shown on the right of the schematic. The parametric model considers a series of free parameters that usually correspond to the pressure-temperature structure of the atmosphere, the chemical composition of the atmosphere, and the presence/properties of clouds/hazes. The parameter estimation scheme derives statistical inferences of the model parameters (e.g., posterior probability density functions) given a data set. The derived inferences on the model parameters can be used to interpret the atmospheric properties of the exoplanet (e.g., chemical abundances of different species). Figure obtained from Madhusudhan (2018).

At its core, a retrieval framework is composed of two parts: a parametric atmospheric model and a parameter estimation scheme (see Figure 7). The parametric atmospheric model is used to compute an atmospheric spectrum given a set of parameters. These free parameters aim to capture the properties of the planet atmosphere, the pressure-temperature profile, the abundances of the different chemical species present in the atmosphere, the presence of clouds and hazes, etc., with no prior assumptions about chemical or radiative equilibrium[2]. The atmospheric

2 While the retrieval frameworks in this dissertation do not have prior assumptions about chemical or radiative equilibrium, other retrieval frameworks have included the a priori imposition of physical processes such as equilibrium chemistry (e.g., Line et al., 2016;

model uses these parametric forms to compute a model spectrum more easily and with fewer physical constraints than the forward models, with several computationally expensive assumptions, discussed previously. Nonetheless, the parametric models in a retrieval framework usually assume hydrostatic equilibrium and local thermodynamic equilibrium.

The second key component in a retrieval framework is a parameter estimation scheme. Such scheme must be able to sample high-dimensional spaces corresponding to the number of free parameters in the model. Additionally, the exploration of the parameter space must be done efficiently as to find all possible model degeneracies and provide a model solution for a given data set. The first retrieval code (Madhusudhan & Seager, 2009) performed the parameter estimation using a large model grid (10^7 models of 10 parameters each). Despite the large number of models in the grid, this approach resulted in a limited exploration of the parameter space. To address these limitations, subsequent studies adopted more robust statistical optimization algorithms (e.g., Madhusudhan & Seager, 2011; Line et al., 2013; Lee et al., 2013; Benneke & Seager, 2013; Waldmann et al., 2015a; Lavie et al., 2017; Wakeford et al., 2017a; MacDonald & Madhusudhan, 2017a; Gandhi & Madhusudhan, 2018). The next iteration of codes (e.g., Madhusudhan & Seager, 2011; Line et al., 2013; Wakeford et al., 2017a) used Markov chain Monte Carlo (MCMC) (e.g., Tegmark et al., 2004; Foreman-Mackey et al., 2013), providing a better parameter exploration of the parameter space but with limitations in calculating the model evidence for model comparison. Concurrently and with a background from solar system studies (e.g., Rodgers, 1976), Optimal Estimation (OE, e.g, Rodgers, 2000) was implemented in retrievals (Irwin et al., 2008; Lee et al., 2013). The next generation of retrieval codes (e.g., Benneke & Seager, 2013; Waldmann et al., 2015a; Lavie et al., 2017; MacDonald & Madhusudhan, 2017a; Gandhi & Madhusudhan, 2018) came to light with the implementation of the nested sampling algorithm (Skilling, 2006), facilitating the parameter space exploration and calculation of model evidence. We present in Chapter 4 a more specialized summary of the existing retrieval frameworks in the field, while Madhusudhan (2018) presents a comprehensive overview of the extensive evolution of retrieval methods.

The absence of thermo-chemical and radiative-convective equilibrium assumptions allow retrievals to capture deviations from theoretical expectations. These inverse methods can explore a wide range of atmospheric properties ranging from 'Earth-like' temperate planets with tem-

Al-Refaie et al., 2019; Zhang et al., 2020) or modules to assess deviations from chemical and radiative-convective equilibrium (e.g., Gandhi & Madhusudhan, 2018).

peratures below 300 K to ultra-hot Jupiters with H-rich atmospheres beyond 3000 K. As a result, retrievals could better inform our understanding of the enormous complexity and diversity in exoplanet atmospheres without being confined to a priori expectations. Nonetheless, while robust in their exploration of the parameter space, inverse methods do not assess the physical plausibility of the inferred properties. Although retrievals are powerful tools, they must be used with due care and their inferences must be contextualized by their model assumptions.

1.4.3 *Forward or Inverse?*

Forward and inverse models are not mutually exclusive. Careful interpretation of exoplanet atmospheres requires both forward and inverse models. While each approach has its own strengths and weaknesses, forward and inverse models are complementary to each other. The thorough characterization of exoplanet atmospheres will benefit from the a priori theoretical understanding that forward models provide and the statistical rigor offered by inverse models. The atmospheric properties derived from an inverse model can be inspected using forward models and assessing their agreement, or lack thereof, with equilibrium assumptions. The presence of any disagreements between modeling approaches signals the need for model refinement and theoretical insight. By using both methods in a complementary fashion, we can place reliable and robust constraints on the physical processes considered by our models and revisit our presumptions about the nature of these alien worlds.

1.5 THE SCIENCE EMBEDDED IN AN EXOPLANET ATMOSPHERE

The science embedded in an atmospheric spectrum is plentiful. There is a myriad of scientific questions that can be addressed using exoplanetary atmospheric observations. Additionally, different observations (e.g., at different spectral ranges) provide distinct windows into the nature of exoplanets and their atmospheres. Below we briefly describe some of the main categories for these science topics.

1.5.1 *Atmospheric Physics*

Naturally, observations of exoplanet atmospheres allow for inferences of the physical and dynamical process taking place in them. The information derived, however, depends on the observations and the regions

of the atmosphere they probe. The atmosphere of an exoplanet and its regions, the processes that may be present in them, and the type of observations that can probe them are represented in the schematic shown in Figure 8. Here we explore the different processes that can occur in an exoplanet atmosphere as a function of pressure.

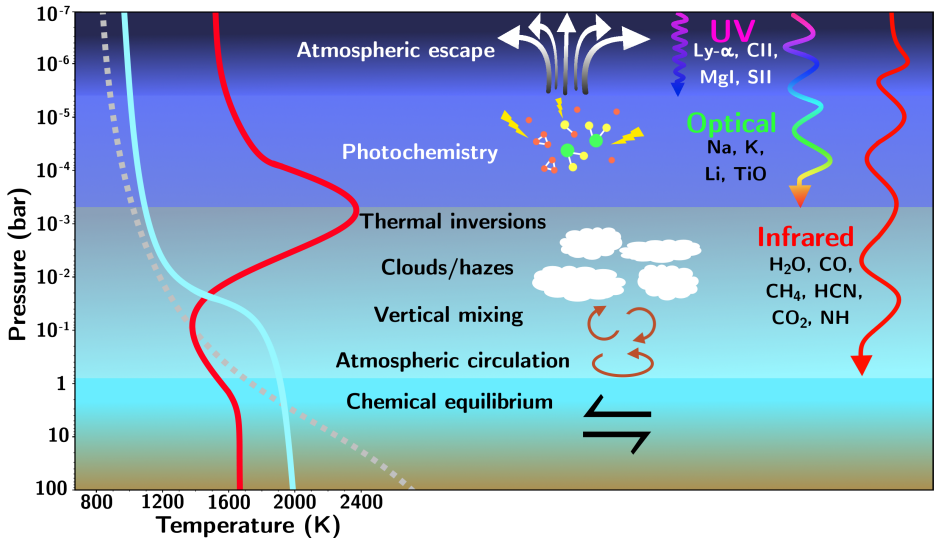

Figure 8 Schematic of the diverse processes that may be present in an exoplanet atmosphere. Different parts of the atmosphere, and different chemical species, can be probed at different wavelengths. The right side of the schematic shows the typical regions of the atmosphere and the parts of the electromagnetic spectrum that can probe them (e.g., infrared, optical, and UV). The middle of the schematic shows the different processes that may be present in an exoplanet atmosphere. The left side shows illustrative temperature profiles for exoplanet atmospheres: profiles for highly irradiated planets with thermal inversions (red) or without thermal inversions (blue), and a profile for poorly irradiated planets (gray).

Deep in the atmosphere, at the highest pressures (e.g., $P \gtrsim 1$ bar in Figure 8), equilibrium conditions such as radiative-convective and thermochemical equilibrium dominate the physics of the atmosphere due to the high pressures, temperatures, opacities, and densities. The high opacities make it difficult to probe this region of the atmosphere directly, as by definition this region is opaque or optically thick. As we move towards lower pressures, the atmospheric density and opacity decrease, making this region of the atmosphere accessible by longer wavelength observations (e.g., infrared, ~ 0.8–20μm). This pressure range, the bar to millibar level, is what is usually probed by transit spectroscopy. As the schematic in Figure 8 shows, this region of the atmosphere is affected by various processes such as atmospheric dynamics (e.g., atmospheric cir-

culation and vertical mixing), thermal inversions (i.e., statospheres, e.g., Haynes et al., 2015; Evans et al., 2017), the formation and presence of clouds and hazes, and their interactions with the incident radiation and atmospheric composition. The interactions between these atmospheric processes, the atmospheric chemical composition, and the atmospheric temperature structure may lead to thermo-chemical disequilibrium. This part of the atmosphere is mainly composed of molecular species such as H_2O, CO, CH_4, NH_3, and others depending on the temperature of the planet (see e.g., Madhusudhan, 2012; Woitke et al., 2018).

The mid to high atmosphere, from the millibar to microbar level, can be probed in the optical. At these lower pressures, and lower densities, photochemical processes may dominate the physics of the atmosphere. The increased radiation received by this part of the atmosphere can lead to photodissociation of some chemical compounds into their constituent atomic species, and the ionization of atomic species. Therefore, this part of the planetary atmosphere is mainly composed of atomic species and some ionic species. The highest part of the atmosphere, at pressures lower than the microbar level, can be susceptible to atmospheric escape (see e.g., Vidal-Madjar et al., 2003; Bourrier et al., 2013; Spake et al., 2018; Allart et al., 2018). This highest part of the atmosphere, where the composition is mostly atomic and ionic, can be probed by UV observations (see e.g., Vidal-Madjar et al., 2003, 2004; Fossati et al., 2010; Bourrier et al., 2013; Ehrenreich et al., 2015; Bourrier et al., 2018; Wakeford et al., 2020).

All together, exoplanets are powerful laboratories to test our atmospheric models. Observations of these exoplanets in the UV, optical, and/or infrared can provide new insights into how nature works over a much wider range of physical conditions than here on planet Earth. Particularly, the short periods of most transiting exoplanets, their strong irradiation, and their tidal lock can make these worlds prime targets to explore and understand strong day-night temperature contrasts, photochemical processes, and additional physical processes uncommon in other astrophysical objects.

1.5.2 *Clouds and Hazes*

Clouds and hazes are ubiquitous in the solar system planets and exoplanet atmospheres. An important distinction, however, is that most exoplanets found and characterized to date are significantly hotter than most planets in the solar system. Therefore, the composition of the clouds

and hazes that may be present in hot exoplanets will be significantly different to our solar system expectations. Indeed, the temperature of these hot Jupiters is close to the condensation temperatures of silicates and iron, making such condensation clouds a theoretical possibility (Seager & Sasselov, 2000). While silicates and metal oxides are expected to be the main cloud components for hotter atmospheres, sulphur-bearing compounds can be expected for cooler atmospheres (e.g., Morley et al., 2012; Wakeford & Sing, 2015; Sing et al., 2016; Helling, 2019). As for their origin, clouds are thought to be the result of condensation chemistry while hazes are thought to be the result of photochemistry or other non-equilibrium chemical process (Marley et al., 2013; Helling, 2019). Clouds and hazes are important for the physical processes in an atmosphere as their presence or absence can have strong implications for the atmospheric chemistry, radiation transport, and energy budget (Marley et al., 2013).

The presence of clouds and hazes is expected to have an imprint in the transit spectra of exoplanets in the form of muted (e.g., weaker) spectral features (e.g., Marley et al., 1999; Brown, 2001; Fortney, 2005; Kitzmann et al., 2011; Sing et al., 2016) and Rayleigh-like slopes in the optical (e.g., Seager & Sasselov, 2000; Pont et al., 2008; Lecavelier Des Etangs et al., 2008). Several forward models have explored the formation and spectral imprint of clouds and hazes in exoplanet atmospheres (e.g., Ackerman & Marley, 2001; Helling et al., 2008; Wakeford & Sing, 2015; Pinhas & Madhusudhan, 2017). These models have ranged from simple one-dimensional semi-analytic/parametric approaches (e.g., Lecavelier Des Etangs et al., 2008; Heng et al., 2012; Pont et al., 2013; Line & Parmentier, 2016; Heng, 2016; Powell et al., 2018), to more complex three-dimensional GCMs (e.g., Parmentier et al., 2013; Lee et al., 2016; Lines et al., 2019; Steinrueck et al., 2021). Nonetheless, sometimes even the most complex of models fail to explain (i.e., fit) current low resolution observations of hot Jupiters (e.g., Lines et al., 2019; Steinrueck et al., 2021). Determining the specific spectral characteristics of clouds and hazes as a function of wavelength, pressure, temperature, chemical composition, particle size, etc., is an active area of research in exoplanet sciences being addressed not only via the theoretical advancements described above but also through state-of-the-art laboratory experiments (e.g., Hörst et al., 2018; Moran et al., 2020).

On the other hand, the inference of clouds and hazes using inverse models is performed adopting parametric models. These parametric models aim to reproduce the theoretically expected imprints of clouds

and hazes in a spectrum (e.g., weaker features due to clouds, or Rayleigh like slopes due to hazes) without necessarily translating to a physical interpretation. The majority of existing parametric cloud and haze treatments in atmospheric retrievals (e.g., Lecavelier Des Etangs et al., 2008; Lee et al., 2013; Line & Parmentier, 2016; MacDonald & Madhusudhan, 2017a; Kitzmann & Heng, 2018; Barstow, 2020) serve the goal of marginalizing their impact so as not to bias inferences of the atmospheric composition or vertical temperature structure. This goal has been deemed acceptable considering current low resolution spectrophotometric observations. Nonetheless, the rapid progress of the field and the promise of next-generation observational facilities invites us to reconsider this goal and explore the possibility of inferring fundamental cloud and haze physical properties using yet to be developed, more sophisticated, parameterizations. Such parameterizations will largely aid from the physical understanding that forward models can provide.

1.5.3 *Planet Formation*

Exoplanet atmospheres can provide a powerful record of their planetary formation and migration history. Their observed chemical composition is a 'journal' describing where the planet formed, how it formed, and the processes experienced during its lifetime. In a nutshell, the present chemical composition of the planet atmosphere is a product of the formation environment (e.g., the composition of the gas and solids in the protoplanetary disk at a particular time and location, Öberg et al., 2011; Eistrup et al., 2018). However, deciphering this 'journal' is non-trivial and is one of the most ambitious goals of exoplanetary science. Several studies have explored the observable composition of exoplanet atmospheres and their connections to different formation pathways (e.g., Mousis et al., 2012; Helling et al., 2014; Madhusudhan et al., 2014c; Mordasini et al., 2016; Booth et al., 2017). Below we present an introductory overview of this active area of research.

Conceptually, the first step is to consider how planets are formed. Two main theories for planet formation are widely considered: gravitational instability (e.g., Boss, 1997, 2000) and core accretion (e.g., Pollack et al., 1996; Lissauer, 2004) . Gravitational instability is the process that happens when thermal pressure inside the disk is overwhelmed by the disk's self gravity and it collapses into planetary-mass fragments (Boss, 1997). Gravitational instability is thought to happen early in the history of the disk, when there has been little time for chemical pro-

cessing (D'Angelo & Lissauer, 2018). Therefore, planets formed by this mechanism are expected to have the same bulk composition as their local protoplanetary disk material. If we assume that the initial composition of the protoplanetary disk is the same as the host star, planets formed by gravitational instability will have the same metallicity as their host stars. Core accretion, on the other hand, refers to the process in which collisions of planetesimals form a protoplanetary core. Once formed, and once the protoplanetary core reaches a threshold mass, the core can accrete surrounding gas from the protoplanetary disk (Pollack et al., 1996). If the accreting core is massive enough to retain sufficient gas, the accretion will happen in a runaway fashion, and the resulting planet will be a gas giant. Otherwise, if the core could not accrete enough gas to reach the runaway accretion stage, the resulting planet could be a super-Earth (Schlichting, 2018). The metallicity of the planets formed by core accretion will depend on the composition of the material accreted in both gas and solid phases.

Theoretical studies have investigated the atmospheric imprint of these formation processes. For instance, using models for the formation and evolution of exoplanets (e.g., so called population synthesis models) Fortney et al. (2013) and Mordasini et al. (2016) suggest that planet formation by core accretion results in increasing atmospheric metallicity (e.g., the abundance of elements other than H and He) with decreasing mass. If the planet is small and cannot accrete significant amounts of gas, the accreted planetesimals will largely contribute to its metallicity. This trend of increasing metallicity with decreasing planetary mass seems to be present for the giant planets in our solar system. The derived metallicity from the methane abundance in Jupiter, Saturn, Neptune, and Uranus (Atreya et al., 2018) shows a trend of decreasing metal enrichment with increasing mass. Therefore, we could extend these predictions to exoplanetary atmospheres and aim to distinguish the process by which they formed. If formed by core accretion, lower mass planets will have a higher metallicity. Conversely, if the planets formed by gravitational instability, the atmospheric composition will be that of the local protoplanetary disk and could in principle match the metallicity of their host star.

A second step in our conceptual understanding of planetary formation is to consider where and when planets form. For that, we must consider the evolution of the protoplanetary disk. The thermodynamic properties of the disk will change with time, especially as the disk cools in time. As the disk cools, the snow lines of different chemical species

(i.e., the regions in space where sublimation happens) move closer to the star. This movement of the snow lines results in the evolution of the composition of the protoplanetary disk as a function of time and space. The snow lines commonly considered are those for H_2O, CO_2, CO, CH_4, and N_2, listed here in order from closest to furthest from the host star. Inside a snow line, the chemical compound contributes to the composition of the gas in the disk, whereas outside the snow line the compound remains in solids. Therefore, for example, the gas composition beyond the CO_2 snow line is dominated by CO and is poor in other oxygen-bearing molecules. This results in an increasing ratio between carbon-bearing molecules and oxygen-bearing molecules (C/O) in the gas composition of the disk (Öberg et al., 2011).

Consequently, the chemical composition of a planet will depend on where and when it formed as the composition of the material available will also change as a function of time and location. Additionally, since planets can migrate through the disk, their composition will be affected by their migration history and the composition of the material they accrete. By comparing the ratios of different chemical compositions (e.g., C/O) we can obtain valuable information about the location in the disk in which the planet formed and the physical properties of the accretion disk. Therefore, constraining the atmospheric C/O ratio in order to constrain the planetary formation and migration mechanisms (e.g., Madhusudhan et al., 2014c) is a key science goal of atmospheric characterization of exoplanets.

Clearly, what started as a basic picture rapidly becomes a more complex history of interconnected and stochastic processes. As such, pinpointing the exact formation history of an exoplanet from its present-day atmospheric abundance alone is a challenging and daunting task. An alternative approach is to address population level hypotheses regarding the origin and evolution of planets by using atmospheric observations of multiple exoplanets and theoretical studies that simulate the different formation and evolution scenarios (e.g., Madhusudhan et al., 2014c; Mordasini et al., 2016; Cridland et al., 2016; Ali-Dib, 2017; Madhusudhan et al., 2017; Booth et al., 2017). Detailed overviews of end-to-end studies, their connection to observations, and planet formation mechanisms are available in Madhusudhan et al. (2016); D'Angelo & Lissauer (2018); Mordasini (2018) and Madhusudhan (2019).

1.5.4 *Habitability and Biosignatures*

Arguably the most tantalizing aspect of exoplanetary atmospheric science is the assessment of habitability and detection of biosignatures. The commonality of Earth-sized exoplanets (e.g., Fulton et al., 2017, see also Section 1.2) and the fact that many of these have equilibrium temperatures conducive for liquid H_2O to exist on their surfaces (Madhusudhan, 2019), suggest that other planets with habitable conditions as we know on Earth could exist. While an Earth-twin has yet to be discovered and atmospherically characterized, the atmospheric characterization of terrestrial exoplanets around M-dwarfs (e.g., TRAPPIST-1, Gillon et al., 2016; de Wit et al., 2018) and the technical improvements in upcoming observational facilities (e.g., JWST, Greene et al., 2016), and the 30m-Class Telescopes (e.g., Snellen et al., 2013; Rodler & López-Morales, 2014) make the detection of life signatures beyond Earth a goal attainable within our lifetime. Below we briefly summarize two aspects related to atmospheric model improvement as a preparatory effort towards the detection of biosignatures and assessment of habitability. We refer the reader to specialized reviews on the multiple considerations surrounding planet habitability and its detectability (e.g., Madhusudhan et al., 2016; Meadows & Barnes, 2018; Fujii et al., 2018; Catling et al., 2018; Seager, 2018; Madhusudhan, 2019).

The existence of an absolute biosignature is an active area of research. As suggested by Seager et al. (2016), a biosignature should not have false positives, it should have strong spectral features to be detectable, and it should be abundant enough to be detectable. Multiple individual chemical species, or combinations of them, have been put forward as possible biosignatures including O_2, O_3, N_2O, and CH_4 (e.g., Lederberg, 1965; Lovelock, 1965; Schindler & Kasting, 2000; Segura et al., 2003; Kaltenegger et al., 2007). Whether these chemicals and their combinations can have abiotic origins is still being investigated (Wordsworth & Pierrehumbert, 2014; Luger & Barnes, 2015; Harman et al., 2015). However, if and when a definitive biosignature is proposed, the reliability of any associated detection will be paramount. As a result, the development of robust and reliable atmospheric models that can help detect such biosignature is a complementary first step that must be taken. When the time comes, atmospheric forward and inverse models will have to inform the confidence of the detection and the atmospheric processes that could have had an impact on it.

Secondly, the information encoded in the atmospheric observations of an exoplanet will advance our understanding of its possibly habitable conditions. An exoplanet residing in the habitable zone of its host star is not habitable by default. Additional considerations such as the amount of UV radiation to which the planet is subject, could determine whether the planet is amenable to life as we know it (e.g., Segura et al., 2010; Kaltenegger, 2017). Moreover, as explained in Section 1.5.1, atmospheric observations of these planets could inform our understanding of their vertical temperature structure, overall chemical composition, and the possibility of chemical disequilibrium, all important factors in the assessment of potential habitability. Recent studies have used these inferences as a starting point for end-to-end modeling of the atmosphere and interior of the planet in order to appraise the potential for habitable conditions (Madhusudhan et al., 2020). Consequently, in our efforts to characterize Earth-like planets around nearby stars, we must acquire a thorough understanding of the limits of the data and models used to reliably extract physical parameters such as atmospheric pressure-temperature and chemical abundances.

1.6 SCOPE OF THIS THESIS

Throughout this introduction, we have presented an overview of the different methods to detect and characterize exoplanet atmospheres. While they are all complementary and powerful in their own ways, this dissertation focuses on the interpretation of transmission spectra. As previously explained, transmission spectra encode information about the atmosphere at the day-night terminator of the planet, through a wavelength dependent change in the apparent size of the planet. Particularly, transmission spectroscopy has been key in detecting and quantifying the abundances of multiple molecules and atoms (e.g., Charbonneau et al., 2002; Deming et al., 2013; Kreidberg et al., 2014b, 2015; Nikolov et al., 2018; Wakeford et al., 2018), as well as providing some insight into the clouds and hazes present in exoplanet atmospheres (e.g., Pont et al., 2008; Sing et al., 2016; Nikolov et al., 2018; Benneke et al., 2019b).

The multiple advancements described above attest to the maturity of the field. However, many areas remain unexplored and in need of development. As we advance towards the next scientific horizon in exoplanet characterization, questions about the robustness and reliability of our interpretations arise. Reliable atmospheric characterization requires deep understanding of the limitations and abilities of our atmospheric models.

Armed with this understanding, we can begin to perform homogeneous studies to interpret currently available spectroscopic observations. Moreover, the promise of an incoming diverse population of exoplanets with spectroscopic observations highlight the need for generalized and agnostic atmospheric interpretation tools. Here we briefly provide an outline of the motivation and underlying questions for the work contained in this thesis.

1.6.1 *Understanding Degeneracies in Retrievals of Exoplanetary Transmission Spectra*

Accurate estimations of atmospheric properties of exoplanets from transmission spectra require the understanding of degeneracies between model parameters and observations that can resolve them. In Chapter 2 we conduct a systematic investigation of such degeneracies using a combination of detailed atmospheric retrievals and a range of model assumptions, focusing on H_2-rich atmospheres. As a case study, we consider the well-studied hot Jupiter HD 209458 b. We perform extensive retrievals with models ranging from simple isothermal and isobaric atmospheres to those with full pressure-temperature profiles, inhomogeneous cloud/haze coverage, multiple molecular species, and data in the optical-infrared wavelengths. Our work aims to provide insights into the following questions:

- What are the data and model combinations that allow for precise estimates of chemical abundances using transmission spectra?
- Are there any inherent model degeneracies that fundamentally hinder parameter inferences?
- What are the minimum model considerations required to adequately interpret current spectroscopic observations?

Through this work we explore the adequacy or inadequacy of both simplified semi-analytic models with isobaric assumptions, and fully numerical models with physically motivated assumptions for reliable retrievals of transmission spectra. Only by performing such a study can we assess our ability to obtain strong constraints on atmospheric abundances of exoplanets with current facilities such as HST, VLT, and the upcoming JWST and ground-based facilities. The contents of this chapter are based on the published work of Welbanks & Madhusudhan (2019).

1.6.2 *Homogeneous Studies of Exoplanetary Transmission Spectra to Determine Population Level Trends*

The key advantage of extra-solar planetary science is the sheer number of objects which enable us to address population level hypotheses regarding the origin and evolution of planets. One major objective is to use measured atmospheric observable chemical abundances to test our hypothesis on the primordial formation pathways of exoplanets. As explained in Section 1.5.3, a key hypothesis is that the metallicity of a planetary atmosphere should increase with decreasing mass (e.g., Fortney et al., 2013; Mordasini et al., 2016), a hallmark of the core-accretion model of planet formation and a trend that appears within the solar system Jovian planet population. Previous studies, focused on HST WFC3 (1.1–1.6 μm), have aimed to determine H_2O abundances relative to solar system planets (e.g., Madhusudhan et al., 2014b; Kreidberg et al., 2014b, 2015; Barstow et al., 2017; Pinhas et al., 2019). While many of these studies were able to determine H_2O abundances, there is tension in the underlying interpretation as there exists an intrinsic degeneracy between the atmospheric metal content and the elemental carbon-to-oxygen ratios, which can result in numerous ways to produce a given H_2O abundance (e.g., Madhusudhan et al., 2014c).

In order to break this intrinsic elemental abundance degeneracy, constraints on more species beyond H_2O are needed. Armed with the model and data understanding derived from the work presented in Chapter 2, we set out to determine population level composition trends leveraging data spanning the optical-to-near-infrared, covering not only H_2O, but the key metallicity tracers, sodium (Na) and potassium (K). While previous studies limited their efforts to hot Jupiters, we extended the sample to mini Neptunes providing a larger, more diverse sample to provide more leverage in scrutinizing key planet formation hypotheses. In total, we retrieve and analyze the atmospheric properties of 19 exoplanets ranging from cool mini Neptunes with temperatures close to 300 K to ultra-hot Jupiters with temperatures above 2700 K. The contents of Chapter 3 are based on the published work of Welbanks et al. (2019), and aim to provide an answer to the following questions:

- Is there a mass-metallicity trend for transiting exoplanets from atmospheric abundances of H_2O, Na, and K?
- If any mass-metallicity trends are observed, are they consistent with solar system expectations? are they consistent within themselves?

- Are there any constraints we can place on planetary formation mechanisms from the derived atmospheric abundances?

1.6.3 *Developing Next-generation, Generalized, Exoplanetary Atmospheric Bayesian Inference Frameworks*

Generally, the model complexity considered in atmospheric retrievals has largely been driven by the fidelity of the data (e.g., overly complex models are often not warranted). Due to their observational favorability, most spectro-photometric observations have been of hot Jupiters (e.g., Deming et al., 2013; McCullough et al., 2014; Kreidberg et al., 2015; Sing et al., 2016; Nikolov et al., 2018; Kirk et al., 2019). Nonetheless, and despite the inherent challenges that their small size represent, advancements in observing facilities (e.g., Gillon et al., 2011), large observing campaigns (e.g., Kreidberg et al., 2014a), as well as the so called M-dwarf opportunity (e.g., Scalo et al., 2007; Charbonneau & Deming, 2007) have allowed for tantalizing transmission spectra of mini Neptunes and super-Earths. Many of these spectroscopic observations have been featureless within current instrumental precisions either due to the presence of clouds muting all spectral features or due to a dense (e.g., non H rich, high mean molecular weight) atmosphere with small spectral features (e.g., Bean et al., 2010; Désert et al., 2011b; Kreidberg et al., 2014a; Knutson et al., 2014a,b; de Wit et al., 2016, 2018; Wakeford et al., 2019). Nevertheless, a handful of mini Neptunes (e.g., Benneke et al., 2019b; Tsiaras et al., 2019; Benneke et al., 2019c; Guo et al., 2020) have shown absorption features on possibly H-rich atmospheres.

As we look towards the future, additional observations of low mass exoplanets, including mini Neptunes and super-Earths theorized to present extreme compositional diversity (i.e., compositions ranging from H rich to H poor, e.g., Moses et al., 2013), promise to be attainable with upcoming facilities like JWST (e.g., Barstow et al., 2015; Greene et al., 2016) and the ELTs (e.g., Rodler & López-Morales, 2014; Kaltenegger, 2017). Moreover, the large number of upcoming spectroscopic facilities underscore the need for combining data sets from multiple observatories to infer the atmospheric properties of an exoplanet. An increasingly diverse planet population and higher fidelity data necessarily demand more flexible and complex Bayesian modeling frameworks.

This next generation of retrieval codes must incorporate the lessons learned from observations and studies of hot Jupiters. Furthermore, and in preparation for the upcoming observations of smaller temperate plan-

ets, methods for characterizing non H-dominated atmospheres must be implemented and updated to be compatible with the latest optimization algorithms. Upcoming codes should be able to expand their modeling functionalities motivated by data requirements. Lastly, with the increasing model complexity and data quality, new retrieval codes must be prepared for assessing multidimensional, highly degenerate problems.

We present in Chapter 4 our response to these needs in the form of Aurora, a new generalized exoplanetary atmospheric Bayesian inference framework for transmission spectra. Aurora is a next-generation atmospheric retrieval framework that builds upon state-of-the-art architectures and incorporates the following key advancements: (a) a generalized compositional retrieval allowing for H-rich and H-poor atmospheres, (b) a generalized prescription for inhomogeneous clouds/hazes, (c) multiple Bayesian inference algorithms for high-dimensional retrievals, (d) modular considerations for refraction, forward scattering, and Mie scattering, and (e) noise modeling functionalities.

Then, in Chapter 5 we validate Aurora on current and/or synthetic observations of the hot Jupiter HD 209458 b, mini Neptune K2-18b, and rocky exoplanet TRAPPIST-1 d. Using current HD 209458 b spectra, we appraise the robustness of our framework and cloud/haze prescription against assumptions of H-rich/H-poor atmospheres, improving on previous treatments. Using real and synthetic spectra of K2-18b, we appraise the agnostic approach to confidently constrain its bulk atmospheric composition and obtain precise abundance estimates. Then, for a rocky exoplanet like TRAPPIST-1 d, we assess our ability to identify the main atmospheric component on multiple atmospheric scenarios including CO_2-rich, and N_2-rich atmospheres.

The content presented in Chapter 4 and Chapter 5, draw from the published work of (Welbanks & Madhusudhan, 2021). Together, these chapters explore the following outstanding questions:

- What are the modeling advancements required to model H-rich and H-poor atmospheres using atmospheric retrieval frameworks?
- Do existing Bayesian inference algorithms provide consistent parameter estimates for exoplanet atmospheres using existing data?
- Can we perform agnostic retrievals on existing and upcoming spectroscopic observations of exoplanetary atmospheres to constrain their bulk composition?
- How many transits using the upcoming JWST are required to characterize a rocky exoplanet?

1.6.4 *Characterization of Exoplanetary Atmospheres Using Ground-based and Space-based Facilities*

Chapter 6 and Chapter 7 present some of the collaborative work we contributed to by performing the interpretation of exoplanetary transmission spectra using retrieval frameworks. The content in these chapters draws from the published works of Chen et al. (2018); von Essen et al. (2019); Chen et al. (2020); Madhusudhan et al. (2020); Colón et al. (2020) and Sheppard et al. (2021). These works illustrate the power of inferring the atmospheric properties of an exoplanet using transmission spectroscopy and retrieval frameworks. These studies include the first atmospheric indications of previously unidentified species in exoplanet literature. All together the contents in these chapters illustrate the broad diversity in planetary atmospheric composition. Broadly, these works explore the following question: What are the achievable atmospheric constraints using the latest spectroscopic data obtained with ground- and space-based facilities?

2

ON DEGENERACIES IN RETRIEVALS OF EXOPLANETARY TRANSMISSION SPECTRA

As explained in Section 1.6, reliable estimations of atmospheric properties of exoplanets from transmission spectra require the understanding of degeneracies between model parameters and the observations that can resolve them. In this chapter[1] we conduct a systematic investigation of such degeneracies using a combination of detailed Bayesian atmospheric retrievals and a range of model assumptions, focusing on H_2-rich atmospheres. In this chapter, we consider the canonical hot Jupiter HD 209458 b as a case study. We perform extensive retrievals with models ranging from simple isothermal and isobaric atmospheres, known to be unphysical, to those with full pressure-temperature profiles, inhomogeneous cloud/haze coverage, multiple chemical species, and data in the optical-infrared wavelengths, more physically plausible. Our study reveals four key insights. First, we find that a combination of models with minimal assumptions and broadband transmission spectra with current facilities allows precise estimates of chemical abundances. In particular, high-precision optical and infrared spectra, along with models including variable cloud coverage and prominent opacity sources, with Na and K being important in the optical, provide joint constraints on cloud/haze properties and chemical abundances. Second, we show that the degeneracy between planetary radius and its reference pressure is well characterized and has little effect on abundance estimates, contrary to previous claims using semi-analytic models. Third, collision-induced absorption due to H_2-H_2 and H_2-He interactions plays a critical role in correctly estimating atmospheric abundances. Finally, our results highlight the inadequacy of simplified semi-analytic models with isobaric assumptions for reliable retrievals of transmission spectra. Transmission spectra obtained with current facilities such as the Hubble Space Telescope and Very Large Telescope can provide strong constraints on atmospheric abundances of exoplanets.

1 The contents of this chapter are based on the published work of Welbanks & Madhusudhan (2019). As explained in Sections 2.2 and 2.3, the retrieval framework used in this work is an adaptation of AURA (Pinhas et al., 2018) developed in Prof. Nikku Madhusudhan's research group. Besides overall supervision of the paper, Prof. Nikku Madhusudhan contributed to the text in Section 2.5.

2.1 INTRODUCTION

Transmission spectroscopy of transiting exoplanets offers a powerful probe to study their atmospheres. Recent observational advancements have enabled high-precision transmission spectra of exoplanets over a broad spectral range ($\lambda \sim 0.3$–$2.0\mu m$). Such observations have been obtained in low resolution ($R = \lambda/\Delta\lambda \sim 100$–$300$) from space using Hubble Space Telescope (HST) spectrographs – the Space Telescope Imaging Spectrograph (STIS) in the NUV/Optical and the Wide Field Camera 3 (WFC3) in the near-infrared (e.g., Deming et al., 2013; Kreidberg et al., 2015; Sing et al., 2016). On the other hand, spectra of comparable quality have also been obtained recently, particularly in the visible range, from large ground-based facilities such as the Very Large Telescope (VLT) and the Gran Telescopio Canarias (e.g., Sedaghati et al., 2017; Chen et al., 2018; Nikolov et al., 2018).

The spectral range accessible to current facilities has the capability to constrain a wide range of atmospheric properties. While the near-infrared spectral range (1.1–1.7 μm) of the WFC3 contains strong spectral features, due to H_2O (Deming et al., 2013), the visible range probes features of several other species expected in hot Jupiters such as Na, K, TiO, VO, etc. (e.g., Sing et al., 2016; Nikolov et al., 2016; Sedaghati et al., 2017). In addition, optical spectra can also provide important constraints on the possibility and properties of clouds and hazes (e.g., Brown, 2001; Line & Parmentier, 2016; Barstow et al., 2017; MacDonald & Madhusudhan, 2017a). Statistical constraints on these various properties have been reported from such datasets using rigorous atmospheric retrieval methods for various planets (e.g., Madhusudhan et al., 2014b; Kreidberg et al., 2015; Barstow et al., 2017; MacDonald & Madhusudhan, 2017a). It is clear from these studies that reliable estimates of atmospheric properties using retrievals of transmission spectra rely heavily on a thorough understanding of the model degeneracies and the capability of the data to resolve the same.

The role of degeneracies in interpreting transmission spectra has been investigated in some detail since the beginning of the field. Several early studies highlighted the importance of various atmospheric properties (e.g., clouds, temperature, composition) on observable spectral features (e.g., Seager & Sasselov, 2000; Brown, 2001; Fortney, 2005). For example, Brown (2001) alluded to possible degeneracies between chemical abundances, temperature structure, and the presence of clouds.

Later, Lecavelier Des Etangs et al. (2008) noted the degeneracy between chemical abundance and the reference pressure in the atmosphere. Using transit spectroscopy to measure the effective radius, it was possible to derive the pressure assuming an abundance or assuming a pressure to derive the abundance.

While the above early works sought to explore the degeneracies using semi-analytic or equilibrium forward models, the advent of retrieval techniques in the last decade (Madhusudhan & Seager, 2009) allowed this problem to be investigated with a rigorous statistical approach. Benneke & Seager (2012) studied the degeneracies involved in retrieving transmission spectra of super-Earths and mini-Neptunes using synthetic spectra. They explored the interplay among chemical composition, cloud top pressure, planetary radius, and/or surface pressure in determining the spectral features and suggested combinations of observables that could resolve the degeneracies in different cases. Benneke & Seager (2013) commented on the degeneracy between the mean molecular mass and cloud top pressure, which is present in transmission spectra especially for low-mass planets.

de Wit & Seager (2013) showed that the slant-path optical depth at the reference radius depends on the scale height, reference pressure, temperature, and the number densities of the absorbers present in the atmosphere in unique ways, making their retrieval possible with high-quality data. Such constraints, in principle, also allow the planetary mass to be determined from the transmission spectrum using the retrieved gravity through the scale height (de Wit & Seager, 2013), but can be challenging for low-mass planets (Batalha et al., 2017b).

Griffith (2014) suggested that there can be a broad range of degenerate solutions to fit infrared data which make constraining molecular abundances challenging. Nonetheless, they suggest ways in which the degeneracy can be resolved. For example, they suggest measuring the radius of the planet at a wavelength where the atmosphere's opacity, is known, e.g., Rayleigh scattering in the optical.

Line & Parmentier (2016) explored the influence of nonuniform cloud coverage in transmission spectra. They quantitatively explored the degeneracy between clouds and mean molecular weight within an atmospheric retrieval framework. They found that partial and fully cloudy atmospheres are distinguishable, and that the visible wavelengths offer an opportunity to break degeneracies between mean molecular weight and cloud coverage.

The effects of clouds and other surfaces have been studied by Bétrémieux (2016) and Bétrémieux & Swain (2017, 2018). Among their findings are the conclusions that spectral signatures in the optical encode information useful to break degeneracies between retrieved abundances and the planet's radius, and that collision-induced absorption (CIA) potentially determines the highest pressures that can be probed in exoplanetary atmospheres in the infrared. An alternative to breaking the innate degeneracy between clouds and chemistry was offered by MacDonald & Madhusudhan (2017a) by introducing a two-dimensional inhomogeneous cloud coverage.

Lastly, Heng & Kitzmann (2017) highlighted a potential three-way degeneracy among H_2O abundance, reference pressure (P_{ref}) and planet radius (R_p) using semi-analytic models. Their conclusions about this degeneracy were based on assumptions of isobaric and isothermal atmospheres with H_2O as the only molecular opacity source. Our present work investigates this further.

In this thesis, we conduct a detailed analysis of the effect of model parameterization and spectral coverage of data on atmospheric retrievals of transmission spectra. Such an analysis also helps us explore some of the key degeneracies previously discussed in the literature using semi-analytic models. Employing retrieval techniques, we test a series of atmospheric models with varying levels of complexity. In Section 2.2, we start by reproducing the results of previous analytic studies. We discuss the validity of their interpretations and use their assumptions as a starting point for our study. In Section 2.3, we perform a step-by-step analysis of model dependencies with retrievals using the canonical hot Jupiter HD 209458 b as our case study.

We start with retrievals assuming a simplistic clear, isothermal, and isobaric planetary atmosphere and using infrared data alone. We sequentially improve the model considerations culminating in a realistic atmospheric model with a full pressure-temperature (P–T) profile, inhomogeneous clouds, collision-induced opacities, and multiple chemical species. We also study the impact of including data in the optical wavelengths instead of using only data in the near-infrared. For each of these cases, we investigate the constraints on the retrieved parameters and our ability to determine the chemical abundances, especially that of H_2O. In Section 2.4, we assess the ability of our retrievals to constrain atmospheres with high cloud fractions. Lastly, in Section 2.5, we revisit the notion of a three-way degeneracy between X_{H_2O}, R_p, and P_{ref}. We show that the degeneracy between R_p and P_{ref} is real and well character-

ized, but has no effect on the abundance estimates, contrary to previous assertions. We also show that the choice of an R_p versus P_{ref} as a free parameter is inconsequential to constraining molecular abundances when a full retrieval study is performed. We summarize our findings in Section 2.6.

2.2 THE R_p–P_{ref}-H_2O DEGENERACY

In this section we illustrate some of the key degeneracies inherent to transmission spectra. We begin with a qualitative illustration using model spectra. We generate four forward models showing different combinations of R_p, P_{ref}, and X_{H_2O}, spanning optical and infrared wavelengths. The forward models are generated using parameters for HD 209458 b with $\log_{10}(g) = 2.963$ in cgs and a stellar radius of 1.155 $R_\odot$ (Torres et al., 2008). The models shown here were chosen by inspection and use a parametric P–T profile with the parameters described by Madhusudhan & Seager (2009) with values of $\log_{10}(P_1) = -1.65$, $\log_{10}(P_2) = -4.02$, $\log_{10}(P_3) = 0.48$, $\alpha_1 = 0.67$, $\alpha_2 = 0.58$ and temperature of $T_0 = 1435$ K. The choice of P–T profile parameters are within 2σ of the best-fit values reported by MacDonald & Madhusudhan (2017a).

The models have 100 pressure layers equally spaced in log-pressure between 10^{-6} and 10^2 bar. Our prescription considers the effects of H_2 Rayleigh scattering and CIA due to H_2-H_2 and H_2-He interactions and is adapted from the work of Pinhas et al. (2018). The only other source of opacity considered in these illustrative models is H_2O. The model setup is discussed in more detail in Section 2.3.

The models are shown in Figure 9 and depict the degeneracies in cloud-free atmospheres. These models show that some spectral features in the infrared can be mimicked by different combinations of H_2O abundance, radius, and reference pressure. While the degeneracy among radius, pressure, and molecular mixing ratio allows multiple models to show similar spectral features in the infrared, there are significant differences at shorter wavelengths (i.e., below 1 μm). These differences at shorter wavelengths are the result of setting the baseline of the spectrum to different levels by changing R_p and/or P_{ref}.

As alluded to in Section 2.1, several works in the past have discussed possible degeneracies in transmission spectra (e.g., Lecavelier Des Etangs et al., 2008; Benneke & Seager, 2012; de Wit & Seager, 2013; Griffith, 2014; Bétrémieux & Swain, 2017). One of the often discussed degeneracies is that between chemical abundance and reference pressure in the

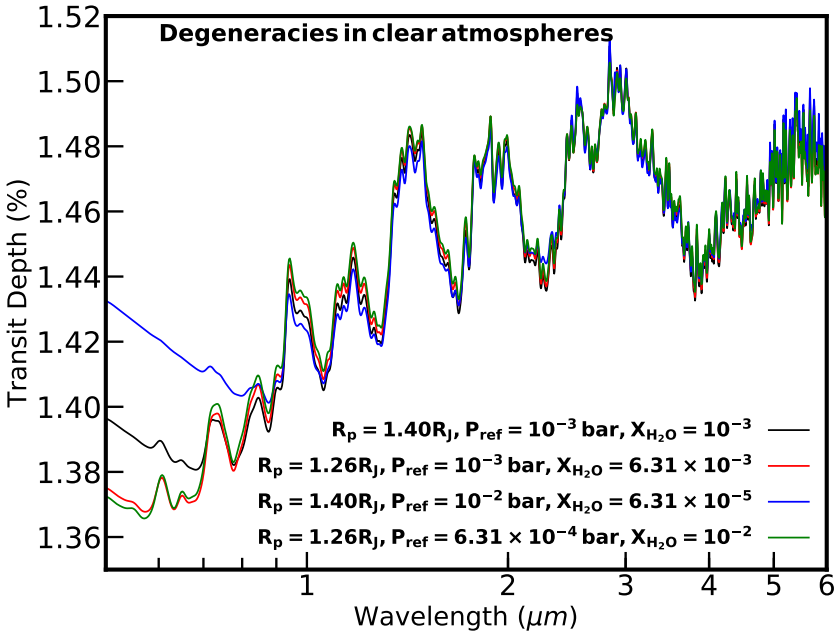

Figure 9 Degeneracies in clear atmospheres. Clear atmospheres can produce similar absorption features while having different chemical and physical properties. Spectra in red, blue, and green include variations of two or three parameters that are still capable of generating features similar to the reference spectrum shown in black. There is a clear difference in the spectra at shorter wavelengths.

atmosphere for the observed radius. Such a degeneracy was formally investigated using semi-analytic models by Lecavelier Des Etangs et al. (2008). Their work presents the effective altitude z of the atmosphere at a wavelength λ as

$$z(\lambda) = H \ln\left(\xi_{abs} P_{z=0} \sigma_{abs} / \tau_{eq} \times \sqrt{2\pi R_P / kT\mu g}\right), \tag{7}$$

where H is the scale height, and σ_{abs} and ξ_{abs} are the cross section and abundance (volume mixing ratio) of the dominant absorbing species, respectively. τ_{eq}, also known as equivalent optical depth, is the slant optical depth at an altitude z_{eq} such that the contribution of an equivalent planet completely opaque below this altitude produces the same absorption as the planet with its translucent atmosphere. $P_{z=0}$ is the reference pressure at an altitude $z = 0$ corresponding to R_P, the measured radius of the planet. Additionally, g is the gravity of the planet, k the Boltzmann constant, T the temperature of the atmosphere, and μ the

mean molecular mass of the atmosphere. This expression is one of the first indications of a degeneracy between the reference pressure and the chemical abundance. Lecavelier Des Etangs et al. (2008) concluded that to derive an abundance, a reference pressure needs to be assumed or vice versa.

Variants of this expression have also been derived from first principles in other studies (de Wit & Seager, 2013; Bétrémieux & Swain, 2017; Sing, 2018). The expression was later used by Heng & Kitzmann (2017, hereafter HK17) in the following form:

$$R = R_0 + H\left[\gamma + \ln\left(\frac{P_0\kappa}{g}\sqrt{\frac{2\pi R_0}{H}}\right)\right], \tag{8}$$

where R_0 is the radius of the planet at the reference pressure (R_p in this chapter), P_0 is the reference pressure (P_{ref} in this chapter), H is the scale height, g is the gravity of the planet, and κ is the cross section per unit mass. The functional form of κ in the work of HK17 is

$$\kappa = \frac{m_{H_2O}}{m} X_{H_2O} \kappa_{H_2O} + \kappa_{cloud}, \tag{9}$$

with $m_{H_2O} = 18$ amu being the molecular mass of H_2O, X_{H_2O} the volume mixing ratio of H_2O, and κ_{H_2O} the water opacity. The additional term, κ_{cloud}, is a constant opacity associated with clouds or aerosols. Inspecting Equations 8 and 9, a potential degeneracy among X_{H_2O}, P_{ref} and R_p becomes evident. However, the derivation of HK17 used assumptions of an isothermal and isobaric opacity along with H_2O as the only molecular opacity source. In what follows, we investigate these assumptions and consider other opacity sources that can be important.

2.2.1 *On the X_{H_2O}–P_{ref}–R_p Degeneracy*

Here, we further investigate the three-way degeneracy claimed by HK17. The basis of the HK17 study is a semi-analytic model shown in Equation 8, which was used to fit an observed transmission spectrum of the hot Jupiter WASP-12b in the near-infrared ($\sim$ 1.15–1.65 μm) obtained using the HST WFC3 spectrograph (Kreidberg et al., 2015). The model assumed an isothermal atmosphere with isobaric opacities, with H_2O as the only molecular opacity source. The model was fit to the near-infrared spectrum using a nonlinear least-squares fitting routine to obtain best-fit

values of different combinations of parameters for an assumed value of R_p. By repeating the fits for a range of R_p values, they investigated the degeneracy among X_{H_2O}–P_{ref}–R_p.

To investigate the potential three-way degeneracy reported by HK17, we follow two approaches. We first reproduce the results of HK17 using their approach, i.e., their semi-analytic model and least-squares fit to the WFC3 transmission spectrum of WASP-12b. We then reproduce the same results using their semi-analytic model in a Bayesian retrieval approach. We later include additional opacity due to H_2-H_2 and H_2-He CIA in the HK17 model to investigate the validity of their assumptions. With CIA included, we follow the same two approaches, i.e., first employing a nonlinear least-squares fit and then a Bayesian retrieval.

We begin by following the approach of HK17 and performing a fit to the WASP-12b WFC3 data using Equation 8 with a least-squares minimization routine (`curve_fit` in Python). Our model considerations are identical to those in HK17, e.g., isothermal atmosphere and isobaric H_2O opacity. The top-left panel of Figure 10 shows our results reproducing Figure 7 of HK17. At the outset, we notice two discrepancies. First, we are able to reproduce the fit in HK17 using the log of $X_{H_2O}(P_{ref}/10\ \text{bar})$ versus R_p. However, HK17 presented their y-axis as $X_{H_2O}(P_{ref}/10\ \text{bar})^{-1}$. We interpret this as a typographical error in HK17. This is especially the case considering that Equation 8 implies the product of X_{H_2O} and P_{ref}, and also considering Figures 3 to 8 of Fisher & Heng (2018) who use the same model and notation. Second, HK17 claimed from this figure that X_{H_2O} is strongly degenerate with R_p, i.e., that the H_2O abundance varies by many orders of magnitude with slight changes in R_p. However, it is not possible to deduce information about the H_2O abundance from this figure alone given that only the product $X_{H_2O}(P_{ref}/10\ \text{bar})$ is shown to be degenerate with R_p and not X_{H_2O} or P_{ref} individually.

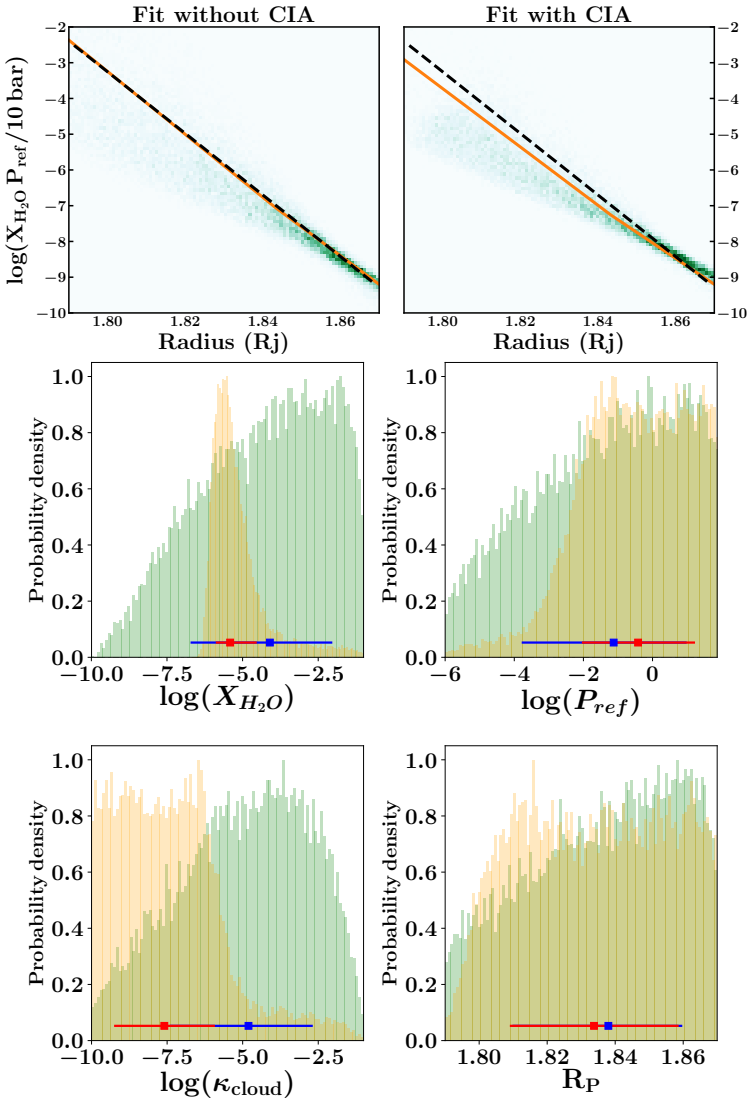

Figure 10 Top row: product of H_2O abundance and reference pressure (P_{ref}) vs. the reference radius (R_p) for simplistic model fits to the WFC3 spectrum of WASP-12b. The left panel shows fits without CIA opacity, and the right panel shows fits considering the effect of CIA. The black dashed line shows the result from Figure 7 of Heng & Kitzmann (2017), hereafter HK17. The orange solid line is our result using the analytic formulation and the same three-parameter fit of HK17. While the orange line matches exactly with the HK17 result in the left panel, it deviates from the same in the right panel, due to the inclusion of CIA opacity. The green two-dimensional histograms in the background show the same quantities using the posterior distributions from Bayesian retrievals of the same parameters. Bottom rows: posterior distributions from the retrievals corresponding to the top panels. Green (orange) shows the histograms for the retrievals without (with) CIA, while the median values and 1σ uncertainties are shown in blue (red). The posterior distributions show the retrieved H_2O abundances (volume mixing ratios), P_{ref} (in bar), κ_{cloud} (in m^2 kg^{-1}), and R_p (in R_J). The introduction of CIA in the right panel improves the constraint on the H_2O abundance.

Next, we study this problem using a Bayesian retrieval approach. Our retrieval code is adapted from the works of Pinhas et al. (2018) to consider the semi-analytic model and assumptions discussed above. We replace the numerical model of Pinhas et al. (2018) with the semi-analytic model of HK17 while retaining the module for Bayesian parameter estimation using the nested sampling algorithm (Feroz et al., 2009; Buchner et al., 2014). The model parameters remain the same as in HK17, namely X_{H_2O}, P_{ref}, κ_{cloud}, R_p, and T, the isothermal temperature. The prior range for the radius is $R_p = 1.79\ R_J$ to $1.87\ R_J$ to match the range shown in Figure 7 of HK17 and the prior range of $\log_{10}(P_{ref})$ is from -6 to 2 in bar. Both the $\log_{10}(X_{H_2O})$ (volume mixing ratio) and $\log_{10}(\kappa_{cloud})$ ($m^2\ kg^{-1}$) priors are from -1 to -10. The temperature prior is from 500 to 2000 K. Similarly, we consider an isothermal atmosphere, isobaric H_2O opacity (at 1mbar), a fixed mean molecular weight of 2.4 amu, and a fixed gravity of $\log_{10}(g) = 2.99$ in cgs (Hebb et al., 2009).

The results from the retrieval are shown in green in the top-left panel of Figure 10. We show the posteriors from the retrieval as a two dimensional histogram of $X_{H_2O}(P_{ref}/10\ bar)$ against the retrieved R_p. The bottom four panels of Figure 10 show the posterior distribution of the H_2O abundance, P_{ref}, κ_{cloud}, and R_p in the green histograms. Our retrieval finds an unconstrained H_2O abundance with a median abundance of $\log_{10}(X_{H_2O}) = -4.10^{+2.06}_{-2.62}$. We find that the posterior distributions from the retrieval closely follow the results from the linear fit (i.e., orange line) as shown in the topmost left panel.

We now investigate the validity of the assumptions of the semi-analytic model above by including CIA as an additional source of opacity. The importance of CIA as a continuum source of opacity is highlighted in several previous studies (e.g., de Wit & Seager, 2013; Bétrémieux & Swain, 2017, 2018), which makes its inclusion imperative in model spectra of giant planets. We amended the total opacity in the formulation of HK17, shown in Equation 9, to

$$\kappa = \frac{m_{H_2O}}{m} X_{H_2O} \kappa_{H_2O} + \kappa_{cloud} + \kappa_{CIA}, \tag{10}$$

where the first two terms remain as explained above. The third term is opacity due to H_2-H_2 and H_2-He CIA. This and other opacity sources are discussed in Section 2.3.

We follow the approach described above by performing a least-squares fit of the amended model to the near-infrared data. The additional opacity source (i.e., CIA) is computed following the same method used to

compute H_2O opacity in HK17, and we preserve the assumption of an isobaric atmosphere by evaluating the opacities at 1 mbar. We find that the inclusion of CIA changes the slope of the resulting linear relationship between $X_{H_2O}(P_{ref}/10\ \text{bar})$ and R_p. Our resulting fit is shown as an orange solid line in the top-right panel of Figure 10, where we also show the fit of HK17 using a dashed black line. This analytic fit shows that the slope of the relation between $X_{H_2O}(P_{ref}/10\ \text{bar})$ and R_p has changed. Again, it is not possible to infer from this result if R_p is degenerate with X_{H_2O} or P_{ref} or both. In comparison, a retrieval approach would provide the necessary insight as pursued above.

We, therefore, now perform a retrieval using the modified model including CIA opacity. Our retrieval approach keeps the previous description although in this case we add the pressure-dependent effects of CIA. This retrieval study finds a better constrained H_2O abundance with a median of $\log_{10}(X_{H_2O}) = -5.41^{+0.88}_{-0.47}$. Similarly to the previous retrieval, we present in the background of the top-right panel of Figure 10 the two dimensional histogram of $X_{H_2O}(P_{ref}/10\ \text{bar})$ against R_p. We also show the posterior distributions of the retrieved parameters including the H_2O abundance for this case in the bottom orange histograms. We find that the inclusion of CIA opacity results in a better constraint on the H_2O abundance even within the framework of this simplistic model.

Our results above demonstrate two main points. First, the retrieved molecular abundance changes with the inclusion of CIA. The inclusion of CIA opacity provides a continuum to the spectrum that sets the maximum pressure probed in the atmosphere, i.e., the line-of-sight photosphere (de Wit & Seager, 2013; Line & Parmentier, 2016; Bétrémieux & Swain, 2018). As a result, the thickness of the atmospheric column probed by the transmission spectrum decreases compared to the non-CIA scenario, thereby requiring a different H_2O abundance to explain the data. Second, the log-linear behavior seen in both panels of Figure 10 is likely strongly influenced by a relation between P_{ref} and R_p, irrespective of the H_2O abundance. We further discuss this relation in detail in Section 2.5. The constraint on the H_2O abundance improves with the inclusion of CIA, irrespective of any degeneracy between P_{ref} and R_p. Nevertheless, the H_2O abundance is still weakly constrained even in the CIA case. However, this is not due to a three-way degeneracy but rather a result of incomplete model assumptions and limited data. We demonstrate this in more detail in the next section.

In summary, these results show that the conclusions of HK17 are likely due to the restricted model assumptions. The lack of consideration of

CIA opacity, among other factors, is likely responsible for their conclusions. We discuss this further in Section 2.5.3. The three-way degeneracy noted in HK17 manifests itself fully under idealized conditions encapsulated in the analytic formalism of Equation 8, namely an isothermal, isobaric, constant mean molecular weight, constant gravity, a single absorber, and a cloud-free atmosphere. In a more realistic atmosphere, this degeneracy is broken in various ways. For example, for high chemical abundances, the mean molecular weight becomes significant enough to affect the scale height and hence the amplitude of the spectral feature (e.g., Benneke & Seager, 2012; Line & Parmentier, 2016). On the other hand, at low abundances, the CIA opacity provides the continuum level for the spectrum (e.g., de Wit & Seager, 2013; Line & Parmentier, 2016). Other effects influencing the spectrum include considerations of clouds, non-isothermal atmospheres, multiple-molecular absorbers, etc. Furthermore, constraining the contributions from these various effects require observed spectra in the visible in addition to the infrared spectra. The importance and effects of such considerations are studied in the rest of this chapter. In what follows, we perform an in-depth study of the effects of model assumptions and data coverage on atmospheric retrievals using transmission spectra.

2.3 HD 209458 b: A CASE STUDY

We now conduct a systematic exploration of the degeneracies in interpreting transmission spectra using fully numerical models within a rigorous retrieval framework. For this study, we choose the canonical hot Jupiter HD 209458 b which has the most data available (Deming et al., 2013; Sing et al., 2016) and has been a subject of several recent retrieval studies (e.g., Madhusudhan et al., 2014b; Barstow et al., 2017; MacDonald & Madhusudhan, 2017a).

We used an atmospheric retrieval code for transmission spectra adapted from the recent work of Pinhas et al. (2018). The code was modified to include the radius of the planet (R_p) as one of the retrieval parameters and, unlike Pinhas et al. (2018), we do not infer any stellar properties. The code computes line by line radiative transfer in a transmission geometry, assuming hydrostatic equilibrium. We consider a parametric P–T profile using the prescription of Madhusudhan & Seager (2009). We consider a one-dimensional model atmosphere consisting of 100 layers in pressure ranging from 10^{-6}–10^{3} bar uniformly spaced in $\log_{10}(P)$. We use the cloud/haze parametrization of MacDonald & Madhusudhan (2017a)

which allows for cloud-free to fully cloudy models, including nonhomogeneous cloud cover. The haze is included as $\sigma = a\sigma_0(\lambda/\lambda_0)^\gamma$, where γ is the scattering slope, a is the Rayleigh-enhancement factor, and σ_0 is the H_2 Rayleigh scattering cross section (5.31×10^{-31} m^2) at the reference wavelength $\lambda_0 = 350$ nm. Cloudy regions of the atmosphere are included as an opaque cloud deck with cloud top pressure P_{cloud}. The fraction of cloud cover at the terminator is given by $\bar{\phi}$.

The absorption cross sections of the molecular and atomic species are obtained from Rothman et al. (2010) for H_2O, CO, and CO_2; Yurchenko et al. (2011) for NH_3; Harris et al. (2006) and Barber et al. (2014) for HCN; Kramida et al. (2018) for Na and K; and Richard et al. (2012) for H_2-H_2 and H_2-He CIA. The cross sections are generated using the methods of Gandhi & Madhusudhan (2017). Our model assumes that the atmosphere has uniform mixing ratio for each species considered and treats these mixing ratios as free parameters. Unlike the retrievals in Section 2.2, these retrievals do not fix the mean molecular weight to a specific value and instead calculate it based on the retrieved molecular abundances and assumption of a H_2-He-dominated atmosphere with a fixed He/H_2 ratio of 0.17 (MacDonald & Madhusudhan, 2017a). Lastly, the reference pressure (P_{ref}) is a free parameter that establishes the pressure in the atmosphere at which the reference radius of the planet (R_p) is located. In summary, our full model has 19 free parameters: R_p, P_{ref}, seven chemical species (H_2O, CO, CO_2, HCN, NH_3, Na, and K), six parameters for the P–T profile, and four parameters for clouds/hazes including the cloud deck pressure P_{cloud} and cloud fraction $\bar{\phi}$.

Our goal is to investigate the effect of each model parameter and/or assumption on the retrieved parameters and their degeneracies. We start with the simplest setup and gradually increase the physical plausibility of the model and extent of the data. We start by considering an isothermal and isobaric atmosphere with only one molecule present, H_2O, to carry on from our reproduction of previous results in Section 2.2. We later increase the number of considerations until we use a full model with a parametric P–T profile, with multiple molecules (H_2O, Na, K, NH_3, CO, HCN, and CO_2) and the presence of clouds/hazes. For our retrievals, we use the spectrum of HD 209458 b reported in Sing et al. (2016). The spectrum has two wavelength ranges observed with HST: near-infrared (1.1–1.7 μm) obtained using WFC3 and full optical range (0.3–1.01 μm) obtained using the STIS instrument. We compare the retrieved radius values to the value reported by Torres et al. (2008) of

Table 1 Summary of the 12 Cases for Which Retrievals were Performed.

	ISOBAR	ISOTHERM	H_2O	WFC3	CIA	P–T	CLOUDS (F/N)	OPTICAL	NA, K	NH_3	CO	HCN	CO_2
Section 2.3.2: Case 1	✓	✓	✓	✓									
Section 2.3.3: Case 2	✓	✓	✓	✓	✓								
Section 2.3.4: Case 3		✓	✓	✓	✓								
Section 2.3.5: Case 4			✓	✓	✓	✓							
Section 2.3.6: Case 5			✓	✓	✓	✓	F						
Section 2.3.7: Case 6			✓	✓	✓	✓	N						
Section 2.3.8: Case 7			✓	✓	✓	✓	N	✓					
Section 2.3.9: Case 8			✓	✓	✓	✓	N	✓	✓				
Section 2.3.10: Case 9			✓	✓	✓	✓	N	✓	✓	✓			
Section 2.3.11: Case 10			✓	✓	✓	✓	N	✓	✓	✓	✓		
Section2.3.12: Case 11			✓	✓	✓	✓	N	✓	✓	✓	✓	✓	
Section 2.3.13: Case 12			✓	✓	✓	✓	N	✓	✓	✓	✓	✓	✓

Note. Each column indicates a model assumption or a free parameter. The WFC3 column indicates the inclusion of data in the near-infrared in the retrieval. On the other hand, optical signifies that data in the optical wavelengths were used in the retrieval. P–T means that we consider a parametric P–T profile in the retrieval. Clouds are implemented in two ways: F stands for a retrieval with full cloud cover in which the cloud fraction is fixed to $\bar{\phi} = 100\%$, and N represents cases with nonuniform clouds in which the cloud fraction $\bar{\phi}$ is a free parameter in the retrieval.

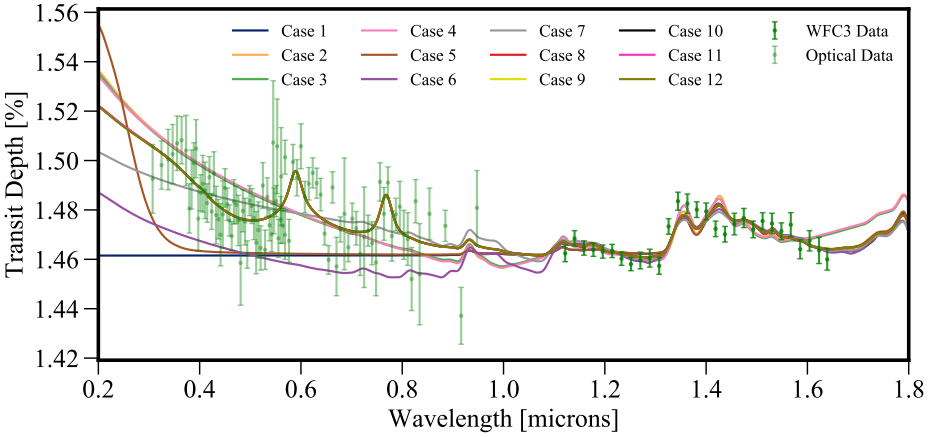

Figure 11 Median retrieved models for each of the cases shown in Table 1. Infrared and optical data from Sing et al. (2016) are shown using green markers. While all models produce some degree of fit to the data in the infrared, only cases 8-12 produce a good fit to all the data.

$R_p = 1.359^{+0.016}_{-0.019}$ R_J, which is consistent with the reported radius by Sing et al. (2016).

The 12 cases of our study are summarized in Table 1. The parameters, priors, and results for all cases are summarized in Tables 11 and 12 in Appendix A. The retrieved median spectra for all the cases are shown in Figure 11. The constraints on the retrieved H_2O abundances for the different cases are illustrated in Figure 12. The posterior distributions for X_{H_2O}, P_{ref}, and R_p for all cases are included in Appendix A.

2.3.1 *Case 0: Reproducing the Semi-analytic Model*

Before conducting our case-by-case study, we first consider case zero, which presents a numerical analog of semi-analytic models. Case zero has the simplest model considerations, i.e., of an isothermal and isobaric atmosphere with H_2O absorption as the only source of opacity. In addition, the mean molecular weight and gravity are fixed quantities. The isobaric assumption means evaluating the molecular cross section at only one pressure, in this case 1 mbar. Following the models in Section 2.2, the mean molecular weight is fixed to a value of 2.4 amu, that of an H_2-rich atmosphere with solar elemental abundances. The fixed value for gravity is $\log_{10}(g) = 2.963$ in cgs for HD 209458 b (Torres et al., 2008).

While generally our numerical model spans a pressure range of 10^{-6} bar to 10^3 bar as discussed above, in the present case, the retrieval is strongly sensitive to the edges of the pressure range, due to the limited

opacity sources. The deepest pressure level in the model atmosphere effectively acts as an opaque surface. In order to circumvent this edge effect, we consider a model atmosphere with an unrealistically extreme range in pressure, from 10^{-14} to 10^{14} bar, uniformly spaced in $\log_{10}(P)$ using 400 layers.

We use this model for a retrieval using a near-infrared WFC3 spectrum of HD 209458 b, similarly to our retrievals in Section 2.2. The model parameters are X_{H_2O}, R_p, P_{ref}, and T, the temperature of the isotherm. The priors on the parameters are $\log_{10}(X_{H_2O}) = [-12, -1]$, $R_P = [1, 3]$ R_J, $\log_{10}(P_{ref}) = [-14, 14]$ bar, and $T = [800 - 2710]$ K. The prior on X_{H_2O} is chosen to be consistent with all cases investigated in this section. The prior range on P_{ref}, which is also the extent of the model atmosphere, is chosen so that the edge effects are avoided as discussed above. The retrieved X_{H_2O} is completely unconstrained with a retrieved value of $\log_{10}(X_{H_2O}) = -6.53^{+3.86}_{-3.80}$. Similarly, P_{ref} is unconstrained with a retrieved value of $\log_{10}(P_{ref}) = 0.28^{+9.68}_{-9.88}$, where P_{ref} is in bar, and R_p is retrieved to $R_p = 1.38^{+0.10}_{-0.10}$ R_J, an unconstrained value consistent with Torres et al. (2008). Lastly, the retrieved isothermal temperature is $T = 818.08^{+9.72}_{-8.44}$ K. The posterior distributions of R_p, P_{ref}, and X_{H_2O} for this retrieval are shown in Appendix A.

Under these simplistic model considerations, there is a strong three-way degeneracy between R_p, P_{ref}, and X_{H_2O} as expected (Heng & Kitzmann, 2017). However, it is important to note that the degeneracy is a result of unrealistic model assumptions. In addition to the factors discussed in Section 2.2 and later in this section, several other factors make this case unphysical. First, it is unrealistic to have an atmosphere expanding to such high pressures (e.g., 10^{14} bar) while maintaining the isobaric assumption for the cross sections, especially evaluating them at 1 mbar. Second, such a deep atmosphere would become opaque at much lower pressures, due to the effects of CIA (e.g., de Wit & Seager, 2013; Bétrémieux & Swain, 2018); this is further explored in Section 2.3.3. Third, assuming a fixed mean molecular weight is unrealistic at high H_2O abundances explored in the retrieval such as $X_{H_2O} \gtrsim 10^{-2}$ (e.g., Benneke & Seager, 2012; Line & Parmentier, 2016). Fourth, maintaining a fixed gravity over the entire atmosphere spanning many orders of magnitude in pressure is also unrealistic. Nevertheless, the present case clearly demonstrates the three-way degeneracy among R_p, P_{ref}, and X_{H_2O} obtained for such a simplistic model while fitting near-infrared data alone.

We now perform a case-by-case retrieval study using more realistic model atmospheres as explained at the beginning of Section 2.3. All of the cases henceforth consider models with a height-dependent g, a variable mean molecular weight, and a pressure range of 10^{-6}–10^{3} bar.

2.3.2 *Case 1: Isobar, Isotherm, H_2O Only and WFC3 Data*

The initial model we now consider is that of an atmosphere that is best described by an isotherm at a temperature T and an isobar with only one molecule present, H_2O. For clarity, we specify that the isobaric assumption means evaluating the molecular cross section at only one pressure, while density, pressure, and gravity are still changing with height. Making only these assumptions in our model means ignoring CIA opacity due to H_2-H_2 and H_2-He. Furthermore, we apply this model on WFC3 data only in order to test the retrievals with a limited wavelength range.

The molecular cross sections are evaluated at 1 mbar following HK17. The result of our retrieval is a H_2O mixing fraction of $\log_{10}(X_{H_2O}) = -9.54^{+0.15}_{-0.15}$, a retrieved $R_p = 1.49^{+0.05}_{-0.08}$ R_J, an unconstrained isotherm with $T = 2003.65^{+248.72}_{-247.72}$ K, and $\log_{10}(P_{ref}) = -3.00^{+3.67}_{-2.21}$ where P_{ref} is in bar. The retrieved radius is consistent within 2σ with the published photometric radius of $R_p = 1.359^{+0.016}_{-0.019}$ R_J (Torres et al., 2008). However, the reference pressure is not tightly constrained, and the retrieved H_2O abundance is ~ 4 orders of magnitude smaller than that in other studies (Madhusudhan et al., 2014b; MacDonald & Madhusudhan, 2017a; Barstow et al., 2017). The retrieved H_2O abundance in this case is also sensitive to the bottom of the model atmosphere for the same reason as in Section 2.3.1. In this case, the bottom of the atmosphere is at $P = 10^3$ bar, which limits the amplitude of the H_2O feature in the model spectrum, similar to the effects of an opaque surface. Changing the bottom pressure of the atmosphere can result in different H_2O abundance constraints. Nevertheless, for the present demonstration, we have assumed a physically realistic pressure range of 10^3–10^{-6} bar. Regardless of the pressure range, the present case is inevitably unrealistic, due to the lack of various other model considerations, which are incorporated in subsequent cases below. More importantly, this edge effect is not relevant once CIA opacities are considered.

2.3.3 *Case 2: Case 1 + H_2/He CIA*

We now consider a slightly more realistic model that includes CIA opacities due to H_2-H_2 and H_2-He given that the test case of HD 209458 b is a gas-giant planet with a H_2-dominated atmosphere. All other assumptions about the isothermal and isobaric characterization of the atmosphere in the model stay the same as in the previous retrieval. However, while we still evaluate the molecular cross sections at 1mbar, we consider the CIA to be pressure dependent. We also consider gaseous Rayleigh scattering due to H_2 in this and all subsequent cases.

The inclusion of CIA decreases the retrieved isothermal temperature to $T = 1070.21^{+87.56}_{-92.10}$ K, but increases the H_2O volume mixing ratio to $\log_{10}(X_{H_2O}) = -5.29^{+0.23}_{-0.20}$, a value close to that found in previous retrieval studies (Madhusudhan et al., 2014b; MacDonald & Madhusudhan, 2017a; Barstow et al., 2017). R_p is now retrieved to be $R_p = 1.41^{+0.02}_{-0.03}$ R_J, and P_{ref} in bar to $\log_{10}(P_{ref}) = -4.51^{+2.53}_{-1.11}$.

The inclusion of CIA has resulted in a value for the H_2O abundance that is consistent with other studies while keeping R_p consistent with the white light radius within 2σ. This highlights the importance of considering CIA for constraints on the molecular abundances, as also discussed in Section 2.2. We find that ignoring CIA leads to erroneous results. CIA opacity determines the highest pressures that can be probed, and as a result provides the continuum to the spectrum (Line & Parmentier, 2016; Bétrémieux & Swain, 2018). The inclusion of CIA raises the slant photosphere of the planet to a higher altitude compared to the previous case. By decreasing the thickness of the observed slant column of the atmosphere along the line of sight, a higher abundance is required to explain the same features. In comparison, case 1, where we did not have CIA opacity, the effective column of the atmosphere is larger and hence requires less H_2O abundance to explain the same features. Our results show that the molecular abundance is much less biased upon the inclusion of CIA.

While the isobaric assumption makes for a simplified problem construction in analytic models, it is not necessary when numerical methods are available. It is computationally inexpensive to evaluate the molecular opacities at the corresponding pressure in the atmosphere instead of assuming a constant pressure of 1 mbar.

2.3.4 *Case 3: Case 2 without an Isobar*

We now remove the assumption of an isobar for the calculation of H_2O opacities. Instead, we calculate the molecular opacities at the corresponding pressure in the atmosphere rather than at a fixed pressure of 1 mbar. We maintain the remaining assumption of an isotherm for the temperature profile of the atmosphere. Our retrievals obtain an isothermal profile with $T = 1046.02^{+89.50}_{-95.51}$ K and $\log_{10}(X_{H_2O}) = -5.46^{+0.19}_{-0.17}$. The corresponding R_p and P_{ref} in bar are $R_p = 1.41^{+0.02}_{-0.03}$ R_J and $\log_{10}(P_{ref}) = -4.35^{+2.63}_{-1.25}$, respectively. The retrieved X_{H_2O} is shown in Figure 12. Retrieved parameters and priors for this and other cases are shown in Tables 11 and 12.

While the consideration of pressure-dependent CIA is essential, assuming molecular line cross sections to be isobaric does not make a significant difference compared to the present case given current data quality. This is because the atmosphere is mostly probed at low pressures as discussed in Section 2.5. However, the isobaric assumption cannot be maintained when considering the effects of CIA as the CIA opacity has a stronger dependence on pressure, being proportional to the pressure squared (de Wit & Seager, 2013).

2.3.5 *Case 4: Case 3 + P–T profile*

We now remove the assumption of an isothermal atmosphere and consider a full P–T profile in our retrieval. We implement the parametrization used in Madhusudhan & Seager (2009) which involves six parameters that capture a typical P–T profile. Along with this, we retrieve X_{H_2O}, P_{ref}, and R_p. This allows the atmosphere to have any P–T profile the data requires.

With the inclusion of the parametric P–T profile, we retrieve nine parameters in total. This retrieval results in $R_p = 1.41^{+0.01}_{-0.03}$ R_J, $\log_{10}(P_{ref}) = -4.36^{+2.35}_{-1.18}$ in bar, and $\log_{10}(X_{H_2O}) = -5.48^{+0.16}_{-0.16}$. The retrieved P–T profile has the following parameters: $\log_{10}(P_1) = -0.77^{+1.88}_{-2.35}$, $\log_{10}(P_2) = -3.61^{+2.40}_{-1.62}$, $\log_{10}(P_3) = 1.45^{+1.10}_{-1.76}$, $\alpha_1 = 0.85^{+0.11}_{-0.14}$, $\alpha_2 = 0.67^{+0.22}_{-0.32}$, and temperature of $T_0 = 870.11^{+82.12}_{-49.12}$ K. The retrieved values did not change significantly compared to the assumption of an isothermal atmosphere as in case 3. These numerical results agree with analytic studies that predict that while non-isothermal atmospheres distort the spectrum of an isothermal one, the effects are subtle considering present data quality with HST (Bétrémieux & Swain, 2018). The retrieved mixing fraction of

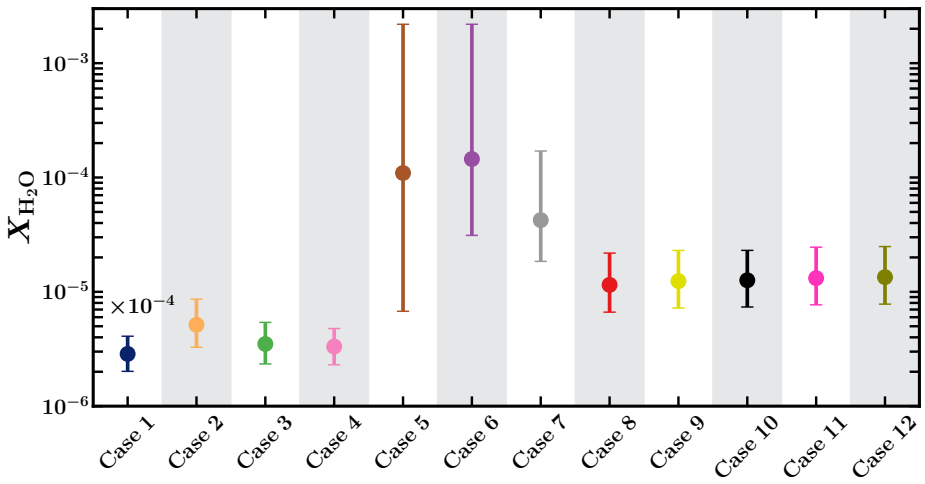

Figure 12 Retrieved H_2O abundances for the different cases shown in Table 1 and Section 2.3. The abundance (i.e., mixing ratio) for case 1 has been increased by 10^4 to be in the same range as the abundances of other cases.

H_2O is consistent with that of other studies (Madhusudhan et al., 2014b; MacDonald & Madhusudhan, 2017a; Barstow et al., 2017).

2.3.6 *Case 5: Case 4 + Full Cloud Cover*

We continue to remove assumptions from our model and now consider the possibility of clouds being present in the atmosphere of the planet. There is no a priori information to assume that the atmosphere of the hot Jupiter HD 209458 b is cloud-free. We consider the cloud prescription of MacDonald & Madhusudhan (2017a) as explained at the beginning of this section. We include four parameters for clouds and hazes. For hazes, we use a, the Rayleigh-enhancement factor, and γ, the scattering slope. For clouds, P_{cloud} and $\bar{\phi}$ characterize the pressure level of the optically thick cloud deck and cloud coverage fraction, respectively. In this particular case, instead of considering a clear atmosphere like we did in case 4, we consider the presence of a fully cloudy planet atmosphere by fixing $\bar{\phi} = 100\%$.

The inclusion of a fully cloudy deck increases the number of retrieved parameters from 9 to 12. The retrieved H_2O abundance is $\log_{10}(X_{H_2O}) = -3.96^{+1.30}_{-1.21}$, while $R_p = 1.38^{+0.04}_{-0.06}$ R_J, and P_{ref} is $\log_{10}(P_{ref}) = -3.84^{+2.17}_{-1.37}$ in bar. The values of the retrieved parameters for the P–T profile are $T_0 = 1940.56^{+251.87}_{-305.81}$ K, $\alpha_1 = 0.68^{+0.20}_{-0.23}$, $\alpha_2 = 0.60^{+0.24}_{-0.25}$, $\log_{10}(P_1) = -1.30^{+1.88}_{-1.78}$, $\log_{10}(P_2) = -3.86^{+1.88}_{-1.39}$, and $\log_{10}(P_3) = 1.19^{+1.16}_{-1.66}$. The cloud parameters are $\log_{10}(a) = 0.39^{+3.81}_{-2.73}$, $\gamma = -12.14^{+7.38}_{-4.97}$, and a cloud

top pressure of $\log_{10}(P_{cloud}) = -2.74^{+1.24}_{-1.27}$. Although the value of the retrieved planetary radius is still consistent with the observed radius, we see that the 1σ limits have increased. Similar effects are seen with the retrieved H_2O abundance.

The interesting effect of the inclusion of a fully covering cloud deck is that the H_2O abundance is now hardly constrained. Because the pressure at which this cloud deck could be located spans several orders of magnitude, so does the H_2O abundance. In this case, the cloud deck mimics a surface (Bétrémieux & Swain, 2017), and the pressure at which the cloud is located is fully degenerate with the retrieved H_2O abundance. A cloud deck at a higher altitude requires higher H_2O abundance to account for the same features, while a lower cloud deck can explain the same features with a lower molecular abundance (e.g., Deming et al., 2013; Barstow et al., 2017). An alternate way to explain this is similar to what happened with the inclusion of CIA in case 2. By lowering the cloud deck altitude (i.e., increasing the cloud top pressure), we are increasing the effective column of the observable atmosphere, which requires lower abundance than a smaller observable atmosphere corresponding to a cloud deck at a higher altitude (i.e., decreasing the pressure). We also notice that the lowest H_2O abundance is consistent with the lowest abundance found in case 2, due to CIA providing the continuum opacity.

2.3.7 *Case 6: Case 4 + Nonhomogeneous Clouds*

We now consider the effects of nonhomogeneous cloud coverage on constraining the H_2O abundance. We include the cloud fraction $\bar{\phi}$ as an extra free parameter. The retrieved parameters are $\log_{10}(X_{H_2O}) = -3.83^{+1.17}_{-0.67}$, $R_p = 1.35^{+0.03}_{-0.05}$ R_J, and a reference pressure of $\log_{10}(P_{ref}) = -3.61^{+2.46}_{-1.48}$ in bar. The P–T profile parameters are $T_0 = 1262.74^{+225.05}_{-230.98}$ K, $\alpha_1 = 0.65^{+0.21}_{-0.21}$, $\alpha_2 = 0.60^{+0.25}_{-0.25}$, $\log_{10}(P_1) = -1.22^{+1.86}_{-1.84}$, $\log_{10}(P_2) = -3.90^{+2.00}_{-1.34}$, and $\log_{10}(P_3) = 1.27^{+1.13}_{-1.65}$. The retrieved cloud parameters are $\log_{10}(a) = 2.09^{+3.93}_{-3.88}$, $\gamma = -8.60^{+7.87}_{-7.40}$, $\log_{10}(P_{cloud}) = -4.70^{+1.33}_{-0.85}$, and $\bar{\phi} = 0.68^{+0.05}_{-0.06}$.

The inclusion of nonhomogeneous clouds does not significantly change the retrieved P–T profile parameters. It, however, allows a constraint on the cloud fraction to be placed at $\sim 68\%$. Furthermore, R_p and P_{ref} are consistent with those of cases 4 and 5.

While the median value of the retrieved H_2O abundance is consistent with that of case 5, the uncertainty is smaller when nonhomogeneous

clouds are considered. Considering a nonhomogeneous cloud cover allows for a better H_2O constraint compared to the assumption of a fully cloudy atmosphere. It is true that the constraints in the case of a clear atmosphere are even tighter (e.g., case 4), but the validity of this assumption is not evident. Furthermore, previous studies suggest that failure to consider nonhomogeneous cloud cover can bias molecular abundance findings (Line & Parmentier, 2016).

We now look into other factors that could help further constrain molecular abundances. Until now, we have only considered HST WFC3 data in the near-infrared for retrievals with different model assumptions. Given that the main differences in spectra with clouds manifest in the optical wavelengths, we now incorporate data in the optical.

2.3.8 *Case 7: Case 6 + Optical Data*

Our seventh case considers the inclusion of an optical spectrum of our case study hot Jupiter HD 209458 b. We included data from 0.30 to 0.95 μm from Sing et al. (2016). The addition of optical data helps constrain the Rayleigh slope and cloud properties (Benneke & Seager, 2012; Griffith, 2014; Line & Parmentier, 2016). This also allows us to evaluate the effects of more data considered in our retrieval. We keep the number of parameters the same as in case 6, for a total of 13. We report a retrieved H_2O abundance of $\log_{10}(X_{H_2O}) = -4.37^{+0.61}_{-0.36}$. The planetary radius retrieved is $R_p = 1.35^{+0.03}_{-0.05}$ R_J, and $\log_{10}(P_{ref}) = -3.59^{+2.49}_{-1.54}$ is the retrieved reference pressure.

The retrieved values for the P–T profile parameters and cloud parameters after including optical data are $T_0 = 1306.40^{+225.24}_{-257.81}$ K, $\alpha_1 = 0.71^{+0.19}_{-0.22}$, $\alpha_2 = 0.67^{+0.21}_{-0.26}$, $\log_{10}(P_1) = -1.34^{+2.02}_{-1.84}$, $\log_{10}(P_2) = -3.79^{+1.99}_{-1.45}$, and $\log_{10}(P_3) = 1.23^{+1.20}_{-1.91}$. The cloud parameters are $\log_{10}(a) = 7.65^{+0.24}_{-0.43}$, $\gamma = -8.97^{+1.07}_{-0.88}$, $\log_{10}(P_{cloud}) = -5.29^{+0.25}_{-0.16}$, and $\bar{\phi} = 0.69^{+0.04}_{-0.05}$.

As expected, the parameters most affected, compared to case 6, are those responsible for clouds and hazes. The inclusion of data in the optical allows us to place tighter constraints on a and γ, which characterize the slope in the optical. The cloud parameters are consistent with those of case 6, with $\bar{\phi}$ mostly unchanged. However, the uncertainty in $\log_{10}(P_{cloud})$ is smaller by almost a factor of 6 compared to the values in case 6. Naturally, given that we now have information in the wavelength range where the scattering slope manifests itself, our cloud and haze prescription can fit for it, in contrast to previous cases where we fit for the slope without adequate data in the optical range.

Furthermore, by constraining the baseline of the spectrum, we are now able to place better constraints on the H_2O abundance. The uncertainties on the H_2O abundance are half as small as the ones from case 6. Thus, it is evident that the inclusion of optical data allows for better estimates of chemical abundances. Our numerical results show the importance of short wavelengths in breaking key degeneracies and in better constraining molecular abundances in agreement with previous analytic studies (e.g., Benneke & Seager, 2012; Griffith, 2014; Line & Parmentier, 2016).

The last step in increasing the physical reality of our model is to allow for the presence of more molecules in our atmosphere. This would prevent our models from trying to explain every spectroscopic feature with only one molecule. Furthermore, a possible way to break the degeneracy between R_p and mixing ratios is to consider the absorption features of different absorbers (Benneke & Seager, 2012). In the next cases, we incorporate several species that can be prominent in hot Jupiter atmospheres, e.g., Na, K, NH_3, CO, HCN, and CO_2 (Madhusudhan et al., 2016).

2.3.9 *Case 8: Case 7 + Na and K*

The first species we incorporate are the alkali atomic species Na and K. Given that their spectroscopic features are present in the range covered by the additional optical data, we investigate the impact these species have on the retrieved H_2O abundances. The values retrieved for the species are $\log_{10}(X_{H_2O}) = -4.94^{+0.28}_{-0.24}$, $\log_{10}(X_{Na}) = -5.55^{+0.53}_{-0.44}$, and $\log_{10}(X_K) = -7.17^{+0.55}_{-0.52}$. The retrieved R_p is $R_p = 1.37^{+0.02}_{-0.04}$ R_J and P_{ref} is $\log_{10}(P_{ref}) = -3.46^{+2.33}_{-1.67}$ in bar. For completion, we continue to show our retrieved values for all other parameters as in previous cases. The P–T profile parameters are $T_0 = 1064.75^{+283.29}_{-185.88}$ K, $\alpha_1 = 0.59^{+0.25}_{-0.17}$, $\alpha_2 = 0.47^{+0.33}_{-0.21}$, $\log_{10}(P_1) = -1.16^{+1.98}_{-1.79}$, $\log_{10}(P_2) = -3.89^{+2.24}_{-1.43}$, and $\log_{10}(P_3) = 1.22^{+1.21}_{-1.60}$. The retrieved nonhomogeneous cloud parameters are $\log_{10}(a) = 4.42^{+0.71}_{-1.26}$, $\gamma = -14.42^{+5.59}_{-3.76}$, $\log_{10}(P_{cloud}) = -4.69^{+0.77}_{-0.50}$, and $\bar{\phi} = 0.49^{+0.06}_{-0.06}$. Our retrieved H_2O abundance for this and other cases is shown in Figure 12, and all retrieved parameters are summarized in Tables 11 and 12.

The inclusion of Na and K has further decreased the 1σ spread of the retrieved H_2O abundance almost by a factor of 2. While the retrieved H_2O abundance is consistent with that of case 7, it is important to note that the posterior distribution has shifted toward a lower H_2O abundance by ~ 0.5 dex. This shift in the median value is as much as the shift between case 6 and case 7 due to the inclusion of optical data. This

suggests that the Na and K, which themselves are constrained by the optical data, also strongly affect the retrieved H_2O abundance. This is due to better fitting the features in the optical. An additional effect is the change in the retrieved cloud fraction from ~ 70% in case 7 to ~ 50%. Evidently, these results will be sensitive to the absorption cross sections being used. Nonetheless, it is clear that including molecules that have signatures in the optical allow us to fit the data in those wavelengths better and further constrain the H_2O abundance. This has little effect on the retrieved R_p and P_{ref}, which continue to be well constrained.

2.3.10 *Case 9: Case 8 + NH_3*

Next, we include NH_3 as a source of opacity. The retrieval gives the following results for molecular and atomic abundances: $\log_{10}(X_{H_2O}) = -4.91^{+0.27}_{-0.24}$, $\log_{10}(X_{Na}) = -5.53^{+0.51}_{-0.43}$, $\log_{10}(X_K) = -7.13^{+0.54}_{-0.51}$, and $\log_{10}(X_{NH_3}) = -8.02^{+1.86}_{-2.64}$. The retrieved planetary radius and reference pressure are $R_p = 1.37^{+0.02}_{-0.04}$ R_J and $\log_{10}(P_{ref}) = -3.39^{+2.43}_{-1.69}$, respectively. The P–T profile parameters and cloud parameters are $T_0 = 1026.44^{+276.52}_{-161.11}$ K, $\alpha_1 = 0.62^{+0.24}_{-0.18}$, $\alpha_2 = 0.49^{+0.32}_{-0.22}$, $\log_{10}(P_1) = -1.18^{+1.97}_{-1.77}$, $\log_{10}(P_2) = -3.95^{+2.19}_{-1.39}$, $\log_{10}(P_3) = 1.25^{+1.18}_{-1.59}$, $\log_{10}(a) = 4.38^{+0.70}_{-1.16}$, $\gamma = -14.67^{+5.19}_{-3.57}$, $\log_{10}(P_{cloud}) = -4.57^{+0.77}_{-0.56}$, and $\bar{\phi} = 0.47^{+0.06}_{-0.08}$.

In comparison to case 8, the inclusion of NH_3 does not significantly change the retrieved H_2O abundance. Meanwhile, R_p and P_{ref} also remain mostly unchanged. Although both NH_3 and H_2O have absorption features in the WFC3 spectral range, the inclusion of NH_3 does not affect our retrieved H_2O abundance. This is because H_2O has generally stronger features than NH_3 in the WFC3 range; H_2O is also expected to be more abundant than NH_3 at hot Jupiter temperatures. As such, the cumulative opacity of NH_3 is generally weaker than that of H_2O, as also seen in previous studies (MacDonald & Madhusudhan, 2017a,b).

2.3.11 *Case 10: Case 9 + CO*

We proceed by adding CO to our model. The retrieved volume mixing ratios are $\log_{10}(X_{H_2O}) = -4.90^{+0.26}_{-0.23}$, $\log_{10}(X_{Na}) = -5.52^{+0.52}_{-0.43}$, $\log_{10}(X_K) = -7.11^{+0.54}_{-0.49}$, $\log_{10}(X_{NH_3}) = -8.14^{+1.95}_{-2.56}$, and $\log_{10}(X_{CO}) = -7.74^{+2.85}_{-2.72}$. The P–T profile parameters are $T_0 = 1026.72^{+262.72}_{-157.60}$ K, $\alpha_1 = 0.61^{+0.23}_{-0.18}$, $\alpha_2 = 0.49^{+0.32}_{-0.22}$, $\log_{10}(P_1) = -1.14^{+1.94}_{-1.77}$, $\log_{10}(P_2) = -3.87^{+2.15}_{-1.44}$, and $\log_{10}(P_3) = 1.29^{+1.15}_{-1.55}$. The cloud parameters are $\log_{10}(a) = 4.38^{+0.69}_{-1.14}$, $\gamma = -14.70^{+5.17}_{-3.55}$, $\log_{10}(P_{cloud}) = -4.57^{+0.76}_{-0.54}$, and $\bar{\phi} = 0.47^{+0.06}_{-0.08}$. Lastly,

the reference pressure and reference radius that we retrieve are $R_p = 1.37^{+0.02}_{-0.04}$ R_J and $\log_{10}(P_{ref}) = -3.42^{+2.33}_{-1.66}$, respectively. With all values being consistent with those presented in case 9, it is clear that the inclusion of CO did not affect the retrieved values because of the weak CO features in the WFC3 band.

2.3.12 *Case 11: Case 10 + HCN*

Second to last, we include HCN, which also has some features in the WFC3 band. The resulting retrieved planetary radius and reference pressure are consistent with those of case 10 with retrieved values of $R_p = 1.37^{+0.02}_{-0.04}$ R_J and $\log_{10}(P_{ref}) = -3.45^{+2.26}_{-1.63}$. The retrieved abundances are also consistent with values of $\log_{10}(X_{H_2O}) = -4.88^{+0.27}_{-0.23}$, $\log_{10}(X_{Na}) = -5.50^{+0.51}_{-0.42}$, $\log_{10}(X_K) = -7.09^{+0.54}_{-0.50}$, $\log_{10}(X_{NH_3}) = -8.11^{+1.90}_{-2.52}$, and $\log_{10}(X_{CO}) = -7.75^{+2.82}_{-2.73}$. The additional molecule resulted in a retrieved abundance of $\log_{10}(X_{HCN}) = -8.60^{+2.26}_{-2.17}$. Also consistent are the retrieved P–T profile parameters at $T_0 = 1013.53^{+248.73}_{-149.27}$ K, $\alpha_1 = 0.62^{+0.23}_{-0.18}$, $\alpha_2 = 0.49^{+0.31}_{-0.22}$, $\log_{10}(P_1) = -1.15^{+1.93}_{-1.78}$, $\log_{10}(P_2) = -3.90^{+2.14}_{-1.42}$, and $\log_{10}(P_3) = 1.26^{+1.16}_{-1.55}$. The cloud parameters are $\log_{10}(a) = 4.34^{+0.69}_{-1.11}$, $\gamma = -14.63^{+4.99}_{-3.59}$, $\log_{10}(P_{cloud}) = -4.52^{+0.73}_{-0.54}$, and $\bar{\phi} = 0.46^{+0.06}_{-0.08}$, which are also consistent. Similar to NH_3, our constraint on HCN is also weaker given current data. Our constraint, however, is consistent with the mixing ratio of $\sim 10^{-6}$, which was required to detect HCN on the day side of the planet (Hawker et al., 2018).

2.3.13 *Case 12: Case 11 + CO_2*

We add one last molecule, CO_2, in order to have what we refer to as a full retrieval. This is the equivalent to a state-of-the-art retrieval in which several molecules and atomic species, a parametric P–T profile, and nonhomogeneous clouds are considered, totaling 19 free parameters. This retrieval provides the following chemical abundance estimates: $\log_{10}(X_{H_2O}) = -4.87^{+0.27}_{-0.24}$, $\log_{10}(X_{Na}) = -5.48^{+0.52}_{-0.43}$, $\log_{10}(X_K) = -7.07^{+0.54}_{-0.51}$, $\log_{10}(X_{NH_3}) = -8.09^{+1.89}_{-2.54}$, $\log_{10}(X_{CO}) = -7.73^{+2.79}_{-2.75}$, and $\log_{10}(X_{HCN}) = -8.57^{+2.24}_{-2.22}$. The additional molecule has a retrieved abundance of $\log_{10}(X_{CO_2}) = -8.46^{+2.43}_{-2.30}$. The retrieved P–T parameters are $T_0 = 1022.15^{+246.41}_{-153.72}$ K, $\alpha_1 = 0.60^{+0.23}_{-0.17}$, $\alpha_2 = 0.50^{+0.31}_{-0.23}$, $\log_{10}(P_1) = -1.03^{+1.88}_{-1.79}$, $\log_{10}(P_2) = -3.86^{+2.16}_{-1.42}$, and $\log_{10}(P_3) = 1.33^{+1.13}_{-1.54}$. The retrieved cloud parameters are $\log_{10}(a) = 4.37^{+0.68}_{-1.08}$, $\gamma = -14.61^{+4.93}_{-3.58}$, $\log_{10}(P_{cloud}) = -4.52^{+0.72}_{-0.55}$, and $\bar{\phi} = 0.46^{+0.06}_{-0.08}$. The retrieved plane-

tary radius is $R_p = 1.37^{+0.02}_{-0.04}$ R_J, and the retrieved reference pressure is $\log_{10}(P_{ref}) = -3.45^{+2.24}_{-1.63}$.

Overall, with the inclusion of all the effects discussed, we find that the combination of near-infrared and optical data allows strong constraints on several important parameters and in resolving key degeneracies. The H_2O abundance is tightly constrained, and it is consistent with values of previous studies (e.g., MacDonald & Madhusudhan, 2017a; Barstow et al., 2017). Other chemical species are less well constrained owing to their weaker opacities in the observed range. Nonetheless, retrieved abundance estimates are consistent with studies that investigate their presence in the planet's atmosphere, e.g., detection of HCN (Hawker et al., 2018). While the abundance of H_2O is retrieved, P_{ref} and R_p are also retrieved, with the latter being consistent with the observed photometric radius of $R_p = 1.359^{+0.016}_{-0.019}$ R_J (Torres et al., 2008). The full retrieval has resolved the degeneracy between X_{H_2O}, R_p, and P_{ref}. Simultaneously, the cloud fraction is retrieved with tight constraints on its value, indicating that the planet is not cloud free. The inclusion of multiple absorbers in our retrievals helps break key degeneracies in our results. One of the advantages of the retrieval technique is that robust models (i.e., those that consider parametric P–T profiles, with many molecules, and partial clouds) can be implemented efficiently. The posterior distributions for the retrieved parameters of interest are included in Appendix A.

2.3.14 *Key Lessons*

Here we summarize the results from our case study of HD 209458 b based on retrievals with various model assumptions. Overall, with the inclusion of all the effects, we find that the combination of near-infrared and optical data are responsible for strong constraints on several important parameters resolving key degeneracies. The combination of data and accurate models allows for high-precision retrievals that impose tight constraints on the H_2O abundance, R_p, P_{ref}, and the cloud fraction. The retrieved H_2O abundances under different model assumptions are shown in Figure 12. The full retrieval is able to also estimate the abundance of other chemical species like HCN.

The retrieval's ability to constrain the H_2O abundance is not affected by R_p and P_{ref}. We find that is is possible to simultaneously retrieve both R_p and P_{ref} and find values for R_p in agreement with the observed photometric radius. We also analyze the impact of the cloud fraction and the potential degeneracy between this parameter, and the planetary radius

and the H_2O abundance. We first find that there are strong differences in the retrieved H_2O abundances between a cloud-free and fully cloudy atmosphere. Assuming a fully cloudy atmosphere introduces a degeneracy between the H_2O abundance and the pressure at which the cloud deck is located, because the cloud deck has the same effect as the optically thick photosphere on the transmission spectrum. An alternative to this is to consider nonhomogeneous cloud coverage in the atmosphere of the planet as there is no a priori information that favors a cloud-free atmosphere or a 100% cloudy atmosphere. On the other hand, theoretical models suggest the presence of partial clouds at the day-night terminators, i.e., the limbs, of planets (e.g., Kataria et al., 2016; Parmentier et al., 2016). We also find that in order to better constrain the clouds and hazes, it is important to consider data points in the optical wavelength range where clouds and hazes manifest themselves. We find that there is no degeneracy between cloud fraction and radius of the planet. Furthermore, it can be seen that it is not necessary to assume a fixed cloud fraction, and instead it is better to allow for the cloud fraction to be a free parameter in the retrieval.

A crucial lesson of our study is that CIA opacity is key in constraining molecular and atomic abundances in both clear and cloudy atmospheres. The lack of CIA due to H_2-H_2, H_2-He in the model skews the retrieved H_2O abundance by several orders of magnitude. Once CIA contribution is considered, the retrieved abundances are consistent within one order of magnitude. The CIA opacity strictly limits the location of the planetary photosphere and, hence, the column of the atmosphere above the photosphere that is probed by the observed spectrum. Without CIA, the photosphere will lie deeper in the atmosphere, increasing the observable column. As such, the molecular abundances will be higher when considering CIA in comparison to models without CIA.

The inclusion of optical data in retrievals is paramount to provide highly constrained H_2O abundances while helping constrain the range of possible planetary radii and their associated reference pressures. In addition, we find that Na and K absorption lines in the optical significantly affect the constraints on H_2O abundances. The availability of a broad spectral range between optical and near-infrared helps provide joint constraints on the H_2O abundance and the reference pressure or the planetary radius. On the other hand, strong degeneracy still persists between the R_p and P_{ref} without affecting the H_2O abundance. This relationship is further discussed in Section 2.5. Optical data also allow for tight constraints on the cloud fraction of the planet, making it possible

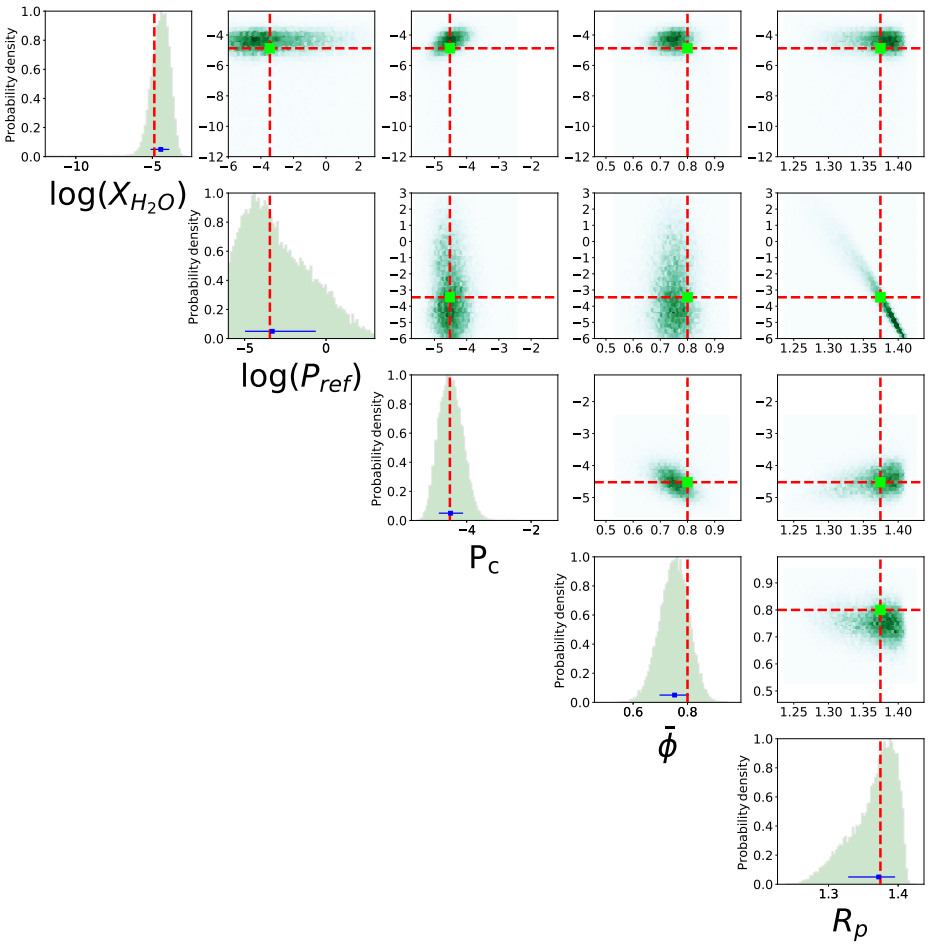

Figure 13 Posterior distributions of the retrieval for simulated data of HD 209458 b with 80% cloud coverage. The red dotted lines show the value of the simulated parameters.

to assess whether a planet is cloud free or not. In the next section, we investigate the effectiveness of the cloud parametrization and its ability to constrain the cloud fraction in the utmost case of a fully cloudy atmosphere.

2.4 SOLUTIONS TO HOMOGENEOUS CLOUD COVER

Here we investigate the robustness with which clouds can be constrained. In particular, we focus on the ability to retrieve the cloud fraction of the atmosphere $\bar{\phi}$ in the worst case scenario of a fully cloudy atmosphere (i.e., $\bar{\phi} = 100\%$). It can be argued that a 100% cloud deck leads to an entirely degenerate set of solutions for the H_2O abundances, as seen in Section 2.3.6. This leads to the question of whether an inhomogeneous cloud prescription can resolve this problem. In order to answer this ques-

tion, we investigate the potential of retrievals to estimate the cloud fraction covering a planet's atmosphere. For this, we consider the median values for the full retrieval of HD 209458 b, performed in Section 2.3.13, which includes data in the near-infrared and optical ranges, multiple molecules, a parametric P–T profile, and clouds. We use these values to generate three synthetic datasets with three different cloud fractions. The simulated data has the same resolution, error, and wavelength range as the data in Sing et al. (2016). In our simulated data, we add random error to the binned transit depth drawn from a normal distribution. The simulated models have cloud fractions of 100%, 90%, and 80%.

Figures 13–15 show the results of our retrievals along with the values of the parameters used in the simulated data. For all cloud fractions ($\bar{\phi}$), our retrieved molecular abundances are consistent with the input value within 2σ. H_2O can be reliably estimated for $\bar{\phi} \lesssim 80\%$. For higher $\bar{\phi}$, only upper limits are found but the $\bar{\phi}$ is accurately retrieved. $\bar{\phi}$ is always retrieved within $\sim 1\sigma$. Furthermore, the retrieved $\bar{\phi}$, R_p, and P_{ref} are consistent with the input values in all cases. These results demonstrate that the retrieval technique can discern the cloud fraction covering the planet's atmosphere without compromising the ability to retrieve other properties.

The worst case scenario would be an atmosphere with 100% cloud coverage at a very high altitude, as in the present case. Such a high-altitude cloud deck mutes almost all spectral features, resulting in a flat spectrum. Although no molecular abundances are reliably constrained for this case, the cloud fraction is still correctly retrieved to be consistent with 100% as shown in Figure 15. In principle, a 100% cloud deck at a lower altitude, e.g., at 10 mbar pressure level, would still have some spectral features. Stronger spectral features result in better constraints on the model parameters even for 100% cloud coverage given adequate data in the optical and infrared. Lower cloud fractions are naturally retrievable in all these cases. These results are consistent with the studies of MacDonald & Madhusudhan (2017a) and agree that nonuniform cloud coverage in models allows for a more precise determination of chemical abundances in transmission spectra in comparison to models that assume a fixed cloud fraction, effectively breaking the cloud-composition degeneracies. These results also show that nonhomogeneous and homogeneous cloud scenarios are distinguishable, in agreement with Line & Parmentier (2016).

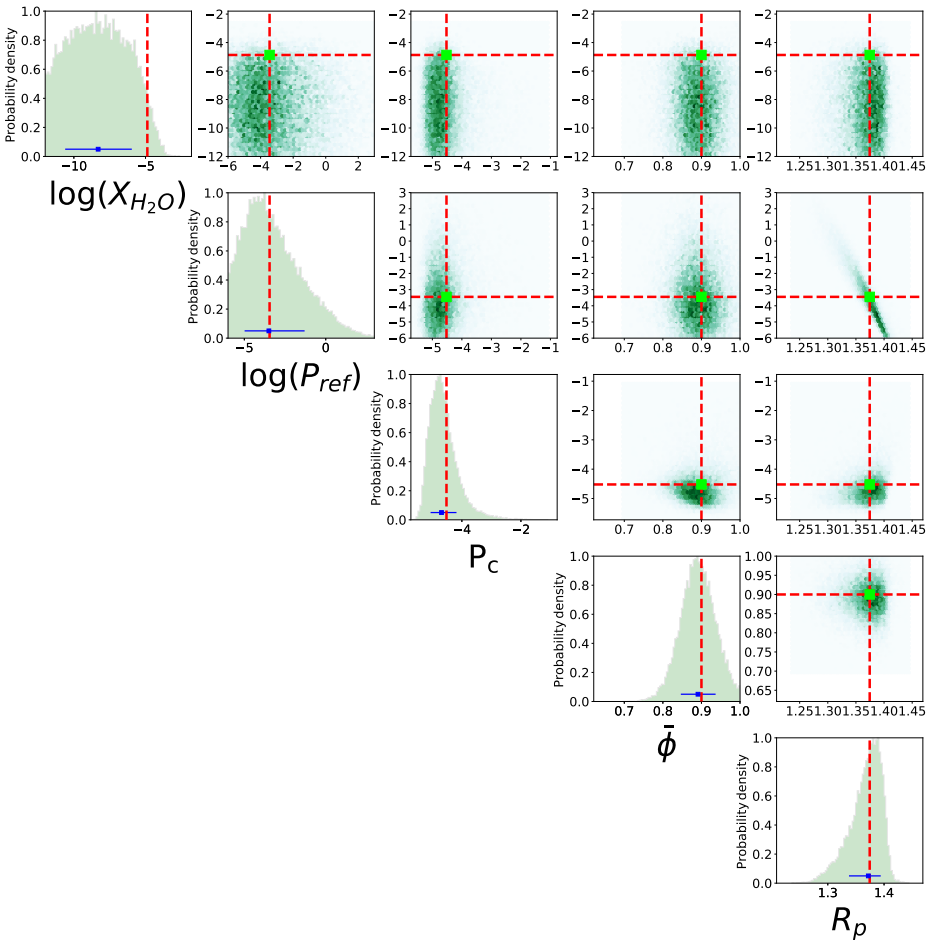

Figure 14 Posterior distributions of the retrieval for simulated data of HD 209458 b with 90% cloud coverage. The red dotted lines show the value of the simulated parameters.

2.5 THE R_p–P_{ref} DEGENERACY

As discussed in Section 2.1, several recent studies have highlighted possible degeneracies between chemical abundances, clouds/hazes, and reference radius in interpreting transmission spectra (e.g., Lecavelier Des Etangs et al., 2008; Benneke & Seager, 2012; de Wit & Seager, 2013; Griffith, 2014; Line & Parmentier, 2016; Heng & Kitzmann, 2017). In Sections 2.3 and 2.4, we demonstrate that the combination of multiband data and realistic models can lead to precise constraints on key chemical abundances, in this case H_2O, along with other properties.

Recently, HK17 inferred a three-way degeneracy among R_p, P_{ref}, and X_{H_2O} as a fundamental hindrance for deriving chemical abundances. They argue that one way to break the three-way degeneracy is to find a functional relationship between R_p and P_{ref}. In this section, we interpret

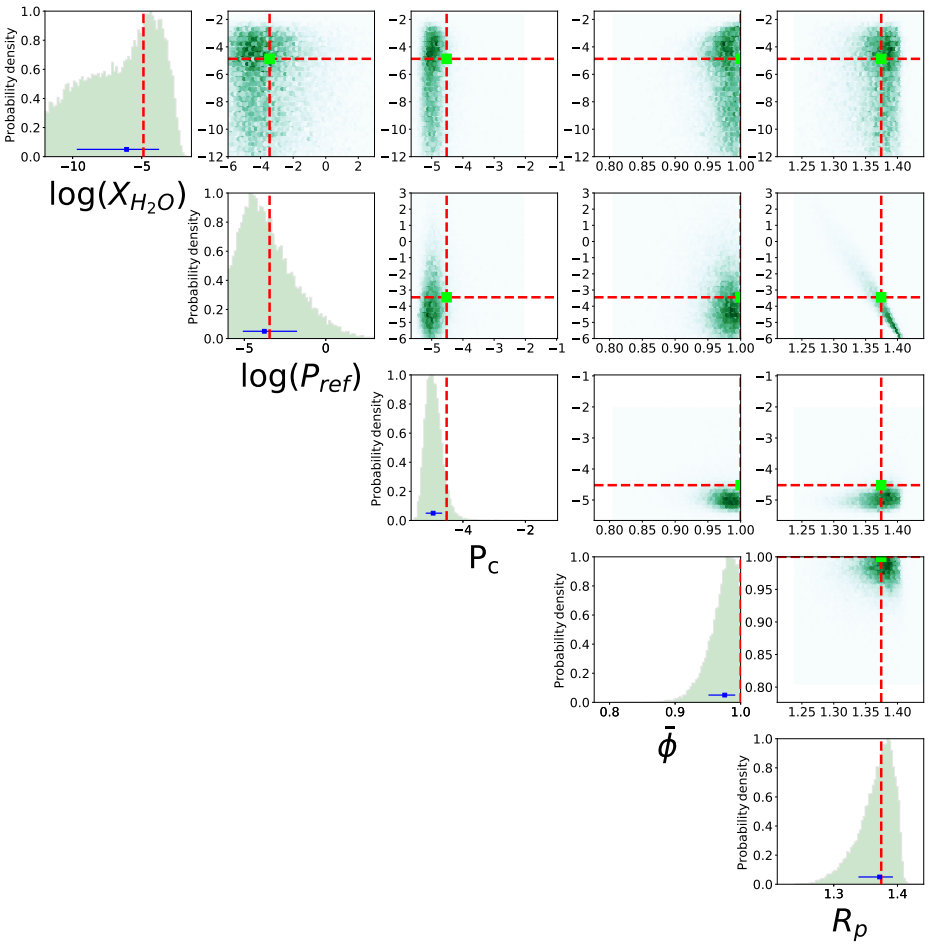

Figure 15 Posterior distributions of the retrieval for simulated data of HD 209458 b with 100% cloud coverage. The red dotted lines show the value of the simulated parameters.

our results from Sections 2.2 and 2.3 and present an empirical relation between R_p and P_{ref}. We show that previous suggestions of a three-way degeneracy are the result of model simplifications and inadequate data, and that the primary degeneracy is between R_p and P_{ref}.

The relationship between R_p and P_{ref} is explored when a fit or retrieval is performed. We briefly revisit our reproduction of previous semi-analytic results from Section 2.2 and our retrievals from Section 2.3. We begin by revisiting Figure 10, which shows a linear relationship between R_p and $\log_{10}(X_{H_2O}P_{ref})$ obtained from fitting a near-infrared WFC3 spectrum of the hot Jupiter WASP-12b. We find that the slope can be described as $m = -1/(H \ln 10)$, where H is the atmospheric scale height. The slope of the linear fit obtained by HK17 and reproduced by us is $m = -85.77$. Using the above relationship, this slope is consistent

with a scale height of 362 km, matching the estimated value for this planet reported in HK17.

We now investigate this empirical finding using the retrievals from Section 2.3, under different model assumptions. The correlations between $\log_{10}(P_{ref})$ and R_p for each of our retrievals of Section 2.3 are shown in Figure 16, along with a linear fit and the corresponding slope. The fit is obtained using `polyfit` included in `NumPy` (Harris et al., 2020). Accompanying this figure we have Figure 17, where we show $\log_{10}(X_{H_2O})$ as a function of R_p for the same cases. Figure 17 shows the posterior distributions of X_{H_2O}, which become more localized as different assumptions are removed from the retrievals. It is clear from Figures 16 and 17 that while $\log_{10}(P_{ref})$ and R_p are strongly degenerate, there is almost no degeneracy between $\log_{10}(X_{H_2O})$ and R_p in most of the cases. The only exception is case 5, with an assumed cloud fraction of 100%. This assumption introduces a degeneracy between the cloud level (i.e., P_{cloud}) and R_p. The different combinations of R_p and P_{cloud} that explain the spectrum for an assumed $\bar{\phi} = 100\%$ result in the wide spread of H_2O abundances observed in Figure 17, case 5.

From Figure 16, it can be observed that there is a log-linear relation between P_{ref} and R_p. The superimposed linear fit gives us an idea of what the scale height for each model is, i.e., $m = -1/(H \ln 10)$, as we did above with our analysis of Figure 10. While the slopes vary between cases ($m = -28$ to -81), they converge to a value of $m = -58$ as the model and data in our retrieval become more robust (i.e., case 7 and above). Figure 16 also shows a temperature estimate for the photosphere of the planet, which we obtain using the slope of the linear fit and assuming a mean molecular weight of 2.4 amu and a planet gravity of $\log_{10}(g) = 2.963$ in cgs. We find that these temperature estimates range between ~ 1012 K and ~ 1910 K for all cases except case 5; we discussed the exception of case 5 previously. The temperature values converge in case 12 to 1430 K, which is consistent with the equilibrium temperature of the planet as well as the photospheric temperature estimated in previous studies (e.g., MacDonald & Madhusudhan, 2017a). These findings suggest that the relationship between R_p and P_{ref} is indeed governed by the atmospheric scale height.

As our retrieval cases build toward full model considerations and adequate data, the estimated slope and the scale height converge. This is to be expected as data at short wavelengths help constrain the continuum and, hence, the molecular abundances, the mean molecular mass, and the scale height (Benneke & Seager, 2012; de Wit & Seager, 2013). As

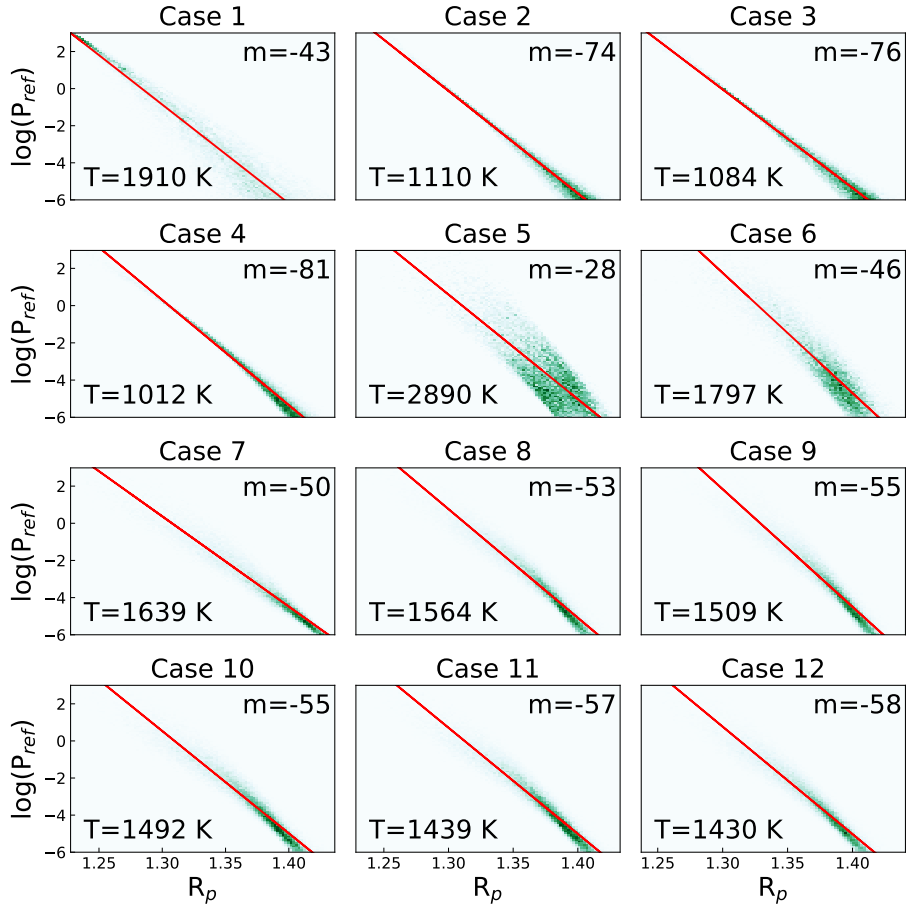

Figure 16 Relationship between the retrieved planetary radius (R_p in units of R_J) and the associated reference pressure (P_{ref} in units of bar). A linear fit is shown in red along with the slope in each panel. In the top-right corner of each panel, the slope of a linear fit is presented. On the bottom-left corner we present the temperature (in units of K) derived from the best-fit slope assuming it is defined as $m = -1/(H \ln 10)$. The 12 panels correspond to the cases explained in Section 2.3.

such, the spread in H_2O abundances seen in Figure 17 is not a result of the R_p–P_{ref} degeneracy, but a result of data quality and model assumptions. The better the data and model, the better the constraints we can impose on the molecular abundances.

Here, we investigate a possible justification for the log-linear relationship we empirically observe between P_{ref} and R_p. Generally, the pressure and distance in a planetary atmosphere are related by the consideration of hydrostatic equilibrium. We explore whether the same can explain the observed P_{ref}–R_p relation.

An observed transmission spectrum consists of transit depths, i.e., $(r/R_s)^2$, as a function of wavelength. By knowing the radius of the star,

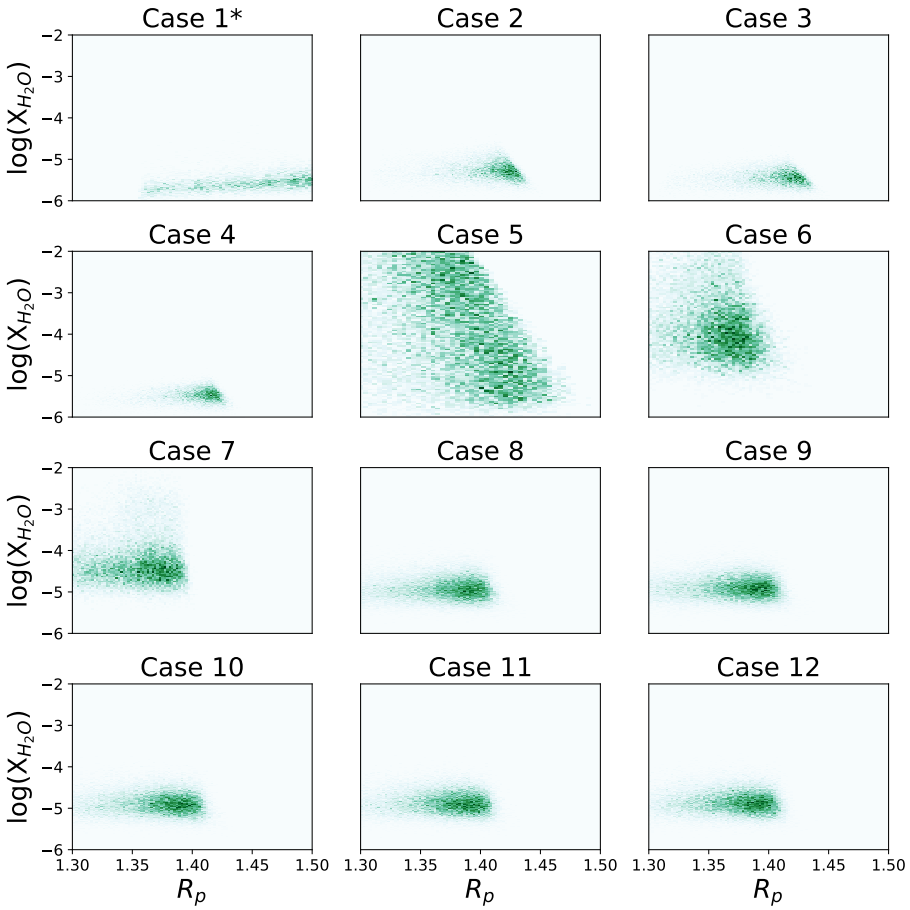

Figure 17 Correlation between the retrieved planetary radius (R_p in units of R_J) and H_2O mixing ratio (X_{H_2O}). The 12 panels correspond to the cases explained in Section 2.3. The spread in the retrieved values changes under different assumptions, with case 12 being the most general case. The H_2O abundance (i.e., mixing ratio) in case 1 has been multiplied by 10^4 to be in the same range as the H_2O abundance of other cases.

we know the observed radius (or effective radius) of the planet as a function of wavelength. An observed effective radius should correspond to an effective height in the atmosphere and the corresponding pressure level, where the atmosphere has a slant optical depth of $\tau_\lambda \sim \tau_{eq}$ (Lecavelier Des Etangs et al., 2008). The equivalent slant optical depth (τ_{eq}) corresponding to the observed spectral features is discussed in more detail in Section 2.5.1.

The pressure (P) and distance (r) in the atmosphere are related by hydrostatic equilibrium as

$$\ln\left(\frac{P}{P_{ref}}\right) = -\frac{\mu g}{k_B}\int_{R_p}^{r}\frac{1}{T}dr'. \tag{11}$$

Here, R_p and P_{ref} are a reference planet radius and the corresponding pressure, respectively. This equation can be solved if the temperature profile with distance is known. Assuming an isotherm, P and r are related by

$$\ln(P) = -\frac{r}{H} + \ln(P_{ref}) + \frac{R_p}{H}, \tag{12}$$

where $H = k_B T(\mu g)^{-1}$ is the scale height.

This relation is linear in $\ln(P)$ and r with a slope of $-1/H$ and an intercept of $\ln(P_{ref}) + R_p/H$. We rewrite Equation 12 as

$$\ln(P) = -a\, r + b. \tag{13}$$

The observed radii also provide another constraint. Given a set of observations $r_{\lambda,i}$'s, the corresponding $P_{\lambda,i}$'s are those for which the slant optical depths satisfy $\tau_{\lambda,i} \sim \tau_{eq}$. From a procedural point of view, a retrieval tries to find the best-fitting model parameters for which the distances in the model atmosphere at $r = r_{\lambda,i}$ satisfy $\tau_\lambda \sim \tau_{eq}$. The atmospheric model consists of a fixed pressure grid, as discussed in Section 2.3. For a given R_p and P_{ref}, among other parameters drawn in a model fit, the pressure grid is related to a distance grid using hydrostatic equilibrium as shown in Equation 12. These properties in turn are used to create a grid of slant optical depths corresponding to the altitude, or pressure, as a function of wavelength. The differential optical depth along the line of sight is given by $d\tau_\lambda = n\sigma_\lambda\, ds$, where σ_λ is the absorption cross section, n is the number density, and s is the distance along the line of sight. Thus, the model has a distance grid on a one-to-one correspondence with the pressure grid and an associated τ_λ map. In a retrieval, the acceptable fit parameters are those for which the locations of the observed $r_{\lambda,i}$ in the model distance grid have $\tau_\lambda \sim \tau_{eq}$.

Thus, from Equation 13, given a set of observations $r_{\lambda,i}$'s the values of a and b can be constrained. a independently constraints the scale height of the planet and the slope of hydrostatic equilibrium because $a = 1/H$. Similarly, b helps determine a unique relationship through $b = R_p/H + \ln(P_{ref})$. Rearranging for $\ln(P_{ref})$ we obtain $\ln(P_{ref}) = -R_p/H + b$, where it is evident that R_p and P_{ref}, by construction, will also need to satisfy hydrostatic equilibrium with the same slope determined by a.

We can thus conclude that there is indeed a degeneracy between P_{ref} and R_p but it is well defined and it does not affect the retrieved molecular

abundance. It is the functional form of b in Equation 13 that seems to explain the $-1/H$ behavior seen in Figures 10 and 16, and what defines the relationship between P_{ref} and R_p. Now, we inspect more closely the requirement imposed for the observed radii to correspond to a constant slant optical depth $\tau_\lambda \sim \tau_{eq}$.

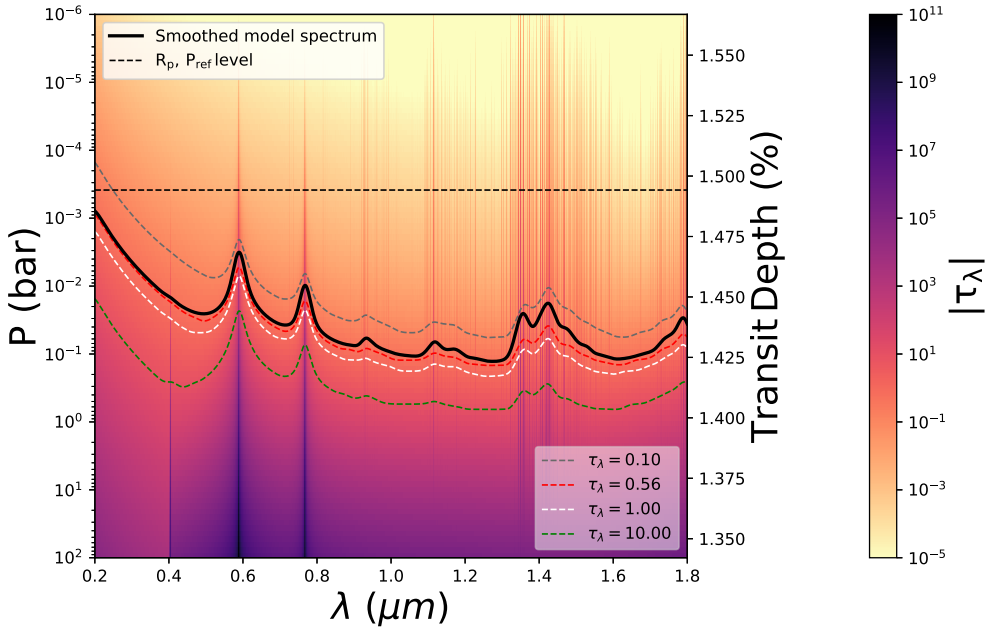

Figure 18 Photospheric level of spectral features. The black solid line shows the cloud-free model spectrum using the median values retrieved for HD 209458 b as explained in Section 2.5.1. The color map represents the slant optical depth (τ_λ) and the $\tau_\lambda = 0.10$, 0.56, 1.00, and 10.00 levels are shown in gray, red, white, and green, respectively. The black dashed line shows the reference pressure level and its corresponding transit depth, which in turn corresponds to the transit depth of the retrieved R_p. The transit depth and radius are related by the expression $\Delta = R_p^2/R_{star}^2$.

2.5.1 *The Slant Photosphere*

Following the previous section, we investigate how the observed radius at a given wavelength corresponds to a pressure through τ_λ. The one-to-one correspondence between a set of observations $r_{\lambda,i}$ and their associated pressures is determined by the slant optical depth τ of the photosphere. In this section, we explore further this notion of the equivalent slant optical depth and how this helps constrain R_p and P_{ref}. To illustrate, we use the retrieved values of HD 209458 b for case 12 in Section 2.3 and

generate a model spectrum for a cloud-free and isothermal atmosphere with temperature set to the retrieved T_0. For each wavelength in our model, we obtain the slant optical depth as a function of the pressure in the atmosphere corresponding to the impact parameter. We show a contour of τ_λ in $P - \lambda$ space in Figure 18.

Figure 18 shows both a pressure axis and a transit depth axis that are related by our selection of R_p and P_{ref} and hydrostatic equilibrium. The color map shows that the equivalent slant photosphere appears at pressures between 0.1 and 0.01 bar for most wavelengths. Furthermore, it is clear from the model spectrum that the slant optical depth at the apparent radius is ~ 0.5. This τ_λ surface is close to $\tau_\lambda = 0.56$, a value first encountered numerically by Lecavelier Des Etangs et al. (2008) and later discussed extensively by de Wit & Seager (2013). The cumulative contribution of the atmosphere to the spectrum is consistent with an opaque planet below the τ_{eq} surface. This factor provides an additional constraint when fitting Equation 13. Following Figure 18, we find that $\tau \gtrsim 0.5$ generally determines the equivalent radius and motivates the condition $\tau_\lambda \sim \tau_{eq}$ discussed in the previous section. This condition is true for hot Jupiters and for most planetary atmospheres as long as R_p/H is between ~ 300 and ~ 3000 (Lecavelier Des Etangs et al., 2008).

2.5.2 *Retrieving* R_p *versus* P_{ref}

So far, the retrievals presented here have both R_p and P_{ref} as parameters in the retrieval. We have shown above that the degeneracy between these variables can be characterized through an empirical relationship. Several retrieval analyzes use only one of R_p or P_{ref} as a free parameter and assume a fixed value for the other (e.g., Benneke & Seager, 2012; Kreidberg et al., 2015; Line & Parmentier, 2016; Sedaghati et al., 2017; Chen et al., 2018; Wakeford et al., 2018; von Essen et al., 2019). Here, we conduct retrievals that assume P_{ref} and retrieve R_p and vice versa, in addition to case 12 in Section 2.3.13 where both were considered to be free parameters. We compare the results and discuss whether the retrievals are sensitive to these assumptions.

We start by assuming a reference pressure and retrieving a planetary radius. Our retrieval is set up in the same way as in Section 2.3.13 for case 12: the model includes volatiles, a parametric P–T profile, inhomogeneous cloud cover, and uses data in the near-infrared and optical. The retrieved planetary radius is $R_p = 1.37^{+0.01}_{-0.01}\ R_J$ at an assumed pressure in bar of $\log_{10}(P_{ref}) = -3.45$. The assumed reference pres-

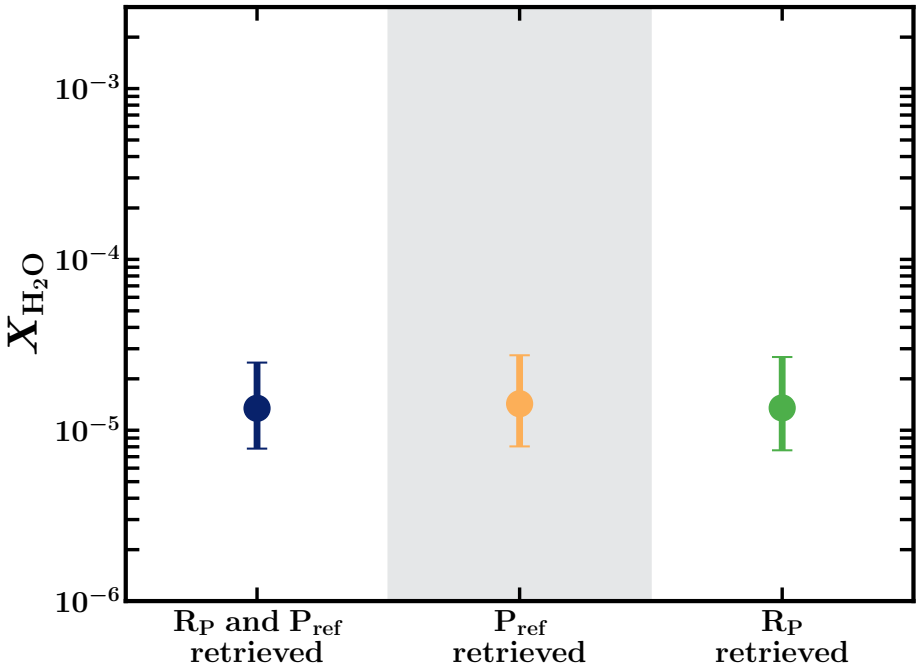

Figure 19 Retrieved H_2O abundances for three model considerations, median value, and 1σ error bars. In blue, we show the case were both R_p and P_{ref} are retrieved. In yellow, only P_{ref} is retrieved for an assumed R_p, and in green, the opposite is shown. All three retrievals provide a consistent H_2O abundance, showing that the assumption of a radius or reference pressure is inconsequential in the retrieval of H_2O abundance.

sure was chosen to match the retrieved value in Section 2.3.13. The H_2O abundance is retrieved to a value of $\log_{10}(X_{H_2O}) = -4.87^{+0.30}_{-0.25}$. The other retrieved chemical abundances are $\log_{10}(X_{Na}) = -5.44^{+0.59}_{-0.45}$ and $\log_{10}(X_K) = -7.04^{+0.60}_{-0.54}$ for the atomic species, and $\log_{10}(X_{NH_3}) = -8.34^{+2.06}_{-2.43}$, $\log_{10}(X_{CO}) = -7.72^{+2.88}_{-2.81}$, $\log_{10}(X_{HCN}) = -8.61^{+2.28}_{-2.23}$, and $\log_{10}(X_{CO_2}) = -8.41^{+2.47}_{-2.35}$ for the molecular species. The retrieved parameters for the P–T profile are $T_0 = 1049.35^{+280.69}_{-173.03}$ K, $\alpha_1 = 0.59^{+0.24}_{-0.16}$, $\alpha_2 = 0.54^{+0.29}_{-0.24}$, $\log_{10}(P_1) = -0.20^{+2.15}_{-2.21}$, $\log_{10}(P_2) = -3.44^{+2.57}_{-1.74}$, and $\log_{10}(P_3) = 1.01^{+1.31}_{-1.71}$. The retrieved parameters for the inhomogeneous cloud prescription are $\log_{10}(a) = 44.42^{+0.68}_{-0.98}$, $\gamma = -14.57^{+5.30}_{-3.68}$, a cloud top pressure of $\log_{10}(P_{cloud}) = -4.56^{+0.70}_{-0.53}$, and a cover fraction of $\bar{\phi} = 0.47^{+0.06}_{-0.08}$. All retrieved values are consistent within 1σ with the obtained values when retrieving both R_p and P_{ref} in case 12.

Then, we perform the retrieval in which we assume a planetary radius and retrieve the reference pressure. Here we assume a radius of $R_p = 1.359\ R_J$, using the value reported by Torres et al. (2008) and retrieve a H_2O abundance of $\log_{10}(X_{H_2O}) = -4.84^{+0.28}_{-0.25}$ and a reference pressure in bar of $\log_{10}(P_{ref}) = -2.48^{+0.46}_{-0.45}$. The retrieved P–T profile parameters

are $T_0 = 1000.05^{+264.42}_{-143.28}$ K, $\alpha_1 = 0.62^{+0.24}_{-0.18}$, $\alpha_2 = 0.48^{+0.33}_{-0.22}$, $\log_{10}(P_1) = -1.16^{+1.98}_{-1.77}$, $\log_{10}(P_2) = -3.92^{+2.19}_{-1.43}$, and $\log_{10}(P_3) = 1.25^{+1.20}_{-1.56}$. The retrieved cloud parameters are $\log_{10}(a) = 4.40^{+0.68}_{-0.99}$, $\gamma = -14.65^{+5.08}_{-3.63}$, $\log_{10}(P_{cloud}) = -4.54^{+0.69}_{-0.53}$, and $\bar{\phi} = 0.47^{+0.06}_{-0.08}$. The retrieved volume mixing ratios are $\log_{10}(X_{Na}) = -5.44^{+0.55}_{-0.45}$, $\log_{10}(X_K) = -7.04^{+0.58}_{-0.53}$, $\log_{10}(X_{NH_3}) = -8.11^{+1.94}_{-2.57}$, $\log_{10}(X_{CO}) = -7.75^{+2.88}_{-2.77}$, $\log_{10}(X_{HCN}) = -8.58^{+2.34}_{-2.24}$, and $\log_{10}(X_{CO_2}) = -8.37^{+2.43}_{-2.35}$. Again, the retrieved values are consistent with those of Section 2.3.13 to within 1σ.

We show the retrieved H_2O abundances and their error bars in Figure 19 for the three cases. First, we show the retrieval in Section 2.3.13 where we retrieved both R_p and P_{ref}. Second, we show the retrieval assuming an R_p and retrieving P_{ref}. The third panel shows the remaining permutation where we assume a P_{ref} and retrieve R_p. All three retrieved H_2O mixing fractions are consistent with each other. These results confirm that it is not necessary to retrieve both R_p and P_{ref}, assuming one will retrieve the other and both will be used to determine the atmospheric structure as discussed in Section 2.5. While the published work (Welbanks & Madhusudhan, 2019) that forms this chapter was under review, a follow-up paper to HK17 was published (Fisher & Heng, 2018), which retracts some of the claims of HK17. They suggest breaking the three-way degeneracy of HK17 for cloud-free atmospheres by deriving a P_{ref} for an R_p assuming it is associated with a part of the atmosphere opaque to optical and infrared radiation, a similar procedure to that suggested in previous studies (e.g., Griffith, 2014). They come to a similar conclusion that it is not necessary to retrieve both R_p and P_{ref}, and that it is possible to assume the value of one or the other, as is common practice in the literature (e.g., Benneke & Seager, 2012; Kreidberg et al., 2015; Line & Parmentier, 2016; Sedaghati et al., 2017; Chen et al., 2018; Wakeford et al., 2018; von Essen et al., 2019). However, here we show that no such assumption of wavelength is necessary. The R_p can be fixed to any measured value and the retrieval will automatically derive the corresponding P_{ref}.

2.5.3 *Limitations of Semi-analytic Analysis*

Based on our above results, here we summarize some key factors that may have limited some previous studies using semi-analytic models for constraining chemical abundances (e.g., Heng & Kitzmann, 2017; Fisher & Heng, 2018). These key factors include ignoring the effects of CIA

opacity, incorrect inferences from least-squares fits, and generalized conclusions drawn from inadequate data.

As we show in Section 2.3, ignoring the effects of CIA leads to an incorrect estimate of molecular abundances by several orders of magnitude. In the work of HK17, CIA effects were not considered, thereby rendering their analytic solution incomplete. While the assumption of isobaric opacities for molecular line absorption does not affect the retrieved molecular abundances substantially, the inclusion of CIA is incompatible with an isobaric assumption. Molecular features in current data are less strongly affected by the pressure dependence, because the spectrum probes lower pressures ($P \lesssim 0.1$ bar) for these features. On the other hand, CIA has strong dependence on the pressure. In other words, CIA is proportional to P^2 (de Wit & Seager, 2013), and its impact on the spectrum is underestimated if evaluated at only one pressure (e.g., Fisher & Heng, 2018) or completely ignored (e.g., Heng & Kitzmann, 2017).

The more problematic assumption in the work of HK17 comes in their inferred H_2O abundances obtained from best fits to the observed WFC3 spectrum of WASP-12b as shown in their Figure 7. In that figure, they claim to be showing values of $X_{H_2O}(P_0/10\text{ bar})^{-1}$ as a function of the assumed planetary radius R_0. A close inspection of this graph suggests that they are instead showing $X_{H_2O}(P_0/10\text{ bar})$ as a function of the assumed planetary radius. The linear trend they obtain in their figure is likely a manifestation of the relationship between P_{ref} and R_p, and not X_{H_2O}. They claim that a small change in the assumed planetary radius leads to a large change in the ordinate and hence the H_2O abundance. While this claim may be partly true, their inference regarding the H_2O abundance is manifestly incorrect. A large change in the product of $X_{H_2O}(P_0/10\text{ bar})$ is not because of a change in H_2O abundance but a change in the reference pressure. Changing the assumed planetary radius will change the associated reference pressure. As shown in Sections 2.3 and 2.5, the inferred H_2O abundance is largely unaffected by the P_{ref}–R_p degeneracy.

Lastly, their work considers only the interpretation of WFC3 data and ignores the effects of optical data. On the other hand, as we have shown here, it is the inclusion of optical data that helps constrain molecular abundances the most. The inclusion of optical data helps constrain the effects of clouds, the reference pressure, and the scale height. These in turn improve the constraint on the H_2O abundance. Thus, retrievals that do not take these factors into account are inherently biased toward in-

correct chemical abundances (e.g., Fisher & Heng, 2018). As such, their abundance estimates (e.g., of HD 209458 b) do not agree with retrievals that use cloudy models and optical data (e.g., MacDonald & Madhusudhan, 2017a; Barstow et al., 2017, and the present study).

In this chapter, we have shown an empirical relationship between R_p and P_{ref} that seems to be related to hydrostatic equilibrium. Furthermore, we show that this relationship is independent of X_{H_2O}, effectively breaking the three-way degeneracy. Complimentary to this is the importance of choosing the right models and assumptions in the model atmospheres. Models ignoring CIA, considering only H_2O opacity, along with constant gravity and mean molecular weight, lead to poor constraints in the retrieved H_2O abundance. Equally important are the consideration of inhomogeneous cloud coverage and inclusion of optical data in constraining molecular abundances.

2.6 SUMMARY AND DISCUSSION

We conduct a detailed analysis of degeneracies in transmission spectra of transiting exoplanets. We investigate the effect of various model assumptions and spectral coverage of data on our ability to constrain molecular abundances. Utilizing atmospheric retrievals, we test simple isobaric and isothermal atmospheric models for their ability to constrain molecular abundances using infrared spectra alone. We later remove these assumptions one by one until a realistic atmospheric model composed of H_2/He CIA, multiple chemical species, a full P–T profile, inhomogeneous cloud coverage, and the inclusion of broadband data spanning infrared to optical is obtained. We conduct this investigation using the canonical example of HD 209458 b, a hot Jupiter that has the best data currently available.

We identify several key properties that need to be accounted for in models for reliable estimates of chemical abundances, in particular H_2/He CIA opacities, a full P–T profile, and possible inhomogeneities in cloud cover. The inclusion of CIA has the most effect in accurately constraining chemical abundances as it provides a natural continuum in the model spectrum.

We find that the degeneracies between molecular abundances and cloud properties can be alleviated by the inclusion of optical data. Optical data provide constraints on the scattering slope in the optical as well as a continuum for the full spectrum. As such, optical data are key to constrain molecular abundances using transmission spectra. When op-

tical data are included, considering Na and K absorption significantly influences the retrieved H_2O abundances, making them more precise. We also find that assuming a cloud fraction a priori (e.g., 100% cloud cover) leads to erroneous estimates on molecular abundances. Leaving the cloud fraction as a free parameter allows for molecular estimates more accurate than those obtained when assuming a fixed cloud cover fraction.

We show, using simulated data, that even in the case of an atmosphere with 100% cloud cover, the retrievals are able to closely retrieve abundances and other properties. In principle, R_p is degenerate with the pressure level of the cloud top. However, the range of altitudes, and hence pressures, of the cloud top where it affects the spectrum is limited. A 100% cloud deck must be at an altitude higher than the line-of-sight photosphere and lower than the level where the atmosphere is optically thin. In the former case, the cloud deck does not contribute significantly, and in the latter case, the cloud deck causes a featureless spectrum, contrary to observed features. On the other hand, we show that an inhomogeneous cloud model accurately retrieves the cloud fraction even for a 100% cloudy case. Among the considerations that we leave unexplored in this set of retrievals are the effect of stellar activity on the transmission spectra and its consequence in resolving degeneracies, and the presence of shifts or offsets between data taken from different instruments. Other aspects to consider in the future include inhomogeneities across the limb due to the 3D structure of an atmosphere (e.g., Caldas et al., 2019), refraction in the atmosphere (e.g., Bétrémieux, 2016), height-varying chemical abundances (e.g., Parmentier et al., 2018), and various cloud properties (e.g., Vahidinia et al., 2014; Barstow et al., 2016a). Future work and retrieval frameworks like that of Pinhas et al. (2018) could help elucidate these aspects. Overall, the quality of the data and the wavelengths they span are fundamental in breaking degeneracies and retrieving molecular abundances.

We also discuss the limitations of semi-analytic studies in fully assessing degeneracies in transmission spectra. One important finding is that the degeneracy between P_{ref} and R_p does not lead to an inability to determine molecular abundances in transit spectroscopy, contrary to previous suggestion. We show an empirical relationship between the planetary radius and the reference pressure that characterizes their degeneracy. We find that $\ln(P_{ref})$ and R_p have a linear relationship with a slope of $-1/H$ and suggest that this behavior is rooted in hydrostatic equilibrium. For each R_p, there is an associated P_{ref} and vice versa. As

such, it is redundant to perform retrievals that consider both quantities as free parameters. Instead, we demonstrate that it is justified to assume a value for one quantity and to retrieve the other. Some studies assume an R_p and retrieve a P_{ref}; here we demonstrate that the inverse is also consistent, i.e., that it is possible to assume a P_{ref} and retrieve the radius of the planet corresponding to that P_{ref}.

We investigate the origins of spectral features in transmission spectra by following the line-of-sight opacity of the planet as a function of the vertical pressure level and wavelength. This allows us to calculate the height and pressure levels in the atmosphere at which the observed features are generated and compare it to the white light radius. We show that the effective radius corresponding to the observed transit depth at a given wavelength corresponds to a level in the atmosphere with a slant optical depth of $\tau \gtrsim 0.5$, as also suggested by previous studies.

Overall, our study demonstrates the effectiveness of high-precision spectra and realistic models to retrieve atmospheric abundances. Data with current facilities such as HST and VLT over the visible and near-infrared can already provide valuable constraints on abundances of key species such as H_2O, Na, K, etc. The upcoming James Webb Space Telescope and ground-based facilities therefore hold great promise for characterizing exoplanetary atmospheres using transmission spectra.

3

MASS-METALLICITY TRENDS IN TRANSITING EXOPLANETS FROM ATMOSPHERIC ABUNDANCES OF H_2O, NA, AND K

Atmospheric compositions can provide powerful diagnostics of formation and migration histories of planetary systems. In this chapter[1], we investigate constraints on atmospheric abundances of H_2O, Na, and K, in a sample of transiting exoplanets using the latest transmission spectra and new H_2 broadened opacities of Na and K. Our sample of 19 exoplanets spans from cool mini Neptunes to hot Jupiters, with equilibrium temperatures between $\sim$ 300 and 2700 K. Using homogeneous Bayesian retrievals we report atmospheric abundances of Na, K, and H_2O, and their detection significances, confirming 6 planets with strong Na detections, 6 with K, and 14 with H_2O. We find a mass-metallicity trend of increasing H_2O abundances with decreasing mass, spanning generally substellar values for gas giants and stellar/superstellar for Neptunes and mini Neptunes. However, the overall trend in H_2O abundances, from mini Neptunes to hot Jupiters, is significantly lower than the mass-metallicity relation for carbon in the solar system giant planets and similar predictions for exoplanets. On the other hand, the Na and K abundances for the gas giants are stellar or superstellar, consistent with each other, and generally consistent with the solar system metallicity trend. The H_2O abundances in hot gas giants are likely due to low oxygen abundances relative to other elements rather than low overall metallicities, and provide new constraints on their formation mechanisms. The differing trends in the abundances of species argue against the use of chemical equilibrium models with metallicity as one free parameter in atmospheric retrievals, as different elements can be differently enhanced.

1 The contents of this chapter are based on the published work of Welbanks et al. (2019). As explained in Section 3.4, the retrieval framework used in this work is an adaptation of AURA (Pinhas et al., 2018) developed in Prof. Nikku Madhusudhan's research group. Nicole F. Allard, Ivan Hubeny, and Fernand Spiegelman contributed to the contents of this chapter by providing the calculation of the Na and K absorption cross sections including the effects of broadening due to H_2, and to the coresponding text in Section 3.3. Dr. Kaisey Mandel contributed to the published work though helpful conversations. Besides overall supervision, Prof. Nikku Madhusudhan contributed to the text on planet formation in Sections 3.5.2 and 3.6.

3.1 INTRODUCTION

Exoplanet science has entered an era of comparative studies of planet populations. Several studies have used empirical metrics for comparative characterization of giant exoplanetary atmospheres based on their transmission spectra (e.g., Heng, 2016; Sing et al., 2016; Stevenson, 2016; Fu et al., 2017). Comparative studies are also being carried out using full atmospheric retrievals, primarily constraining H_2O abundances and/or cloud properties from transmission spectra (e.g., Madhusudhan et al., 2014b; Barstow et al., 2017; Pinhas et al., 2019). Besides H_2O, Na and K are the most observed chemical species in giant exoplanetary atmospheres using space- and ground-based telescopes (e.g., Charbonneau et al., 2002; Redfield et al., 2008; Wyttenbach et al., 2015; Sing et al., 2016; Nikolov et al., 2018). As observations improve in precision, recent studies have begun to retrieve Na and K abundances from transmission spectra (e.g Nikolov et al., 2018; Fisher & Heng, 2019; Pinhas et al., 2019).

Previous ensemble studies have focused on H_2O and found low abundances compared to solar system expectations (e.g., Madhusudhan et al., 2014b; Barstow et al., 2017; Pinhas et al., 2019). However, it has been unclear if the low H_2O abundances are due to low overall metallicities, and hence low oxygen abundances, or due to high C/O ratios (Madhusudhan et al., 2014b) or some other mechanism altogether. Therefore, abundance estimates of other elements such as Na and K provide an important means to break such degeneracies, and provide potential constraints on planetary formation mechanisms (e.g., Öberg et al., 2011; Madhusudhan et al., 2014c; Thorngren et al., 2016; Mordasini et al., 2016). In the present chapter, we conduct a homogeneous survey of Na, K, and H_2O abundances for a broad sample of transiting exoplanets, and investigate their compositional diversity.

3.2 OBSERVATIONS

We consider transmission spectra of 19 exoplanets with masses ranging from 0.03 to 2.10 M_J and equilibrium temperatures from 290 to 2700 K, as shown in Table 2. The spectral range covered in the observations generally spans 0.3–5.0 μm obtained with multiple instruments, including Hubble Space Telescope (HST) Space Telescope Imaging Spectrograph (STIS) (~ 0.3–1.0 μm), HST Wide Field Camera 3 (WFC3) G141 (~ 1.1–1.7 μm), and Spitzer photometry (3.6 and 4.5 μm), for most planets and ground-based optical spectra (~ 0.4–1.0 μm) for some planets. We select

the sample of 10 hot Jupiters with HST and Spitzer observations from Sing et al. (2016). We expand the sample by including five other planets that have ground-based transmission spectra in the optical: GJ3470b (Chen et al., 2017; Benneke et al., 2019b), HAT-P-26b (Stevenson et al., 2016; Wakeford et al., 2017a), WASP-127b (Chen et al., 2018), WASP-33b (von Essen et al., 2019), and WASP-96b (Nikolov et al., 2018). We include four more planets with strong H_2O detections: WASP-43b (Kreidberg et al., 2014b; Stevenson et al., 2017), WASP-107b (Spake et al., 2018), K2-18b (Benneke et al., 2019a), and HAT-P-11b (Chachan et al., 2019).

For the sample of Sing et al. (2016) we use the data selection from Pinhas et al. (2019), with the exception of WASP-39b for which we use the combined transmission spectrum of Kirk et al. (2019), and WASP-19b for which we use a ground-based transmission spectrum from the FORS2 Spectrograph at the Very Large Telescope (VLT; Sedaghati et al., 2017). The VLT spectrum is of higher resolution than the STIS spectrum and showed evidence for spectral features; we note that the same features were not seen by Espinoza et al. (2019) in a ground-based spectrum obtained with GMT at a different epoch, albeit with lower resolution. For each data set, we follow the same data treatment for retrieval as in the corresponding work.

The spectral range of the data allow simultaneous constraints on Na, K, and H_2O, along with other atmospheric properties. The optical range probes the prominent spectral features of Na ($\sim$ 589 nm) and K ($\sim$ 770 nm), and contributions from scattering phenomena such as Rayleigh scattering and clouds/hazes (e.g., Sing et al., 2016), as well as absorption from other chemical species such as TiO (e.g., Sedaghati et al., 2017). On the other hand, the HST WFC3 and Spitzer bands probe molecular opacity from volatile species such as H_2O, CO, and HCN (Madhusudhan, 2012).

3.3 H_2 BROADENED ALKALI CROSS SECTIONS

Given our goal of constraining abundances of Na and K based on optical transmission spectra it is important to ensure accurate absorption cross sections of these species in the models. We use the latest atomic data on Na and K absorption including broadening due to H_2 which is the dominant species in gas giant atmospheres. The Na line data is obtained from Allard et al. (2019) and the K line data is obtained from Allard et al. (2016). The line profiles are calculated in a unified line shape semi-classical theory (Allard et al., 1999) that accounts both for the centers of

the spectral lines and their extreme wings, along with accurate ab initio potentials and transition moments.

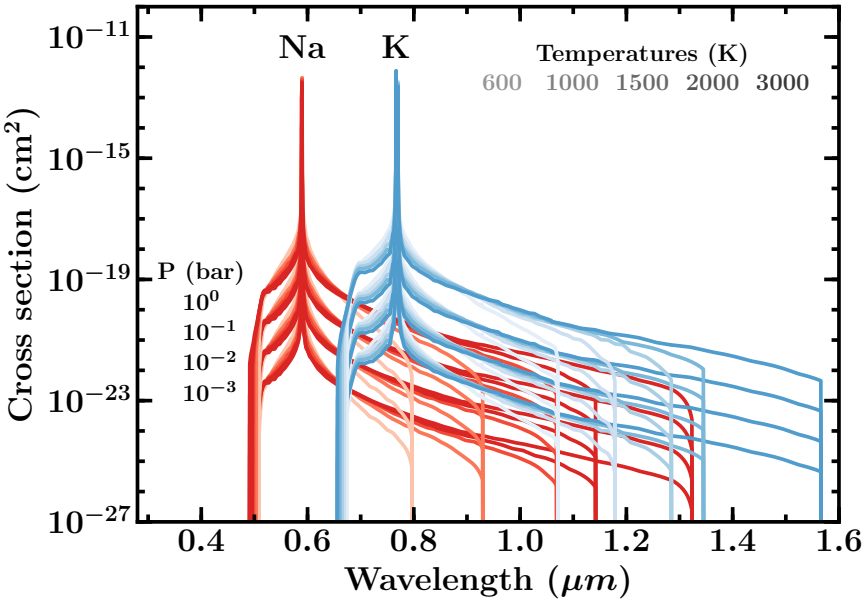

Figure 20 Absorption cross sections of Na and K broadened by H_2 at different pressures and temperatures. Line profiles for each pressure appear as a group. In each group, the darker colors (broader wings) denote hotter temperatures.

We compute the cross section for H_2 broadened Na for both the D1 and D2 doublets at 5897.56 Å and 5891.58 Å respectively. We calculate the contributions from the core of the lines and their broadened wings for 500, 600, 725, 1000, 1500, 2000, 2500, and 3000 K for pressures equally spaced in log space from 10^{-5} to 10^{2} bar. We repeat this procedure for H_2 broadened K for the D1 and D2 doublet peaks at 7701.10 Å and 7667.02 Å, at 600, 1000, 1500, 2000, and 3000 K. Figure 20 shows the H_2 broadened cross sections of Na and K for a range of pressures and temperatures. The extended wings of our alkali cross sections, particularly of K, stop below ~ 1.4 μm for the typical pressures and temperatures probed by transmission spectra. As such, these cross sections do not provide an extended continuum to the spectrum in the HST WFC_3 band, which results in retrieved H_2O abundances that are conservatively higher. Future calculations including other transition lines in the near-infrared and their H_2 broadening could extend Na/K opacity into the WFC_3 range.

3.4 ATMOSPHERIC RETRIEVAL

We follow the retrieval approach in Welbanks & Madhusudhan (2019) based on the AURA retrieval code (Pinhas et al., 2018). The code allows for the retrieval of chemical abundances, a pressure-temperature profile, and cloud/haze properties using spectra from multiple instruments. The model computes line by line radiative transfer in a transmission geometry and assumes hydrostatic equilibrium and uniform chemical volume mixing ratios in the atmosphere. A full description of the retrieval setup can be found in Pinhas et al. (2019) and Welbanks & Madhusudhan (2019), see also Chapter 2.

Besides the new H_2 broadened alkali species discussed in Section 3.3, we include opacities due to other chemical species possible in hot giant planet atmospheres (Madhusudhan, 2012). Our retrievals generally consider absorption due to H_2O (Rothman et al., 2010), Na (Allard et al., 2019), K (Allard et al., 2016), CH_4 (Yurchenko & Tennyson, 2014), NH_3 (Yurchenko et al., 2011), HCN (Barber et al., 2014), CO (Rothman et al., 2010), and H_2-H_2 and H_2-He collision induced absorption (CIA; Richard et al., 2012). Additionally, following previous studies (Chen et al., 2018; von Essen et al., 2019; Sedaghati et al., 2017; MacDonald & Madhusudhan, 2019), we include absorption due to Li (Kramida et al., 2018) for WASP-127b, AlO (Patrascu et al., 2015) for WASP-33b, TiO (Schwenke, 1998) for WASP-19b, and CrH (Bauschlicher et al., 2001), TiO, and AlO for HAT-P-26b. We exclude absorption due to Na and K for K2-18b, GJ-3470b, and WASP-107b as it is not expected for these species to remain in gas phase at the low temperatures of these planets (e.g., Burrows & Sharp, 1999). The absorption cross sections are calculated using the methods of Gandhi & Madhusudhan (2018).

The parameter estimation and Bayesian inference is conducted using the nested sampling algorithm implemented using PyMultiNest (Buchner et al., 2014). We choose log uniform priors for the volume mixing ratios of all species between -12 and -1. We further expand this prior to -0.3 for planets less massive than Saturn ($\sim 0.3\ M_J$) to allow for extremely high ($\sim 50\%$) H_2O abundances. The temperature prior at the top of the atmosphere is uniform with a lower limit at 0 K for $T_{eq.} < 900$ K, 400 K for 900 K $< T_{eq.} <$ 1200 K, and 800 K for $T_{eq.} > 1200$ K, and a higher limit at $T_{eq.} + 100$ K. Our retrieval of WASP-19b allows for a wavelength shift relative to the model for VLT FORS2 data only, as performed by Sedaghati et al. (2017). The retrievals performed in this study have in general 18 free parameters: 7 chemical abundances, 6 for the

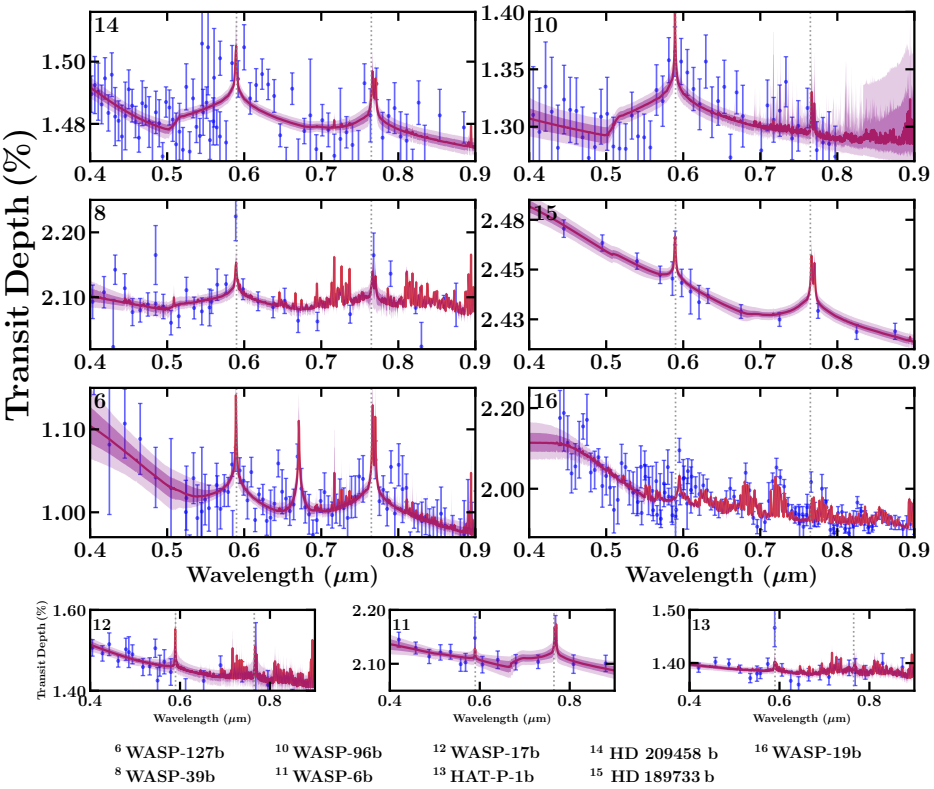

Figure 21 Observations and retrieved model transmission spectra of exoplanets showing evidence of Na and/or K in the optical wavelengths. Dotted lines show the wavelength positions for Na (~ 0.589 μm) and K (~ 0.770 μm). Observations are shown in blue while median retrieved models and confidence intervals (1σ and 2σ) are shown in red and purple respectively. The top six panels show planets with evidence for Na or K above 2σ, and the bottom three show those with weaker evidence (see Table 2).

pressure-temperature profile, 4 for clouds and hazes, and 1 for the reference pressure at the measured observed radius of the planet.

3.5 RESULTS

The atmospheric constraints for our sample of 19 transiting exoplanets, ranging from hot Jupiters to cool mini Neptunes are shown in Table 2. Priors and posterior distributions are available in Appendix B. The detection significance is calculated from the Bayes factor (Benneke & Seager, 2013; Buchner et al., 2014). We consider reliable abundance estimates to be those with detection significances larger than 2σ.

Table 2 Planetary Properties and Retrieved H_2O, Na, and K Abundances (Mixing Ratio) for 19 Exoplanets.

#	PLANET NAME	$M_P(M_J)$	T_{EQ} (K)	$\log_{10}(X_{H_2O})$	DS_{H_2O}	$\log_{10}(X_{Na})$	DS_{Na}	$\log_{10}(X_K)$	DS_K
1	K2-18b	0.03	290	$-2.36^{+1.17}_{-1.16}$	3.26	N/A	N/A	N/A	N/A
2	GJ3470b	0.04	693	$-2.83^{+0.87}_{-0.77}$	3.75	N/A	N/A	N/A	N/A
3	HAT-P-26b	0.06	994	$-1.83^{+0.46}_{-0.57}$	8.61	$-9.08^{+2.04}_{-1.88}$	N/A	$-10.56^{+1.21}_{-0.96}$	N/A
4	HAT-P-11b	0.07	831	$-3.66^{+0.83}_{-0.57}$	4.12	$-9.36^{+2.04}_{-1.67}$	N/A	$-9.80^{+1.62}_{-1.42}$	N/A
5	WASP-107b	0.12	740	$-2.87^{+0.95}_{-0.73}$	5.70	N/A	N/A	N/A	N/A
6	WASP-127b	0.18	1400	$-2.13^{+0.65}_{-3.63}$	2.07	$-2.19^{+0.81}_{-4.41}$	3.66	$-2.89^{+0.80}_{-3.44}$	4.77
7	HAT-P-12b	0.21	960	$-5.70^{+1.22}_{-3.36}$	1.57	$-8.97^{+2.33}_{-1.94}$	N/A	$-8.33^{+2.32}_{-2.09}$	N/A
8	WASP-39b	0.28	1120	$-0.65^{+0.14}_{-1.83}$	8.92	$-3.62^{+1.14}_{-2.69}$	3.83	$-5.62^{+2.30}_{-2.05}$	2.37
8	WASP-39b*	0.28	1120	$-2.43^{+0.27}_{-0.24}$	9.20	$-6.17^{+0.50}_{-0.51}$	3.97	$-7.24^{+0.71}_{-1.06}$	2.45
9	WASP-31b	0.48	1580	$-4.55^{+1.77}_{-4.33}$	1.65	$-8.08^{+2.28}_{-2.37}$	N/A	$-3.48^{+1.38}_{-2.31}$	2.89
10	WASP-96b	0.48	1285	$-4.95^{+2.25}_{-4.19}$	1.61	$-5.26^{+0.75}_{-0.59}$	5.16	$-9.27^{+1.46}_{-1.60}$	N/A
11	WASP-6b	0.50	1150	$-8.12^{+2.52}_{-2.41}$	N/A	$-8.25^{+3.10}_{-2.30}$	N/A	$-3.22^{+1.21}_{-3.79}$	2.55
12	WASP-17b	0.51	1740	$-3.84^{+1.27}_{-0.51}$	3.36	$-8.65^{+1.76}_{-1.67}$	1.09	$-9.62^{+1.78}_{-1.45}$	N/A
13	HAT-P-1b	0.53	1320	$-2.54^{+0.75}_{-0.67}$	3.17	$-8.58^{+1.20}_{-1.79}$	1.32	$-8.93^{+2.01}_{-1.93}$	N/A
14	HD 209458 b	0.69	1450	$-4.54^{+0.33}_{-0.27}$	6.80	$-5.47^{+0.61}_{-0.48}$	6.77	$-7.00^{+0.59}_{-0.49}$	3.90
15	HD 189733 b	1.14	1200	$-4.66^{+0.35}_{-0.33}$	5.26	$-4.19^{+0.67}_{-0.73}$	5.51	$-5.54^{+0.49}_{-0.44}$	3.34
16	WASP-19b	1.14	2050	$-3.43^{+0.47}_{-0.52}$	7.12	$-5.11^{+1.00}_{-1.05}$	3.48	$-10.85^{+1.20}_{-0.80}$	N/A
17	WASP-12b	1.40	2510	$-3.23^{+1.42}_{-0.80}$	5.41	$-6.64^{+2.13}_{-2.98}$	1.58	$-8.94^{+2.35}_{-1.92}$	N/A
18	WASP-43b	2.03	1440	$-3.68^{+0.92}_{-0.88}$	3.31	$-6.95^{+3.21}_{-3.22}$	N/A	$-7.50^{+3.02}_{-2.87}$	N/A
19	WASP-33b	2.10	2700	$-6.64^{+3.15}_{-3.25}$	1.29	$-8.98^{+2.28}_{-1.89}$	N/A	$-6.77^{+2.83}_{-3.16}$	N/A

Note. The detection significance (DS) is included for each individual species. N/A means that the model without the chemical species had more evidence than the model including it (e.g., $B < 1$), that the corresponding species was not included in the model or, in the case of WASP-43b, that it is not possible to provide a DS since no optical data was utilized. Planet mass and equilibrium temperature, with uniform redistribution, are quoted as nominal values; uncertainties in these values are not considered. WASP-39b* corresponds to the case with an upper end of prior on the volume mixing ratios at -1 rather than -0.3.

3.5.1 *Abundances of H_2O, Na, and K*

We confirm detections of H_2O, Na, and K in 14, 6, and 6 planets, respectively, at over 2σ confidence, as shown in Table 2. Figure 21 shows the observed spectra and model fits for planets where at least one of either Na or K is detected. Our retrieved abundances (volume mixing ratios) for these species are broadly consistent with previous surveys and studies on each planet, as discussed in Sections 3.1 and 3.2. The abundances can be assessed relative to expectations from thermochemical equilibrium for solar elemental composition (Asplund et al., 2009). For solar composition (C/O = 0.54), at $T \gtrsim 1200$ K roughly half the oxygen is expected to be in H_2O, at 1 bar pressure (Madhusudhan, 2012). Thus, $\log_{10}(X_{H_2O}) \sim -3.3$ and -3.0 for T above and below 1200 K, respectively. Similarly, $\log_{10}(X_{Na}) \sim -5.76$, and $\log_{10}(X_K) \sim -6.97$ for $T \gtrsim 1100$–1200 K, below which they enter molecular states (Burrows & Sharp, 1999). Figure 22 shows the abundances of Na, K, and H_2O relative to expectations based on their stellar elemental abundances as described above for solar composition. The stellar abundances (e.g., Brewer et al., 2016) used here are presented in Appendix B. For stars without [Na/H], [O/H], or [K/H] estimates we adopt the [Fe/H] values.

The best constraints are obtained for H_2O across the sample, with precisions between ~ 0.3 and 1 dex for many of the planets, as shown in Figure 22. The median H_2O abundances for most of the gas giants are substellar, with some being consistent to stellar values within $\sim 1\sigma$. On the other hand, smaller planets show an increase in H_2O abundances, albeit with generally larger uncertainties. In the ice giants and mini Neptunes the median abundances are nearly stellar, with the exception of HAT-P-26b and HAT-P-11b, which are significantly superstellar and substellar, respectively. An exception is the hot Saturn WASP-39b for which anomalously high H_2O was reported with the latest data (Wakeford et al., 2018; Kirk et al., 2019). We find its abundance estimates to be sensitive to the choice of priors; we report two estimates with different priors in Table 2.

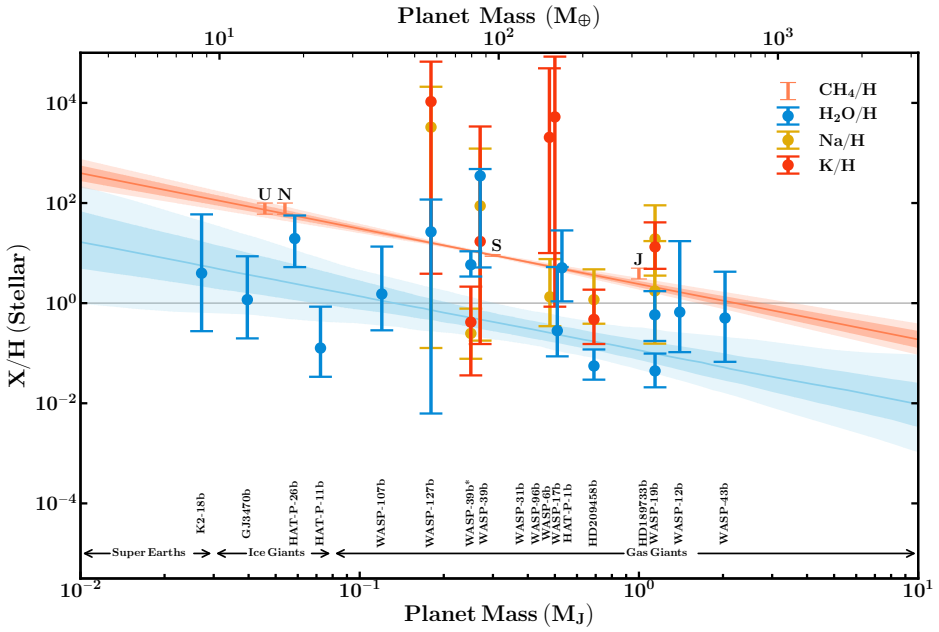

Figure 22 Mass-metallicity relation for planets with chemical detections above 2σ significance (see Table 2). The H_2O/H, Na/H, and K/H abundances are shown in blue, yellow, and orange, respectively. All the abundances are normalized to expectations based on their host stars, as described in Section 3.5.1. The metallicity estimates for the solar system giant planets using their methane (CH_4) abundances (Atreya et al., 2018) are shown in coral. The coral shaded regions show the 1σ and 2σ metallicity trend for the solar system planets resulting from a linear fit. The corresponding fit to the exoplanet H_2O abundances, excluding WASP-39b (see Section 3.5.2), and the confidence intervals are shown in the blue line and sky blue shaded regions. The fits are $\log_{10}(CH_4/H) = -1.11^{+0.11}_{-0.10}\log_{10}(M/M_J) + 0.38^{+0.06}_{-0.06}$ and $\log_{10}(H_2O/H) = -1.09^{+0.34}_{-0.33}\log_{10}(M/M_J) - 0.95^{+0.21}_{-0.19}$. The alkali ($H_2O$) abundances for the sample are generally above (below) the solar system trend. Results for WASP-39b* (see Table 2) and some labels have been offset in mass for clarity.

Contrary to H_2O, the median abundances of Na and K are nearly stellar or superstellar across the seven gas giants. The alkali abundances are retrieved only for the gas giants in our sample, with uncertainties larger than those for H_2O. For planets where they are nearly stellar (e.g., HD 209458 b) Na and K are still more enhanced relative to H_2O, as with the other planets. The retrieved alkali abundances represent the population of ground state species. While previous studies noted the effect of non-LTE ionization on the absorption strength of alkali lines (Barman et al., 2002; Fortney et al., 2003), others (e.g., Fisher & Heng, 2019) show that the effect is less pertinent for interpretation of low resolution spectra as in the present study. Our retrieved Na abundances are consistent with

Fisher & Heng (2019) for the same planets. Nonetheless, as discussed in Welbanks & Madhusudhan (2019, see Chapter 2), the simplified model assumptions in Fisher & Heng (2019, e.g., isotherms, limited absorbers, and no CIA opacity) likely affect the precision and accuracy of their abundance constraints, perhaps explaining their unphysically high temperatures even in LTE. Furthermore, alkali broadening in Fisher & Heng (2019) is inconsistent with the more accurate broadening (Allard et al., 2019) used in the present chapter.

3.5.2 *Abundance Ratios and Mass-Metallicity Relation*

The abundances of Na, K, and H_2O provide constraints on their differential enhancements in hot gas giant atmospheres relative to their host stars. Figure 23 shows abundances of different species, relative to their host stars, compared against each other. Planets with significant indications of Na and K, i.e., WASP-127b, WASP-39b, HD 189733 b, and HD 209458 b, have a normalized K/Na ratio consistent with unity. Thus, the abundances of Na and K closely follow their stellar proportions; they are enhanced or depleted together in the planetary atmosphere relative to the star. On the contrary, the H_2O/Na ratios deviate significantly from their stellar expectations, especially for those planets with the tightest constraints: HD 209458 b and HD 189733 b. The right panel in Figure 23 shows that for the small sample of planets with strong detections ($\gtrsim 2\sigma$) of both Na and H_2O, most have preferential enhancement of Na relative to H_2O compared to stellar expectations; the only exception being WASP-39b. A similar trend can be inferred for H_2O/K, i.e., of K-enhancement and H_2O-depletion, given the Na/K ratios consistent with unity (left panel in Figure 23). Given the present small sample of objects ($N = 4$) with strong detections of all three species (Na, K, and H_2O), future observations for more objects are required to further assess the Na/K trends seen here.

The H_2O abundances retrieved across our diverse sample of planets allow us to investigate a mass-metallicity relation for their atmospheres. In the solar system giant planets, CH_4 is thought to contain most of the carbon given their low temperatures. Thus, the CH_4 abundance has been used as a proxy for the carbon abundance and hence the metallicity (Atreya et al., 2018). A linear fit to the solar system CH_4 abundances leads to a "mass-metallicity" relation of $\log_{10}(CH_4/H) = -1.11^{+0.11}_{-0.10} \log_{10}(M/M_J) + 0.38^{+0.06}_{-0.06}$. As discussed in Section 3.5.1, the H_2O abundances in our exoplanet sample also show a gradually in-

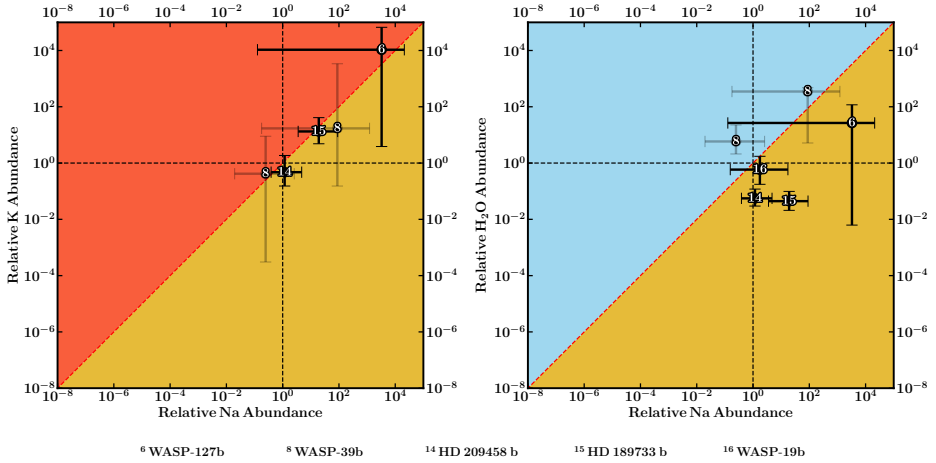

Figure 23 Normalized abundances of Na, K, and H_2O for detections above 2σ significance. Left: K vs. Na abundances normalized by host stellar abundances. Right: normalized H_2O vs. Na abundances. Abundances are normalized following the description in Section 3.5.1. The red dashed diagonal line in each plot shows the "unity line" where the normalized abundance ratio between species is equal to 1. The black dashed lines show individual normalized mixing ratios equal to 1. Two values are shown for WASP-39b corresponding to Table 2 in a lighter shade.

creasing trend with decreasing mass as shown in Figure 22. However, the H_2O abundances across the entire sample, down to the mini Neptunes, largely fall below the solar system metallicity trend based on CH_4 abundances. A linear fit to the retrieved exoplanetary H_2O abundances, excluding WASP-39b due to its strong prior dependence, yields an H_2O "mass-metallicity" relation of $\log_{10}(H_2O/H) = -1.09^{+0.34}_{-0.33} \log_{10}(M/M_J) - 0.95^{+0.21}_{-0.19}$, which is inconsistent with the solar system CH_4 measurements at over 6σ. On the other hand, the Na and K abundances for the gas giants are mostly consistent with the solar system carbon trend, albeit aided by their larger uncertainties.

3.6 DISCUSSION

Our study reveals three key trends in the atmospheric compositions of our exoplanet sample. First, from mini Neptunes to hot Jupiters, H_2O abundances are generally consistent with or depleted compared to equilibrium expectations based on stellar abundances, and lower than the solar system metallicity trend. Second, the gas giants exhibit Na and K abundances consistent with or higher than those of their host stars

and the solar system trend. Lastly, the Na and K elemental ratios are consistent with each other.

The overall low H_2O abundances across the sample contrasts with solar system predictions. Besides the carbon enhancements seen in the solar system (Figure 22), other elements such as nitrogen, sulfur, phosphorous, and noble-gases are also enhanced in Jupiter (Atreya et al., 2018); the oxygen abundance is unknown as H_2O condenses at the low temperatures of solar system giants. Considering that oxygen is the most cosmically abundant element after H and He, it is expected to be even more enhanced than carbon in giant planets, according to solar system predictions (Mousis et al., 2012). Therefore, the consistent depletion of H_2O abundances in our sample suggest different formation pathways for these close-in exoplanets compared to the long-period solar system giants.

The H_2O abundance is likely representative of the oxygen abundance (O/H) for our cool Neptunes/mini Neptunes. The H_2O abundance is less sensitive to C/O for $T \lesssim 1200$ K, with most of the O bound in H_2O regardless of C/O (Madhusudhan, 2012). Thus, the H_2O abundances for our exo-Neptunes and mini Neptunes ($T \lesssim 1200$ K) indicate somewhat lower metallicities in their atmospheres than solar system expectations (Atreya et al., 2018). On the other hand, for hot gas giant photospheres ($T \gtrsim 1200$ K), the H_2O abundance depends on both the O/H and C/O ratios. A C/O $\sim$ 1 can lead to $\sim 100\times$ depletion in H_2O compared to solar C/O (0.54). Thus, even for a solar or super-solar O/H the H_2O in hot gas giants can be subsolar if the C/O is high.

The low H_2O abundances in hot gas giants are therefore unlikely to be due to low O/H or low overall metallicities, considering the higher alkali enrichments in some planets. An atmosphere depleted up to $100\times$ in O/H while being enriched in other elements is unlikely (Madhusudhan et al., 2014c). Instead, the H_2O underabundance and alkali enrichment are likely due to superstellar C/O, Na/O, and K/O ratios, i.e., an overall stellar or superstellar metallicity but oxygen depleted relative to other species. This addresses the degeneracy between C/O and metallicity prevalent since the first inferences of low H_2O abundances in hot Jupiters (Madhusudhan et al., 2014b).

These H_2O abundances in hot gas giants, while generally inconsistent with expectations from solar system and similar predictions for exoplanets (e.g., Mousis et al., 2012; Thorngren et al., 2016), could suggest other formation pathways. The combination of stellar or superstellar metallicities and high C/O ratios in hot Jupiters can instead be caused by primar-

ily accreting high C/O gas outside the H_2O and CO_2 snow lines (Öberg et al., 2011; Madhusudhan et al., 2014c). The high Na and K abundances could potentially be caused by accretion of planetesimals rich in alkalis at a later epoch, potentially even in close-in orbits. Another possibility is the formation of giant planets by accreting metal-rich and high C/O gas caused by pebble drift (Öberg & Bergin, 2016; Booth et al., 2017). Future studies could further investigate these avenues to explain the observed trends.

Finally, our study highlights important lessons for the interpretation of atmospheric spectra of gas giants. The differing trends in the abundances of species argue against the use of chemical equilibrium models with the metallicity and C/O ratio as the only free chemical parameters in atmospheric retrievals; different elements can be differently enhanced. Atmospheric models also need to consider the effect of H_2 broadening of alkali opacities on abundance estimates. With better quality data and targeted observations, comparative atmospheric characterization of exoplanets as pursued here will likely continue to unveil trends that may inform us about their formation and evolutionary mechanisms.

4

METHODS FOR A GENERALIZED RETRIEVAL FRAMEWORK FOR EXOPLANETARY TRANSMISSION SPECTRA

As explained in Chapter 1, atmospheric retrievals of exoplanetary transmission spectra provide important constraints on various properties, such as chemical abundances, cloud/haze properties, and characteristic temperatures, at the day-night atmospheric terminator. To date, most spectra have been observed for giant exoplanets due to which retrievals typically assume hydrogen-rich atmospheres. However, recent observations of mini Neptunes/super-Earths, and the promise of upcoming facilities including the James Webb Space Telescope (JWST), call for a new generation of retrievals that can address a wide range of atmospheric compositions and related complexities.

In this chapter[1] we elaborate on the methods required for building a generalized retrieval framework for exoplanetary transmission spectra. Here we report Aurora, a next-generation atmospheric retrieval framework that builds upon the AURA retrieval framework (Pinhas et al., 2018). As part of the process of producing Aurora, we have refactored AURA. We have maintained part of the essential infrastructure of AURA, such as the numerical model for calculating radiative transfer in a transmission geometry, the methods for interpolating opacities into a given temperature grid (also adapted after the work of Gandhi & Madhusudhan 2018), and the methods for binning down a spectrum to the resolution of the input observations. We adapted the internal structure of the code to consider new opacity sources, calculate the planetary spectrum at a specific resolution, retrieve a reference pressure and/or planetary radius (see e.g., Chapter 2), consider instrumental and wavelength shifts (see e.g., Chapter 3), and redesigned AURA beyond its specific H-rich scope (Pinhas et al., 2018). As part of the redevelopment and reimplementation of AURA into Aurora, we have incorporated the following key advancements (a) a generalized compositional retrieval allowing for H-rich and H-poor atmospheres (b) a generalized prescription for inho-

1 The contents of this chapter are based on the published work of Welbanks & Madhusudhan (2021). As explained in Section 4.2, Aurora builds upon the AURA retrieval framework (Pinhas et al., 2018) developed in Prof. Nikku Madhusudhan's research group. Siddharth Gandhi and Arazi Pinhas provided help with the AURA retrieval code which is the progenitor of Aurora and through various helpful discussions.

mogeneous clouds/hazes, (c) multiple Bayesian inference algorithms for high-dimensional retrievals, (d) modular considerations for refraction, forward scattering, and Mie scattering, and (e) noise modeling functionalities.

4.1 INTRODUCTION

Atmospheric spectra of exoplanets are routinely interpreted using retrieval methods. Introduced in Madhusudhan & Seager (2009), atmospheric retrievals of exoplanets aim to solve the inverse problem - to obtain statistical constraints on the atmospheric properties of an exoplanet from an observed spectrum. A retrieval code is composed of a parametric atmospheric model that computes a synthetic spectrum, coupled with an optimization algorithm that derives the model parameters given the observed spectrum. Although here we focus on retrieval codes for transmission spectroscopy, as discussed below, a plethora of retrieval codes have been developed for other applications (see e.g., Madhusudhan, 2018, for a recent review). Retrieval codes have been developed for the analysis of thermal emission spectra of exoplanets (e.g., Madhusudhan & Seager, 2009, 2011; Lee et al., 2012; Line et al., 2013, 2014a; Waldmann et al., 2015b; Gandhi & Madhusudhan, 2018; Brogi & Line, 2019; Gandhi et al., 2019), phase curves (e.g., Changeat & Al-Refaie, 2020; Feng et al., 2020; Irwin et al., 2020), spectra of directly imaged exoplanets (e.g., Lee et al., 2013; Barstow et al., 2014; Lupu et al., 2016; Lavie et al., 2017; Nayak et al., 2017; Damiano & Hu, 2020), as well as spectra of brown dwarfs (e.g., Line et al., 2014b, 2015; Burningham et al., 2017; Zalesky et al., 2019; Kitzmann et al., 2020; Piette & Madhusudhan, 2020) and solar system planets (e.g., Rodgers, 2000; Irwin et al., 2001, 2008, 2014; Irwin & Dyudina, 2002).

Retrievals of transmission spectra have become ubiquitous in atmospheric characterization studies (see Madhusudhan, 2018, for a review). The first retrieval code for exoplanetary atmospheres (Madhusudhan & Seager, 2009) performed a grid-based parameter exploration using a large model grid ($\sim 10^7$ models of 10 parameters each). Subsequent studies adopted more robust statistical optimization algorithms. The next iteration of retrieval codes used Markov Chain Monte Carlo (MCMC) methods (e.g., Tegmark et al., 2004; Foreman-Mackey et al., 2013), providing a better parameter exploration of the parameter space but with limitations in calculating the model evidence for model comparison. Retrieval codes utilizing MCMC methods include Madhusudhan & Seager

(2011); Benneke & Seager (2012); Madhusudhan et al. (2014b), CHIMERA (e.g., Line et al., 2013; Kreidberg et al., 2014b), MassSpec (de Wit & Seager, 2013), ATMO (e.g., Evans et al., 2017; Wakeford et al., 2017a), BART (e.g., Blecic, 2016; Cubillos, 2016), PLATON (Zhang et al., 2019), and METIS (Lacy & Burrows, 2020). Concurrently, the retrieval code NEMESIS (Irwin et al., 2008) developed for solar system studies using gradient-descent optimization methods, such as Optimal Estimation (OE), has also seen applications to exoplanetary transmission spectra (e.g., Barstow et al., 2017).

The next generation of retrieval codes came to light with the implementation of the nested sampling algorithm (e.g., Skilling, 2006), facilitating more efficient parameter space exploration and calculation of model evidence. Transmission retrieval codes like SCARLET (e.g., Benneke & Seager, 2013; Benneke et al., 2019b,c), TauREx (e.g., Waldmann et al., 2015a), POSEIDON (e.g., MacDonald & Madhusudhan, 2017a), AURA (e.g., Pinhas et al., 2018), and petitRADTRANS (Mollière et al., 2019), among others (e.g., Fisher & Heng, 2018, 2019; Brogi & Line, 2019; Min et al., 2020; Seidel et al., 2020), adopted the MultiNest nested sampling algorithm (Feroz et al., 2009). Although MultiNest has been extensively used, other nested sampling algorithms have been implemented like Nestle (Barbary, 2015) in PLATON, Dynesty (Speagle, 2020) in PLATON II (Zhang et al., 2020), and PolyChord (Handley et al., 2015a) in TauREx III (Al-Refaie et al., 2019).

The extensive availability of computational methods and packages for statistical inference has made it possible for retrieval codes to update their capabilities and include multiple optimization algorithms. For instance, CHIMERA has used OE, Bootstrap Monte Carlo (BMC), MCMC, as well as MultiNest nested sampling (e.g., Line et al., 2013; Colón et al., 2020). NEMESIS has been adapted, beyond OE, to use MultiNest nested sampling (e.g., Krissansen-Totton et al., 2018). Similarly, TauREx, through different updates, has used MCMC and diverse nested sampling algorithms (e.g., Waldmann et al., 2015b; Al-Refaie et al., 2019).

Parallel efforts are being made toward exploring the viability of machine learning algorithms as a replacement for or aid to traditional Bayesian optimization algorithms. Some studies have used the Random Forest algorithm (e.g., Breiman et al., 1984) to train estimators and predict the parameters that better explain an observed spectrum (e.g., Márquez-Neila et al., 2018; Fisher et al., 2020; Guzmán-Mesa et al., 2020; Nixon & Madhusudhan, 2020). Other studies have used Deep Belief Neural Networks (albeit in studies of emission spectroscopy, e.g., Waldmann, 2016),

Generative Adversarial Networks (Zingales & Waldmann, 2018), Deep Neural Networks (Soboczenski et al., 2018), and Bayesian Neural Networks (Cobb et al., 2019) in an effort to predict atmospheric properties of exoplanets. A complementary approach has been to use machine learning to help inform the priors in a traditional retrieval (e.g., Hayes et al., 2020). These advancements in retrievals are an active area of research, and future work may elucidate on the synergies between traditional retrievals and these novel machine learning techniques.

There have also been developments in model considerations for atmospheric retrievals of transmission spectra. Recent works have investigated the impact of cloud and hazes in atmospheric retrievals (e.g., Line & Parmentier, 2016; MacDonald & Madhusudhan, 2017a; Pinhas et al., 2018; Mai & Line, 2019; Barstow, 2020). Similarly, studies have investigated the relative importance of various model and data considerations, including temperature structures, clouds, and optical data (e.g., Welbanks & Madhusudhan, 2019, see also Chapter 2) over simpler isobaric, isothermal, semianalytic model assumptions. Other works have looked into the effect of uncertainties in the system parameters (e.g., de Wit & Seager, 2013; Fisher & Heng, 2018; Batalha et al., 2019; Changeat et al., 2020) or temperature and abundance inhomogeneities (Caldas et al., 2019; Changeat et al., 2019; MacDonald et al., 2020) in the retrieved properties of the atmosphere. Further efforts have investigated the impact of stellar contamination in transmission spectra (e.g., Pinhas et al., 2018; Iyer & Line, 2020; Bruno et al., 2020).

While the studies above have focused primarily on retrievals for giant planets with H-rich atmospheres, some studies have also developed retrieval frameworks for smaller planets where the atmosphere may not be assumed to be H rich a priori. Benneke & Seager (2012) investigated an agnostic retrieval framework for super-Earths, which could have a wide range of atmospheric compositions. They highlight that assuming log-uniform priors for the mixing ratios of the chemical species sampled in a retrieval can lead to a highly asymmetric prior for the last species derived using the unit-sum constraint, which is unfavorable in the absence of a priori knowledge of the dominant species in the atmosphere, e.g., for super-Earths. To overcome this limitation, Benneke & Seager (2012) suggest a reparameterization of the chemical compositions applicable to both H-rich and non-H-rich atmospheres. The parameterization, based on centered-log-ratio transformations (e.g., Aitchison, 1986), allows for equal prior probability distributions for all the chemical species considered; we discuss this in depth in Section 4.4. In a subsequent work,

Benneke & Seager (2013) demonstrate the potential of using Bayesian model comparisons along with high-precision transmission spectra of super-Earths/mini Neptunes to differentiate between cloudy H-rich atmospheres and those of high mean molecular weight, e.g., H_2O rich.

After this decade of revolutionary work on retrievals, the next generation of retrieval codes is upon us. Such retrievals must incorporate the lessons learned from atmospheric studies of giant exoplanets and also be adaptable to low-mass planets. In preparation for upcoming observations of temperate mini Neptunes and super-Earths, the methods for non-H-dominated atmospheres must be implemented and updated to be compatible with the latest optimization algorithms. Upcoming codes should be able to expand their modeling functionalities motivated by data requirements. Lastly, with the increasing model complexity and data quality, new retrieval codes must be prepared for assessing multi-dimensional, highly degenerate problems.

We introduce Aurora, a next-generation retrieval framework for the atmospheric characterization of H-rich and non-H-rich planets. Our code incorporates new key features on the previous retrieval code AURA (Pinhas et al., 2018). First, we reparameterize the volume mixing ratios in the atmosphere expanding the previous scope beyond H-rich atmospheres, adapting methods previously used for super-Earths (e.g., Benneke & Seager, 2012) and other areas of compositional data analysis (e.g., Aitchison, 1986; Aitchison & Egozcue, 2005; Pawlowsky-Glahn & Buccianti, 2011). Second, Aurora incorporates the next-generation nested sampling algorithms PolyChord and Dynesty, as well as maintaining compatibility with MultiNest. Third, Aurora includes a new generalized parametric treatment for inhomogeneous clouds and hazes. Compared to previous prescriptions, our new treatment of clouds/hazes is robust against assumptions of whether the atmosphere is H rich or not.

Lastly, Aurora incorporates different modular capabilities that enhance the study of transmission spectra using retrievals and forward models. These include assessing stellar heterogeneity (e.g., Rackham et al., 2017; Pinhas et al., 2018), allowing for underestimated variances in the data (e.g., Foreman-Mackey et al., 2013; Colón et al., 2020), and considering correlated noise using Gaussian processes (e.g., Rasmussen & Williams, 2006). Additionally, our forward-modeling capabilities can account for light refraction and forward scattering (Robinson et al., 2017), as well as Mie scattering due to a variety of condensate species (Pinhas & Madhusudhan, 2017). Aurora's modular capabilities can be incorporated in

retrievals should observations require it. In what follows, we present our retrieval framework and its methods.

4.2 OVERVIEW OF THE AURORA RETRIEVAL FRAMEWORK

Aurora builds upon the AURA retrieval framework (Pinhas et al., 2018) developed by our group and, among other features, expands the retrieval capabilities to rocky exoplanets without the assumption of H-rich atmospheres. The core retrieval methodology for H-rich atmospheres is explained in Pinhas et al. (2018), with its implementation previously explained in Welbanks & Madhusudhan (2019, Chapter 2) and employed in different retrieval studies (e.g., Chen et al., 2018; von Essen et al., 2019; Welbanks et al., 2019; Colón et al., 2020, see Chapter 3, Chapter 6, and Chapter 7). Here, we reintroduce the basic retrieval methodology of the AURA code and discuss the new enhancements made in Aurora. Figure 24 shows the schematic diagram of the Aurora framework.

Like any contemporary retrieval framework (Madhusudhan, 2018), AURA and Aurora comprise a forward model that is interfaced with a Bayesian inference and parameter estimation scheme. The forward model computes a transmission spectrum given a set of parameters for the temperature structure, chemical composition, and presence of clouds/hazes on the planet's atmosphere. The parameter estimation scheme explores the model's parameter space in search of regions of high likelihood that can explain a set of observations. The Bayesian inference scheme estimates the model evidence and posterior probability distributions of the model parameters and is performed using the nested sampling algorithm. In what follows, we describe each of these components for our retrieval framework. We highlight the following key advancements introduced in Aurora.

- Generalized inhomogeneous cloud/haze parameterization
- Generalized considerations for H-poor/H-rich compositions
- Adaptable Bayesian inference algorithms
- Modular functionalities for considering:
  - Refraction and forward scattering
  - Mie scattering with a library of condensates
  - Error inflation and Gaussian processes to treat correlated noise.

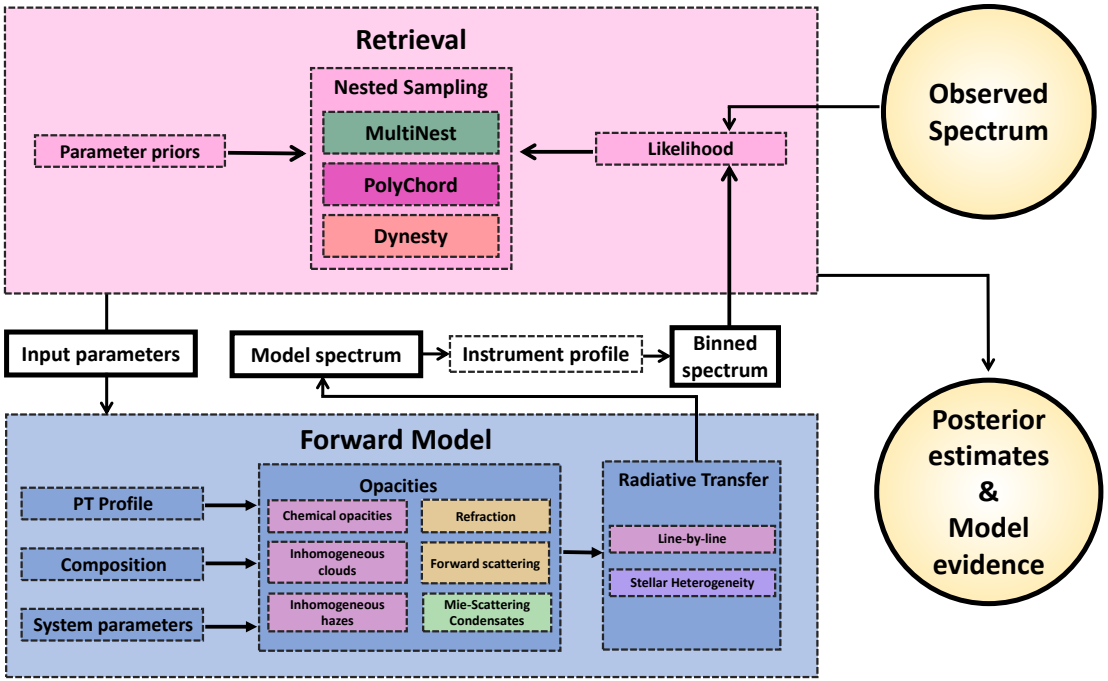

Figure 24 Schematic of Aurora's retrieval framework. The retrieval framework combines an atmospheric forward model with a Bayesian inference and parameter estimation algorithm to derive the model evidence and posterior probability distributions of the model parameters given an observed spectrum. Aurora also has modular capabilities for including additional effects in the atmospheric model if required, e.g., light refraction, forward scattering, and Mie scattering.

We first discuss the standard features that we retain from the retrieval framework of Pinhas et al. (2018), followed by a description of the new features in the Aurora framework.

4.3 FORWARD MODEL

Aurora computes the transmission spectrum of an exoplanet in transit assuming plane-parallel geometry. Our forward model is comprised of a parametric pressure-temperature (P–T) profile; parametric chemical abundances and consideration for multiple sources of opacity including atomic and molecular-line opacity, Rayleigh scattering, and collision-induced absorption (CIA); a treatment for inhomogeneous clouds and hazes; and a line by line radiative transfer solver under hydrostatic equilibrium. The forward model can consider light refraction, forward scattering, Mie scattering, and stellar heterogeneity (see Section 4.6).

4.3.1 *Pressure-Temperature Profile*

The temperature in the atmosphere of an exoplanet as a function of pressure is determined by the P–T profile. We follow the parametric prescription of Madhusudhan & Seager (2009). We choose this profile as it is motivated by the profiles observed in the solar system and has been successfully applied to exoplanet studies (e.g., Madhusudhan & Seager, 2009, 2011; Madhusudhan et al., 2014b; Blecic et al., 2017). The equations for temperature in this parameterization divide the model atmosphere into three distinct regions:

$$T = T_0 + \left(\frac{\log(P/P_0)}{\alpha_1}\right)^2, \; P_0 < P < P_1, \tag{14}$$

$$T = T_2 + \left(\frac{\log(P/P_2)}{\alpha_2}\right)^2, \; P_1 < P < P_3, \tag{15}$$

$$T = T_2 + \left(\frac{\log(P_3/P_2)}{\alpha_2}\right)^2, \; P > P_3, \tag{16}$$

where we maintain the empirical choice of Madhusudhan & Seager (2009) to set their parameters $\beta_1 = \beta_2 = 0.5$. Here, T_0 is the temperature at the top of the model atmosphere P_0 (e.g., 10^{-6} bar in this dissertation), P_1 is the boundary between the first and second regions, P_3 is the boundary between the second and third regions, P_2 is the pressure in the parameterization that can capture possible thermal inversions if

$P_2 > P_1$, and α_1 and α_2 are the values that determine the curvature of the profile in the different layers. We restrict our temperature profiles to those with $P_2 \leqslant P_1$, for observations of the day-night terminator where thermal inversions are not expected. Aurora has the option of considering an isothermal profile in which case the free parameter is T_0. Then, the temperature at all points in the model atmosphere is assumed to be T_0.

4.3.2 *Sources of Opacity*

The presence of different chemical species in the atmosphere of an exoplanet is retrieved by considering their contribution to the starlight's extinction. The extinction coefficient $\kappa(\lambda, P, T)$ of the atmosphere is a pressure-, temperature-, and wavelength-dependent quantity that contributes to the differential optical depth,

$$d\tau(\lambda, P, T) = \kappa(\lambda, P, T)ds \tag{17}$$

along the line of sight s. The extinction coefficient for each species is given by $\kappa_i(\lambda, P, T) = n_i\,\sigma_i(\lambda, P, T)$, where n_i is the number density and σ_i the absorption cross section of the species. The number density, n_i, is parameterized through the volume mixing ratio, $X_i = n_i/n_{tot}$, where n_{tot} is the total number density. The volume mixing ratio of each species is a free parameter and assumed to be uniform in the atmosphere. For H-rich atmospheres, Aurora calculates the volume mixing ratio of H_2 and He by assuming a particular He/H_2 ratio (X_{He}/X_{H_2}) and the following relations:

$$X_{H_2} = \frac{1 - \sum_{i, i\neq He, H_2}^{n} X_i}{1 + \frac{X_{He}}{X_{H_2}}}, \qquad X_{He} = X_{H_2}\,\frac{X_{He}}{X_{H_2}}, \tag{18}$$

where we adopt a solar value of $X_{He}/X_{H_2} = 0.17$ (Asplund et al., 2009) and consider a total of n species in the model atmosphere. The treatment of the volume mixing ratios when a H-rich atmosphere is not assumed a priori is described in Section 4.4.

Aurora in general considers the opacity sources expected in the atmospheres of hot Jupiters, mini Neptunes, and temperate rocky planets (e.g., Madhusudhan, 2012, 2019; Moses et al., 2013). The opacity

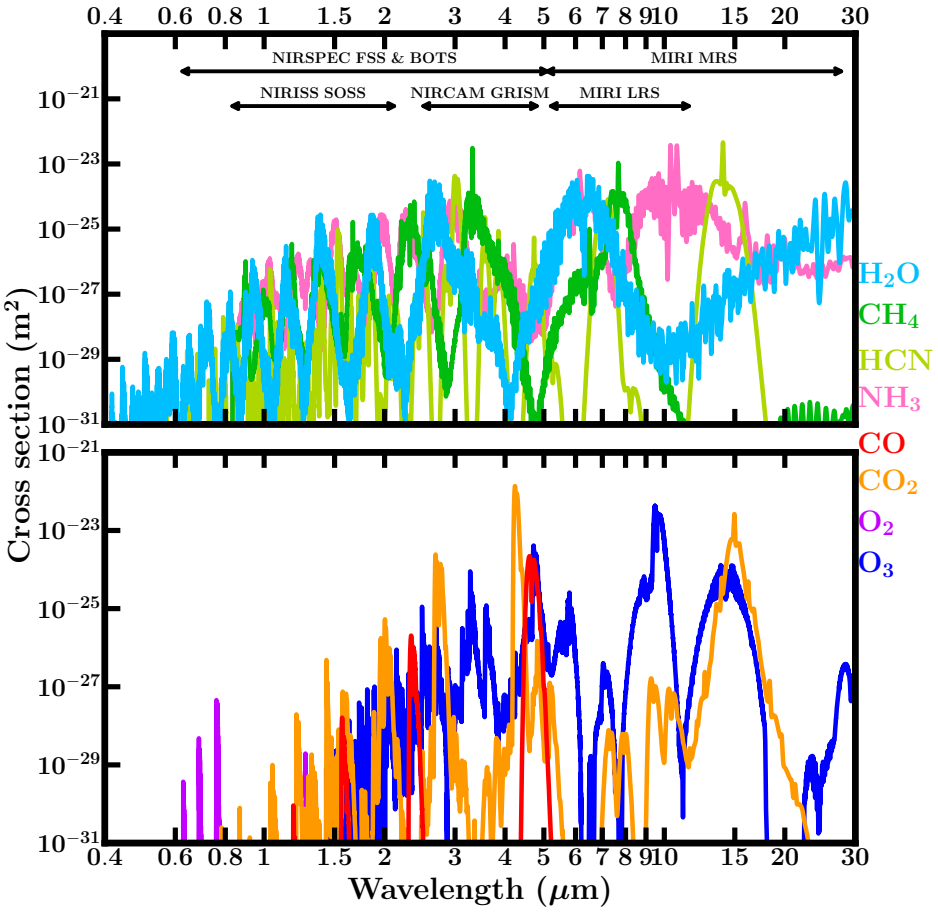

Figure 25 Top and bottom panels show the absorption cross sections for some of the molecular opacity sources included in Chapter 4 and Chapter 5 at a pressure of 1 bar and a temperature of 300 K. The cross sections are shown in the wavelength region where JWST is expected to perform observations. JWST instrument ranges are indicated on the top panel using black lines and arrows.

sources considered in this chapter and Chapter 5 are H_2-H_2 and H_2-He CIA (Richard et al., 2012) and line opacity due to CH_4 (Yurchenko & Tennyson, 2014), CO (Rothman et al., 2010), CO_2 (Rothman et al., 2010), H_2O (Rothman et al., 2010), HCN (Barber et al., 2014), K (Allard et al., 2016), Na (Allard et al., 2019), N_2 (Rothman et al., 2010), NH_3 (Yurchenko et al., 2011), O_2 (Rothman et al., 2010), and O_3 (Rothman et al., 2010). The opacities for the chemical species are computed following the methods of Gandhi & Madhusudhan (2017), with the updated values of Gandhi & Madhusudhan (2018), and with H_2-broadened Na and K cross sections as explained in Welbanks et al. (2019, see also Chapter 3).

Aurora also incorporates a continually updated library of cross sections of various other atomic and molecular species (Gandhi et al., 2020). Figure 25 shows the cross section for most of the molecular opacity sources considered in this dissertation for a pressure of 1 bar and a temperature of 300 K, from 0.4 to 30 μm, covering the wavelength range expected to be observable by JWST. The Na and K profiles can be seen in Figure 1 of Welbanks et al. (2019) or Figure 20 in Chapter 3.

The resulting extinction coefficient is

$$\kappa(\lambda, P, T) = \sum_i X_i n_{tot}(P, T)\, \sigma_i(\lambda, P, T) + X_{H_2} n_{tot}^2(P, T) \times \left[X_{H_2} \sigma_{H_2\text{-}H_2}(\lambda, T) + X_{He} \sigma_{H_2\text{-}He}(\lambda, T)\right], \quad (19)$$

where $\sigma_{H_2\text{-}H_2}$ and $\sigma_{H_2\text{-}He}$ are the H_2–H_2 and H_2-He CIA cross sections. The extinction coefficient can be amended to remove H_2–He and H_2–H_2 CIA and/or include CIA due to other species. Furthermore, the total extinction coefficient can include H_2 Rayleigh scattering:

$$\kappa_{H_2\text{-Rayleigh}}(\lambda, P, T) = X_{H_2} n_{tot}(P, T) \sigma_{H_2\,scat}(\lambda), \quad (20)$$

where the wavelength-dependent cross section in cgs is given analytically by Dalgarno & Williams (1962) as

$$\sigma_{H_2\,scat}(\lambda) = \frac{8.14 \times 10^{-45}}{\lambda^4} + \frac{1.28 \times 10^{-54}}{\lambda^6} + \frac{1.61 \times 10^{-64}}{\lambda^8} + \mathcal{O}(\lambda^{-10}) \quad (21)$$

and is incorporated up to its third term in Aurora.

Aurora also includes opacity sources relevant for modeling H-poor atmospheres of rocky planets. This library contains CIA cross sections of CO_2-CO_2, N_2-N_2, O_2–O_2, O_2–CO_2, O_2–N_2, among others obtained from HITRAN (Karman et al., 2019). These additional CIA cross sections are generated within the temperature and wavelength limits available in the HITRAN data. The cross sections for temperatures beyond those limits are set to values at the boundaries. We assume no opacity for wavelengths beyond the database range, as these values are not known. Future efforts, both experimental and theoretical, on extending and revising opacity databases would help obtain cross sections over the full range of wavelengths and temperatures applicable for such planets. Aurora can also include Rayleigh scattering due to a variety of species

including O_2, N_2, Ar, Ne, CO_2, CH_4, H_2O, CO, and N_2O (Shardanand & Prasad Rao, 1977; Sneep & Ubachs, 2005; Thalman et al., 2014). Rayleigh scattering due to species i is $\kappa_{i\text{-Rayleigh}}(\lambda, P, T) = X_i n_{tot}(P, T)\sigma_{i\,scat}(\lambda)$. We include CIA due to CO_2–CO_2, N_2-N_2, as well as Rayleigh scattering due to N_2, H_2O, and CO_2 in the H-poor models presented in Section 5.4.

4.3.3 *A New Cloud and Haze Parameterization*

We introduce a new cloud and haze treatment for inhomogeneous cover that considers a total of four distinct spatial areas (sectors) covering the planet. These four areas are (1) a clear, cloud-free and haze-free, area affected only by Rayleigh scattering, (2) an area covered by hazes only, (3) an area covered by a gray cloud deck with Rayleigh scattering above the cloud deck, and (4) an area covered by a gray cloud deck and hazes above it. The total transit depth is a linear superposition of the transit depths of each sector:

$$\begin{aligned}\Delta_{planet}(\lambda) = {} & \phi_{hazes}\Delta_{hazes}(\lambda) + \phi_{clouds}\Delta_{clouds}(\lambda) \\ & + \phi_{clouds+hazes}\Delta_{clouds+hazes}(\lambda) + \phi_{clear}\Delta_{clear}(\lambda),\end{aligned} \tag{22}$$

where the cover fractions are free parameters in the model and ϕ_{clear} is determined by a unit-sum constraint, i.e., $\phi_{clear} = 1 - \phi_{hazes} - \phi_{clouds} - \phi_{clouds+hazes}$.

Hazes, e.g., small-size particles resulting from photochemical processes, are implemented into our model atmosphere by parameterizing their effect on the spectrum as deviations from H_2 Rayleigh scattering (Lecavelier Des Etangs et al., 2008). The parameterization provides a cross section $\sigma_{hazes} = a\sigma_0(\lambda/\lambda_0)^\gamma$, where γ is the scattering slope, a is the Rayleigh-enhancement factor, and σ_0 is the H_2 Rayleigh-scattering cross section at the reference wavelength λ_0. We adopt values of $\sigma_0 = 5.31 \times 10^{-31}$ m^2 and $\lambda_0 = 350$ nm for consistency with previous works (e.g., MacDonald & Madhusudhan, 2017a; Welbanks et al., 2019). Future observations of non-H-rich planets could motivate the use of scattering cross sections for different species. The extinction due to hazes is $\kappa_{haze}(\lambda, P, T) = X_{H_2} n_{tot}(P, T)\sigma_{hazes}(\lambda)$.

The regions of the atmosphere covered by a gray cloud deck are included by adopting a parameter for the cloud top pressure P_{cloud}. The optical depth for all pressures higher than P_{cloud} is considered to be infi-

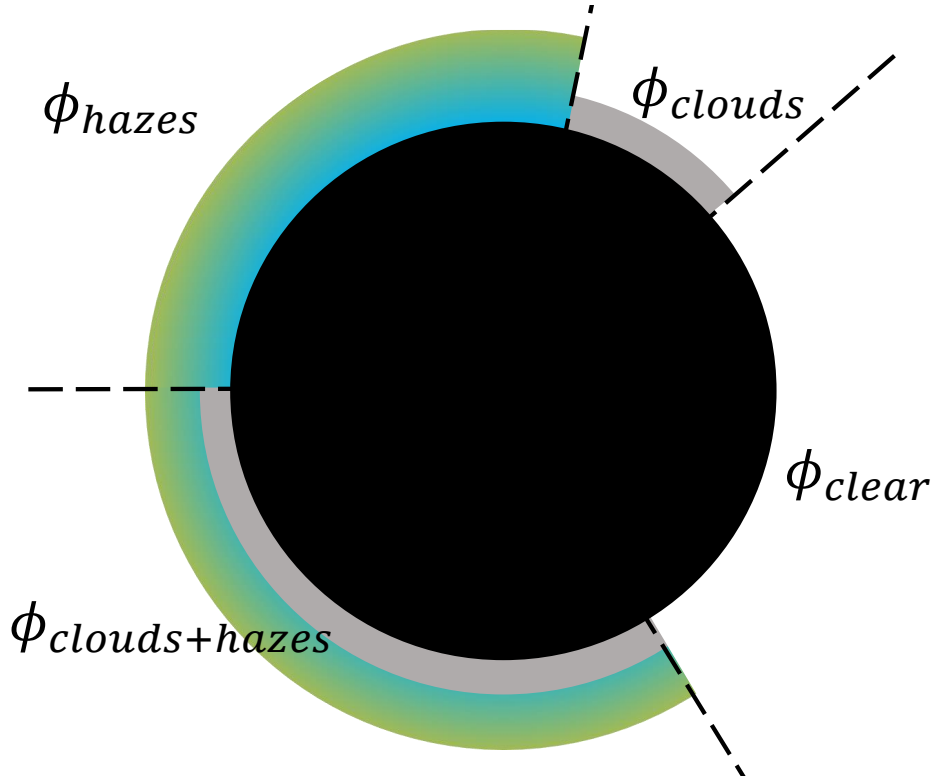

Figure 26 Schematic of the four-sector generalized parameterization of inhomogeneous clouds and hazes introduced in this chapter. The planet is enveloped by its atmosphere, which is divided into four regions. These are (1) a clear, cloud-free and haze-free, sector, (2) a sector with hazes only, (3) a sector with clouds only, and (4) a sector with clouds and hazes.

nite. The extinction coefficient due to the cloud deck $\kappa_{\text{clouds}}(P)$ is infinite for $P > P_{\text{cloud}}$ or zero for $P < P_{\text{cloud}}$.

Previous studies have considered the effects of patchy clouds in transmission spectra (e.g., Line & Parmentier, 2016; MacDonald & Madhusudhan, 2017a; Barstow, 2020). Our model here generalizes the approach of previous studies while being able to reduce to previous treatments under specific conditions. If the model prefers to consider the presence of clouds and hazes together, the fractions ϕ_{hazes} and ϕ_{clouds} approach zero and we obtain previous treatments for inhomogeneous cover (e.g., MacDonald & Madhusudhan, 2017a; Welbanks & Madhusudhan, 2019). On the other hand, if the combined fraction is zero (e.g., $\phi_{\text{clouds+hazes}} = 0$), our approach allows us to consider the effect of clouds and hazes separately and distinguish whether the contribution to the spectrum is mostly due to deviations from H_2 Rayleigh scattering produced by the hazes or muted features due to a gray cloud deck. Lastly, if the combined fraction is zero and so is the haze only fraction (e.g., $\phi_{\text{hazes}} =$

$\phi_{\text{clouds+hazes}} = 0$) we recover the expression for patchy clouds of Line & Parmentier (2016). By following this approach, we obtain a more robust and flexible treatment compared to our previous prescription that combines the effects of clouds and hazes into one sector (e.g., MacDonald & Madhusudhan, 2017a; Welbanks & Madhusudhan, 2019). We present a schematic of our cloud and haze treatment in Figure 26.

We find the generalized treatment of clouds and hazes introduced in this dissertation leads to consistent abundance estimates regardless of whether or not a H-rich atmosphere is assumed. In other words, the existing degeneracies between clouds/hazes and composition are treated equally irrespective of the assumption of the bulk atmospheric composition of the planet. On the other hand, combining clouds and hazes into one individual sector as previously performed (e.g., MacDonald & Madhusudhan, 2017a; Pinhas et al., 2018; Welbanks & Madhusudhan, 2019) can lead to biases and an incomplete exploration of the parameter space that results in distinct solutions when assuming a H-rich atmosphere or not on the same data set. This is mitigated by our new cloud and haze prescription. We discuss these aspects further in the case study of the hot Jupiter HD 209458 b in the next chapter, in Section 5.1.

4.3.4 *Radiative Transfer*

Our model solves line by line radiative transfer in transmission geometry in a plane-parallel atmosphere. The model atmosphere is divided into a predetermined number of pressure layers equally spaced logarithmically. The number of layers and their span in pressure space can be arbitrarily established by the user depending on the application. For the models in this chapter and Chapter 5, and based on the empirical results of Welbanks & Madhusudhan (2019, see also Chapter 2), we use 100 pressure layers uniformly spaced in $\log_{10}(P)$ from 10^{-6} to 10^{2} bar under hydrostatic equilibrium. Our calculation of hydrostatic equilibrium is performed considering the retrieved composition through the atmospheric mean molecular weight (e.g., $\mu = \sum X_i m_i$, where X_i and m_i are the volume mixing ratio and the atomic/molecular mass of species i, respectively), the retrieved P–T profile, and altitude-dependent gravity.

We solve numerically for the transit depth of the planet:

$$\Delta_\lambda = \frac{R_p^2 + 2\int_{R_p}^{R_p+H_A} b\left(1 - e^{-\tau_\lambda(b)}\right) db - 2\int_0^{R_p} b e^{-\tau_\lambda(b)} db}{R_{star}^2}, \quad (23)$$

where R_{star} is the stellar radius, H_A is the maximum height of the planetary atmosphere, τ_λ is the total slant optical depth and integral of Equation 17, b is the impact parameter, and R_p is the radius of the planet. We present Equation 23 as a three-part expression to highlight the fact that the chosen R_p may not correspond to an optically thick surface. If R_p corresponds to an optically thick surface, the last integral in Equation 23 evaluates to zero. Otherwise, the integral considers the contribution of the nonoptically thick parts of the atmosphere, below the arbitrarily chosen position in the planet, to the transit depth.

The selected value of R_p, at a given reference pressure P_{ref}, is used to construct a radial distance grid. The distance and pressure grids follow a one-to-one correspondence determined by hydrostatic equilibrium. It is possible in a retrieval to choose a value of R_p for which the P_{ref} parameter will be retrieved, to choose a value of P_{ref} for which the associated radius R_p will be retrieved, or leave both R_p and P_{ref} as free parameters. In Chapter 2, Welbanks & Madhusudhan (2019), we showed that the retrieval results remain mostly unchanged regardless of the choice of free parameter (R_p and/or P_{ref}). In Chapter 5, we choose to keep R_p as our independent variable for which we retrieve P_{ref}.

4.4 CONSIDERATIONS FOR NON-H-RICH ATMOSPHERES

A core assumption present in most atmospheric retrieval codes for hot Jupiters is that the atmosphere is H rich. Such assumption can be appropriate for massive planets that, from a formation perspective, captured a gas mixture of predominantly H and He in cosmic proportions from their protoplanetary nebula (Seager & Deming, 2010). However, when characterizing the atmospheres of less massive planets or when pursuing an agnostic approach applicable to atmospheres of general composition, such assumption may need to be relaxed. Instead of assuming a H-rich atmosphere, studies could attempt to retrieve the main gas component of the atmosphere. Such an approach would aim to explore a

wider range of atmospheric compositions like N_2-rich or CO_2-rich atmospheres, and not be constrained to H-rich atmospheres only.

However, when pursuing this agnostic approach, the unit-sum constraint, i.e., the requirement that all the volume mixing ratios in the atmosphere must add up to one, must be incorporated into the statistical modeling appropriately. Incorporating such constraint is nontrivial and has been the subject of study in a subfield of statistical analysis called compositional data analysis (e.g., Pearson, 1897; Tanner, 1949; Chayes, 1960; Aitchison, 1986). The tools developed by this subfield of statistics have been implemented in a number of different disciplines like medicine, chemistry, economy, geophysics, among many others (see Aitchison & Egozcue, 2005, for a review of the history of compositional data). The concepts of compositional data analysis were introduced to the exoplanet retrieval literature through the work of Benneke & Seager (2012).

Implementing the same methods used for the retrieval of H-rich atmospheres to retrievals in which the main atmospheric constituent is not known can result in biased results that do not explore all compositions equally. The traditional method would sample the volume mixing ratios of $n-1$ species (i.e., minor species) and assign the volume mixing ratio of the nth species (i.e., H_2 in the case of a H-rich atmosphere) following the unit-sum constraint. Benneke & Seager (2012) highlight that following this approach will result in a highly asymmetric prior (see Figure 1 of Benneke & Seager, 2012) for the nth species. Under these circumstances, the retrieval is not truly agnostic, and the resulting atmospheric composition will be dependent on which molecule was chosen to be the nth species.

To circumvent this problem, one must allow for all species to have the same prior probability density in a permutation-invariant prescription. If the prior probability for all species is identical, it is safe for the retrieval to sample over the parameter space of all n species. The solution is the centered-log-ratio transformation, defined as

$$z_i = \log\left(\frac{X_i}{g(X)}\right), \tag{24}$$

where $g(X)$ is the geometric mean $g(X) = (X_1 ... X_N)^{1/N}$ (Aitchison, 1986). The transformed z_i values, also called compositional parameters, treat all parts of the gas symmetrically.

In Aurora, when not assuming a H-rich atmosphere, we reparameterize the volume mixing ratios (X_i) using the centered-log-ratio transformation and obtain the compositional parameters (z_i). We assume that the combination of H_2 and He is one single part ($z_{(H_2+He)}$), which we then use to determine the separate H_2 and He volume mixing ratios using a He/H_2 ratio. Then, we sample over the entire transformed space for all n gas components with the assumption that one of those is a mixture of H_2 and He in solar proportion.

Once sampling is performed in the space of the centered-log-ratio transformation, and to maintain the descriptions above about the treatment of different opacity sources, the inverse transformation (Pawlowsky-Glahn & Buccianti, 2011)

$$X_j = \frac{\exp(z_j)}{\sum_{i=1}^{N} \exp(z_i)} \tag{25}$$

is calculated and the volume mixing ratios X_i's are used in our calculations.

It is important to highlight that the compositional parameters (z_i) have slightly different properties from their counterparts, the volume mixing ratios (X_i). While the typical prior range for X_i is $10^{-12} < X_i < 1$, the limits for z_i is $-\infty < z_i < \infty$ where $-\infty$ is the limit of a species not being present and ∞ means the species is the only one in the atmosphere. While a straightforward expression for the scenario in which all volume mixing ratios are equal is not available, the compositional parameters are present in equal parts when all $z_i = 0$. Lastly, the unit-sum constraint for the volume mixing ratios is $\sum X_i = 1$ and transforms to $\sum z_i = 0$ for the compositional parameters.

4.5 MULTIALGORITHMIC STATISTICAL INFERENCES

The strength in the retrieval approach when assessing the properties of an exoplanet's atmosphere resides in its ability to provide robust statistical estimates of the parameters and models used to explain the observations. As explained in Section 4.1, many statistical approaches exist in exoplanetary atmospheric retrievals: grid-based searches (e.g., Madhusudhan & Seager, 2009), MCMC (e.g., Madhusudhan & Seager, 2011; Benneke & Seager, 2012; de Wit & Seager, 2013; Line et al., 2013; Madhusudhan et al., 2014b; Cubillos, 2016; Wakeford et al., 2017a; Zhang

et al., 2019), nonlinear optimal estimators (e.g., Lee et al., 2013; Barstow et al., 2017), among others (see Madhusudhan, 2018, for a review). Of the different approaches available, Bayesian inference tools ease the comparison of models while providing estimates of the posterior distributions of the model parameters. One of these methods, nested sampling (Skilling, 2006), has been successfully incorporated into exoplanetary retrieval literature (e.g., Benneke & Seager, 2013; Line et al., 2013; Waldmann et al., 2015a; MacDonald & Madhusudhan, 2017a; Gandhi & Madhusudhan, 2018; Krissansen-Totton et al., 2018; Pinhas et al., 2018; Mollière et al., 2019; Zhang et al., 2020) due to its ability to handle high-dimensionality problems, sample the complete parameter space of the model, and use prior information on the model parameters. An overview of the Bayesian approach to inference problems is available in Sivia & Skilling (2006) and Trotta (2008, 2017).

The likelihood of observing the data ($\mathcal{D}$) given a specific set of model parameters ($\theta_{\mathcal{M}}$) for a model ($\mathcal{M}$) is

$$\mathcal{L} = P(\mathcal{D}|\theta_{\mathcal{M}}, \mathcal{M}). \tag{26}$$

Considering the Bayesian approach, where the degree of belief on the model assumptions must be accounted for, one must incorporate the prior distribution (π) on the model parameters $\pi = P(\theta_{\mathcal{M}}|\mathcal{M})$. The marginalized likelihood, also known as evidence, is obtained by integrating the likelihood over the full parameter space:

$$\mathcal{Z} = \int P(\mathcal{D}|\theta_{\mathcal{M}}, \mathcal{M}) P(\theta_{\mathcal{M}}|\mathcal{M}) d\theta_{\mathcal{M}} = P(\mathcal{D}|\mathcal{M}). \tag{27}$$

The model evidence is the quantity we are interested in evaluating when comparing different models. This is also the quantity different nested sampling algorithms aim to provide. Furthermore, using Bayes' theorem, it is possible to obtain the posterior probability distribution for each parameter given the data

$$P(\theta_{\mathcal{M}}|\mathcal{D}, \mathcal{M}) = \frac{P(\mathcal{D}|\theta_{\mathcal{M}}, \mathcal{M}) P(\theta_{\mathcal{M}}|\mathcal{M})}{P(\mathcal{D}|\mathcal{M})}. \tag{28}$$

Aurora uses a likelihood function for data with independently distributed Gaussian errors

$$\mathcal{L}\left(\mathcal{D}|\theta_{\mathcal{M}}, \mathcal{M}_i\right) = \prod_k^N \frac{1}{\sqrt{2\pi}\sigma_k} \exp\left(-\frac{[\mathcal{D}_k - \mathcal{M}_{i,k}]^2}{2\sigma_k^2}\right) \tag{29}$$

for a data set of length N and computed for each model realization $\mathcal{M}_i$. Aurora follows the same binning strategy as AURA (see Section 2.1.6 in Pinhas et al., 2018) where a model spectrum at a much higher resolution than the data is convolved with the point-spread function (PSF) of the instrument with which the observations were obtained and then binned down to the spectral resolution of the data.

The prior distributions employed in Chapter 5, where we conduct the validation of our framework, are shown in Table 16 in Appendix C.3. The priors for the parameters are mostly standard prescriptions adopted from previous studies (e.g., Pinhas et al., 2019; Welbanks et al., 2019, see also Appendix B). The priors for molecular abundances generally span the complete detectable range unless stated otherwise, with the prior distribution either log-uniform for the volume mixing ratios for H-rich retrievals or uniform in the corresponding compositional parameters (z_i), discussed in Section 4.4, for non-H-rich retrievals. The priors for the parameters associated with other physical properties, e.g., P–T profile and cloud/haze parameters, are also uniform or log-uniform and span the corresponding physically plausible ranges.

4.5.1 *Next-generation Bayesian Inference Algorithms*

The main functionality of a nested sampling algorithm is to obtain the model evidence ($\mathcal{Z}$) while also deriving the posterior probability distributions of the model parameters as a by-product. A full description of the nested sampling algorithm is available in Skilling (2004); Skilling (2006); Feroz et al. (2009). In Aurora, we implement three different algorithms, MultiNest (Feroz et al., 2009, 2019) through its implementation PyMultiNest (Buchner et al., 2014), PolyChord (Handley et al., 2015a,b) through its implementation PyPolyChord, and Dynesty (Speagle, 2020). Each nested sampling algorithm is different and the in-depth description for each implementation is available in their release papers listed above.

Generally, a nested sampling algorithm generates a number of live points drawn from the prior distribution, which sample the parameter space (Feroz et al., 2009). In each iteration, the point with the lowest likelihood is replaced by a new one which ought to have a larger like-

lihood. This means that the live points sample the prior volume using continuously shrinking isolikelihood contours, which with every iteration converge to the highest likelihood regions of the parameter space. At each step, every sampled value creates a model realization that results in an evaluation of the likelihood function. The process finishes when a termination condition, like a preset fractional change in the model likelihood, is met. Upon completion, the combination of all sampled points can be used to estimate the model evidence. The procedure to generate new live points can vary between different implementations of the nested sampling algorithm, which are briefly discussed below.

MultiNest has been previously implemented in exoplanet retrievals (e.g., Benneke & Seager, 2013; Line et al., 2013; Waldmann et al., 2015a; MacDonald & Madhusudhan, 2017a; Gandhi & Madhusudhan, 2018; Krissansen-Totton et al., 2018; Pinhas et al., 2018; Mollière et al., 2019; Zhang et al., 2020). To draw unbiased samples from the likelihood-constrained prior, MultiNest uses what is called an ellipsoidal rejection sampling scheme. The basis for this scheme is that the replacement point is sought from within the set of ellipsoids described by the full set of live points at any iteration (Feroz et al., 2019). With each iteration, the ellipsoids described by the isolikelihood contours shrink. This procedure is optimal for a small number of parameters but has an exponential scaling with dimensionality.

PolyChord, on the other hand, uses what is called slice-based sampling. In this procedure, the algorithm samples uniformly within the parameter space for which the posterior probability is higher than a given probability level or “slice". Unlike the exponential scaling problem with MultiNest at higher dimensions, PolyChord’s scaling is $\sim \mathcal{O}(D^3)$ (Handley et al., 2015b). This makes MultiNest preferred for low-dimensionality problems, while PolyChord is preferred at higher dimensionalities (see Figure 7 in Handley et al., 2015b).

Lastly, Dynesty (Speagle, 2020) uses a generalisation of nested sampling, in which the number of live points is variable, called dynamic nested sampling (Higson et al., 2019). In dynamic nested sampling, an initial run with a constant number of live points is used by the algorithm to approximate areas in prior space of the highest likelihood. Then, the algorithm proceeds to iteratively calculate the range of likelihoods where a larger number of live points will have the greatest result in accuracy. In dynamic nested sampling, the number of live points is dynamically allocated to control the resolution at which the prior space is sampled. This would allow for runs that focus on sampling the poste-

rior distribution or better estimate the model evidence. Dynesty allows for both dynamic and static nested sampling. Furthermore, Dynesty has four main approaches to generating samples: uniform sampling (including from ellipsoids like MultiNest), random walks, multivariate slice sampling (similar to PolyChord), and Hamiltonian slice sampling. Each approach has its benefits and impediments and can be better suited for different problem dimensionalities. Speagle (2020) offers an extensive overview of each feature available in Dynesty.

Every algorithm for nested sampling offers different capabilities. While Dynesty is able to handle both static and dynamic sampling, it comes at the cost of multiple tuning parameters that can affect the behavior of a given run. PolyChord is able to handle problems of higher dimensionality more efficiently than MultiNest, but MultiNest still outperforms PolyChord in the number of likelihood evaluations required for problems in low dimensions ($\lesssim$ 80 dimensions, Handley et al., 2015b). Aurora offers the tools to perform retrievals optimizing for evaluation of the model evidence, parameter posterior distributions, or both. The user has the freedom to choose the correct sampling algorithm for their needs depending on the complexity of the problem and its dimensionality.

4.5.2 *Model Comparison and Detection Significance*

The difference in evidence ($\mathcal{Z}$) between models can be used to derive an equivalent detection significance (DS), a figure of merit traditionally used to compare different models. The detection significance is traditionally expressed in units of 'sigma' (σ) and corresponds to the number of standard deviations away from the mean of a normal distribution (Trotta, 2008). Expressing a result in 'sigmas' does not necessarily mean the detection of new physics or a species in the spectrum of a planet. Instead, it is a useful way to translate the odds in favor of a more complex model into a frequentist metric. The relevance of a model preference can be somewhat arbitrary, and different authors suggest different categories for expressing them. For instance, Trotta (2008) suggests that a difference of 2.0σ to 2.6σ is weak at best, while Kass & Raftery (1995) suggest that the equivalent of $\sim 2.1\sigma$ is positive evidence. A way to transform the difference in model evidence to a detection significance was proposed by Benneke & Seager (2013). We perform the comparison of our models by solving Equation 11 in Benneke & Seager (2013) and obtaining a detection significance as

$$\mathrm{DS} = \sqrt{2}\,\mathrm{erfc}^{-1}\left[\exp\left(\mathcal{W}_{-1}\left(-\frac{1}{\mathrm{B}\,e}\right)\right)\right], \tag{30}$$

where erfc is the complementary error function, $\mathcal{W}_{-1}$ is the Lambert $\mathcal{W}$ function in its lower branch (i.e., $k = -1$ branch), e is Euler's number, and B is the Bayes factor defined as $\mathrm{B} = \mathcal{Z}_1/\mathcal{Z}_2$, with the set requirement of $\mathcal{Z}_1 \geqslant \mathcal{Z}_2$ so the Bayes factor is greater than or equal to unity.

4.6 MODULAR CAPABILITIES

Aurora's design is modular, ensuring that future capabilities can be easily incorporated into the existing retrieval framework. As part of this modular structure, we include in Aurora preexisting features in AURA (Pinhas et al., 2018), such as the functionality to retrieve stellar properties from a transmission spectrum. Furthermore, we introduce new modular capabilities that aid in the analysis of transmission spectra in the context of retrievals and forward models. These key additions include new considerations for noise modeling and forward models considering light refraction, forward scattering, and Mie scattering.

4.6.1 *Stellar Heterogeneity*

One of the main features of AURA (Pinhas et al., 2018) was to retrieve stellar properties embedded in the transmission spectrum as well as the planetary properties. Inhomogeneities in the stellar photosphere were modeled by retrieving the areal fraction of the projected stellar disk covered by heterogeneities (δ), hot faculae or cool spots, the heterogeneity temperature (T_{het}), and the photospheric temperature (T_{phot}). Aurora inherits this capability but we do not include it in the present study.

4.6.2 *New Noise Modeling Modules*

Aurora has the capability to treat noise models that are different from the traditionally assumed white noise. Aurora can consider the possibility of underestimated variance in the data by retrieving an error bar inflation, which is a free parameter (Foreman-Mackey et al., 2013). This approach assumes that the variance is underestimated and can be expressed as

$$S^2 = \sigma_{obs}^2 + f^2 \Delta_{mod}^2, \tag{31}$$

where σ_{obs} is the error in the observations, and Δ_{mod} is the model's transit depth. This term replaces the variance term in Equation 29. This functionality has been tested on the recent spectroscopic observations of KELT-11b (Colón et al., 2020).

Aurora also has the capability to consider correlated noise in the data being analyzed. To do so, we have incorporated `Celerite` (Foreman-Mackey et al., 2017) and `George` (Ambikasaran et al., 2015) to model the covariance function and compute the likelihood of a Gaussian Process (GP) model (Rasmussen & Williams, 2006). The effects of a GP in transmission spectra fall beyond the scope of this thesis and we reserve it for a future study.

4.6.3 *Refraction and Forward Scattering*

In Aurora, we have incorporated the analytic descriptions for forward scattering and refraction of transit spectra proposed by Robinson et al. (2017). These prescriptions have been incorporated in the context of producing forward models and synthetic observations.

Refraction effects are calculated using the prescription for maximum pressure at which the effect of refraction is large enough to cause a light ray from one side of the planet to come from the far limb (i.e., opposite side) of the host star (Robinson et al., 2017). We incorporate the wavelength-dependent refractivity (Robinson et al., 2017) and use it to calculate the maximum pressure probed (P_{max}) at each wavelength following Equation 15 of Robinson et al. (2017). The optical depth for pressures higher than P_{max} is set to infinity. Figure 27 shows the effect of considering refraction in forwards models of K2-18b. For these forward models, we consider refraction due to H_2, H_2O, or N_2. The forward models are determined by the median retrieved parameters in Section 5.2, in Chapter 5. Figure 27 shows that the effects of refraction are almost negligible, $\sim$ 4 ppm. Additional models considering the effect of refraction for a rocky exoplanet are shown in Appendix C.1.

The standard forward model in Aurora combines the absorption and scattering optical depths into the total optical depth as seen in Equation 17. However, it is possible that a portion of the scattered light in the planet's atmosphere will be directed toward the observer. This portion of light is said to be forward scattered. The additional fraction of

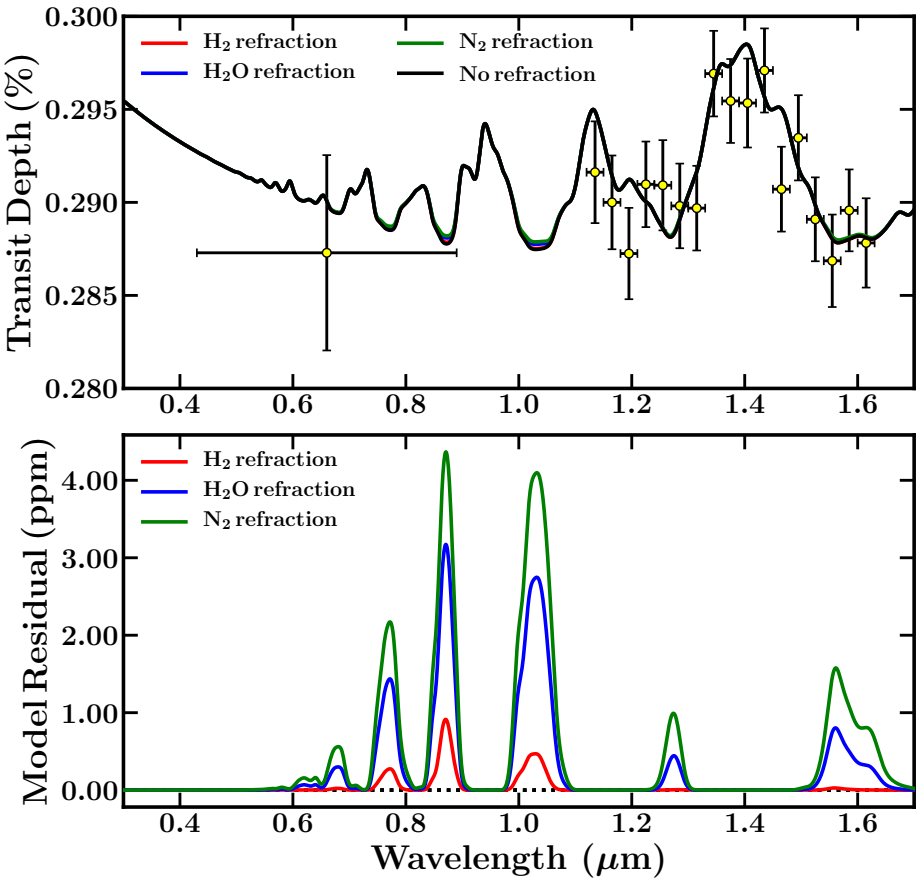

Figure 27 Forward models including the effects of wavelength-dependent refraction for the mini Neptune K2-18b. Top: no-refraction model shown in black while the red, blue, and green lines show the effects of H_2, H_2O, and N_2 refraction, respectively. Black error bars with yellow markers show current K2 and HST/WFC3 observations for reference. Bottom: residual of the refraction models relative to the no-refraction model.

light reaching the observer results in attenuation to the transit depth. In Aurora, we can model this by correcting the effective optical depth for the effects of forward scattering. The modified optical depth is $d\tau_{eff} = d\tau_\lambda(1 - f\tilde{\omega}_o)$, where f is the forward-scattering correction factor and $\tilde{\omega}_o$ is the single scattering albedo (Robinson et al., 2017). We calculate the correction factor f using the analytic correction expressed in Equation 6 of Robinson et al. (2017) for the Henyey-Greenstein phase function (Henyey & Greenstein, 1941). The correction proposed by Robinson et al. (2017) is a function of the stellar radius, the planet-star physical separation, and the asymmetry parameter g. Figure 28 shows the decrease in transit depth due to considering forward scattering, in the same H_2-

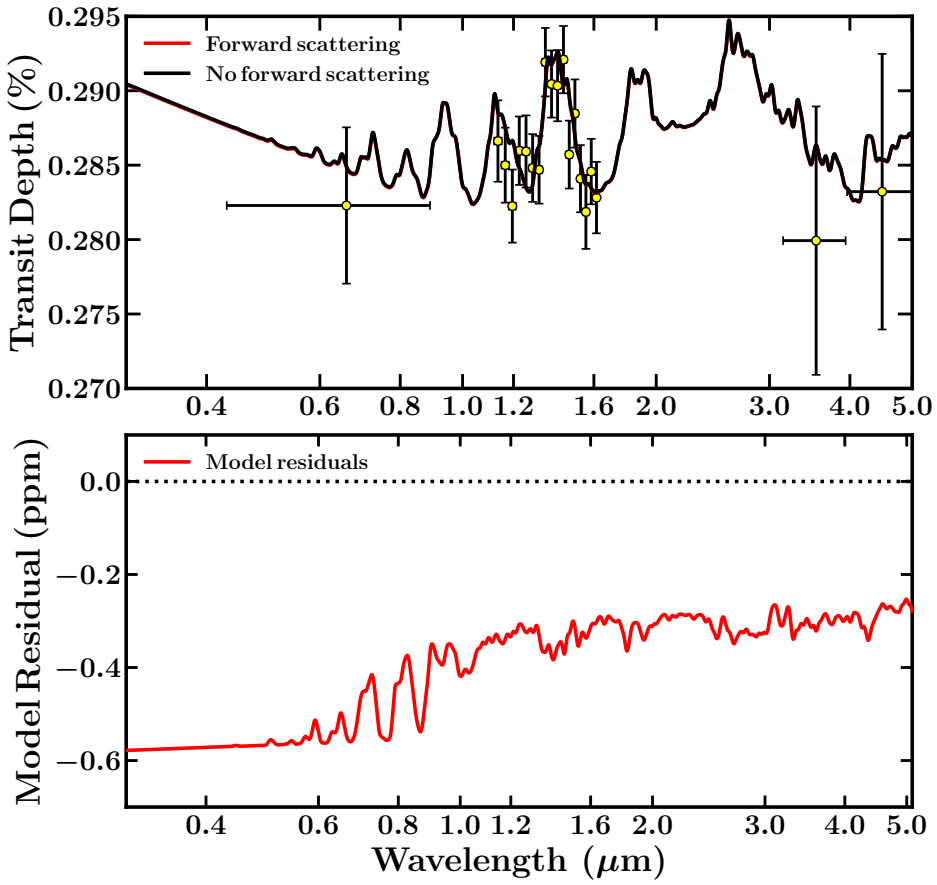

Figure 28 Forward-scattering models for the atmosphere of the mini Neptune K2-18b. Top: forward-scattering model shown in red, and in black, the model without forward scattering. Black error bars with yellow markers show current K2, HST/WFC3, and Spitzer observations for reference. Bottom: residual of the forward-scattering mode relative to the non-forward-scattering model.

rich forward model for K2-18b described above, assuming $g = 0.95$ and $\tilde{\omega}_0 = 1$. The effect of incorporating forward scattering in the model of K2-18b results in a difference of less than 1 ppm. Models considering forward scattering for a rocky exoplanet are shown in Appendix C.1.

The detectability of these secondary effects remains to be confirmed. Current observations using Hubble Space Telescope (HST), and ground-based observatories do not possess the precision necessary to identify them. In the meantime, Aurora possesses the capabilities to model these effects in transmission spectra of exoplanets in the context of forward models. The implementation of these models in the context of retrievals remains a possibility for future studies should the data require so.

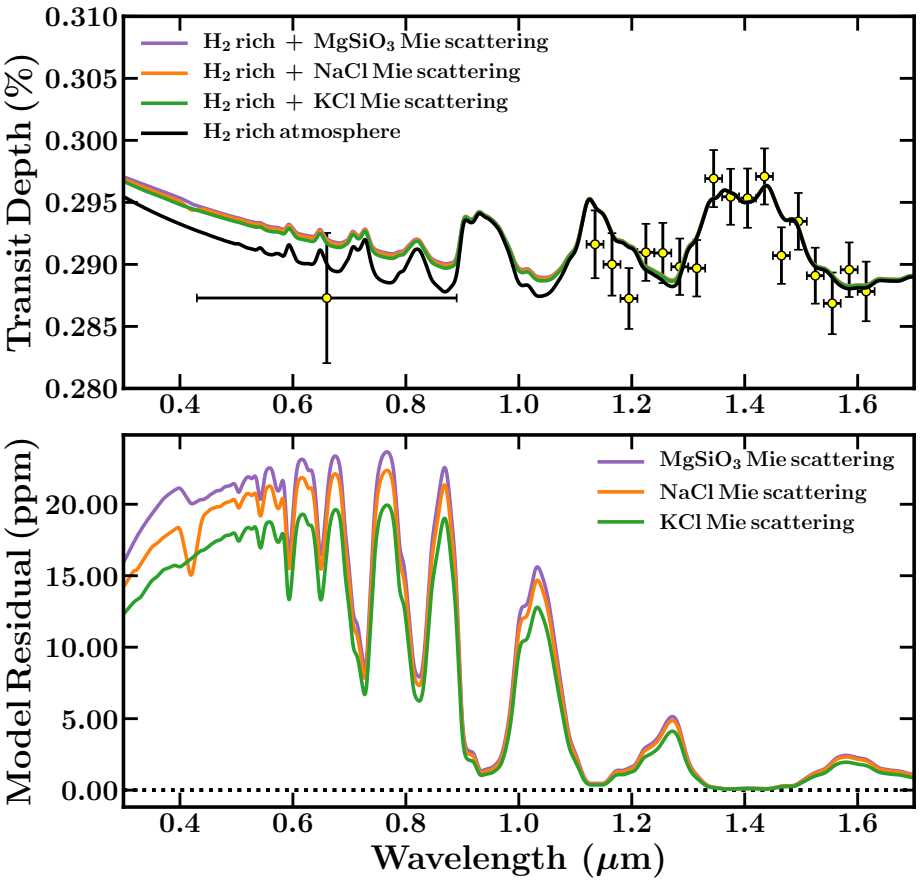

Figure 29 Top: forward models including the effects of Mie scattering for the mini Neptune K2-18b. The condensates shown are $MgSiO_3$ (purple), NaCl (orange), and KCl (green). In black, the H_2-rich-only model is shown. Black error bars with yellow markers show current K2 and HST/WFC3 observations for reference. Bottom: model residuals.

4.6.4 *Mie-scattering Forward Models*

Aurora includes Mie scattering in the forward models due to condensates with different particle sizes and compositions adopted from Pinhas & Madhusudhan (2017). The effective cross section for these species is calculated using their extinction and scattering coefficients, along with the corresponding asymmetry parameter g following Equation 11 of Pinhas & Madhusudhan (2017), obtained using Mie theory.

Figure 29 shows the spectroscopic features of Mie scattering for different compositions in the H_2-rich atmosphere of K2-18b. The models assume the retrieved chemical abundances from the results in Section 5.2, in Chapter 5. The models shown include H_2 Rayleigh scattering and H_2-H_2 and H_2-He CIA. In black, we show the H_2-rich atmosphere

only, while in purple, orange, and green the effects of Mie scattering due to $MgSiO_3$, NaCl, and KCl are shown, respectively. The assumed abundances for the condensate species is 10^{-16}, similar to expectations for NaCl and KCl from equilibrium chemistry calculations (e.g., Woitke et al., 2018) for the equilibrium temperature of the planet of $T_{eq.} \sim 290$ K (e.g., Welbanks et al., 2019, Chapter 3), with a particle size of 4.89×10^{-2} μm (< 0.1 μm, e.g., Adams et al., 2019; Lavvas et al., 2019). As shown in the bottom panel of Figure 29, the maximum difference between the clear H_2-rich model and the models considering Mie scattering is $\sim$ 25 ppm, within the precision limits of current observations. Future observatories with high-precision measurements in the optical wavelengths may be able to distinguish the effects of these condensate species in the atmospheres of exoplanets.

4.7 SUMMARY

In this chapter, we introduce Aurora, a next-generation atmospheric retrieval framework for transmission spectra of a wide range of exoplanets: from gas giants with H-rich atmospheres to rocky exoplanets with secondary non-H-rich atmospheres. Aurora retains the capabilities from previous retrieval codes and presents advancements for the analysis of future observations. Aurora, as its predecessor AURA, is comprised of a forward model interfaced with a Bayesian inference and parameter estimation algorithm. However, Aurora introduces key advancements for generalized retrievals of H-rich and H-poor atmospheres, there are:

- Aurora can retrieve the bulk composition of any exoplanet atmosphere without the assumptions of a H-rich atmosphere. The tools of compositional data analysis allow for reparameterizing the volume mixing ratios, used in traditional retrievals of exoplanet atmospheres, into compositional parameters. The implementation of this method results in prior probability densities, for the chemical components in the atmosphere, that are permutation-invariant. This advancement allows for agnostic retrievals where the bulk composition of the atmosphere is inferred from the data instead of being assumed a priori.

- We introduce a new generalized treatment for inhomogeneous clouds and hazes. The new cloud and haze prescription explores a larger parameter space compared to previous treatments. This new ap-

proach mitigates some biases and limitations in previous prescriptions and is robust when assuming a H-rich atmosphere or not.

- Aurora incorporates in its retrieval framework the next generation of nested sampling algorithms. These are highly adaptable and designed for handling highly degenerate problems and problems of higher dimensionality. This advancement is key in the development of multidimensional retrieval techniques and alleviates some of their computational needs.

- Aurora has a modular structure designed to evolve with the needs of future spectroscopic observations. The new modular capabilities include:
  - Noise modeling capabilities beyond the traditional assumed independently distributed Gaussian errors. These include the ability to retrieve an inflation for the standard deviation of observations and consider correlated noise using Gaussian processes.
  - Forward models considering the effects of light refraction, forward scattering, and Mie scattering due to condensates.

Having introduced the methods in Aurora, we now benchmark the retrieval framework. In the next chapter, Chapter 5, we validate this new retrieval framework on current and synthetic observations of exoplanets. We demonstrate the applicability of Aurora to a diverse population of exoplanets. We present case studies for characterizing atmospheres using the canonical hot Jupiter HD 209458 b, the temperate mini Neptune K2-18b, and the rocky exoplanet TRAPPIST-1 d.

5

AGNOSTIC RETRIEVALS OF EXOPLANETARY ATMOSPHERES

In Chapter 4, we have introduced the methods for a generalized retrieval framework which we have called Aurora. This more advanced modeling framework aims to reliably extract the atmospheric properties from existing and upcoming spectroscopic observations. Aurora is designed to retrieve the atmospheric properties of any type of exoplanet atmosphere, both H-rich and H-poor. Additionally, this new framework considerably expands the model flexibility required for explaining higher fidelity observations by considering new prescriptions for inhomogeneous clouds and hazes and next-generation Bayesian inference algorithms. As we look towards the future, characterizing the atmospheres of an increasingly diverse planet population through higher fidelity data will require more flexible and complex Bayesian modeling frameworks.

Here[1] we validate Aurora's new retrieval features on real and synthetic spectrophotometric observations. First, we validate our H-rich and non-H-rich approaches as well as the new prescription for inhomogeneous cloud and haze cover on the prototypical hot Jupiter HD 209458 b (Charbonneau et al., 2000; Henry et al., 2000) using observations from Sing et al. (2016). We demonstrate the robustness of our framework and cloud/haze prescription against assumptions of H-rich/H-poor atmospheres, improving on previous treatments. Next, we test the different nested sampling algorithms included in Aurora using the most recent observations of K2-18b (Foreman-Mackey et al., 2015) from Benneke et al. (2019c) and investigate the robustness of the retrieved abundance estimates comparing them to previous works (e.g., Benneke et al., 2019c; Welbanks et al., 2019; Madhusudhan et al., 2020). Using real and synthetic spectra of K2-18b, we demonstrate the agnostic approach to confidently constrain its bulk atmospheric composition and obtain precise abundance estimates. Lastly, we investigate future atmospheric constraints of rocky exoplanets using synthetic observations. We demonstrate Aurora on synthetic observations of the rocky exoplanet TRAPPIST-1 d. We find that 10 James Webb Space Telescope (JWST) NIRSpec transits can enable identification of the main atmospheric component for

1 The contents of this chapter are based on the published work of Welbanks & Madhusudhan (2021).

cloud-free, CO_2-rich, and N_2-rich atmospheres and abundance constraints on trace gases. We find that the same 10 JWST-NIRSpec transits may enable initial indications of O_3 if present at enhanced levels ($\sim 10\times$–$100\times$ Earth levels).

5.1 VALIDATION OF AURORA ON HOT JUPITER HD 209458 B.

We perform a series of retrievals on the transmission spectrum of HD 209458 b from Sing et al. (2016), composed of spectrophotometric observations with HST/STIS, HST/WFC3, and Spitzer. We use the standard model setup described in Welbanks & Madhusudhan (2019); Pinhas et al. (2019); Welbanks et al. (2019), also described in Chapter 2 and Chapter 3. Our sources of opacity include H_2-H_2 and H_2-He CIA, H_2 Rayleigh scattering, and line opacity due to H_2O, Na, K, CH_4, NH_3, HCN, CO, and CO_2. We conduct a range of retrievals with different cloud and haze prescriptions, and assumptions of whether or not the atmosphere is H rich.

We perform retrievals using four models with different considerations for clouds and hazes allowed by our generalized prescription explained in Section 4.3.3. Model 0 considers a clear atmosphere (i.e., $\phi_{\text{clouds}} = \phi_{\text{hazes}} = \phi_{\text{clouds+hazes}} = 0$). Model 1 considers one sector for a clear atmosphere and one sector for the combined effects of clouds and hazes (i.e., $\phi_{\text{clouds}} = \phi_{\text{hazes}} = 0$). Model 2 considers one sector for a clear atmosphere, one sector for the presence of clouds only, and one sector for the presence of hazes only (i.e., $\phi_{\text{clouds+hazes}} = 0$). Model 3 considers one sector for a clear atmosphere, one sector for clouds only, one sector for hazes only, and one sector for the combined presence of clouds and hazes (i.e., the full inhomogeneous cloud and haze prescription introduced in this dissertation, Chapter 4). For each cloud and haze model above, we perform a retrieval assuming a H-rich atmosphere and a retrieval relaxing such assumption. In summary, we perform eight retrievals in this section with the models above, four assuming a H-rich atmosphere and four not assuming a H-rich atmosphere.

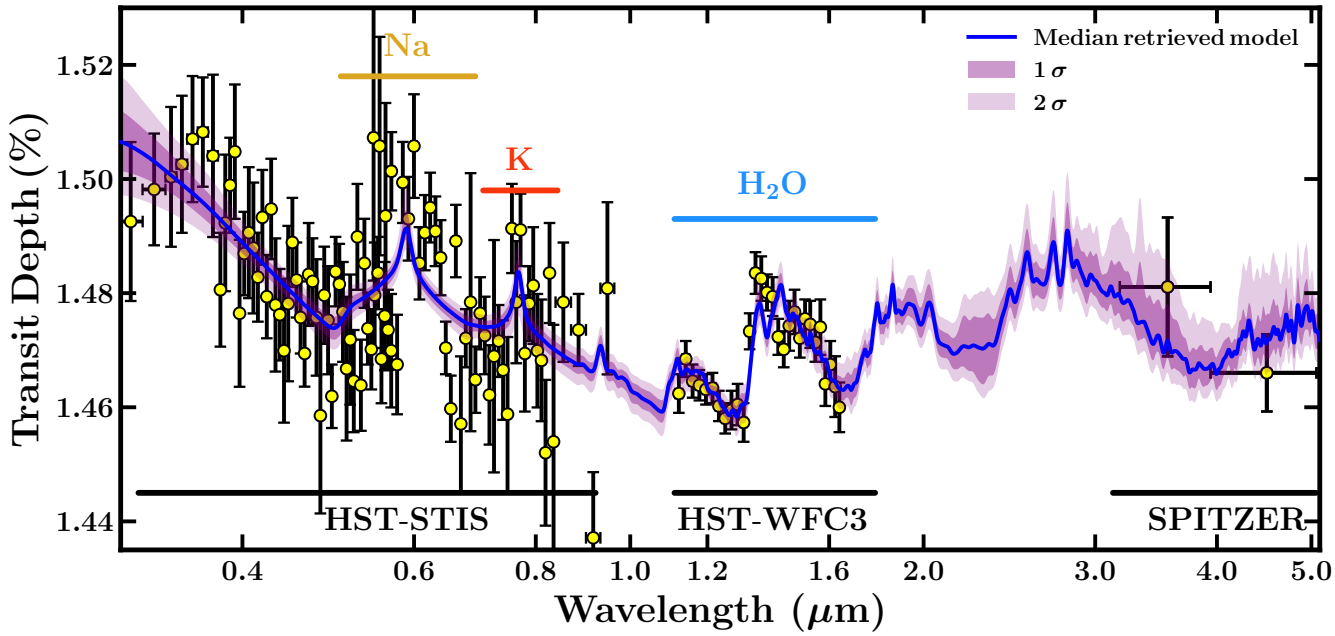

Figure 30 Validation of Aurora's retrieval framework on the spectrum of HD 209458 b. Retrieved median model (blue line), 1σ and 2σ confidence intervals (purple shaded regions), and spectroscopic observations (black error bars with yellow markers) for the highest evidence model (model 3; see Table 17). Horizontal lines at the bottom of the figure show the wavelength coverage of HST/STIS, HST/WFC3, and Spitzer. Yellow, orange, and blue horizontal lines show the approximate wavelength regions where Na, K, and H_2O spectral features are expected, respectively.

5.1.1 *A Generalized Cloud and Haze Prescription*

We consider a generalized cloud and haze prescription in order to explore a larger parameter space than available when restricting the presence of clouds and hazes to one sector only (i.e., model 1). We find that assuming a H-rich atmosphere or not can result in different solutions when restricting the clouds and hazes to the same region, as in model 1 (e.g., MacDonald & Madhusudhan, 2017a). This is not the case for any of the other models in this section (i.e., model 0, model 2, or model 3). When assuming a H-rich atmosphere, we find that, using any of the models for inhomogeneous cloud/haze cover, the spectrum of HD 209458 b can be explained by two possible scenarios. The first is the known solution with median values of subsolar[2] H_2O of $\log_{10}(X_{H_2O}) \sim -4.5$, $\log_{10}(X_{Na}) \sim -5.2$, $\log_{10}(X_K) \sim -7.0$ and a cloud and haze cover of roughly 50% (e.g., MacDonald & Madhusudhan, 2017a; Pinhas et al., 2019; Welbanks & Madhusudhan, 2019; Welbanks et al., 2019); the second is a physically implausible solution with high Na abundances that make up for $\sim 20\%$ of the atmosphere's composition and an atmosphere fully covered by clouds and hazes (e.g., $\log_{10}(X_{H_2O}) \sim -2.5$, $\log_{10}(X_{Na}) \sim -0.7$, $\log_{10}(X_K) \sim -2.4$). Both modes are simultaneously retrieved by model 2 and model 3, regardless of whether or not a H-rich composition is assumed. However, when treating clouds and hazes together (i.e., model 1), while assuming a H-rich atmosphere results in the two modes as discussed above, relaxing the H-rich assumption results in only the high Na abundance solution. Therefore, model 1 may be susceptible to potential biases in retrieved solutions when the dominant atmospheric composition may not be assumed to be H rich a priori. On the other hand, models 2 and 3 provide more generalized parameterizations that do not depend strongly on the H-rich assumption. In what follows, we restrict the prior space of the $\log_{10}$ abundances of Na, K and CO to an upper limit of -1.5, consistent with assumptions in previous studies (e.g., MacDonald & Madhusudhan, 2017a; Pinhas et al., 2019; Welbanks & Madhusudhan, 2019; Welbanks et al., 2019, Chapter 2 and Chapter 3). We implement this upper limit by rejecting the unphysical solutions.

2 We clarify that in this context, we refer to abundances of H_2O as subsolar by assessing them relative to expectations from thermochemical equilibrium for solar elemental abundances (Asplund et al., 2009). For a solar composition, the expectation is a H_2O abundance of $\log_{10}(X_{H_2O}) \sim -3.3$ for a planet with the equilibrium temperature of HD 209458 b (Madhusudhan, 2012).

5.1.2 *Effect of Cloud and Haze Prescriptions*

We rerun all eight cases with the new constraints on the abundances of Na, K and CO. We present the complete set of retrieved parameters for the four cloud and haze models assuming a H-rich atmosphere and not assuming a H-rich atmosphere in Table 17 included in Appendix C.4. Figure 30 shows the median retrieved spectrum for model 3, which results in the highest model evidence, while Figure 31 shows the H_2O, Na, and K posterior distributions for all four cloud and haze models.

Considering a cloud-free atmosphere (model 0) results in tight H_2O abundance constraints with precisions smaller than 0.5 dex. Regardless of the treatment for the main gas constituent in the atmosphere, both cloud-free retrievals result in subsolar H_2O abundances with abundance estimates smaller than the models considering clouds and hazes. These low abundances are the consequence of having a larger observable atmo-

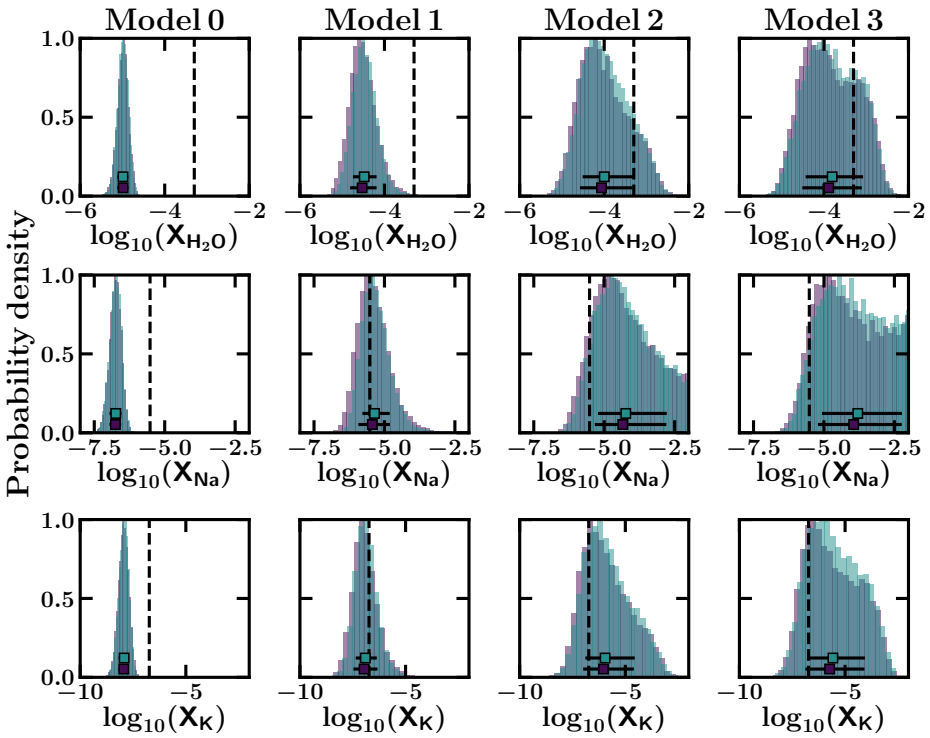

Figure 31 Posterior distributions for H_2O, Na and K abundances under the four different cloud and haze models. The purple (blue) distributions correspond to retrievals (not) assuming a H-rich atmosphere. Solar abundance expectations are shown using vertical black dashed lines. The markers in the posterior distributions show the median value (square marker) and the 1σ (error bars) range covering $\sim 68.27\%$ of the samples around the median value.

sphere (i.e., larger atmospheric column), unocculted by clouds, in which a small abundance of H_2O can contribute enough to explain the observations (see e.g., Welbanks & Madhusudhan, 2019, Chapter 2).

Contrary to the cloud-free solutions, the cloudy and hazy scenarios (i.e., models 1, 2, and 3) result in higher H_2O abundances, although with still generally subsolar values. Models 1, 2, and 3 are consistent in their retrieved parameters when assuming a H-rich atmosphere and when relaxing this assumption. The retrieved H_2O abundances are consistent with each other and within 1σ between all three cloud and haze models. The same is true for the Na and K abundances. Model 1, consisting of one fraction combining clouds and hazes as in MacDonald & Madhusudhan (2017a), results in tighter constraints relative to models 2 and 3. These tighter constraints indicate that part of the parameter space explored by the other two prescriptions was not considered in model 1. The increase in model evidence for model 2 and model 3 relative to model 1 indicates that the increased parameter space contains previously unsampled regions of high likelihood. The retrieved P–T profiles are consistent between models 1, 2, and 3, with a retrieved temperature near the photosphere for model 3 assuming a H-rich atmosphere of $T_{100mbar} = 1308^{+345}_{-278}$ K, consistent with previous studies (e.g., Welbanks & Madhusudhan, 2019; Welbanks et al., 2019, Chapter 2 and Chapter 3). On the other hand, the retrieved P–T profile for model 0 is tightly constrained at colder temperatures (e.g., $T_{100mbar} = 852^{+20}_{-12}$ K for the retrieval assuming a H-rich atmosphere) and inconsistent with the planet's equilibrium temperature ($T_{eq.}$ ~1450 K, e.g., Welbanks et al., 2019, Chapter 3).

When comparing the retrievals assuming H-rich atmospheres, model 3 has the highest model evidence with a value of $\log(\mathcal{Z}) = 958.40$. Using model 3 as our reference, model 0 is strongly disfavored at 4.6σ; model 1 is disfavored at 1.8σ; and model 2 is weakly disfavored at 1.4σ. A similar interpretation is available when comparing the non-H-rich retrievals among themselves.

5.1.3 *H-rich versus Non-H-rich Assumptions*

We also compare retrievals assuming a H-rich atmosphere against retrievals not assuming a H-rich atmosphere. Relaxing the assumption of a H-rich atmosphere requires an additional parameter to retrieve the volume mixing ratio of a mixture of H_2 and He in solar proportions. This additional parameter results in a decrease in model evidence relative to

retrievals assuming a H-rich atmosphere. Retrievals using model 3 favor assuming a H-rich atmosphere at 2.82σ over not assuming a H-rich atmosphere. Despite this decrease in evidence, retrievals not assuming a H-rich atmosphere find that 99.9% of the atmosphere is made up of H_2 and He. By not assuming a H-rich atmosphere a priori, our models are able to robustly confirm that the data corresponds to the atmosphere of a H-rich planet. Our results indicate that assuming a H-rich atmosphere is appropriate for the spectrum of HD 209485b as expected. These results demonstrate for gas giants that both approaches, whether or not assuming a H-rich atmosphere, are consistent and that the retrieved parameter estimates are robust against either methodology.

5.1.4 *Assessing the Highest Evidence Model*

The highest evidence model (i.e., model 3, H-rich assumption) results in retrieved abundance estimates for H_2O, Na, and K that are consistent with previous results (e.g., Barstow et al., 2017; MacDonald & Madhusudhan, 2017a; Pinhas et al., 2019; Welbanks & Madhusudhan, 2019; Welbanks et al., 2019, Chapter 2 and Chapter 3). However, their precisions are wider with retrieved abundances of $\log_{10}(X_{H_2O}) = -3.89^{+0.78}_{-0.62}$, $\log_{10}(X_{Na}) = -3.95^{+1.71}_{-1.27}$, and $\log_{10}(X_K) = -5.73^{+1.65}_{-1.15}$. The wider estimates result in a median H_2O abundance that is still subsolar based on expectations of thermochemical equilibrium, but consistent with a solar value to within 1σ. Importantly, while the H_2O abundance is largely subsolar, both Na and K abundances are significantly super-solar, implying a relative depletion in H_2O compared to Na and K as found in Welbanks et al. (2019, Chapter 3). The retrieved cloud and haze parameters indicate a nonclear atmosphere covered by clouds and hazes with a cloud deck located above the expected photosphere. The retrieved fractions are $\phi_{clouds} = 0.34^{+0.18}_{-0.20}$, $\phi_{hazes} = 0.27^{+0.09}_{-0.10}$, and $\phi_{clouds+hazes} = 0.24^{+0.19}_{-0.16}$.

Noteworthy, too, are the retrieved values for the Rayleigh-enhancement factor. Model 3 (H-rich) retrieves a Rayleigh-enhancement of $\log_{10}(a) = 3.28^{+1.01}_{-1.13}$, while model 2 (H-rich) retrieves $\log_{10}(a) = 2.88^{+0.91}_{-0.85}$. Both retrieved Rayleigh-enhancement factors have median values and upper limits smaller than the retrieved median value for model 1 (e.g., $\log_{10}(a) = 4.35^{+0.71}_{-1.01}$ for the H-rich case). This may indicate a tendency to over estimate the Rayleigh-enhancement factor in the hazes when using model 1 (e.g., MacDonald & Madhusudhan, 2017a). If true, this possibility must be accounted for when studying the nature of super-Rayleigh slopes as performed in recent studies (e.g., Ohno & Kawashima, 2020). Similarly,

although consistent with each other, the retrieved median value for the scattering slope γ is higher for model 1 than for models 2 and 3. The constraints from the H-rich retrievals are $\gamma = -14.04^{+4.53}_{-3.94}$ for model 1, $\gamma = -16.57^{+3.15}_{-2.37}$ for model 2, and $\gamma = -16.15^{+3.36}_{-2.60}$ for model 3. We note that the interpretation of the Rayleigh-enhancement factor (α) should be done in conjunction with the value for the scattering slope (γ) as these parameters are correlated. Lastly, the retrieved cloud top pressure for the gray cloud deck is consistent within 1σ between all approaches with a retrieved value of $\log_{10} P_{\rm cloud}) = -4.72^{+0.99}_{-0.84}$ for the model with the highest evidence.

Finally, we compare model 2 to model 3. The retrieved parameters are consistent between the two approaches and have similar precisions. Due to their similar performance and relatively small difference in model evidence, we consider both approaches interchangeable for the effects of this chapter. In what follows we consider model 2 (i.e., one sector for a clear atmosphere, one sector for clouds only and one sector for hazes only) as our preferred model due to its smaller number of parameters and similar performance to model 3 (i.e., full inhomogeneous cloud and haze prescription). We utilize model 2 as our approach for inhomogeneous cloud and hazes in the remaining of the results section unless otherwise stated.

5.2 TESTING MULTIPLE NESTED SAMPLING ALGORITHMS

We validate the different nested sampling algorithms in Aurora by performing retrievals using the same model and the same data. We discuss three nested sampling algorithms in Section 4.5.1. Four retrievals are performed, one using MultiNest, one using PolyChord, one using Dynesty in its static nested sampling mode, and one using Dynesty in its dynamic nested sampling mode. We use the observed transmission spectrum of K2-18b from Benneke et al. (2019c) including K2 band photometry, HST/WFC3 G141 grism spectra, and Spitzer IRAC photometric observations. The model considers an isothermal and clear atmosphere. We assume a H-rich atmosphere and consider the absorption due to H_2–H_2 and H_2-He CIA, H_2O, CH_4, NH_3, CO and CO_2. In total, the model has seven free parameters: five molecular species, one parameter for the temperature of the isotherm, and one parameter for the reference pressure. The retrieved parameters are used to produce the forward models in Sections 4.6.3 and 4.6.4.

When initializing the nested sampling algorithms, different parameters responsible for the algorithm's settings can be modified. Examples of such parameters are the maximum number of iterations in the sampling algorithm (PyMultiNest), parameters to increase the number of posterior samples produced (PyPolyChord), or the maximum number of likelihood evaluations before terminating (Dynesty). We keep most settings for the nested sampling algorithms to their default values. We only modify parameters needed for a direct comparison, e.g., the number of live points used to sample the prior distributions.

MultiNest was set up with 2000 live points. PolyChord was also set up with 2000 live points and 7 repeats. The number of repeats is specific to PolyChord's settings, and it corresponds to the length of the sampling chain used to generate a new live point. The longer the chain, the less correlated the live points and the more reliable the evidence inference is; however, the run takes longer to complete. The default value for the number of repeats used by PolyChord is $5\times$ the number of dimensions in the problem, that is, $5\times$ the number of model parameters. Because we do not need an estimate for the model evidence in this exercise, as we are not comparing the model evidence between samplers, we do not need to choose a significantly larger number of repeats. We find that for our atmospheric model with seven free parameters (i.e., seven dimensions), our choice of seven repeats (i.e., $1\times$ the number of dimensions) is sufficient.

For Dynesty, two separate runs were performed: one using static nested sampling and the other using dynamic nested sampling. For the static Dynesty run, we used 2000 live points. Similarly, the dynamic Dynesty run had an initial number of 2000 live points. The Dynesty runs were set up to generate the new live points using multiellipsoidal decomposition with uniform sampling; this is so that their sampling methods were similar to MultiNest.

Figure 32 presents the retrieved spectra for the data of K2-18b when using each of the different nested sampling algorithms in Aurora, along with the posterior distributions for the parameters of interest when comparing to previous works (e.g., Benneke et al., 2019c; Welbanks et al., 2019; Madhusudhan et al., 2020). The complete list of retrieved parameters is shown in Table 3.

All four nested sampling algorithms included in Aurora retrieve values consistent with each other and with previous works. The retrieved H_2O abundance for MultiNest is $\log_{10}(X_{H_2O}) = -2.28^{+1.16}_{-1.15}$, for PolyChord it is $\log_{10}(X_{H_2O}) = -2.21^{+1.24}_{-1.20}$, for Dynesty in its static run is

Table 3 Retrieved Parameters for the Spectrum of K2-18b Using Different Nested Sampling Algorithms as Explained in Section 5.2.

PARAMETER	MULTINEST	POLYCHORD	DYNESTY STATIC	DYNESTY DYNAMIC
$\log_{10}(X_{H_2O})$	$-2.28^{+1.16}_{-1.15}$	$-2.21^{+1.24}_{-1.20}$	$-2.29^{+1.20}_{-1.15}$	$-2.32^{+1.20}_{-1.12}$
$\log_{10}(X_{CH_4})$	$-8.33^{+2.63}_{-2.35}$	$-8.11^{+2.64}_{-2.65}$	$-8.09^{+2.63}_{-2.51}$	$-8.18^{+2.65}_{-2.49}$
$\log_{10}(X_{NH_3})$	$-8.82^{+2.27}_{-2.09}$	$-8.73^{+2.37}_{-2.22}$	$-8.67^{+2.26}_{-2.15}$	$-8.73^{+2.27}_{-2.14}$
$\log_{10}(X_{CO})$	$-6.89^{+3.53}_{-3.33}$	$-6.63^{+3.58}_{-3.71}$	$-6.70^{+3.54}_{-3.42}$	$-6.71^{+3.42}_{-3.36}$
$\log_{10}(X_{CO_2})$	$-7.49^{+3.42}_{-2.97}$	$-7.31^{+3.28}_{-3.15}$	$-7.25^{+3.23}_{-3.12}$	$-7.21^{+3.17}_{-3.13}$
T_0 (K)	$179.70^{+57.86}_{-44.47}$	$185.27^{+64.87}_{-50.45}$	$182.81^{+59.85}_{-49.08}$	$181.45^{+57.28}_{-46.58}$
$\log_{10}(P_{ref})$ (bar)	$-0.86^{+0.37}_{-0.44}$	$-0.89^{+0.39}_{-0.44}$	$-0.86^{+0.37}_{-0.44}$	$-0.86^{+0.37}_{-0.43}$

$\log_{10}(X_{H_2O}) = -2.29^{+1.20}_{-1.15}$, and for Dynesty in its dynamic run it is $\log_{10}(X_{H_2O}) = -2.32^{+1.20}_{-1.12}$. These H_2O abundances are consistent within 1σ with the works of Benneke et al. (2019c); Welbanks et al. (2019, see also Chapter 3) and Madhusudhan et al. (2020, see also Chapter 7). In agreement with previous works, the retrieved CH_4 and NH_3 median abundances are lower than expectations from chemical equilibrium. Comparing between the four sampler setups, the posterior distributions obtained for the parameters studied are largely consistent with each other. The retrieved precision on the model parameters is consistent between samplers, with a precision on the H_2O abundance of ~ 1.2 dex.

Our comparison shows that despite the differences in sampling algorithms, the parameter posterior distributions are mostly independent of the method employed for a problem of this dimensionality (i.e., seven model parameters) and with current data quality. We assess the different run times for each of the nested sampling algorithms by performing these retrievals on one thread of a four-core Intel Core i7-4700MQ CPU at 2.40 GHz. The fastest Nested algorithm under these conditions was MultiNest, followed by the static run of Dynesty ($\sim 3\times$ longer), the dynamic run of Dynesty ($\sim 5\times$ longer), and Polychord ($\sim 6\times$ longer). These run times are not necessarily representative of the full potential of each sampler. Different parameters in the setup of each algorithm can result in different run times.

In general, we have shown that Aurora includes the capabilities to retrieve the atmospheric properties of an exoplanet spectrum using different nested sampling algorithms. For current data and models, MultiNest is an optimal tool that retrieves the posterior distribution of our parame-

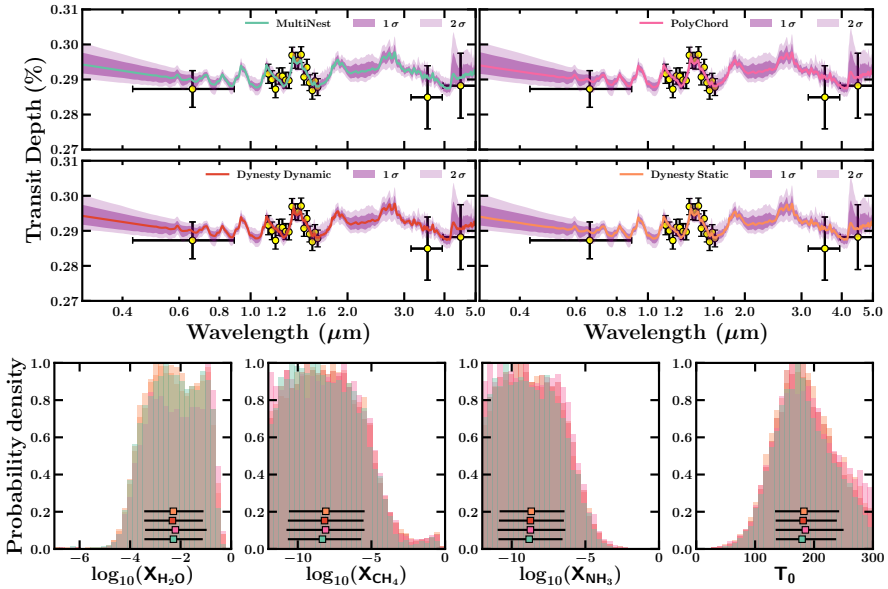

Figure 32 Comparison between retrievals with different nested sampling algorithms. Top four panels show the retrieved median model (colored line), 1σ and 2σ confidence intervals (shaded purple regions), and K2, HST/WFC3, and Spitzer observations (black error bars with yellow markers). Bottom row shows the posterior distributions for H_2O, CH_4, NH_3, and T_0, the isothermal temperature. The posterior distributions and colored lines are shown in green for MultiNest, pink for PolyChord, red for Dynesty in its dynamic mode, and coral for Dynesty in its static mode. All retrievals are consistent with each other.

ters efficiently. As data increases and possible degeneracies between the parameters in our models are exacerbated, or as the dimensionality of our problems and models increases, PolyChord and Dynesty are tools that offer alternative ways to perform retrievals. The user in Aurora has the freedom to choose the optimal tool for the problem at hand.

5.3 APPLICATION TO MINI NEPTUNE K2-18B

We validate Aurora's retrieval framework on current observations of K2-18b (Benneke et al., 2019c), including K2, HST/WFC3, and Spitzer, spectrophotometric data. Unlike the previous section, we perform retrievals not assuming a H-rich atmosphere. Using a full Bayesian approach, we test the validity of previous assumptions of a H-rich atmosphere when analyzing the most recent transmission spectrum of this mini Neptune. Then, we perform retrievals on HST/STIS and JWST-NIRSpec synthetic observations of the same planet and assess the constraints on the chemical abundances and cloud/haze properties.

5.3.1 *Case Study: Current Observations of K2-18b*

While previous studies have assumed that K2-18b has a H-rich atmosphere (e.g., Tsiaras et al., 2019; Benneke et al., 2019c; Welbanks et al., 2019; Madhusudhan et al., 2020), the robustness of this assumption has remained untested. Here, we apply the new functionality of Aurora, to retrieve atmospheric properties of an exoplanet without assuming a H-rich atmosphere to the broadband transmission spectrum of K2-18b. As discussed in Sections 5.2 and 5.3, we include spectroscopic observations from the HST/WFC3 G141 grism (1.05–1.7 μm), as well as photometric data in the Spitzer IRAC 3.6 and 4.5 μm bands, and K2 optical bands (0.43–0.89 μm) from Benneke et al. (2019c). We also redo an analysis assuming the planet has a H-rich atmosphere and with more model considerations than the results in Section 5.2. By performing both sets of retrievals, we can compare their model evidences and assess if the assumption of a H-rich atmosphere is preferred by our retrievals. Furthermore, we expand on previous studies and consider the possibility of O_2 and O_3 absorption for illustration.

The retrievals on the full broadband spectrum of K2-18b consider absorption due to H_2O, N_2, CH_4, HCN, NH_3, CO, and CO_2, and H_2-H_2 and H_2-He CIA. A second set of retrievals expands the number of absorbers included by considering O_2 and O_3 absorption. Our models employ a full parametric P–T profile, include the presence of H_2 Rayleigh scattering, and follow our new inhomogeneous cloud and haze treatment using two distinct cloud/haze sectors (i.e., model 2 in Section 5.1). We perform retrievals by assuming the atmosphere is H rich as well as relaxing this assumption. The retrieved parameters are shown in Table 4. Figure 33 shows the retrieved spectra and a subset of the retrieved posterior distributions for the highest evidence models assuming a H-rich atmosphere and not assuming a H-rich atmosphere.

We first assess the retrievals when assuming a H-rich atmosphere. The retrieved H_2O abundances are consistent when considering the possibility of O_2 and O_3 absorption and when not. With retrieved H_2O abundances of $\log_{10}(X_{H_2O}) = -2.10^{+1.07}_{-1.20}$ (not considering O_2 or O_3) and $\log_{10}(X_{H_2O}) = -2.12^{+1.09}_{-1.24}$ (considering O_2 and O_3), the results are in agreement with the estimates of Benneke et al. (2019c); Welbanks et al. (2019, see also Chapter 7) and Madhusudhan et al. (2020, see also Chapter 7). Likewise, both retrievals find a depletion of CH_4 and NH_3 despite the strong absorption of these species in the HST/WFC3 and Spitzer bands, in agreement with retrievals in previous studies. The limited spec-

Table 4 Retrieved Parameters for Current Observations of K2-18b, Assuming and Not Assuming a H-rich Atmosphere

	PARAMETER	H-RICH RETRIEVAL W/O O_2, O_3	H-RICH RETRIEVAL W O_2, O_3	NO H-RICH RETRIEVAL W/O O_2, O_3	NO H-RICH RETRIEVAL W O_2, O_3
Chemical Species	$\log_{10}(X_{H_2+He})$	N/A	N/A	$-0.09^{+0.09}_{-5.71}$	$-0.14^{+0.13}_{-6.64}$
	$\log_{10}(X_{H_2O})$	$-2.10^{+1.07}_{-1.20}$	$-2.12^{+1.09}_{-1.24}$	$-1.20^{+1.15}_{-1.81}$	$-1.22^{+1.18}_{-2.03}$
	$\log_{10}(X_{N_2})$	$-6.29^{+3.38}_{-3.45}$	$-6.59^{+3.49}_{-3.40}$	$-5.53^{+3.24}_{-3.23}$	$-5.66^{+3.28}_{-3.25}$
	$\log_{10}(X_{CH_4})$	$-8.16^{+2.54}_{-2.41}$	$-8.20^{+2.60}_{-2.31}$	$-6.71^{+3.84}_{-2.57}$	$-6.59^{+5.10}_{-2.79}$
	$\log_{10}(X_{HCN})$	$-8.07^{+2.53}_{-2.46}$	$-8.03^{+2.51}_{-2.45}$	$-6.78^{+2.89}_{-2.48}$	$-6.81^{+3.05}_{-2.61}$
	$\log_{10}(X_{NH_3})$	$-8.73^{+2.16}_{-2.03}$	$-8.64^{+2.11}_{-2.08}$	$-7.58^{+2.30}_{-2.02}$	$-7.61^{+2.39}_{-2.10}$
	$\log_{10}(X_{CO})$	$-6.64^{+3.23}_{-3.34}$	$-6.64^{+3.18}_{-3.24}$	$-5.76^{+3.11}_{-3.10}$	$-5.78^{+3.14}_{-3.13}$
	$\log_{10}(X_{CO_2})$	$-7.16^{+3.00}_{-2.99}$	$-7.25^{+2.97}_{-2.99}$	$-6.16^{+2.87}_{-2.91}$	$-6.27^{+2.95}_{-2.88}$
	$\log_{10}(X_{O_2})$	N/A	$-6.33^{+3.40}_{-3.39}$	N/A	$-5.72^{+3.28}_{-3.21}$
	$\log_{10}(X_{O_3})$	N/A	$-7.44^{+2.96}_{-2.84}$	N/A	$-6.26^{+3.06}_{-2.92}$
P–T Parameters	T_0 (K)	$162.12^{+73.73}_{-67.26}$	$166.50^{+72.47}_{-67.41}$	$192.49^{+68.43}_{-77.90}$	$194.86^{+67.88}_{-79.54}$
	α_1	$1.32^{+0.43}_{-0.48}$	$1.32^{+0.43}_{-0.48}$	$1.20^{+0.49}_{-0.52}$	$1.17^{+0.50}_{-0.51}$
	α_2	$1.20^{+0.50}_{-0.54}$	$1.19^{+0.51}_{-0.54}$	$1.17^{+0.51}_{-0.55}$	$1.16^{+0.51}_{-0.55}$
	$\log_{10}(P_1)$ (bar)	$-1.64^{+1.61}_{-1.65}$	$-1.74^{+1.62}_{-1.63}$	$-1.77^{+1.58}_{-1.61}$	$-1.69^{+1.56}_{-1.64}$
	$\log_{10}(P_2)$ (bar)	$-4.00^{+1.74}_{-1.32}$	$-4.03^{+1.70}_{-1.27}$	$-4.11^{+1.65}_{-1.22}$	$-4.09^{+1.65}_{-1.24}$
	$\log_{10}(P_3)$ (bar)	$0.56^{+0.95}_{-1.33}$	$0.52^{+0.97}_{-1.29}$	$0.50^{+0.97}_{-1.29}$	$0.58^{+0.93}_{-1.28}$
	$\log_{10}(P_{ref})$ (bar)	$-1.27^{+0.54}_{-0.62}$	$-1.23^{+0.54}_{-0.61}$	$-1.27^{+0.72}_{-0.58}$	$-1.19^{+0.76}_{-0.62}$
Cloud-Haze Parameters	$\log_{10}(a)$	$0.76^{+4.28}_{-2.98}$	$1.03^{+4.40}_{-3.19}$	$1.55^{+4.54}_{-3.46}$	$1.55^{+4.39}_{-3.46}$
	γ	$-10.17^{+6.91}_{-6.39}$	$-9.97^{+6.78}_{-6.31}$	$-10.06^{+6.98}_{-6.16}$	$-9.88^{+6.71}_{-6.18}$
	ϕ_{hazes}	$0.27^{+0.25}_{-0.17}$	$0.27^{+0.24}_{-0.18}$	$0.28^{+0.25}_{-0.18}$	$0.29^{+0.26}_{-0.19}$
	$\log_{10}(P_{cloud})$ (bar)	$-1.57^{+1.99}_{-2.46}$	$-1.38^{+1.89}_{-2.21}$	$-1.23^{+1.88}_{-2.16}$	$-1.19^{+1.88}_{-2.19}$
	ϕ_{clouds}	$0.30^{+0.24}_{-0.19}$	$0.29^{+0.25}_{-0.18}$	$0.30^{+0.26}_{-0.19}$	$0.29^{+0.25}_{-0.19}$
	$\log(\mathcal{Z})$	179.15	179.08	176.84	176.49

Note. All retrievals were computed using MultiNest. N/A means that the parameter in question was not considered in the model by construction.

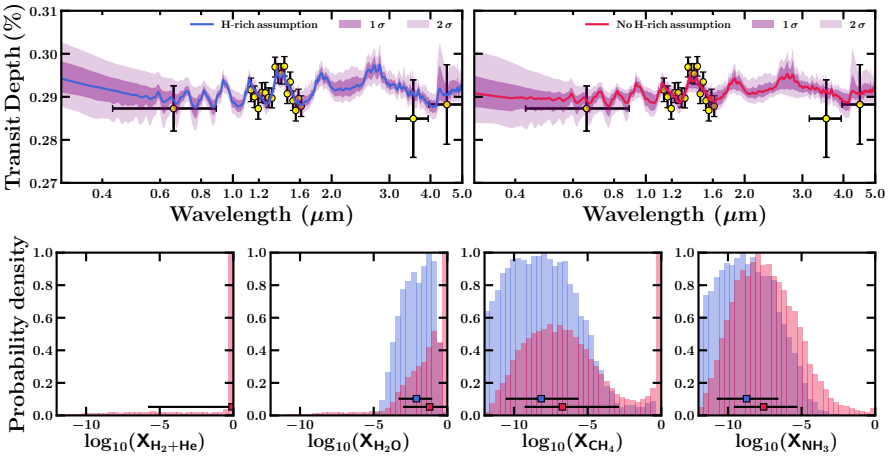

Figure 33 Retrieval of current K2-18b observations with and without the assumption of a H-rich atmosphere. Top: retrieved model spectra and observations for the two cases. Each panel shows the retrieved median model (blue for H rich and red for non H rich), 1σ and 2σ confidence intervals (shaded purple regions), and the K2, HST/WFC3, and Spitzer observations (black error bars with yellow markers). These cases do not consider O_2/O_3 as these molecules were not preferred by the data (see Table 4). Bottom row shows the posterior distributions for H_2+He, H_2O, CH_4, and NH_3 for the two retrievals.

tral information in the optical wavelengths results in weak constraints on the cloud and haze parameters. The use of a more complex cloud and haze parameterization (i.e., more parameters) relative to previous studies (e.g., Welbanks et al., 2019; Madhusudhan et al., 2020, Chapter 3 and Chapter 7), does not result in better constraints on the presence of clouds and hazes. The derived parameters are largely consistent with a clear atmosphere, i.e., small retrieved cloud cover fractions and haze cover fractions, and cloud-deck top pressures mostly near or below the photosphere.

The retrieved parameters when not assuming a H-rich atmosphere are consistent, within 1σ, with the retrieved parameters when assuming a H-rich atmosphere discussed above. Although consistent, this second approach results in wider and higher abundance estimates for all the chemical species considered. The retrieved H_2O abundances have median values almost 1 dex higher than those obtained when assuming a H-rich atmosphere. These retrieved abundances are $\log_{10}(X_{H_2O}) = -1.20^{+1.15}_{-1.81}$ (not considering O_2 or O_3) and $\log_{10}(X_{H_2O}) = -1.22^{+1.18}_{-2.03}$ (considering O_2 and O_3).

Despite the higher H_2O abundance estimates, the retrievals indicate that the main component of the atmosphere is H_2 and He with retrieved

abundances of $\log_{10}(X_{H_2+He}) = -0.09^{+0.09}_{-5.71}$ (not considering O_2 or O_3) and $\log_{10}(X_{H_2+He}) = -0.14^{+0.13}_{-6.64}$ (considering O_2 and O_3). The retrieved H_2+He abundance estimates correspond to a median of ~ 72%-81%, and allow for H_2+He abundances of less than 1% within 1σ as shown in Figure 33. Assuming a solar He/H_2 ratio of 0.17 (Asplund et al., 2009), the retrieved median H_2+He abundance estimate of $\log_{10}(X_{H_2+He}) = -0.09$ (H_2 and He volume mixing ratio of ~ 81%) indicates a $\log_{10}(X_{H_2}) = -0.16$ (H_2 volume mixing ratio of ~ 69%) and $\log_{10}(X_{He}) = -0.93$ (He volume mixing ratio of ~ 12%). All other chemical abundances are poorly constrained, with most uncertainties greater than 3 dex. Similarly, the cloud and haze parameters remain unconstrained. Overall, retrieving the main gas constituent in the atmosphere of K2-18b using current observations results in a H_2 and He-rich atmosphere (~ 72%-81% median volume mixing ratio) with strong H_2O absorption (~ 6% median volume mixing ratio), consistent with previous retrieval studies (e.g., Benneke et al., 2019c; Welbanks et al., 2019; Madhusudhan et al., 2020, Chapter 3 and Chapter 7).

The highest model evidence corresponds to the retrieval assuming a H-rich atmosphere and not considering absorption due to O_2 or O_3. Neither approach, assuming a H-rich atmosphere or not, favors the presence of O_2 and O_3 absorption in the atmosphere of K2-18b. In the H-rich approach, the additional parameter space due to considering the presence of these extra two absorbers dilutes the model evidence to a 1.17σ equivalent level. Likewise, the non-H-rich approach results in a decrease in model evidence equivalent to a 1.54σ level when considering absorption due to O_2 or O_3.

Increasing the parameter space to retrieve the abundance of H_2 and He results in a decrease in model evidence. When not considering O_2 and O_3 absorption, the model evidence for the H-rich assumed retrieval is higher at a 2.68σ level compared to the retrieval without a priori assumptions on the bulk composition of the atmosphere. Similarly, the H-rich assumption is preferred at a 2.79σ level over the non-H-rich assumed model when considering absorption due to O_2 and O_3. This preference of almost 3σ for the H-rich model should not be interpreted as a detection of a H-rich atmosphere on K2-18b but instead must be understood as an indication that the additional parameter space explored by the non-H-rich approach is of lower likelihood. On the other hand, the fact that both retrieval approaches infer a H-rich atmosphere can be interpreted as a demonstration that current data favor a H-rich atmosphere on K2-18b.

5.3.2 *Future Spectroscopic Observations: K2-18b*

In order to investigate the abundance constraints that may be possible with future observations, we generate synthetic HST/STIS and JWST-NIRSpec observations of K2-18b based on the retrieved median H_2O abundance for our highest evidence model in Section 5.3.1. We choose abundances for CH_4 and NH_3 that are $\sim 1\times$ solar ($\log_{10}(X_{CH_4}) = -3.3$, $\log_{10}(X_{NH_3}) = -3.9$; e.g., Woitke et al., 2018; Madhusudhan et al., 2020), consistent with their apparent depletion relative to the retrieved $\sim 10\times$ solar H_2O abundance (see Section 5.3.1, e.g., Madhusudhan et al., 2020). The input model also includes absorption due to HCN, CO, and CO_2, with an input nominal abundance of 1 ppm. We generate a model spectrum at a constant spectral resolution of $R = 5000$ between 0.3 and 5.5 μm. Given that current observations of K2-18b do not place strong constraints on the presence of clouds and hazes, we use input values for the cloud and haze prescription that fall within 1σ of the retrieved parameters in Section 5.3.1. These input parameters are a Rayleigh-enhancement factor $a = 10$, a slope $\gamma = -10$, a gray cloud deck with a top pressure in bar of $\log_{10}(P_{cloud}) = -1.6$, and a 25% cover due to the hazes and 30% cover due to clouds. The input P–T profile is set by the retrieved parameters for the highest evidence model in Section 5.3.1.

The synthetic JWST observations are generated using PANDEXO (Batalha et al., 2017a). We generate observations for a transmission spectrum of K2-18b observed with JWST-NIRSpec using its three high-resolution gratings (G140H/F100LP, G235H/F170LP, and G395H/F290LP) in the subarray SUB2048 mode, i.e., a total of three transits. Further details on the model inputs to PANDEXO are described in Appendix C.2.1. We also model synthetic HST/STIS observations covering the optical wavelengths from ~ 0.3 to 1.0 μm. Comparing an observed HST/WFC3 transmission spectrum of K2-18b (Benneke et al., 2019c) with that of HD 209458 b (Deming et al., 2013), it is seen that nine transits of K2-18b provide data of comparable quality, in terms of precision per spectral bin, to one transit of HD 209458 b. Because there are no HST/STIS observations of K2-18b available, we derive a synthetic HST/STIS spectrum of K2-18b by scaling the uncertainties and resolution from an observed HST/STIS spectrum of HD 209458 b (Sing et al., 2016) in the same proportion as that of the HST/WFC3 spectra between the two planets. We note that the resulting synthetic observations of K2-18b would require a significantly larger number of transits with HST/STIS than the nine observed with HST/WFC3. Nevertheless, we consider this optimistic

scenario as a test case to demonstrate our retrievals. Our synthetic observations have Gaussian-distributed uncertainties with a mean precision of ~ 72 ppm in the STIS G430L band and ~ 71 ppm in the STIS G750L band.

The resulting synthetic observations are shown in Figure 34. The synthetic HST/STIS and JWST-NIRSpec observations provide a spectral range of ~ 0.3–5.0 μm, encoding information about the presence of clouds, hazes, and absorption due to different species like H_2O, CH_4, and NH_3. We perform a retrieval on these observations considering absorption due to H_2O, CH_4, HCN, NH_3, CO, CO_2, N_2, O_2, and O_3, and H_2-H_2 and H_2–He CIA. We employ the same cloud and haze prescription employed in Section 5.3.1. We do not assume the bulk composition of the atmosphere and retrieve it instead.

Figure 34 shows the retrieved posterior probability distributions for H_2+He, the detected species H_2O, CH_4, and NH_3, and some relevant cloud/haze parameters. The full posterior distribution is shown in the Appendix C.5, Figure 57. The bottom half in Figure 34 also shows (in gray) the probability distributions obtained with current K2, HST/WFC3, and Spitzer spectrophotometric observations (first column in Table 4). Comparing both gray and green probability distributions, it is possible to appreciate that abundance estimates will be largely improved using JWST observations. For the assumed synthetic model and data considerations, we retrieve the abundances to be consistent with the input values at $\log_{10}(X_{H_2O}) = -1.66^{+0.50}_{-0.55}$, $\log_{10}(X_{CH_4}) = -2.94^{+0.35}_{-0.37}$ and $\log_{10}(X_{NH_3}) = -3.79^{+0.36}_{-0.40}$. The corresponding detection significances of the molecules are ~ 5σ, ~ 7σ, and ~ 3σ for H_2O, CH_4, and NH_3 respectively. In principle, even better abundance precisions and detection significances may be attained by combining with other observations (e.g., JWST-MIRI, JWST-NIRISS, HST/WFC3), or considering data of higher resolution. We also note that these precisions and detection significances are dependent on the input model assumptions: ~ 10×solar H_2O and ~ 1×solar CH_4 and NH_3. Nevertheless, these results demonstrate the capability of Aurora to precisely retrieve the true input values of a mini Neptune like K2-18b.

Furthermore, the retrieval on synthetic data demonstrates Aurora's ability to retrieve the bulk atmospheric composition of a mini Neptune like K2-18b. With a retrieved abundance of $\log_{10}(X_{H_2+He}) = -0.013^{+0.010}_{-0.024}$, Aurora correctly identifies H_2 and He as the bulk composition of the atmosphere as shown in Figure 34. The retrieved median abundance indicates that H_2 and He account for more than 97% of the atmosphere's

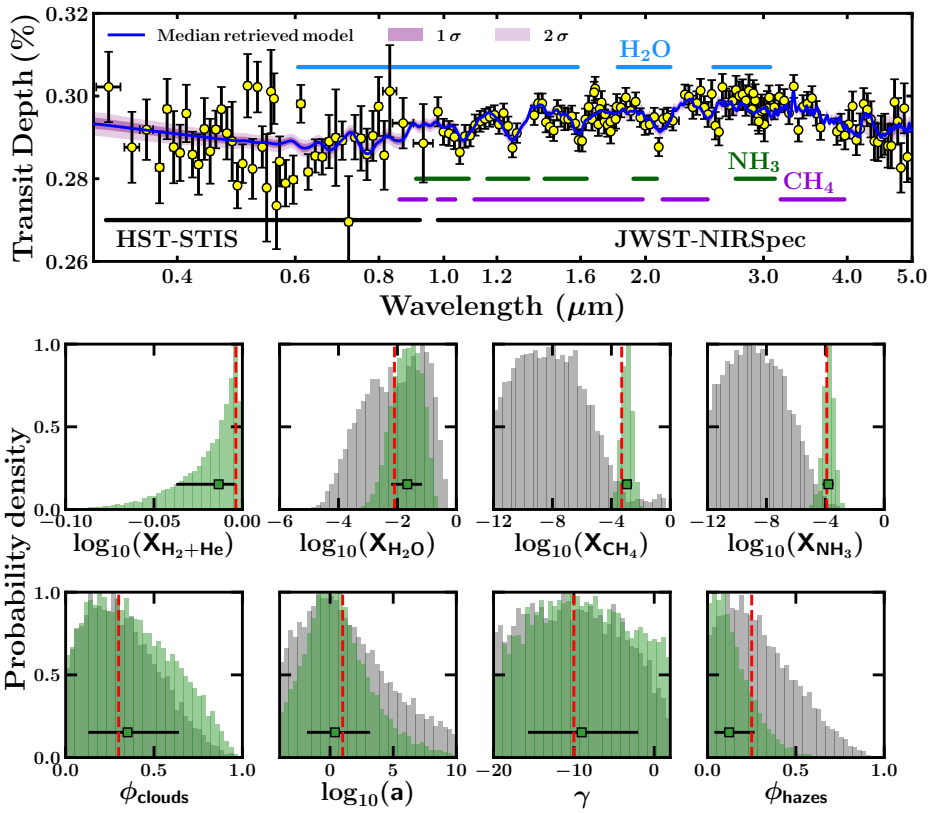

Figure 34 Retrieval of synthetic observations of K2-18b. Top: synthetic observations (black error bars with yellow markers) and median retrieved model (dark blue) for STIS G430L and G750L, and NIRSpec G140H, G235H, and G395H. The 1σ and 2σ confidence intervals (shaded purple areas) are not entirely visible as their span is much smaller than the spread in the data. Horizontal lines at the bottom of the figure show the wavelength coverage of HST/STIS and JWST-NIRSpec. Blue, green, and purple horizontal lines show, respectively, the approximate wavelength regions where H_2O, NH_3, and CH_4 spectral features are expected. Bottom: retrieved posterior distributions for H_2+He, H_2O, CH_4, and NH_3 abundances, and relevant cloud and haze parameters. The green posterior distributions in the foreground correspond to the retrieval using synthetic observations. The vertical red dashed lines indicate the true model input values for this synthetic retrieval. The gray posterior distributions in the background show estimates obtained with existing real observations of K2-18b as discussed in Section 5.3.1, illustrating constraints possible with current data. We note that the red vertical lines are unrelated to the gray posteriors.

composition, consistent with the input model. Future observations with JWST will make it possible to unequivocally retrieve the bulk gas composition in the atmosphere of K2-18b, improving on present-day estimates derived using current K2, HST/WFC3, and Spitzer observations.

The cloud and haze parameters in the input model are motivated by current constraints on K2-18b using existing data, as discussed above, which indicate a relatively cloud-/haze-free atmosphere. Under these cloud/haze assumptions, the retrieved abundance estimates and their detection significances are not strongly affected when only JWST-NIRSpec observations are considered in our retrievals. The retrieved cloud and haze parameters are mostly unconstrained, consistent with the cloud-/haze-free input model, and similar to constraints obtained with current data (e.g., gray posterior distributions in Figure 34). Even when both HST/STIS and JWST-NIRSpec observations are considered, the cloud/-haze constraints are only marginally improved, as shown in Figure 34 and Appendix C.5, as expected considering the low cloud/haze cover in the input model. Regardless of the cloud/haze constraints, however, the chemical abundances are still derived precisely as discussed above.

In principle, further spectroscopic observations, including those with other JWST instruments like NIRISS and MIRI, could help obtain better constraints than those reported here. At the same time, it could also be important to revisit the model assumptions in present retrievals (e.g., by considering higher-dimensional models, temporal variability, etc.) when confronted with observations of higher quality (e.g., higher resolution, better signal-to-noise ratio, broader wavelength coverage) expected in the near future. We discuss these implications and the prospect for future works in Section 5.5.

5.4 APPLICATION TO ROCKY EXOPLANETS

We demonstrate Aurora's capabilities to identify the composition of atmospheres that are not H rich. We use synthetic JWST-NIRSpec observations of the rocky exoplanet (i.e., terrestrial-size exoplanet) TRAPPIST-1 d ($R_p = 0.788\ R_\oplus$, $M_p = 0.388\ M_\oplus$; Gillon et al., 2017; Agol et al., 2021) to validate Aurora's retrieval capability for H-poor atmospheres. Of all seven TRAPPIST-1 planets, TRAPPIST-1 d is the closest to Earth in terms of insolation (see Figure 35). This makes TRAPPIST-1 d an appealing candidate for characterization with JWST, especially in the context of planets residing in their habitable zone. This opportunity has been recognized by the JWST Guaranteed Time Observations (GTO) program by planning to observe two transits of the planet using the NIRSpec prism (GTO 1201, PI: David Lafreniere).

Figure 35 shows the planet radius versus stellar insolation for the planets in the TRAPPIST-1 system. When compared to planets in the solar

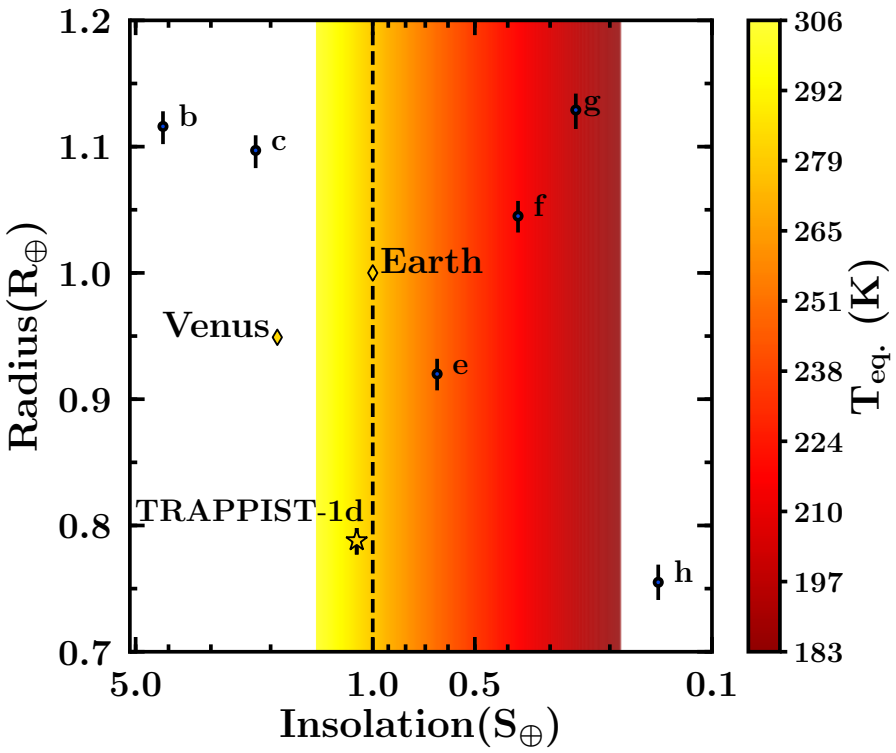

Figure 35 Planet radius vs. stellar insolation for the TRAPPIST-1 system. The seven TRAPPIST-1 planets (values from Agol et al., 2021) are shown alongside Earth and Venus (yellow diamonds). The shaded region represents the optimistic habitable zone for an M dwarf at the temperature of TRAPPIST-1 (Kopparapu, 2013). TRAPPIST-1d (gold star) is at the inner edge of the optimistic habitable zone of TRAPPIST-1 and is the closest to Earth in terms of insolation. Equilibrium temperature calculated assuming full redistribution and zero albedo.

system, TRAPPIST-1 d falls between Venus and Earth in terms of insolation. As such, we consider two possible model configurations for our application of Aurora: a CO_2-rich atmosphere (e.g., loosely similar to Venus' atmosphere) and a N_2-rich atmosphere (e.g., loosely similar to Earth's atmosphere with enhanced O_3). The CO_2-rich atmosphere is composed of 98% CO_2, 1% H_2O, 11.7 ppm H_2+He, and N_2 in the remaining percentage (~ 0.99%). The N_2-rich atmosphere is composed of 77.51% N_2, 21.38% O_2, 1% H_2O, 0.1% CO_2, and 0.01% O_3. We note that this O_3 abundance is ~ 10×–100× higher than present-day Earth's atmospheric abundance in the stratosphere (e.g., Anderson, 1987; Barstow et al., 2016b). The atmospheres are modeled to follow an isotherm at 250 K. We considered three cases for each composition: (1) a clear atmosphere, (2) an atmosphere with a gray cloud deck covering the entire

planet at a cloud top pressure $P_{cloud} = 0.1$ bar, and (3) a gray cloud deck covering the entire planet at a cloud top pressure $P_{cloud} = 1$ mbar. The model spectra are generated at a constant resolution of $R = 5000$ between 0.3 and 5.5 μm.

Besides demonstrating Aurora's capabilities, we explore the number of JWST transits required for the spectroscopic observations to provide chemical detections and abundance constraints of TRAPPIST-1 d's atmosphere. We consider observations from 1, 2, 3, 5, and 10 JWST transits. We consider 2 transits motivated by the upcoming GTO 1201 program, and an upper limit at 10 transits based on estimates for characterizing the TRAPPIST-1 system from Batalha et al. (2018; see Section 5.5.2). We empirically find that 10 transits with JWST-NIRSpec prism can provide chemical constraints of ~ 1 dex or better and robust detections ($\gtrsim 3\sigma$) for multiple chemical species in both the CO_2-rich and N_2-rich model atmospheres. The synthetic observations are generated using PANDEXO (Batalha et al., 2017a) for the NIRSpec prism using subarray SUB512. The synthetic observations include Gaussian white noise. Additional details are described in Appendix C.2.2.

The synthetic observations are generated using models that consider CO_2–CO_2 and N_2–N_2 CIA, as well as Rayleigh scattering due to N_2, CO_2, and H_2O. The models in the retrievals do not assume a H-rich atmosphere and consider absorption due to H_2O, CO_2, N_2, O_2, and O_3. Including the effects of H_2-H_2 and H_2-He CIA, and following the description for non-H-rich atmospheres in Section 4.4, the retrieval considers a total of six chemical components: H_2+He, H_2O, CO_2, N_2, O_2, and O_3. The model also considers one parameter for an isothermal temperature profile and one parameter for P_{ref}. We do not consider the full cloud and haze prescriptions presented in Chapter 4 due to the lack of observations in the optical required to robustly constrain the presence of hazes. However, we consider the presence of inhomogeneous clouds using two parameters: one for the cloud cover (ϕ_{clouds}) and one for the cloud top pressure ($\log_{10}(P_{cloud})$). In summary, the retrieval model has a total of 10 parameters: 6 parameters for the chemical components, 1 parameter for the isothermal temperature, 1 parameter for the reference pressure, and 2 parameters for the presence of inhomogeneous clouds.

		1 Transit	2 Transits	3 Transits	5 Transits	10 Transits	0.1 bar	1 mbar
CO_2 rich atmosphere	CO_2 98%	<2σ	~2σ	2.3σ	2.5σ	4.7σ	4.3σ	~2σ
	H_2O 1%	<2σ	<2σ	~2σ	2.3σ	4.3σ	<2σ	<2σ
		1 Transit	2 Transits	3 Transits	5 Transits	10 Transits	0.1 bar	1 mbar
N_2 rich atmosphere + enhanced O_3	CO_2 0.1%	<2σ	<2σ	<2σ	<2σ	2.4σ	~2σ	<2σ
	H_2O 1%	2.5σ	4.3σ	4.4σ	5.2σ	6.1σ	4.1σ	<2σ
	N_2 77.51%	<2σ	<2σ	<2σ	<2σ	~2σ	<2σ	<2σ
	O_3 100 ppm	<2σ	<2σ	<2σ	<2σ	≳2σ	<2σ	<2σ

Figure 36 Detection significance for different chemical species in the atmosphere of TRAPPIST-1 d as a function of the observed number of transits with JWST-NIRSpec. Top: CO_2-rich atmosphere. Bottom: N_2-rich atmosphere, with enhanced O_3. Left boxes show the results for a cloud-free atmosphere observed with 1, 2, 3, 5, and 10 transits. Right boxes show the results for observing 10 transits of a fully cloudy atmosphere with a cloud-deck top pressure of 0.1 bar and 1 mbar.

We begin by analyzing the results from our exploration of the number of transits required to characterize TRAPPIST-1 d's atmosphere. Figure 36 shows a summary of the chemical detections for the various numbers of transits considered. We perform this exploration following a conservative approach in which any model preference $< 2\sigma$ does not constitute a detection (red squares), model preferences $> 2\sigma$ and $< 3\sigma$ are suggestive of a chemical detection (yellow squares), and model preferences $> 3\sigma$ may be considered detections (green squares). Our search suggests that for a CO_2-rich clear atmosphere, 10 transits with JWST-NIRSpec will be able to provide detections of CO_2 and H_2O. Likewise, for an N_2-rich clear atmosphere, 10 transits would provide detections of H_2O, and possibly O_3 if present at enhanced levels (10×–100× Earth levels) as assumed in the input model described above. For the N_2-rich atmosphere, although N_2 is found to be the main atmospheric component, its lack of spectral features makes its robust detection difficult.

However, considering clear atmospheres only results in optimistic estimates that may be revised when considering the presence of clouds and hazes. We consider observing the cloudy cases described above using the same number of transits (right columns of Figure 36). As expected, the presence of a cloud deck mutes several of the spectral features resulting in weaker chemical detections or nondetections.

Next, we present the retrieved constraints using Aurora for the cases with the strongest chemical detections, i.e., 10 transits for a cloud-free model, starting with a clear CO_2-rich atmosphere. The retrieved chemical abundances of interest and retrieved spectrum are shown in Figure 37 along with the synthetic observations. The retrieved abundances for the species included in the true input model are $\log_{10}(X_{H_2+He}) = -5.53^{+3.01}_{-3.02}$, $\log_{10}(X_{H_2O}) = -1.64^{+0.63}_{-0.92}$, $\log_{10}(X_{CO_2}) = -0.07^{+0.06}_{-0.78}$, and $\log_{10}(X_{N_2}) = -4.27^{+3.35}_{-3.76}$. The retrieved values are consistent within $\sim 1\sigma$ of the true model input values. Aurora is capable of accurately distinguishing the main constituent of the modeled CO_2-rich atmosphere, with the posterior distribution of CO_2 corresponding to high abundances. Furthermore, the precisions on the retrieved H_2O abundance is $\lesssim 1$ dex, comparable to current chemical constraints for gas giants (e.g., Welbanks et al., 2019, Chapter 3).

Although the input model corresponds to a cloud-free atmosphere, we consider in our retrieval model the possibility of inhomogeneous cloud cover. The cloud parameterization retrieves a cloud cover of $\phi_{clouds} = 0.37^{+0.39}_{-0.25}$ and $\log_{10}(P_{cloud}) = 0.09^{+1.22}_{-3.08}$, consistent with a clear atmosphere (e.g., relatively small cloud fraction cover) with the gray cloud deck

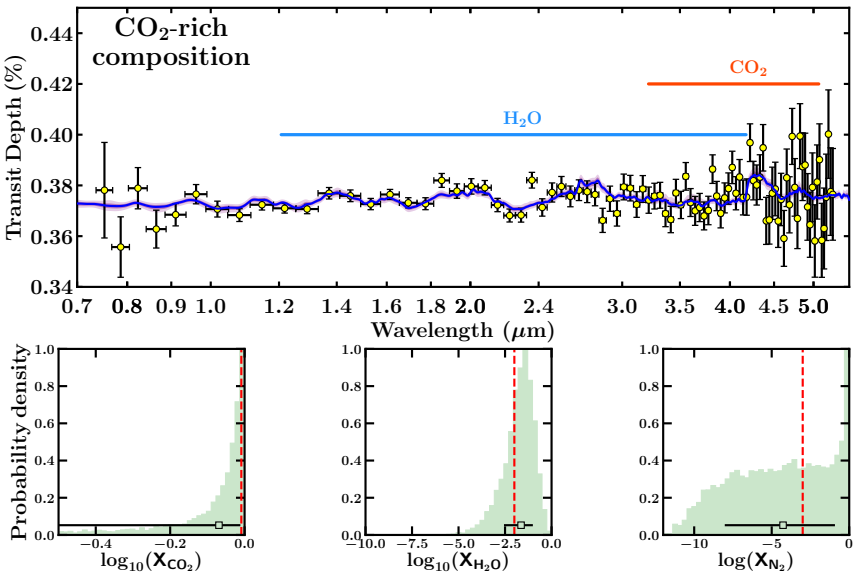

Figure 37 Retrieval of synthetic TRAPPIST-1 d observations for a CO_2-rich atmosphere. Top: synthetic observations (gold markers, black error bars) and median retrieved model (blue line) for NIRSpec prism. Shaded purple areas indicate 1σ and 2σ confidence intervals. Blue and red horizontal lines show, respectively, the approximate wavelength regions where H_2O and CO_2 spectral features are expected. Bottom: posterior distributions for CO_2, H_2O, and N_2. Vertical red dashed lines show the true input values.

placed below the expected photosphere (e.g., not muting spectral features) in agreement with the input model. Overall, these results indicate that the chemical characterization of a CO_2-rich, cloud-free atmosphere is possible with 10 JWST-NIRSpec transits. Under these conditions, Aurora is capable of detecting the main component of the atmosphere (CO_2) at 4.7σ and the trace gas (H_2O) at 4.3σ.

We briefly mention the results from considering the more challenging scenario of a cloudy CO_2-rich atmosphere. As described above, we consider scenarios with 100% cloudy atmospheres with cloud top pressures of 0.1 bar and 1 mbar. While both cases indicate a CO_2-rich atmosphere, the muted spectral features result in weaker detections of the main atmospheric constituent (e.g., 4.3σ for 0.1 bar and ~ 2σ for 1 mbar; see Figure 36). Although not resulting in strong detections, Aurora can correctly identify that the observations correspond to a cloudy atmosphere, with the 1 mbar case retrieving $\phi_{\text{clouds}} = 0.82^{+0.13}_{-0.25}$ and $\log_{10}(P_{\text{cloud}}) = -2.80^{+1.25}_{-1.24}$ (i.e., relatively high cloud cover fraction and a top cloud-deck pressure above the expected photosphere). In agreement with other studies (see Section 5.5.2), our results suggest that robustly

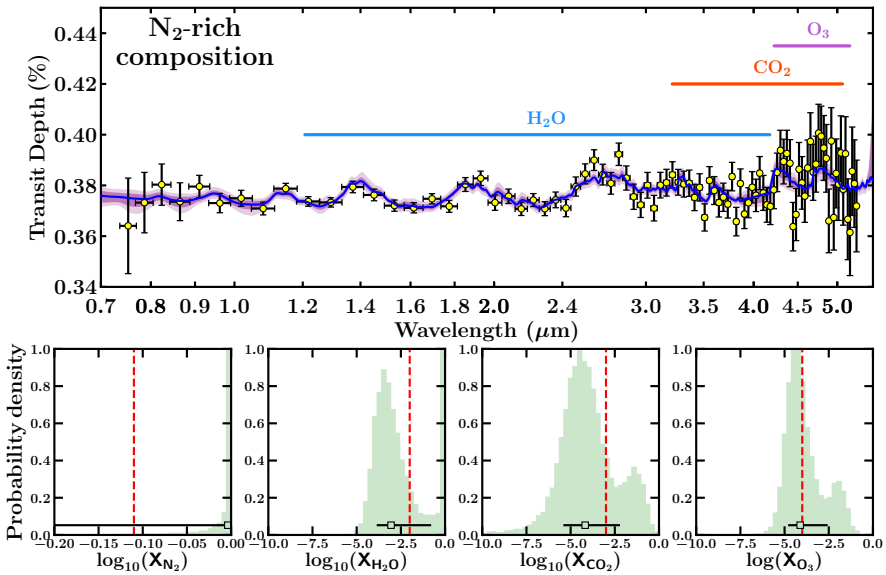

Figure 38 Retrieval of synthetic TRAPPIST-1 d observations for a N_2-rich atmosphere with enhanced O_3. Top: synthetic observations (gold markers, black error bars) and median retrieved model (blue line) for NIRSpec prism. Shaded purple areas indicate 1σ and 2σ confidence intervals. Blue, red, and purple horizontal lines show, respectively, the approximate wavelength regions where H_2O, CO_2, and O_3 spectral features are expected. Bottom: posterior distributions for N_2, H_2O, CO_2, and O_3. Vertical dashed lines show the true input values.

characterizing the atmosphere of a cloudy rocky exoplanet will need more than 10 JWST-NIRSpec transits.

Next, we present the results from retrieving the clear N_2-rich atmosphere with 10 JWST-NIRSpec transits. Aurora retrieves abundances of $\log_{10}(X_{N_2}) = -0.0037^{+0.0035}_{-2.2195}$, $\log_{10}(X_{H_2O}) = -3.06^{+2.27}_{-0.81}$, $\log_{10}(X_{CO_2}) = -4.18^{+1.97}_{-1.23}$, and $\log_{10}(X_{O_3}) = -4.12^{+1.56}_{-0.68}$, for the species with detection significances $\gtrsim 2\sigma$. The retrieved values are consistent within 1σ of the input parameter despite the white noise in the observations. The retrieved cloud parameters are $\phi_{clouds} = 0.51^{+0.31}_{-0.34}$ and $\log_{10}(P_{cloud}) = -0.34^{+1.12}_{-1.86}$, consistent with a cloud-free atmosphere due to the retrieved cloud-deck top pressure being below the expected photosphere. Figure 38 presents the synthetic observations as well as the retrieved spectrum and the posterior distributions for the chemical species of interest.

Although the retrieval indicates that N_2 is the main component of the atmosphere, the lack of strong spectral features results in a moderate detection of N_2 with 10 JWST-NIRSpec transits. Besides identifying the main component of the atmosphere, Aurora is able to detect H_2O (6.1σ) and O_3 ($\gtrsim 2\sigma$) with 10 transits and provide constraints in their abun-

dances to a precision of $\sim$ 1.5 dex. Although optimistic, these estimates present a tantalizing prospect for the detection of possible biosignatures in habitable zone rocky exoplanets. If present in $\sim$ 10$\times$–100$\times$ higher abundance than present-day Earth stratospheric levels (e.g., Anderson, 1987, see Section 5.5.2), 10 NIRSpec prism transits could provide an initial indication of O_3 in TRAPPIST-1 d.

As performed in the CO_2-rich case, we investigate the effect of a cloud deck at 0.1 bar and 1 mbar on the estimates above. As shown in Figure 36, the presence of a cloud deck results in weaker or no chemical detections. Nonetheless, the retrieved cloud parameters are mostly consistent with the input cloudy models, with the 1 mbar case retrieving $\phi_{\text{clouds}} = 0.89^{+0.07}_{-0.12}$ and $\log_{10}(P_{\text{cloud}}) = -4.62^{+1.07}_{-0.87}$. In agreement with the CO_2-rich case, and as expected, this N_2-rich case suggests that a cloudy atmosphere is more difficult to characterize than a clear atmosphere.

The number of transits with JWST required for the chemical characterization of rocky exoplanets can vary depending on the system parameters, the instrument of choice, and the desired precision on the retrieved atmospheric properties. As such, our result of 10 JWST-NIRSpec transits is specific to the cases considered here. We discuss additional considerations that could revise these results as well as future considerations in Section 5.5.2.

5.5 SUMMARY AND DISCUSSION

In this chapter, we have validated Aurora's Bayesian retrieval framework using up-to-date existing observations of the hot Jupiter HD 209458 b and the mini Neptune K2-18b. We further validate Aurora's retrieval framework using HST/STIS and JWST-NIRSpec synthetic observations for K2-18b, and JWST-NIRSpec synthetic observations for the rocky exoplanet TRAPPIST-1 d. Our results highlight four findings:

- For hot Jupiters, the retrieved parameter estimates are robust against assumptions of a H-rich atmosphere or not. The cloud and haze prescription introduced in this dissertation results in a higher model evidence than previous inhomogeneous cloud and haze prescriptions when applied to current observations of the well-studied hot Jupiter HD 209458 b.

- For current observations of mini Neptunes, we have demonstrated that the atmosphere of K2-18b is H rich. Furthermore, the different nested sampling algorithms included in Aurora retrieve almost

identical parameter estimates. The retrieved properties of K2-18b are consistent with previous results.

- For future observations of mini Neptunes with JWST, abundance estimates could result in precisions of $\sim$ 0.5 dex or better. Abundance estimates obtained with JWST observations can be robust even in the absence of observations in the optical wavelengths, for relatively low cloud/haze covers as for the case of K2-18b.

- For future observations of rocky exoplanets, Aurora can robustly identify their dominant atmospheric composition as well as reliably detect and constrain the abundance of trace gases. For example, 10 JWST transits of TRAPPIST-1 d could enable clear detections and abundance constraints of H_2O in a cloud-free, N_2-rich or CO_2-rich atmosphere. Furthermore, 10 JWST transits could enable initial indications of O_3 if present at enhanced levels ($\sim$ 10$\times$–100$\times$ present-day Earth's stratospheric abundances) in a cloud-free N_2-rich atmosphere.

We discuss the implications of our results for the analysis of current and future observations of hot Jupiters, mini Neptunes and rocky exoplanets.

5.5.1 *Constraining the Composition of Mini Neptunes*

Recent spectroscopic observations (e.g., Benneke et al., 2019b,c; Tsiaras et al., 2019) have demonstrated that mini Neptunes are advantageous targets in the search of H_2O vapor and other possible molecular features in low-mass exoplanets. The lack of an analog for this type of planet in our solar system represents a unique opportunity to learn about the diversity of planet configurations and compositions. Straddling the gap between terrestrial planets and ice giants, it is not always clear whether the atmospheres of some of these planets are H rich or not. Similar to our approach in Section 5.3.1, we suggest that the interpretation of future observations of mini Neptunes and possible super-Earths should begin by not assuming a bulk atmospheric composition. One should perform an agnostic retrieval first, and retrieve the main atmospheric constituent. Then, and if the data suggests the planet's atmosphere is H-rich, a second retrieval assuming an H-rich atmospheric composition could be informative and should be performed. In this context, the two retrieval approaches should be seen as complementary and informative.

Considerations about the presence of clouds and hazes in these mini Neptunes remain to be explored. The possible absence of clouds in the observable atmosphere of temperate planets like K2-18b, as presented here and in agreement with previous studies (e.g., Welbanks et al., 2019; Madhusudhan et al., 2020, Chapter 3 and Chapter 7), represents a surprise when compared to hotter cloudy planets like GJ 1214b (Kreidberg et al., 2014a). On the other hand, the possibility of Mie-scattering clouds as recently argued in the atmosphere of GJ 3470b (Benneke et al., 2019b) could indicate a complex diversity in the presence of condensates in this type of planets.

Future studies could investigate the need for more complex cloud and haze models in retrievals when interpreting observations of mini Neptunes. For instance, while Benneke et al. (2019b) develop and implement a new Mie-scattering cloud parameterization for atmospheric retrievals in order to explain the observations of GJ 3470b, Welbanks et al. (2019, Chapter 3) explain the same observations without invoking Mie scattering and implementing previous prescriptions for inhomogeneous clouds and hazes. Investigating the performance of those cloud prescriptions and the one introduced here could elucidate whether the apparent drop in transit depth in the spectrophotometric observations of GJ 3470b indeed requires invoking Mie-scattering particles. Furthermore, incorporating the Mie scattering module available in Aurora into its retrieval framework could provide further insights into the atmospheric nature of this and other planets. Likewise, future studies may investigate how the limitations of previous inhomogeneous cloud and haze prescriptions unveiled in this dissertation affect recent studies that investigate the influence of cloud model choices on retrieval solutions (e.g., Barstow, 2020). A full exploration of the different degeneracies and biases in different prescriptions for the clouds and hazes will be key in refining future parametric prescriptions and part of the future outlook described in Chapter 8.

Nonetheless, in order to robustly constrain the presence and properties of clouds and hazes, spectroscopic observations in the optical wavelengths are essential (e.g., Line & Parmentier, 2016; Welbanks & Madhusudhan, 2019, Chapter 2). While the results in Section 5.3.2 suggest that state-of-the-art spectroscopic observations in the optical with HST/STIS may not be precise enough to robustly constrain the properties of cloud and hazes for the marginal cloud/haze cover in our K2-18b test case, achievable constraints with HST/STIS for instances with enhanced cloud and haze cover and for other mini Neptunes remain to be

explored. Future studies could also explore constraints on the properties of clouds and hazes using observations from multiple instruments on JWST, HST, and ground-based facilities.

5.5.2 *Constraining the Composition of Rocky Exoplanets*

Constraining the chemical composition of rocky exoplanets with heavy mean molecular weight atmospheres needs dedicated observational efforts. Exploratory studies using synthetic observations, as performed here and other studies discussed below, can inform the requirements for future observational campaigns. On the number of transits required for the characterization of a TRAPPIST-1 d-like planet, our results are broadly consistent with previous studies of the TRAPPIST-1 planets (e.g., Morley et al., 2017; Batalha et al., 2018; Krissansen-Totton et al., 2018; Lustig-Yaeger et al., 2019; Wunderlich et al., 2019).

For instance, Batalha et al. (2018), using models for TRAPPIST-1 f that consider the presence of a gray cloud deck and an information-content-based approach (Batalha & Line, 2017), find that the NIRSpec prism could detect and constrain the dominant atmospheric absorber in H_2O-rich and CO_2-rich atmospheres of rocky exoplanets by the 10th transit to uncertainties smaller than 0.5 dex. Batalha et al. (2018) argue that if the dominant absorber has not been observed by the 10th transit it is unlikely that more transits could provide more information. Naturally, our suggestion of characterizing a rocky exoplanet using 10 JWST transits is valid only if a featureless spectrum has been ruled out using the first few transits.

If not pursuing a robust chemical characterization, a fewer number of transits could help identify spectroscopic features and reject a featureless spectrum. Our results broadly agree with the study of Lustig-Yaeger et al. (2019), who find that two NIRSpec prism transits are enough to rule out a featureless spectrum for TRAPPIST-1 d, although they use a signal-to-noise metric and we use a Bayesian detection significance metric. Additionally, Lustig-Yaeger et al. (2019) employ atmospheric models from Lincowski et al. (2018) considering self-consistent atmospheric compositions and find that CO_2 could be weakly detected in TRAPPIST-1 d using one transit of the JWST-NIRSpec prism in a variety of O_2- and CO_2-rich atmospheres. While based on simpler atmospheric models and limited to the CO_2-rich composition, our results suggest that for a cloud-free atmosphere, two transits of JWST-NIRSpec prism may suffice

to provide initial detections ($\sim 2\sigma$) of the main atmospheric component in TRAPPIST-1 d.

Nevertheless, our results are limited to the specific model considerations we have investigated. Modifying our model assumptions of a cloud-free atmosphere, a limited number of absorbers, lack of stellar contamination, isothermal temperature profile, among others, could result in a larger number of transits required for the desired atmospheric constraints. For instance, using more complex general circulation models, Komacek et al. (2020) demonstrate that $\sim$ 10 NIRSpec prism transits would be required to detect H_2O vapor in the atmosphere of a terrestrial-size exoplanet orbiting a late-type M dwarf when ignoring the effect of clouds and using a similar signal-to-noise metric to Lustig-Yaeger et al. (2019). This result is broadly consistent with our estimate and that of other studies (e.g., Batalha et al., 2018). However, when the effect of clouds is considered, Komacek et al. (2020) find that 63 or more transits are required to detect water. Their results, and our exploration of cloudy models in CO_2-rich and N_2-rich atmospheres, suggest that the presence of clouds may significantly increase the number of transits required to detect water features.

Similarly, considering the effect of stellar contamination could significantly affect our interpretations. Recently, Rackham et al. (2018) argue that the stellar contamination impact in the transmission spectra of the TRAPPIST-1 planets can be comparable to or larger than the signal produced by an atmospheric feature. In that case, not accounting for stellar contamination could result in a false positive and be a limiting factor in obtaining reliable abundance constraints. Future studies could investigate the effect of stellar contamination in retrievals (e.g., as in Pinhas et al., 2018) for super-Earths/mini Neptunes using the stellar heterogeneity module included in Aurora and revisit our reported estimates.

Furthermore, considering more complex atmospheric compositions with multiple absorbers as investigated by Morley et al. (2017) could better inform our estimates. In their study, Morley et al. (2017) use radiative-convective models of the TRAPPIST-1 planets assuming Earth-like, Venus-like, and Titan-like atmospheres to determine the number of NIRSpec/NIRISS transit observations required to rule out a flat spectrum at $\sim 5\sigma$ confidence. Their results suggest that as few as 13 transits could rule out a flat spectrum for a Venus-like atmospheric composition on TRAPPIST-1 d. While our results seem to be broadly consistent with those of Morley et al. (2017), albeit more optimistic, the impact of

non-isothermal profiles and other chemical compositions on our results remains to be investigated.

Lastly, the number of transits required for characterizing H_2O and CO_2 may not be representative of the requirements for detecting and characterizing other chemical species, including possible biosignatures. For instance, Barstow & Irwin (2016) investigate the number of transits required to detect O_3 in the atmosphere of TRAPPIST-1 d. Their study assumes atmospheric chemistry identical to Earth's present-day atmosphere and employs an optimal estimation retrieval algorithm with isothermal models with clouds deep in the atmosphere where they do not have a significant effect on the spectrum. Their results suggest that present-day Earth levels of O_3 would be detectable with 30 transits of NIRSpec prism and MIRI Low-Resolution Spectrometer. Our results suggest that 10 transits of TRAPPIST-1 d with NIRSpec prism could provide initial indications of O_3 in a N_2-rich cloud-free atmosphere if present at enhanced abundances ($\sim 10\times$–$100\times$ present-day stratospheric Earth levels, e.g., Anderson, 1987; Barstow et al., 2016b; Barstow & Irwin, 2016). Future studies using Aurora could further investigate the requirements for the detection and robust characterization of O_3 and other possible biosignatures (e.g., Krissansen-Totton et al., 2018; Wunderlich et al., 2019).

The characterization of rocky exoplanets with JWST remains an attractive avenue in the search for atmospheric features in habitable zone planets and the search for possible biosignatures. Although our results indicate that precise abundance constraints will be possible with the upcoming generation of telescopes, several outstanding considerations mentioned above need to be explored. Particularly, the presence of clouds, hazes, and stellar contamination may present a significant hindrance in the characterization of rocky exoplanets. If true, temperate cloud-free sub-Neptunes like K2-18b may be the best targets for atmospheric characterization of low-mass exoplanets.

5.5.3 *On Multidimensional Effects*

Modeling the presence of inhomogeneities in the atmospheric properties of a planet requires models beyond one-dimensional considerations. Depending on their degree of inhomogeneity, these irregularities can potentially affect the retrieved atmospheric properties. For instance, in this chapter, we have explored how inhomogeneities in cloud and haze cover affect the retrieved chemical abundances when assuming or not

a H-rich atmosphere. Aurora currently employs a combination of one-dimensional models to capture the multidimensional effect of inhomogeneous cloud and haze cover. Nonetheless, other heterogeneities and their multidimensional nature can also affect the retrieved atmospheric properties. Recent studies have explored possible limitations of one-dimensional retrievals in the context of transmission spectroscopy (e.g., Changeat et al., 2019; MacDonald et al., 2020; Pluriel et al., 2020).

For instance, compositional differences in the atmospheric chemistry of exoplanets are an effect largely expected for ultra-hot Jupiters (UHJs) with day-side temperatures $\gtrsim$ 2200 K (e.g., Arcangeli et al., 2018; Parmentier et al., 2018; Baxter et al., 2020). These highly irradiated, tidally locked planets, can exhibit large contrasts between the atmospheric temperature of their day side and their night side, which in turn can result in strong variations in their atmospheric composition. Retrievals of UHJs should not assume a homogeneous chemical composition or temperature structure. Aurora's retrieval framework is currently designed for planets without strong temperature inhomogeneities across the terminator (e.g., low or moderately irradiated planets). However, we have designed Aurora with the implementation of multidimensional effects in mind.

Our current retrieval framework can be readily generalized to incorporate multidimensional P–T profiles and nonuniform mixing ratios, just as we have done for clouds and hazes. The inclusion of new nested sampling algorithms, optimized for the treatment of high-dimensional parameter spaces and highly degenerate solutions, aids our retrieval framework in these future developments. Future works can expand the current retrieval framework to consider the effects necessary for the appropriate study of UHJs. Nevertheless, these considerations are not imperative for the planets considered in this study where large compositional/temperature gradients between the day side and night side of a planet are not expected.

5.5.4 *Concluding Remarks*

Currently, over 50 transiting exoplanets have been observed with transmission spectroscopy and nearly 20 chemical species have been detected in exoplanetary atmospheres (e.g., Madhusudhan, 2019). While observations of hot gas giants with H-rich atmospheres have been the most abundant, advancements in observing facilities (e.g., Gillon et al., 2011, 2017), large observing campaigns (e.g., Kreidberg et al., 2014a; Benneke

et al., 2019c), as well as the so-called M-dwarf opportunity (e.g., Charbonneau & Deming, 2007; Scalo et al., 2007) have allowed for tantalizing transmission spectra of mini Neptunes and super-Earths. The imminent launch of JWST and the continuous observing efforts with HST and ground facilities promise to reveal many more spectra of transiting exoplanets, including the prospect of spectral features in non-H-rich atmospheres. From hot Jupiters to temperate low-mass exoplanets, their spectra could provide further insights into their formation paths, possible trends in compositions, and maybe even their prospects for habitability. It is in this context that retrieval capabilities like Aurora could play an important role in the accurate interpretation of spectroscopic observations.

6

CHARACTERIZATION OF EXOPLANET ATMOSPHERES WITH GROUND-BASED FACILITIES

As previously mentioned throughout this dissertation, state of the art instruments have enabled high quality spectroscopic observations of transiting exoplanets with ground-based facilities. These spectroscopic observations, mostly in the optical wavelengths, allow for inferences on the presence of multiple alkali species such as Na and K, and important molecules for our understanding of thermal inversions (e.g., Hubeny et al., 2003; Fortney et al., 2008; Spiegel et al., 2009; Gandhi & Madhusudhan, 2019; Piette & Madhusudhan, 2020) such as TiO and VO. Additionally, these observations can provide important constraints on the presence of clouds and hazes. As demonstrated in Chapter 2, high-precision optical spectra are key for providing joint constraints on the presence of clouds, hazes, and chemical abundances. The power of ground-based observations has recently allowed for inferences of cloud free atmospheres with broad absorption signatures from alkali metals, complementary wavelength coverage to those obtained with space-based facilities such as the Hubble Space Telescope (HST), and suggestions of metal oxides in the atmospheres of these alien worlds (e.g., Nikolov et al., 2016; Kirk et al., 2019; Sedaghati et al., 2017).

With that landscape in mind, here we look into the atmospheric characterization of exoplanets using ground-based facilities. This chapter[1] presents part of the collaborative work we have contributed to by performing data interpretations using atmospheric retrievals. We present the atmospheric retrieval on the transmission spectra of WASP-127b in Section 6.2, WASP-33b in Section 6.3, and WASP-21b in Section 6.4. The observations presented in this chapter were obtained with the OSIRIS spectrograph mounted at the 10 m Gran Telescopio Canarias (GTC); although the case of WASP-127b includes re-analyzed spectra obtained with the 2.5 m Nordic Optical Telescope (NOT). The contents of this

1 The contents of this chapter are based on the published work of Chen et al. (2018); von Essen et al. (2019) and Chen et al. (2020). As explained in Section 6.1 the retrieval framework used in this work is an adaptation of AURA (Pinhas et al., 2018) and HyDRA (Gandhi & Madhusudhan, 2018) developed in Prof. Nikku Madhusudhan's research group. The data analysis and reduction that produced the spectra interpreted in this chapter was conducted by the co-authors in the respective published works. These co-authors additionally contributed to the manuscript and figure preparation for the manuscripts from which this chapter is based.

chapter are based on the published works of Chen et al. (2018); von Essen et al. (2019) and Chen et al. (2020).

An important distinction is that, while the retrieval analysis for WASP-127b and WASP-33b has already been presented in Chapter 3 as part of the homogeneous analysis of transmission spectra, the work presented in this chapter corresponds to the initial interpretation of the observed spectra and the possible indications of previously unidentified chemical species in these exoplanetary atmospheres. Notably, the results presented here suggest the presence of lithium (Li) in WASP-127b, aluminum oxide (AlO) in WASP-33b, and Na in WASP-21b. If these chemical indications are confirmed by subsequent studies, the works summarized here add to the rapidly growing chemical diversity in exoplanet atmospheres. On the other hand, if future observations render these initial indications inaccurate, the works in this chapter may highlight the importance of obtaining exoplanetary spectra in overlapping and complementary wavelengths (e.g., Sedaghati et al., 2017; Espinoza et al., 2019; Sedaghati et al., 2021). In what follows, we present the method for our retrieval analysis and the retrieved atmospheric properties of WASP-127b, WASP-33b, and WASP-21b. We summarize our findings and discuss their implications in Section 6.5.

6.1 ATMOSPHERIC RETRIEVAL CONFIGURATION

To infer the atmospheric properties at the day-night terminator region of WASP-127b, WASP-33b, and WASP-21b, we performed a spectral retrieval modeling on their transmission spectrum. The retrieval framework employed is an adaptation of the AURA atmospheric retrieval framework for transmission spectra (Pinhas et al., 2019), which is a derivative of the HyDRA atmospheric retrieval framework for emission spectra (Gandhi & Madhusudhan, 2018)[2]. The employed framework computes line-by-line radiative transfer in a transmission geometry assuming a plane parallel planetary atmosphere in hydrostatic equilibrium. Our model retrieves the pressure-temperature (P–T) profile of the atmosphere utilizing the six-parameter prescription of Madhusudhan & Seager (2009) in an atmosphere that spans from 10^2 to 10^{-6} bar in pressure. The model also considers the reference pressure (P_{ref}) as a free parameter, which is the pressure at an assumed radius R_p.

2 For clarity, we emphasize that we did not perform the retrieval analysis using Aurora, the framework introduced in Chapter 4 and Chapter 5.

In the retrieval framework, the volumetric mixing ratios of the chemical species in the atmosphere are free parameters and assumed to be constant. We consider absorption due to molecules and atomic species that could be present in hot Jupiter atmospheres (Madhusudhan et al., 2016). The chemical opacity sources considered in these works include:

- For all planets: H_2-H_2 and H_2-He collision induced absorption (CIA; Richard et al., 2012), CH_4 (Yurchenko & Tennyson, 2014), CO (Rothman et al., 2010), CO_2 (Rothman et al., 2010), H_2O (Rothman et al., 2010), NH_3 (Yurchenko et al., 2011), TiO (Schwenke, 1998), and AlO (Patrascu et al., 2015).
- Additional sources for WASP-127b: FeH (Dulick et al., 2003; Hargreaves et al., 2010; Wende et al., 2010), TiH (Burrows et al., 2005), CrH (Bauschlicher et al., 2001), Na, K, Li, V and Fe (Kramida et al., 2018).
- Additional sources for WASP-33b: VO (McKemmish et al., 2016), FeH (Dulick et al., 2003; Hargreaves et al., 2010; Wende et al., 2010), TiH (Burrows et al., 2005), CrH (Bauschlicher et al., 2001), Na and K (Kramida et al., 2018).
- Additional sources for WASP-21b: VO (McKemmish et al., 2016), HCN (Barber et al., 2014), K (Allard et al., 2016), and Na (Allard et al., 2019).

The opacities for the chemical species were computed following the methods of Gandhi & Madhusudhan (2017), with the updated values of Gandhi & Madhusudhan (2018) if available at the time of preparing the manuscripts upon which this chapter is based. Likewise, the use of H_2-broadened Na and K cross sections (e.g., as in the case of WASP-21b) is the result of these sources of opacity becoming available at the time of preparing the associated manuscript (Chen et al., 2020). The H_2-broadened Na and K cross sections were computed following the method described in Chapter 3.

Our models consider the possibility of inhomogeneous cloud and haze cover using the parametrization of MacDonald & Madhusudhan (2017a). The model considers cloudy regions of the atmosphere to consist of an opaque cloud deck with a cloud top pressure P_{cloud} in units of bar and scattering due to hazes above the clouds. In the parametrization, hazes are included as $\sigma = a\sigma_0(\lambda/\lambda_0)^{\gamma}$, where γ is the scattering slope, a is the Rayleigh-enhancement factor, and σ_0 is the H_2 Rayleigh scattering cross section (i.e., 5.31×10^{-31} m^2) at a reference wavelength

(i.e., $\lambda_0 = 350$ nm). The inhomogeneous clouds and scattering hazes are included through the parameter $\bar{\phi}$, which is the cloud/haze fraction cover in the planet's atmosphere. The retrieval framework allows for the possibility of a flat spectrum (e.g., due to weak gaseous absorption and/or a gray homogeneous cloud cover) in the explored parameter space. The Bayesian inference and parameter estimation is conducted using the nested sampling algorithm implemented via the MultiNest application (Feroz et al., 2009) through the Python interface PyMultiNest (Buchner et al., 2014).

6.2 THE EXTREMELY INFLATED SUB-SATURN-MASS EXOPLANET WASP-127B

WASP-127b is one of the rare short-period super-Neptunes in the transition gap from Jupiter-mass to Neptune-mass (Mazeh et al., 2016), and the characterization of its atmosphere could help understand its formation mechanisms. It has a mass of 0.18 ± 0.02 M_J and a radius of 1.37 ± 0.04 R_J, and orbits a G5 star every 4.17 days (Lam et al., 2017). Its large atmospheric scale height $H_{eq} = kT/(\mu g) \approx 2365$ km (assuming $T_{eq} = 1400$ K, $\mu = 2.3$ amu, $g_p = 2.14$ m s^{-1}), together with its bright host star ($V = 10.2$), makes it one of the most ideal targets for atmospheric characterization. Palle et al. (2017) studied its atmosphere via transmission spectroscopy with the ALFOSC spectrograph at the 2.5 m Nordic Optical Telescope (NOT), and found evidences of a Rayleigh scattering slope at the blue optical, a hint of Na absorption, and a spectroscopic signal attributed to TiO/VO absorption.

6.2.1 *Observations*

One transit of WASP-127b was observed on the night of January 19, 2018 with the OSIRIS spectrograph (Sánchez et al., 2012) at the GTC. The observation lasted from 00 : 26 UT to 07 : 16 UT, while the morning twilight started at 06 : 42 UT. For a detailed description of the data reduction and light curve analysis, elements beyond the scope of this dissertation, we refer the reader to Chen et al. (2017).

6.2.2 *Retrieved Atmospheric Properties*

The optical transmission spectrum of WASP-127b provides strong constraints on its atmospheric composition. We report the detection of K at a

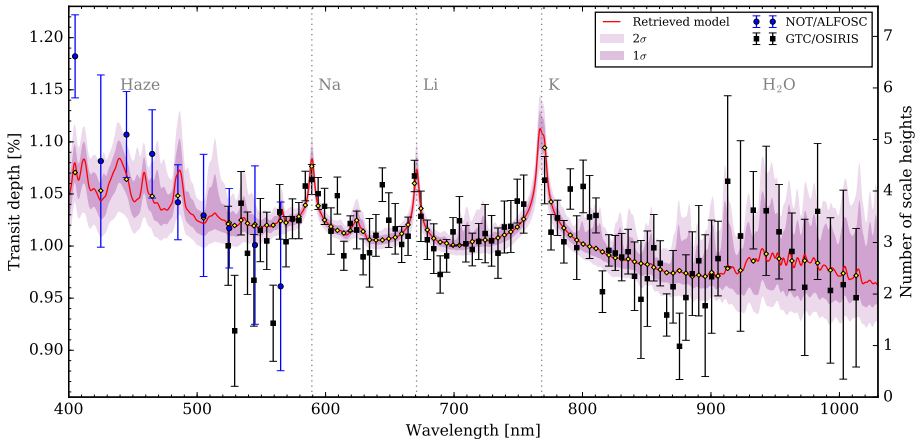

Figure 39 WASP-127b's transmission spectrum and retrieved models. The blue circles and black squares with error bars are the observed spectrum by NOT/ALFOSC and GTC/OSIRIS, respectively. It shows an enhanced slope at the blue-optical, strong absorption peaks at 589.3 nm, 670.8 nm, and 768.2 nm, and another bump at the red-optical. These features can be explained by the model spectrum when including opacities resulting from haze, Na, Li, K, and H_2O, respectively. The red curve shows the retrieved median model while the shaded areas show the 1σ and 2σ confidence regions. The yellow diamonds show the binned version for the retrieved median model.

confidence level of 5.0σ, Na at 4.1σ, and Li at 3.4σ in the spectrum along with an indication of H_2O (see Table 5 for the Bayesian model comparison). Figure 39 shows the best-fit spectrum to the data along with the significance contours. The models without Na, K, or Li fail to explain the peaks in absorption at $\sim$ 589.3 nm, $\sim$ 670.8 nm, and $\sim$ 768.2 nm. We do not have statistically significant detections of any other chemical species considered in the model.

We retrieved atomic volume mixing ratios of $\log_{10}(X_{Na}) = -3.17^{+1.03}_{-1.46}$, $\log_{10}(X_K) = -2.13^{+0.85}_{-1.32}$, and $\log_{10}(X_{Li}) = -3.17^{+0.97}_{-1.51}$ for Na, K, and Li, respectively. The retrieved Na, K, and Li abundances are super-solar (Asplund et al., 2009). The retrieved Li abundance is also significantly higher than the super-solar value of the host star ($\log_{10}(X_{Li}) = -10.03$; Lam et al., 2017). We verified that the retrieved volume mixing ratios remain consistent within the 1σ error bar even if the reference planet radius is a free parameter instead of assumed as $R_p = 1.37\ R_{Jup}$, consistent with the findings presented in Chapter 2. The retrieved haze is $\sim$ 8500–250000$\times$ (68.3% confidence interval) stronger than H_2 Rayleigh scattering, has a coverage of $\phi = 52^{+10}_{-9}\%$, and a power-law exponent of $\gamma = -7.36^{+2.33}_{-2.56}$. The P–T profile is relatively unconstrained by the data (see Figure 40).

Table 5 Bayesian Model Comparison for WASP-127b. Detections of Atmospheric Compositions at the Terminator of WASP-127b

Model	Evidence $\ln(\mathcal{Z})$	Bayes factor $\mathcal{B}_{0i}$	Detection of Ref.
Reference	619.0	Ref.	Ref.
No K	608.1	54838.7	5.0σ
No Na	612.1	1008.3	4.1σ
No Li	614.6	79.6	3.4σ
No H_2O	617.8	3.4	2.1σ

The posterior distributions for the retrieval of WASP-127b are shown in Appendix D, Figure 58.

Our models also considered the presence of H_2O in the atmosphere of the planet. Although the spectral shape in the wavelength range 833–1018 nm resembles an H_2O feature, the current error in the data within 900–1018 nm is relatively large and does not constrain the abundance of H_2O in the global atmospheric retrieval. We find a nominal H_2O signature with a relatively weak abundance constraint of $\log_{10}(H_2O) = -2.60^{+0.94}_{-4.56}$, which can be confirmed with HST near-infrared spectroscopy in the near term, and with James Webb Space Telescope (JWST) in the future.

6.3 THE HIGHLY IRRADIATED HOT JUPITER EXOPLANET WASP-33B

WASP-33b (Collier Cameron et al., 2010) orbits an A-type star with a period of ~ 1.22 days, making it one of the strongest irradiated planets known till date (Smith et al., 2011; von Essen et al., 2015). Lehmann et al. (2015) carried out a spectroscopic follow-up of the host star, characterizing the mass of the planet to be around 2.1 M_J. WASP-33b shows an unusually large radius (~ 1.6 R_J), making it inflated (Collier Cameron et al., 2010) and ideal for transmission spectroscopy studies. Considering the reported equilibrium temperature for the planet of $T_{eq.} \sim 2700$ K (e.g., Smith et al., 2011, see also Chapter 3), and assuming $\mu = 2.3$ amu and $g_p \sim 29$ m s^{-1} (e.g., Nugroho et al., 2017), WASP-33b has a scale height of $H_{eq} \approx 336$ km. Below we present the results of performing a retrieval analysis on the optical spectrum of WASP-33b.

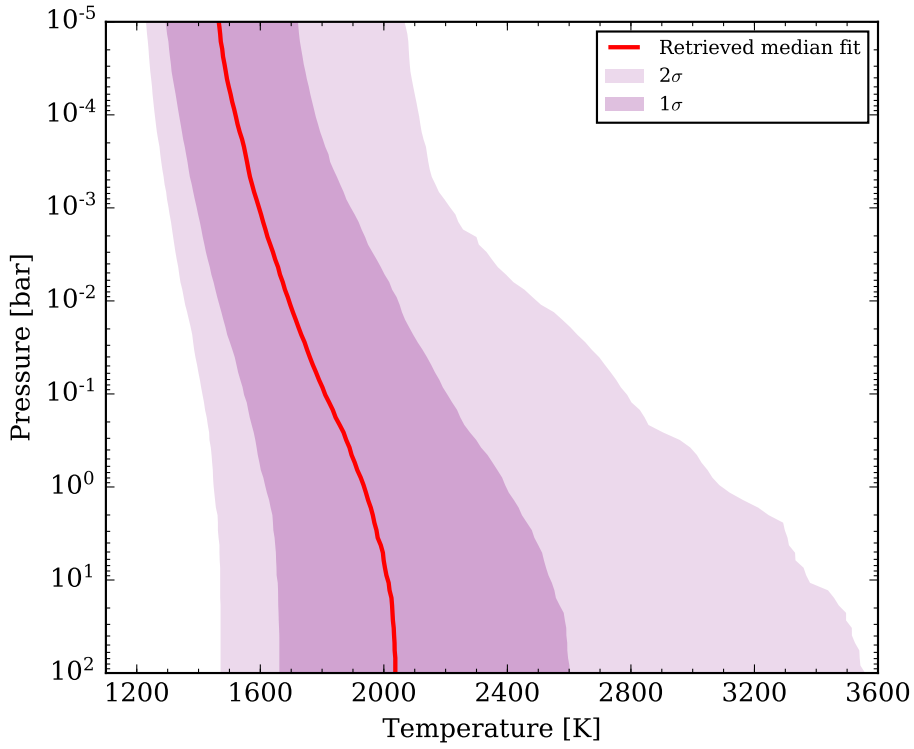

Figure 40 WASP-127b's retrieved P–T profile. The shaded areas show the 1σ and 2σ confidence regions.

6.3.1 *Observations*

The spectra in this work are the result of a search for oxides and clouds/-hazes at the terminator region of the atmosphere of WASP-33b by transmission spectroscopy in the optical. We exploit two transit observations taken 18 orbits apart with the 10 meter GTC. The observations occurred on the nights of August 7 (henceforth observing run 1, OR1) and August 30 (observing run 2, OR2), 2014. The observations were taken using the OSIRIS spectrograph. A complete description of the data acquisition and reduction is available in von Essen et al. (2019).

6.3.2 *Retrieved Atmospheric Properties*

The analysis of the transmission spectrum of WASP-33b provides initial constraints on its atmospheric composition. Figure 41 shows the retrieved median fit to the observations along with the 1σ and 2σ confidence contours. In particular, we report a possible detection of AlO at 3.3σ significance as shown in Table 6. We retrieve a volume mixing ratio of $\log_{10}(X_{AlO}) = -4.58^{+0.67}_{-0.79}$ for AlO. Although we do not

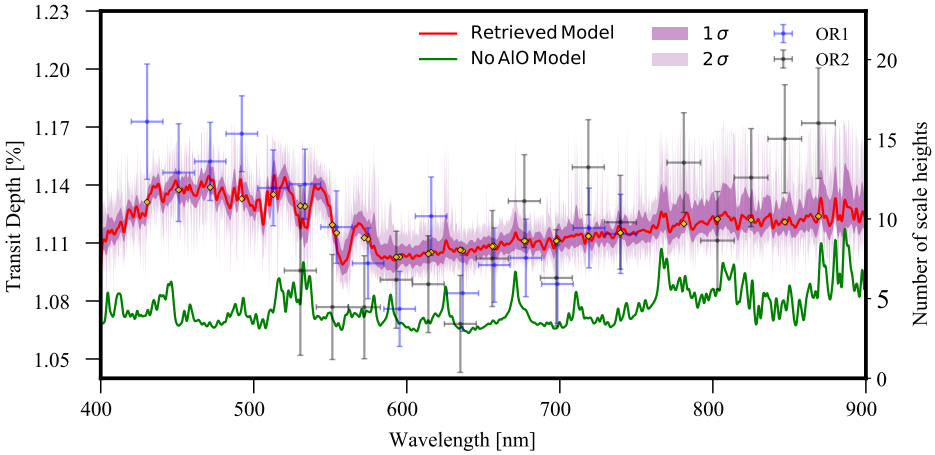

Figure 41 Transmission spectrum of WASP-33b and retrieved models. The blue and black circles represent transit depths from OR1 and OR2, respectively. Horizontal lines indicate the size of the wavelength bin. Error bars are at the 1σ level. The red curve shows the retrieved median model and the 1σ and 2σ confidence envelopes are shown by the shaded regions. The gold diamonds are the binned median model at the same resolution as the data. The spectrum shows a feature from ~ 450–550 nm that is explained by the model spectrum including AlO.

find statistically significant evidence for the other species considered in our retrieval, the upper limits at the 99 percentile for TiO and VO are $\log_{10}(X_{TiO}) = -7.52$ and $\log_{10}(X_{VO}) = -6.74$. Although H_2O was considered in our models, the long-wavelength data do not show any features corresponding to H_2O absorption. Models without AlO fail to explain the features from 450–550 nm, as can be seen in Figure 41.

We use Bayesian model comparisons to evaluate the detection significance of AlO as shown in Table 6. We find that our full 28-parameter model with AlO is preferred over a 27-parameter model without AlO at a 3.3σ significance. We also investigate fits to the data with a featureless spectrum represented by a constant transit depth, i.e., a 1-parameter flat line model, using MultiNest. We find that the full 28-parameter model is preferred over the 1-parameter flat spectrum model at 4.2σ significance. We present the Bayesian evidence and model comparisons in Table 6.

The retrieved P–T profile is shown in Figure 42. We obtain a relatively unconstrained profile consistent with the equilibrium temperature of $T_{eq.} \sim 2700$ K, reported in Smith et al. (2011), within the 2σ region. The retrieved median fit for the P–T profile varies from ~ 3200 K at the top of the atmosphere to ~ 3600 K at the 1 bar surface. The retrieved P–T profile is also consistent with the average day-side brightness temperature of 3144 ± 114 K in the near-infrared reported in Zhang

Table 6 Bayesian Model Comparison for WASP-33b. Detections of Atmospheric Compositions at the Terminator of WASP-33b.

Model	Evidence $\ln(\mathcal{Z})$	Bayes factor $\mathcal{B}_{0i}$	Detection of Ref.
Reference	215.1	Ref.	Ref.
No AlO	211.3	46.7	3.28σ
Flat line model	208.0	1232.3	4.18σ
No hazes/clouds	215.8	0.5	N/A

et al. (2018). Transmission spectra probe the day-night terminator region, sampling temperatures of both the day side and night side of the atmosphere. Furthermore, transmission spectra in the optical probe higher regions in the atmosphere than emission spectra. If WASP-33b has a thermal inversion (e.g., Haynes et al., 2015) it is conceivable that the upper atmosphere probed by a transmission spectrum may be comparable in temperature to that of the day-side photosphere reported by Zhang et al. (2018). Our model considers the presence of clouds and hazes in the atmosphere of WASP-33b. However, the data does not constrain the cloud/haze properties of the planet. The data in the optical wavelengths lacks features indicative of a scattering slope. We performed a retrieval test for a clear atmosphere and the molecular abundances remained unchanged. A clear atmosphere is consistent with studies showing that the condensation temperatures of expected cloud and haze forming species are well below that of WASP-33b (Pinhas & Madhusudhan, 2017; Wakeford et al., 2017b). The posterior distributions for the relevant parameters are shown in Appendix D, Figure 59.

Our detection significance for AlO of 3.3σ represents a conservative limit. Given the large number of model parameters used for completeness in our full retrieval the evidence, and hence the significance, is conservative. In practice, several of the 28 model parameters do not contribute significantly in the observed visible band. Retrieval with a model considering only the parameters that affect the visible spectrum constitute a more meaningful measure of the detection significance. To further test the significance of the AlO detection we consider an additional simplified retrieval. Given that our full retrieval was not able to constrain the cloud properties of WASP-33b or the P–T profile, our simplified model is a clear atmosphere with absorption from TiO and AlO only, and an isothermal temperature profile, i.e, four free parameters. The result-

ing retrieval obtains a log evidence of 217.7. Using this four-parameter model with AlO as our reference in a Bayesian model comparison, we estimate its detection significance relative to models without AlO. We find that the reference model is preferred over a three-parameter model without AlO at 4.7σ significance. Similarly, the reference models is preferred over a one-parameter flat line model at 4.8σ significance. Although this analysis suggests that our detection of AlO is at a confidence level higher than 3.3σ, we still adopt the more conservative detection significance obtained using the full 28-parameter model.

Our retrieved AlO abundance constrains the Al/H ratio in the atmosphere. The volume mixing ratio of $\log_{10}(X_{AlO}) = -4.58^{+0.67}_{-0.79}$ corresponds to an abundance of $\log_{10}(AlO/H) = -4.81^{+0.67}_{-0.79}$. Assuming all the Al is contained in AlO, our derived estimate of Al/H is consistent with a solar value of $\log_{10}(Al/H) = -5.55 \pm 0.03$ (Asplund et al., 2009). However, Al can also be present in other refractory species, in which case our derived estimate is a lower limit on the true Al/H abundance in the atmosphere of WASP-33b. In particular, the dominant Al-containing species in a solar-composition atmosphere in equilibrium, at temperatures near 3000 K, include Al and AlH (Woitke et al., 2018). Under such conditions, our retrieved AlO abundance is $\sim 10^3 \times$ higher than that predicted in chemical equilibrium with solar abundances. Future studies may investigate the feasibility of our retrieved abundance of AlO in WASP-33b, possibly due to chemical disequilibrium or other mechanisms. Additionally, future observations may also provide better constraints on the same.

6.4 THE HOT SATURN EXOPLANET WASP-21B

Here we present the retrieval analysis of the low resolution transit observations of the Saturn-mass hot Jupiter WASP-21b. This low-density planet has an equilibrium temperature of $T_{eq} = 1333 \pm 28$ K and a low surface gravity of $g_p = 5.07 \pm 0.35$ m s^{-1} (Bouchy et al., 2010), which could potentially exhibit a transit depth variation of ~ 250 ppm per scale height (i.e., $H_{eq} \approx 950$ km, assuming $\mu = 2.3$ amu), making it a good target for atmospheric characterization via transmission spectroscopy. WASP-21b orbits a G3V thick disc star in a circular orbit every 4.32 days (Bouchy et al., 2010), which is one of the most metal-poor planet hosts ([Fe/H] $= -0.46 \pm 0.11$). Bouchy et al. (2010) observed a single transit with both 1.5 m Cassini Telescope and 1.2 m Calar Alto Telescope, and presented the latest revised physical parameters for the system. They

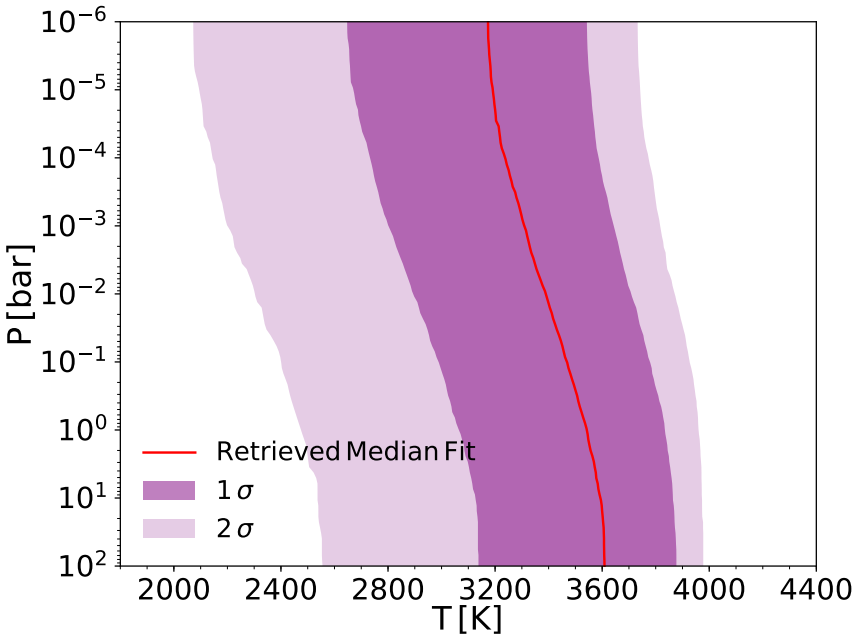

Figure 42 WASP-33b's retrieved P–T profile. The retrieved median profile is shown in red and the 1σ and 2σ confidence intervals are shown as the shaded areas.

derived 0.890 ± 0.079 $M_\odot$ and 1.136 ± 0.051 $R_\odot$ for the host star, and 0.276 ± 0.019 M_J and 1.162 ± 0.054 R_J for the planet.

6.4.1 *Observations*

One transit of WASP-21b was observed on the night of September 11, 2012 (program GTC47-12B, PI: E. Pallé), using the OSIRIS spectrograph at the GTC. The publication from which part of this chapter is taken (e.g., Chen et al., 2020) includes details about the acquisition and analysis of high-resolution spectra for the same planet taken with HARPS-N at the Telescopio Nazionale Galileo, and HARPS at the ESO 3.6 m telescope in La Silla, Chile. Full details about the data reduction and analysis, for both the high and low resolution spectra, are available in Chen et al. (2020).

6.4.2 *Retrieved Atmospheric Properties*

We perform an initial exploratory retrieval considering possible absorption due to all 11 chemical species considered in this work, inhomogeneous cloud and haze cover, and a parametric P–T profile. As expected,

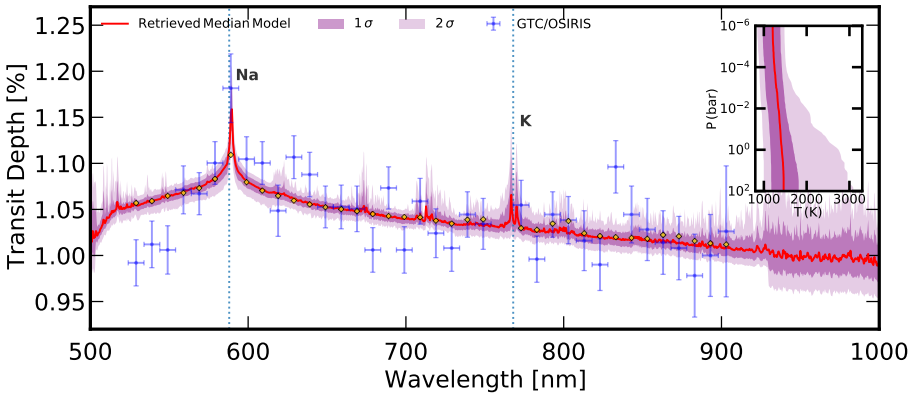

Figure 43 WASP-21b's transmission spectrum and retrieved models. The blue crosses are the error bars and bin width of the observed spectrum by GTC/OSIRIS. It shows a strong absorption peak at ~ 589 nm. This feature is preferentially explained by our retrieval models by including the opacity resulting from Na. We show in an inset the retrieved P–T profile for the data using our fiducial model. The red curve shows the retrieved median model while the purple shaded areas show the 1σ and 2σ confidence regions. The yellow diamonds show the binned version for the retrieved median model.

we find that the only chemical species relatively constrained by the data are those with strong spectroscopic signatures in the optical wavelengths. Therefore we use a fiducial model to consider absorption due to H_2O, Na, K, TiO, AlO and VO only, as well as a parametric P–T profile and inhomogeneous cloud and haze cover. The fiducial model has a total of 17 parameters: 6 chemical abundances, 6 parameters for the P–T profile, 4 parameters for the cloud and haze prescription, and 1 parameter for the reference pressure corresponding to the reference planetary radius of 1.162 R_J

Figure 43 shows the retrieved median model to the observations along with the 1σ and 2σ confidence regions. It also shows in an inset the retrieved P–T profile for the fiducial model. Our results suggest that the features in the spectrum can be explained by the presence of Na in the planet's atmosphere. Using the fiducial model as reference we report a possible detection[3] of Na at a confidence level of 3.5σ. The retrieved Na abundance is $\log_{10}(X_{Na}) = -2.57^{+0.84}_{-1.24}$. Besides Na, K also shows possible spectroscopic signatures at ~ 770 nm. Our models do not exhibit a strong preference for the presence of K in the spectrum of WASP-21b and derive a largely unconstrained abundance of $\log_{10}(X_K) = -7.42^{+2.22}_{-2.65}$. Similarly, the data does not provide strong constraints on the P–T pro-

3 The high-resolution transmission spectrum of WASP-21b further confirms the presence of Na in its atmosphere at higher altitudes (Chen et al., 2020).

Table 7 Bayesian Model Comparison for WASP-21b. Detections of Atmospheric Compositions at the Terminator of WASP-21b.

Model	$\log_{10}(X_{Na})$	Na detection significance	$\log_{10}(X_K)$	$\ln(\mathcal{Z})$
Fiducial	$-2.57^{+0.84}_{-1.24}$	3.5σ	$-7.42^{+2.22}_{-2.65}$	235.79
Simplified	$-3.31^{+1.34}_{-1.77}$	4.9σ	$-7.53^{+2.26}_{-2.80}$	239.12

file or the presence of clouds and hazes in the atmosphere of WASP-21b. The retrieved cloud and haze parameters are unconstrained and consistent with a mostly clear atmosphere, partly due to the lack of features in the data indicating a scattering slope. The P–T profile remains largely unconstrained with a derived temperature at 100 mbar, close to the photosphere, of $T_{100\ mbar} = 1371^{+254}_{-230}$ K consistent with the equilibrium temperature of the planet.

Given that current spectroscopic observations do not place strong constraints on the P–T profile or the presence of clouds and hazes we consider a simplified model retrieval. The simplified model considers absorption due to Na and K only, an isothermal P–T profile, and a clear atmosphere. The simplified model retrieved abundances are $\log_{10}(X_{Na}) = -3.31^{+1.34}_{-1.77}$ and $\log_{10}(X_K) = -7.53^{+2.26}_{-2.80}$, consistent with the fiducial model. The derived Na abundance is marginally consistent with expectations from solar abundance chemistry of $\log_{10}(Na/H) = -5.76$ (Asplund et al., 2009). Similarly, the retrieved temperature for the isotherm is $T = 1224^{+181}_{-208}$ K, consistent with the equilibrium temperature and the derived temperature at 100 mbar in the fiducial model. Using this simplified model as reference, Na is detected at a confidence level of 4.9σ. The posterior distribution for this retrieval is shown in Appendix D, Figure 60 and our retrieval results summarized in Table 7.

6.5 SUMMARY AND DISCUSSION

The spectroscopic observations analyzed in this chapter demonstrate the crucial role of ground-based facilities in providing high quality optical transmission spectroscopy. With these exquisite observations, we can inform our atmospheric models and use reliable retrieval frameworks to derive important constraints on the atmospheric P–T profile of the planet, its atmospheric chemical composition, and the presence of clouds and hazes. By performing a model comparison, we can assess the preference for certain model considerations and assess the possible presence

of different chemical species in these exoplanet atmospheres. While expressing the odds in favor of a more complex model does not necessarily mean the detection of new physics or a species in the spectrum of a planet (see e.g., Section 4.5.2 in Chapter 4), these suggestions can inform future spectroscopic surveys and provide initial insights into exoplanet diversity. Below we discuss and summarize the results for each of the planets in this chapter.

The transmission spectrum of the super-Neptune WASP-127b enabled the inference of a scattering haze at the blue wavelengths, the pressure-broadened spectral profiles of Na, K and Li absorption, and found a hint of water absorption at the red wavelengths. The inferred Na and K abundances are consistent with super-solar values. These spectra were reanalyzed in Chapter 3 considering H_2 broadened Na and K cross sections and the results were found consistent with those presented here. The results presented here for WASP-127b showcase that large-aperture ground-based telescopes could result in high-quality spectroscopy and that is comparable to, or even better than, what HST can do (also see Sedaghati et al., 2017).

Later observations of WASP-127b with HST (Spake et al., 2021) confirmed the Na detection presented in this chapter. Additionally in the near-infrared, Spake et al. (2021) were able to confirm at very high confidence (13.7σ) the suggestions of H_2O in the atmosphere of WASP-127b presented in Chen et al. (2018) and this chapter from an unresolved H_2O absorption feature. While the HST/STIS observations of WASP-127b show absorption due to Na, Spake et al. (2021) did not recover Li or K absorption in the spectrum. The agreement between ground-based and space-based observations in the Na absorption wavelengths, coupled with the apparent disagreement in the K absorption wavelengths, is a conundrum that could be resolved with future spectroscopy and independent data reanalysis.

The retrieval analysis presented in Spake et al. (2021) resulted in super-solar Na and O measured under assumptions of chemical equilibrium. However, when considering a free chemistry model, where uniform volume mixing ratios are treated as free parameters, Spake et al. (2021) instead measured subsolar H_2O and Na abundances. This discrepancy further highlights one of the important lessons from Chapter 3 in which the differing trends in the abundances of species argue against the use of chemical equilibrium models in atmospheric retrievals. Future homogeneous studies, such as the one presented in Chapter 3, could further investigate the derived chemical abundances from the combined ground-

based and space-based transmission spectra of WASP-127b. Additionally, if later confirmed, the detection of Li in the planet atmosphere could open a new window to understand lithium depletion in planet-host stars and an additional tracer into planet formation history (e.g., Bouvier, 2008; Israelian et al., 2009; Baraffe & Chabrier, 2010).

For WASP-33b, the main spectral feature of the optical transmission spectrum analyzed in this chapter is an increase in the planet-star radius ratio blueward of about 560 nm. Spectral absorption features by gaseous AlO have not been reported in the literature of exoplanet observations prior to the work of von Essen et al. (2019), though atmospheric models predict its importance in hot Jupiters (Gandhi & Madhusudhan, 2019). Aluminum compounds such as corundum (i.e., Al_2O_3, the crystaline form of aluminum oxide) have been described as potential condensates forming clouds or hazes in very hot exoplanet atmospheres (e.g., Lodders, 2002; Wakeford et al., 2017b; Pinhas & Madhusudhan, 2017). Subsequent observational efforts have yet to confirm the presence of AlO in the atmosphere of WASP-33b. However, as shown by the detection of TiO (e.g., Nugroho et al., 2017; Cont et al., 2021) and subsequent skepticism on such detection (e.g., Herman et al., 2020; Serindag et al., 2021), confirming the presence of oxides and other chemical species in the atmosphere of WASP-33b will require observations at both high and low resolution for the day side and night side of the planet. More observations of the transmission spectrum of WASP-33b in the visible, both from ground-based facilities (e.g., Sedaghati et al., 2017; Chen et al., 2018) as well as with HST (e.g., Sing et al., 2016), could help improve upon the present constraints.

The retrieval analysis on the transmission spectrum of the Saturn-mass planet WASP-21b reports the detection of Na at a confidence level $> 3.5\sigma$. While a fiducial model leads to a Na detection at 3.5σ significance, a simplified model provides a detection at 4.9σ significance. This detection was confirmed using high resolution spectroscopy in Chen et al. (2020). WASP-21b is an exemplary case in which a chemical detection is simultaneously confirmed using both low and high resolution transmission spectra, demonstrating the potential for both techniques. In low resolution, the retrieved super-solar abundance is consistent with the alkali enrichment observed for other exoplanets in Welbanks et al. (2019) and Chapter 3. Future observations in the optical and the near-infrared could inform if the spectrum of WASP-21b presents absorption features due to other chemical species, and whether the Na enhancement

is accompanied by an O depletion as it is the case with other exoplanets (see e.g., Chapter 3).

In summary, we have shown in this chapter that high quality spectroscopic observations with ground-based facilities offer a unique window into the atmospheres of exoplanets. Their wavelength coverage, usually spanning the optical wavelengths, enables crucial constraints on the chemical composition of exoplanet atmospheres. Particularly, alkali species such as Na and K, and trace species including metal oxides can be initially inferred and their abundances constrained when using robust retrieval frameworks. Recent improvements in ground-based facilities are enabling increasingly higher quality spectra. These high quality data will also necessitate concomitant improvements in the models inevitably employed to infer basic planetary conditions (e.g., Chapter 5). As we look towards the future, ground-based observations alongside those from space-based observatories (e.g., HST and JWST, see also Chapter 7) will provide further constraints on the atmospheric chemical compositions of exoplanets and their formation histories.

7

CHARACTERIZATION OF EXOPLANET ATMOSPHERES WITH SPACE-BASED FACILITIES

The bulk of the spectroscopic observations of exoplanet atmospheres in the near-infrared have been performed using space-based facilities, mostly with the Hubble Space Telescope (HST). Indeed, a new era in transit spectroscopy for exoplanets started after the installation of the Wide Field Camera 3 (WFC3) instrument and the refurbishment of the Space Telescope Imaging Spectrograph (STIS) on HST. Both instruments have spearheaded the characterization of exoplanet atmospheres in the optical and infrared, allowed for chemical detections in tens of exoplanets, and provided us with key observations to constrain the presence of clouds and hazes in these alien worlds (see Chapter 1).

HST WFC3 grisms.
G102: ~ 0.8–1.2 μ*m*
G141: ~ 1.1–1.7 μ*m*
UVIS G280:
~ 0.2–0.8 μ*m.*

WFC3 has provided numerous well-validated indications of the presence of water vapor (e.g., Deming et al., 2013; Huitson et al., 2013; Mandell et al., 2013; Kreidberg et al., 2014b; Sing et al., 2016; Tsiaras et al., 2019; Benneke et al., 2019c), and has opened the field to population studies looking at H_2O abundance and metallicity as a function of stellar and planetary properties (e.g., Madhusudhan et al., 2014b; Sing et al., 2016; Tsiaras et al., 2018; Barstow et al., 2017; Fisher & Heng, 2018; Pinhas et al., 2019, see also Chapter 3). Additionally, the upgraded STIS instrument has been key for detecting the absorption signatures of alkali metals and demonstrating the critical role that clouds and aerosols play in transmission spectra (e.g., Pont et al., 2013; Nikolov et al., 2014; Sing et al., 2016; Carter et al., 2020). Besides HST, the Spitzer Space Telescope with its Infrared Array Camera (IRAC) in its 3.6 and 4.5 μm photometric channels has been key for determining the transit depth of many exoplanets beyond the wavelength limits of HST (e.g., Beaulieu et al., 2008; Désert et al., 2009, 2011a; Baxter et al., 2021), and has enabled tantalizing inferences for what may be signatures of Mie-scattering and absorption due to carbon bearing species in some exoplanet atmospheres (e.g., Benneke et al., 2019b; Spake et al., 2021). Beyond the facilities already mentioned, recent studies have supplemented their observations with photometry from the the Keppler/K2 Space Telescope (~ 0.4–0.9 μm) or the recently launched Transiting Exoplanet Survey Satellite (TESS, ~ 0.6–1.0 μm) to better inform the baseline of their spectra (e.g., Benneke et al., 2019c; Chachan et al., 2020; Spake et al., 2021).

HST STIS gratings.
G430L:
~ 0.3–0.6 μ*m*
G750L:
~ 0.5–1.0 μ*m.*

From hot Jupiters to mini Neptunes, the above space-based observatories have changed the way we think about exoplanet atmospheres. Moreover, at the dawn of what will be a new era for space telescopes with the imminent launch of the James Webb Space Telescope (JWST), existing space-based observatories have been essential to lay the groundwork towards characterization of exoplanets with high-precision spectra. The increasing data quality in recent years demands rigorous and credible atmospheric modeling to maximize the scientific output from these arduous observational efforts. Therefore, exploring the advantages and limitations of our atmospheric models and the inferences they enable is paramount. Moreover, we can begin to explore the influence of instrumental systematics (e.g., instrumental offsets, overestimated data precision) on the inferred atmospheric properties to better analyze current and upcoming data.

In this chapter[1], we present part of the collaborative work we have performed to interpret exoplanetary transmission spectra obtained with space-based facilities using atmospheric retrievals. The contents of this chapter are based on the published works of Madhusudhan et al. (2020); Colón et al. (2020), and Sheppard et al. (2021). We begin this chapter by describing the configuration of our atmospheric retrieval framework in Section 7.1. Then, we present in Section 7.2 the atmospheric retrieval of the transmission spectrum of K2-18b, a temperate mini Neptune. Next, in Section 7.3 we present the atmospheric retrieval of KELT-11b, an inflated sub-Saturn-mass exoplanet with an unusual transmission spectrum. Lastly, we present in Section 7.4 the analysis of the transmission spectrum of HAT-P-41b, a hot Jupiter with what may be a metal-rich atmosphere. We summarize our results and discuss their implications in Section 7.5.

7.1 ATMOSPHERIC RETRIEVAL CONFIGURATION

We analyze the transmission spectra of K2-18b, KELT-11b, and HAT-P-41b using an adaptation of the retrieval code AURA (Pinhas et al., 2018) as described in Chapter 6. Here we briefly recapitulate the characteristics

1 The contents of this chapter are based on the published work of Madhusudhan et al. (2020); Colón et al. (2020), and Sheppard et al. (2021). As explained in Section 7.1 the retrieval framework used in this work is an adaptation of AURA (Pinhas et al., 2018) developed in Prof. Nikku Madhusudhan's research group. The data analysis and reduction that produced the spectra interpreted in this chapter was conducted by the co-authors in the respective published works. These co-authors additionally contributed to the text and figure preparation for the manuscripts from which the content in this chapter is derived.

of our retrieval framework. The atmospheric model calculates the transit depth of a planet by computing line by line radiative transfer in a transmission geometry. We consider a one-dimensional atmosphere divided into 100 layers uniformly spaced in $\log_{10}(P)$ from 10^{-6} to 10^{2} bar under hydrostatic equilibrium. The parametric pressure-temperature (P–T) profile follows the prescription of Madhusudhan & Seager (2009), and the presence of inhomogeneous clouds and hazes follows the parametric prescription of MacDonald & Madhusudhan (2017a), as employed in Welbanks & Madhusudhan (2019, Chapter 2) and described in Chapter 6, Section 6.1. The retrievals, unless stated otherwise, consider the reference pressure (P_{ref}) at an assumed radius R_p as a free parameter.

As in the previous Chapter, the sources of opacity considered in our retrieval framework correspond to molecules and atomic species expected in exoplanet atmospheres (Madhusudhan, 2012; Madhusudhan et al., 2016). The models for all three planets consider H_2-H_2 and H_2-He collision induced absorption (CIA; Richard et al., 2012), H_2O (Rothman et al., 2010), CH_4 (Yurchenko & Tennyson, 2014), NH_3 (Yurchenko et al., 2011), HCN (Barber et al., 2014), and CO_2 (Rothman et al., 2010). The models for KELT-11b and HAT-P-41b consider additional sources of opacity expected in hotter exoplanets: Na (Allard et al., 2019), K (Allard et al., 2016), CO (Rothman et al., 2010), TiO (Schwenke, 1998), AlO (Patrascu et al., 2015), and VO (McKemmish et al., 2016). The opacities for the chemical species in this chapter are obtained from Gandhi & Madhusudhan (2017) with the updated values of Gandhi & Madhusudhan (2018) where available. The H_2-broadened Na and K cross sections were computed following the methods described in Chapter 3.

Specific model considerations were included for each of the planets in this work. The retrieval configuration in the analysis of the spectrum of K2-18b considers four different cloud and haze model configurations[2]: (1) a full model including inhomogeneous clouds and hazes, (2) a clear atmosphere (i.e., no clouds or hazes), (3) an atmosphere with an opaque cloud deck but no hazes, and (4) an atmosphere with inhomogeneous clouds but no hazes. Model 3 is achieved by neglecting the contribution of hazes in the prescription of MacDonald & Madhusudhan (2017a), rendering a prescription similar to that of Line & Parmentier (2016). On the other hand, model 4 is achieved by neglecting the inhomogeneous cloud fraction parameter in model 3, and renders a prescription similar to that implemented in Benneke et al. (2019c).

2 These model configurations can be achieved using the generalized cloud and haze prescription introduced in Chapter 4.

The retrievals for KELT-11b consider the possibility of an error-bar inflation free parameter (e.g., Foreman-Mackey et al., 2013). Using this approach, it is assumed that the variance is underestimated and can be expressed as

$$S^2 = \sigma_{obs}^2 + f^2 \Delta_{mod}^2 \tag{32}$$

where σ_{obs} is the error in the observations and Δ_{mod} is the model's transit depth[3]. Finally, the retrievals for KELT-11b and HAT-P-41b allow for instrumental offsets in the data. This instrumental offset is applied to the observations from one or more telescope instruments relative to a fixed reference, usually another set of observations from a different instrument. These offsets are applied using Gaussian or uniform priors. For all the retrievals discussed above, the Bayesian parameter estimation is conducted using the nested sampling algorithm MultiNest (Feroz et al., 2009), through PyMultiNest (Buchner et al., 2014).

7.2 THE HABITABLE ZONE EXOPLANET K2-18B

Two factors mentioned in Chapter 1, namely the M-dwarf opportunity (e.g., Scalo et al., 2007; Charbonneau & Deming, 2007) and the high occurrence rates of low-mass planets orbiting M-dwarf hosts (Dressing & Charbonneau, 2015; Mulders et al., 2015), have allowed for detections of sub-Neptune-mass exoplanets in the habitable-zones of their host stars. A recent particularly good example is the habitable-zone transiting exoplanet K2-18b (Montet et al., 2015; Foreman-Mackey et al., 2015). The brightness and small size of its host star make precise measurements of the planetary mass, radius, and atmospheric spectra viable (Benneke et al., 2017; Cloutier et al., 2019), as exemplified by the recent detection of H_2O in its atmosphere (Tsiaras et al., 2019; Benneke et al., 2019c). Given its mass ($8.63 \pm 1.35\ M_\oplus$, Cloutier et al. 2019) and radius ($2.610 \pm 0.087\ R_\oplus$, Benneke et al. 2019c), K2-18b has a bulk density of $2.67^{+0.52}_{-0.47}$ g/cm^3 (Benneke et al., 2019c). This density, between that of Earth and Neptune, may be thought to preclude a purely rocky or icy interior and require a hydrogen-rich outer envelope.

Here we report the atmospheric retrieval of the broadband transmission spectrum reported by Benneke et al. (2019c) as presented in Madhusudhan et al. (2020). This analysis is different from that presented in

3 This noise treatment is also described in Chapter 4.

Chapter 3 as the observations employed here correspond to the revised work of Benneke et al. (2019c) and not those of Benneke et al. (2019a) used in Welbanks et al. (2019). The complete data used in this retrieval include observations from the HST WFC3 G141 grism (1.1–1.7 μm), photometry in Spitzer IRAC 3.6 μm and 4.5 μm bands, and optical photometry in the K2 band (0.4–1.0 μm). The atmospheric inferences from the atmospheric retrieval on the transmission spectrum of K2-18b, alongside the observed bulk properties of K2-18b (i.e., planetary mass and radius), were used to investigate mass constraints on different components of the planetary interior as well as the thermodynamic conditions at the interface between the atmosphere and interior in Madhusudhan et al. (2020).

7.2.1 *Retrieved Atmospheric Properties*

We retrieve the atmospheric properties of K2-18b using the atmospheric retrieval configuration described in Section 7.1. The full atmospheric model comprises 16 free parameters: abundances of 5 molecules, 6 parameters for the P–T profile, 4 cloud/haze parameters, and 1 parameter for the reference pressure P_{ref} at R_p. As explained in Section 7.1, we use four model configurations: (case 1) a full model including inhomogeneous clouds and hazes, (case 2) a clear atmosphere, (case 3) an atmosphere with an opaque cloud deck but no hazes, and (case 4) an atmosphere with inhomogeneous clouds but no hazes. The summary of the retrieved atmospheric constraints are shown in Figure 44 and Table 8.

We confirm the high-confidence detection of H_2O in a H_2-rich atmosphere as reported by Benneke et al. (2019c); Tsiaras et al. (2019), and Welbanks et al. (2019, see also Chapter 3). Our abundance estimates are consistent to within 1σ between all four model configurations and with Benneke et al. (2019c). The derived H_2O volume mixing ratio ranges between 0.02–14.80%, with median values of 0.7–1.6% between the 4 model cases, as shown in Table 8. The case with an opaque cloud deck (a clear atmosphere) retrieves slightly higher (lower) H_2O abundances as expected (Welbanks & Madhusudhan, 2019, see also Chapter 2). Our derived H_2O abundance range corresponds to an O/H ratio of 0.2–176.8 × solar, assuming all the oxygen is in H_2O as expected in H_2-rich atmospheres at such low temperatures (Burrows & Sharp, 1999). The median H_2O abundance is 9.3 × solar for the full model, case 1. We cannot compare our results with Tsiaras et al. (2019) as their retrievals were

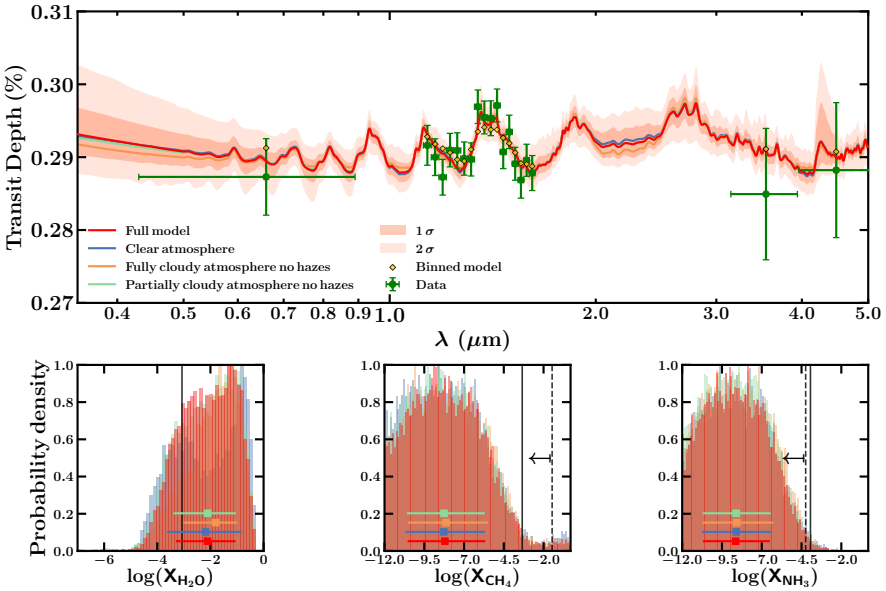

Figure 44 Atmospheric retrieval from the transmission spectrum of K2-18b. Top: observations (green) and retrieved model spectra for the four different model considerations in Table 8. Shaded regions represent 1σ and 2σ confidence intervals for the full model, with yellow points showing the model binned to the data resolution. The observations were adopted from Benneke et al. (2019c). Bottom: posterior distributions for the retrieved volume mixing ratios of H_2O, CH_4, and NH_3. The 99% upper limits for the full model on CH_4 and NH_3 are shown by the arrows and dashed lines. Equilibrium solar values are shown by solid black lines.

based on only the HST WFC3 data and used older measurements of the planetary mass and radius which could have biased their inferences.

We find a depletion of CH_4 and NH_3 in the atmosphere. For a H_2-rich atmosphere at ~ 300 K, CH_4 and NH_3 are expected to be dominant carriers of carbon and nitrogen, respectively, in chemical equilibrium (Burrows & Sharp, 1999), as also seen for the gas and ice giants in the solar system (Atreya et al., 2018). Assuming solar elemental ratios (i.e., C/O = 0.55, N/O= 0.14), the CH_4/H_2O (NH_3/H_2O) ratio is expected to be ~ 0.5 (~ 0.1). However, we do not detect CH_4 or NH_3 despite their strong absorption in the HST WFC3 and/or Spitzer 3.6 μm bands. As shown in Figure 44, the retrieved posteriors of the CH_4 and NH_3 abundances are largely sub-solar, with 99% upper limits of 3.47×10^{-2} and 5.75×10^{-5}, respectively. These sub-solar values are in contrast to the largely super-solar H_2O, arguing against chemical equilibrium at solar elemental ratios.

Table 8 Retrieved Atmospheric Properties from the Transmission Spectrum of K2-18b.

MODEL	$\log_{10}(X_{H_2O})$	$\log_{10}(X_{CH_4})$	$\log_{10}(X_{NH_3})$	$\ln(\mathcal{Z})$	DETECTION OF REF.
Case 1	$-2.11^{+1.06}_{-1.19}$	$-8.20^{+2.53}_{-2.34}$	$-8.64^{+2.15}_{-2.06}$	179.15	Reference
No H_2O	N/A	$-1.11^{+0.53}_{-1.22}$	$-7.27^{+2.91}_{-2.92}$	175.30	3.25
Case 2	$-2.18^{+1.35}_{-1.44}$	$-8.27^{+2.59}_{-2.42}$	$-8.60^{+2.19}_{-2.16}$	179.05	1.20
Case 3	$-1.80^{+0.81}_{-1.22}$	$-8.13^{+2.64}_{-2.41}$	$-8.57^{+2.30}_{-2.17}$	179.09	1.06
Case 4	$-2.10^{+1.07}_{-1.28}$	$-8.26^{+2.56}_{-2.34}$	$-8.61^{+2.18}_{-2.10}$	179.41	N/A

Note. Four model configurations are considered with different treatments of clouds and hazes (cases 1-4, see Section 7.2.1). For each model, the volume mixing ratios ($\log_{10}(X_{H_2O})$, $\log_{10}(X_{CH_4})$, and $\log_{10}(X_{NH_3})$) are shown along with the Bayesian evidence ($\ln(\mathcal{Z})$) and the detection of the reference model (i.e., detection significance, DS). The DS is derived from the Bayesian evidence and a value below 2.0σ is considered weak (Trotta, 2008). The preference of the reference model (case 1) over other models is quantified by the DS. For example, the DS for case 2 implies that case 1 is preferred over case 2 at 1.2σ. H_2O is detected at 3.25σ and clouds/hazes at only $\sim 1\sigma$.

We do not find strong evidence for clouds/hazes in the atmosphere. Our model preference for clouds/hazes, relative to the cloud-free case, is marginal (1.2σ) compared to Benneke et al. (2019c, 2.6σ). Our retrieved cloud top pressure (P_c) for the full case is weakly constrained to 0.1 mbar to 2 bar, close to the observable photosphere. Finally, we retrieve P_{ref} for the full case to be 12–174 mbar corresponding to R_p. We discuss the implications of these atmospheric constraints in Section 7.5.

7.3 THE INFLATED SUB-SATURN KELT-11B

In this section, we present the atmospheric retrieval on the spectrophotometric observations of KELT-11b to constrain its atmospheric properties at the day-night terminator. KELT-11b has a mass of 0.171 ± 0.015 M_J and a radius of 1.35 ± 0.10 R_J, making it extremely inflated and giving it one of the lowest surface gravities of any planet discovered to date (Beatty et al., 2017; Pepper et al., 2017). With a period of 4.74 days, KELT-11b also has a high equilibrium temperature ($T_{eq.} = 1712^{+51}_{-46}$ K, Pepper et al., 2017). This planet is notably part of an emerging population of low surface gravity sub-Saturn-mass exoplanets, also called "inflated sub-Saturns", that are ideal targets for atmospheric characterization via transmission spectroscopy. Other notable planets in this population include WASP-39b (Faedi et al., 2011), WASP-107b (Anderson et al., 2017), and WASP-127b (Lam et al., 2017). These other notable planets have been

characterized in Chapter 3 and Chapter 6, leaving KELT-11b as one of the remaining inflated sub-Saturns to be explored in this dissertation.

7.3.1 *Observations*

To add to the above described sample of well-characterized inflated exoplanets, Colón et al. (2020) undertook an investigation of the atmosphere of the inflated sub-Saturn KELT-11b using observations from HST, Spitzer, and TESS. The spectro-photometric observations interpreted with our atmospheric retrieval come from:

- A single transit of KELT-11b with HST/WFC3 on UT 2018 April 18 between 04 : 10 UT and 17 : 35 UT as part of the HST Program GO 15255 (Co-PIs K. Colón and L. Kreidberg). The observations spanned 9 HST orbits.
- A single transit of KELT-11b previously observed with Spitzer/IRAC Channel 1 (3.6 μm) starting on UT 2016 April 4 as part of Spitzer Program GO 12096 (PI: T. Beatty)
- Observations of KELT-11 by TESS for approximately 27 days in Sector 9 (UT 2019 February 28 to UT 2019 March 26). Five complete transits and one partial transit of KELT-11b were observed in that time.

The reduction and analysis of the above observations was conducted by other co-authors in Colón et al. (2020), where additional details about the observations, data reduction, and light curve analyses are available. Below we present our contribution to the work of Colón et al. (2020); the interpretation of these observations using atmospheric retrievals.

7.3.2 *Retrieved Atmospheric Properties*

We retrieve the atmospheric properties of KELT-11b employing models with different degrees of complexity with the retrieval configuration explained in Section 7.1. We begin by performing an initial exploratory retrieval considering absorption due to all the species listed in Section 7.1, inhomogeneous clouds and hazes, and a parametric P–T profile. This exploratory retrieval helps indicate the parameters and species that ought to be considered in the fiducial model and helps assess which chemical species may be present in the transmission spectrum of KELT-11b. We opt for this approach to avoid over-fitting the data and including

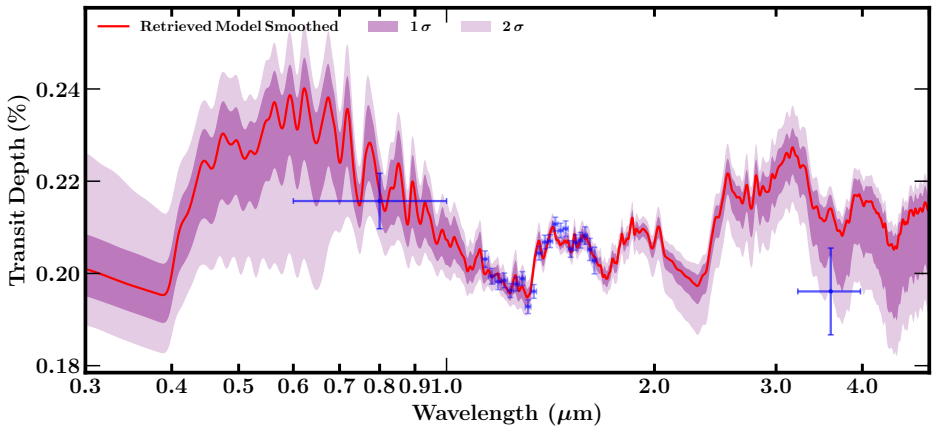

Figure 45 Retrieved transmission spectrum of KELT-11b for the fiducial 17 parameter model. The retrieved median transmission spectrum is shown in red with 1σ and 2σ contours shown in purple shaded regions. TESS, HST/WFC3, and Spitzer observations are shown using blue markers. The best fit model has a χ^2 of 29.97 for six degrees of freedom. The p value is 3.98×10^{-5} and the BIC is 83.27.

more parameters than there are observations. We determine a fiducial model that considers absorption due to H_2O, Na, K, HCN, AlO, and TiO, six parameters for the P–T profile, one parameter for the reference pressure (P_{ref}) at the radius of the planet R_p, and four parameters for clouds/hazes. This model with 17 free parameters is used to retrieve the atmospheric properties of KELT-11b using the complete transmission spectrum comprising of the TESS optical, HST/WFC3 near-infrared, and Spitzer infrared observations; a total of 23 spectral points.

The retrieved model and observations are shown in Figure 45. The posterior distributions for the constrained chemical species, temperature at the top of the atmosphere (T_0), and cloud parameters are shown in Figure 61 in Appendix E. The retrieval finds a strong detection of H_2O at 3.6σ with an abundance of $\log_{10}(X_{H_2O}) = -4.03^{+0.43}_{-0.53}$ and indications of HCN at 2.7σ with an abundance of $\log_{10}(X_{HCN}) = -3.84^{+0.45}_{-0.56}$ based on the HST/WFC3 transmission spectrum. The bluest part of the transmission spectrum and higher transit depth of the TESS data point relative to the HST/WFC3 observations are preferentially explained by AlO or TiO, at 2σ and 0.9σ, respectively. The retrieved abundances are $\log_{10}(X_{AlO}) = -7.64^{+0.71}_{-0.90}$ and $\log_{10}(X_{TiO}) = -6.75^{+0.78}_{-1.53}$.

Our fiducial model does not find strong constraints on the P–T profile of the atmosphere of KELT-11b or the presence of clouds and hazes. We retrieve a temperature near the photosphere at 100 mbar of $T_{100\ mbar} = 1982^{+341}_{-184}$ K. Replacing the parametric P–T profile for an isothermal pro-

file in our fiducial model results in a decrease in model evidence equivalent to 1.5σ. Similarly, removing inhomogenous clouds and hazes from our model in favor of a clear atmosphere results in a decrease of the model evidence equivalent to a 1.8σ level. Neither decrease in model evidence is significant enough to robustly claim constraints on the P–T profile or the presence of clouds and hazes nor can they be confidently ruled out.

To further consider the robustness of these inferences, we consider the possibility of an error-bar inflation free parameter as explained in Section 7.1. Following this approach results in an increase in model evidence relative to our fiducial model equivalent to a 1.6σ level. This means that the additional parameter is preferred at 1.6σ. The best fit model results in a χ^2 of 23.40 for 5 degrees of freedom compared to the χ^2 of 29.97 for 6 degrees of freedom in the fiducial model. The p value is 2.83×10^{-4} and the BIC is 79.84, while for the fiducial model the p value is 3.98×10^{-5} and the BIC is 83.27. The retrieved value for the error-inflation factor is $\log_{10}(f) = -1.93^{+0.12}_{-0.11}$. While considering the possibility of an error-bar inflation factor results in better fits to the data, the inferred H_2O and HCN abundances are still consistent with those from the fiducial model. The retrieved abundances are $\log_{10}(X_{H_2O}) = -4.49^{+0.63}_{-0.84}$ and $\log_{10}(X_{HCN}) = -4.62^{+0.94}_{-3.95}$. When considering the error-bar inflation factor, H_2O and HCN are still preferred by the model at a 3.1σ detection and 1.7σ inference, respectively. On the other hand, AlO and TiO are not preferred by the model. In the error-bar inflation model, the higher transit depth of the TESS data point can be explained by any of the species with signatures in the optical, namely Na, K, TiO, AlO, with no species being strongly preferred over other.

We perform an additional set of retrievals on the complete transmission spectrum of KELT-11b considering the possibility of instrumental vertical offsets. We include two additional free parameters corresponding to possible offsets in transit depth in the TESS optical and HST/WFC3 near-infrared bands relative to the Spitzer infrared bands. We consider two treatments for the prior on the offsets – uniform and Gaussian priors. One set of retrievals considers a uniform prior on each offset ranging between [−80,80] ppm. Another set of retrievals assume the prior distribution to be a Gaussian centered on zero with a standard deviation (σ) of 80 ppm. A possible unaccounted shift of 80 ppm or higher is both generous and unlikely considering 80 ppm is $\sim 1.5\times$ the precision of the TESS observations and $\gtrsim 3\times$ the average precision of the HST observations. When considering these possible offsets, our results

remain mostly unchanged with molecular abundances consistent with those obtained using the fiducial model. The presence of vertical offsets results in slightly better constraints on the abundance of TiO. On the other hand, the retrieved H_2O abundances remain unchanged. These results suggest that the retrieved molecular abundances using the fiducial model are robust against possible instrumental offsets and that our reported TiO abundance is a conservative estimate.

7.3.2.1 *Analysis of the HST/WFC3 Transmission Spectrum*

We further investigate the inferred chemical abundances and detections in KELT-11b when considering the HST/WFC3 observations alone. We perform a retrieval on the HST/WFC3 transmission spectrum using the same 17 parameter fiducial model described above. The retrieved transmission spectrum is shown in Figure 46. This retrieval confirms the strong detection of H_2O at a confidence level of 4.6σ with an abundance of $\log_{10}(X_{H_2O}) = -4.01^{+0.67}_{-0.98}$. As in the retrieval of the complete transmission spectrum, this retrieval also explains the HST/WFC3 observations with HCN absorption at a preference level of 2.5σ and with an abundance of $\log_{10}(X_{HCN}) = -3.84^{+0.69}_{-1.01}$. In contrast to the retrieval using the complete set of observations, this retrieval prefers TiO over AlO to explain the bluest spectral points in the HST/WFC3 observations. The retrieved TiO abundance is $\log_{10}(X_{TiO}) = -5.91^{+0.73}_{-1.06}$ at a detection significance of 2.9σ. On the other hand, the retrieved AlO abundance is $\log_{10}(X_{AlO}) = -8.65^{+1.43}_{-1.91}$. When using the HST/WFC3 observations only, removing AlO from the model results in an increase in model evidence indicating absorption due to this species is not preferred by the data. The cloud/hazes parameters and the temperature profile remain mostly unconstrained, with a retrieved temperature at 100 mbar of $T_{100\ \mathrm{mbar}} = 1959^{+242}_{-157}$ K. The posterior distributions for the relevant parameters are shown in Appendix E, Figure 62.

Similarly to our analysis of the full transmission spectrum, we consider the possibility of underestimated error bars by retrieving an error-bar inflation parameter on the HST/WFC3 observations only. This approach retrieves an error-bar inflation factor of $\log_{10}(f) = -2.07^{+0.14}_{-0.16}$ and abundances of $\log_{10}(X_{H_2O}) = -4.73^{+1.13}_{-1.51}$, $\log_{10}(X_{HCN}) = -4.52^{+1.15}_{-4.17}$, $\log_{10}(X_{TiO}) = -7.24^{+1.75}_{-1.93}$, and $\log_{10}(X_{AlO}) = -9.86^{+1.93}_{-1.27}$, consistent with the non-inflated error-bar approach. Considering the error-bar inflation factor results in a decrease in the model evidence relative to the fiducial model without error-bar inflation comparable to a 2.8σ level. This means that the additional error-bar inflation is not preferred at a 2.8σ

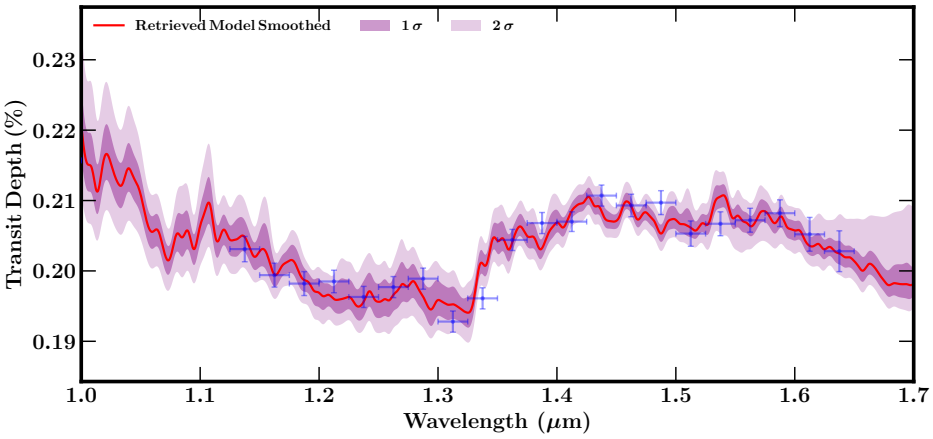

Figure 46 Retrieved transmission spectrum of KELT-11b for the 17 parameter fiducial model using HST/WFC3 observations only. The retrieved median transmission spectrum is shown in red with 1σ and 2σ contours shown in purple shaded regions. HST/WFC3 observations are shown using blue markers. The best fit model has a χ^2 of 23.28 for four degrees of freedom. The p value is 1.11×10^{-4} and the BIC is 75.03.

level. Similarly, this approach does not result in a better fit to the data by some frequentist metrics. The best fit model goes from a χ^2 of 23.28 for four degrees of freedom in the non-inflated error-bar approach to a χ^2 of 20.42 for three degrees of freedom when considering error-bar inflation. The p value and BIC go from 1.11×10^{-4} and 75.03, respectively, in the non-inflated error-bar approach to 1.39×10^{-4} and 75.22 when fitting for an error-bar inflation parameter.

Lastly, given that current observations do not place strong constraints on the P–T profile or cloud and haze cover in the atmosphere of KELT-11b, we investigate the effects of considering a simpler model in the retrieved abundance estimates using the HST/WFC3 observations only. We retrieve the atmospheric properties of KELT-11b using an isothermal P–T profile, a clear atmosphere, and considering absorption due to H_2O, HCN, and TiO. This retrieval results in abundances of $\log_{10}(X_{H_2O}) = -6.18^{+0.13}_{-0.12}$, $\log_{10}(X_{HCN}) = -6.65^{+0.53}_{-3.20}$, and $\log_{10}(X_{TiO}) = -7.96^{+0.33}_{-0.27}$. While the median H_2O abundance is lower than that retrieved under different model considerations, the retrieved value is consistent with the estimates above. The abundances of HCN and TiO are also consistent with the estimates from the different model configurations. The TiO abundance is tightly over-constrained under these simplified considerations. The retrieved isothermal temperature is consistent with previous estimates with a value of $T = 1867^{+93}_{-152}$ K. The retrieved transmission spectrum is shown in Figure 47, while the posterior distributions are shown in Fig-

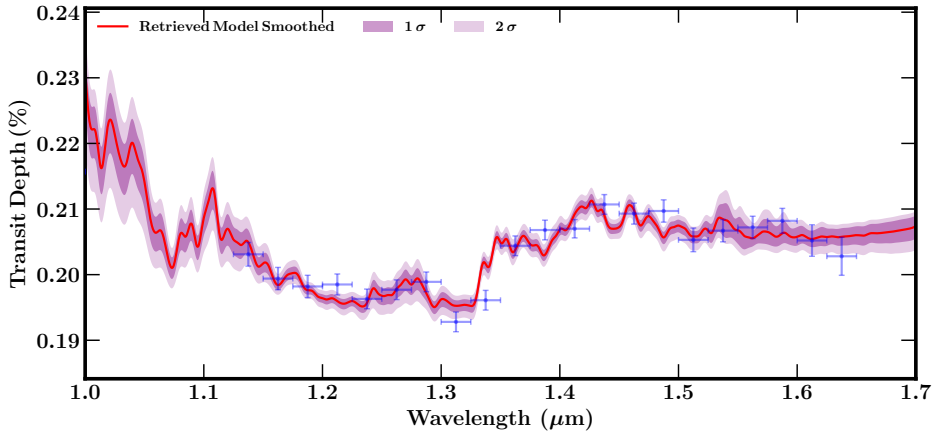

Figure 47 Retrieved transmission spectrum of KELT-11b for an isothermal and clear atmosphere with limited absorbers using HST/WFC3 observations only. The retrieved median transmission spectrum is shown in red with 1σ and 2σ contours shown in purple shaded regions. HST/WFC3 observations are shown using blue markers. The best fit model has a χ^2 of 28.85 for 16 degrees of freedom. The p value is 2.50×10^{-2} and the BIC is 44.07.

ure 63 in Appendix E. The reduced number of parameters results in a larger number of degrees of freedom, which in turn translates to a better fit by frequentist metrics. The best fit model has a χ^2 of 28.85 for 16 degrees of freedom. The p value is 2.50×10^{-2} and the BIC is 44.07.

We use these retrieved model parameters to produce a contribution plot. Figure 48 shows the contribution of H_2O, HCN, and TiO to explain the HST/WFC3 observations using the retrieved median values from the simplified model above. The red curve in Figure 48 shows the contribution to the transmission spectrum of all three species. The blue, orange, and green curves show the model without the contribution of H_2O, HCN, and TiO respectively. In olive, we show the contribution due to H_2-H_2 and H_2-He CIA. From this figure, it can be seen that the H_2O contribution to the model is used to fit the spectral feature at $\sim$ 1.4 μm. On the other hand, the red-most part of the transmission spectrum at $\gtrsim$ 1.5 μm is unusually flat (compared to typical transmission spectra; e.g., Iyer et al. 2016; Tsiaras et al. 2018) and is explained by HCN and CIA. The blue-most part of the transmission spectrum is being fit by absorption due to TiO.

For completion, we run one more retrieval considering the error-bar inflation parameter on the simplified model using the HST/WFC3 observations only. The retrieved chemical abundances are consistent with the non-inflated error-bar model. These are $\log_{10}(X_{H_2O}) = -6.18^{+0.14}_{-0.12}$,

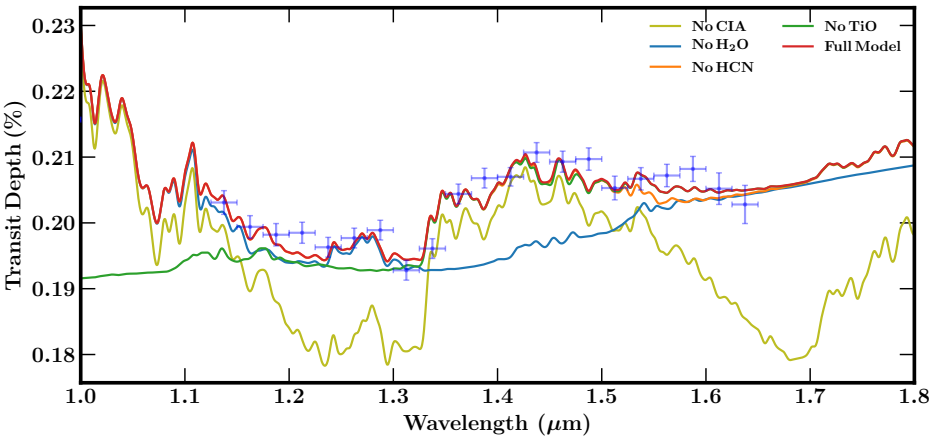

Figure 48 Contribution plot for the simplified, five-parameter model on the HST/WFC3 observations. The red line shows a forward model with the median retrieved parameters. The blue, orange, green, and olive lines line shows the model without the contribution of H_2O, HCN, TiO, and H_2-H_2 and H_2-He CIA. HST/WFC3 observations are shown using blue markers.

$\log_{10}(X_{HCN}) = -6.79^{+0.62}_{-3.04}$, and $\log_{10}(X_{TiO}) = -8.01^{+0.31}_{-0.33}$. The retrieved error-bar inflation factor is $\log_{10}(f) = -3.41^{+1.35}_{-4.17}$. Following this approach results in an even better fit by frequentist metrics. The best fit model has a χ^2 of 18.66 for 15 degrees of freedom. The p value is 2.30×10^{-1} and the BIC is 36.92. The model evidence for the model with error-bar inflation is slightly smaller, $\sim 1\sigma$ level, than that of the model without error-bar inflation. This decrease in model evidence indicates that the use of the additional error-bar inflation parameter is not preferred from a Bayesian perspective. We note that in this particular case while the inclusion of error inflation results in better fits to the data, i.e., better χ^2 due to larger uncertainties on the data, the precision on the retrieved abundance is not highly affected. This is due to the use of simplified isothermal and cloud-free models on WFC3 data only that result in lower abundance estimates with small uncertainties (see e.g., Welbanks & Madhusudhan, 2019, Chapter 2). We present in Table 9 a summary of the retrieved atmospheric properties of KELT-11b using models without instrumental offsets. The retrieved atmospheric properties of KELT-11b for models considering instrumental offsets are shown

in Table 18 in Appendix E. We comment on the possible implications of the retrieved properties of KELT-11b in Section 7.5.

Table 9 Summary of Retrievals for KELT-11b Without Instrumental Offsets.

Scenario	Abundance Constraint	D.O.F.	χ^2	p value	BIC
Full Model All Data	$\log_{10}(X_{H_2O}) = -4.03^{+0.43}_{-0.53}$ $\log_{10}(X_{HCN}) = -3.84^{+0.45}_{-0.56}$ $\log_{10}(X_{TiO}) = -6.75^{+0.78}_{-1.53}$ $\log_{10}(X_{AlO}) = -7.64^{+0.71}_{-0.90}$	6	29.97	3.98×10^{-5}	83.27
Full Model All Data Error Inflation	$\log_{10}(X_{H_2O}) = -4.49^{+0.63}_{-0.84}$ $\log_{10}(X_{HCN}) = -4.62^{+0.94}_{-3.95}$	5	23.40	2.83×10^{-4}	79.84
Full Model WFC3 Only	$\log_{10}(X_{H_2O}) = -4.01^{+0.67}_{-0.98}$ $\log_{10}(X_{HCN}) = -3.84^{+0.69}_{-1.01}$ $\log_{10}(X_{TiO}) = -5.91^{+0.73}_{-1.06}$ $\log_{10}(X_{AlO}) = -8.65^{+1.43}_{-1.91}$	4	23.28	1.11×10^{-4}	75.03
Full Model WFC3 Only Error Inflation	$\log_{10}(X_{H_2O}) = -4.73^{+1.13}_{-1.51}$ $\log_{10}(X_{HCN}) = -4.52^{+1.15}_{-4.17}$ $\log_{10}(X_{TiO}) = -7.24^{+1.75}_{-1.93}$ $\log_{10}(X_{AlO}) = -9.86^{+1.93}_{-1.27}$	3	20.42	1.39×10^{-4}	75.22
Simple Model WFC3 Only	$\log_{10}(X_{H_2O}) = -6.18^{+0.13}_{-0.12}$ $\log_{10}(X_{HCN}) = -6.65^{+0.53}_{-3.20}$ $\log_{10}(X_{TiO}) = -7.96^{+0.33}_{-0.27}$	16	28.85	2.50×10^{-2}	44.07
Simple Model WFC3 Only Error Inflation	$\log_{10}(X_{H_2O}) = -6.18^{+0.14}_{-0.12}$ $\log_{10}(X_{HCN}) = -6.79^{+0.62}_{-3.04}$ $\log_{10}(X_{TiO}) = -8.01^{+0.31}_{-0.33}$	15	18.66	2.30×10^{-1}	36.92

Note. There are 23 data-points in the complete transmission spectrum (TESS+HST+Spitzer) and 21 in the HST transmission spectrum. For reference, solar abundances at 12 mbar and 1730 K from self-consistent models in Colón et al. (2020) are: $\log_{10}(X_{H_2O}) = -3.44$, $\log_{10}(X_{HCN}) = -9.62$, $\log_{10}(X_{TiO}) = -11.63$, $\log_{10}(X_{AlO}) < -14$. The (uninflated) retrievals tend to produce χ^2/N_{data} between 1.1–1.3. The median retrieved H_2O abundances are sub-solar (~ 0.002–0.3 × solar) while the median HCN, TiO, and AlO abundances are far out of equilibrium when compared to the expected values using self-consistent models from Colón et al. (2020). Retrieved values for the models considering vertical offsets are shown in Table 18 in Appendix E.

7.4 THE INFLATED HOT JUPITER HAT-P-41B

Discovered in 2012, HAT-P-41b is among the most inflated hot Jupiters known to date ($R = 1.69\ R_J$, $M = 0.8\ M_J$, Hartman et al., 2012). This exoplanet orbits an F-star every ~ 2.7 days, making of HAT-P-41b a highly irradiated Jupiter-sized exoplanet with an equilibrium temperature of $T_{eq.} \approx 1940$ K (Hartman et al., 2012)[4]. As a member of the rapidly growing family of hot Jupiters with transmission spectra (e.g., Tsiaras et al., 2018; Sing et al., 2016), HAT-P-41b may offer important insights for population studies exploring trends in atmospheric metallicity as a function of planetary mass (e.g., Kreidberg et al., 2014b; Madhusudhan et al., 2014b; Sing et al., 2016; Tsiaras et al., 2018; Barstow et al., 2017; Pinhas et al., 2019; Welbanks et al., 2019, see Chapter 3). Particularly, with a radius close to that of the canonical hot Jupiter HD 209458 b, the atmospheric metallicity of HAT-P-41b may be informative of planet formation models for close-in Jupiter-sized planets. In this section we perform an atmospheric retrieval to interpret the day-night terminator atmospheric properties of HAT-P-41b from its transit spectrum using the transit observations from HST/STIS, HST/WFC3, and Spitzer presented in Sheppard et al. (2021).

7.4.1 *Observations*

The work of Sheppard et al. (2021) presents the 0.3–5.0 μm transmission spectrum of HAT-P-41b using transit observations from HST/STIS, HST/WFC3, and Spitzer. The HST/STIS G430L and G750L observations were taken as part of the Panchromatic Comparative Exoplanet Treasury (PanCET) Treasury Program (GO 14767; PIs: Sing and López-Morales). The HST/WFC3 G141 spectrum presented is a re-analysis of the observations form the same program. Additionally, Sheppard et al. (2021) present an independent Spitzer IRAC1 and IRAC2 transit depth determination (Program 13044; PI D. Deming). The WFC3 observations were taken on October 16, 2016. Then, the STIS data were acquired on September 4, 2017 (G430L); May 7, 2018 (G430L); and June 11, 2018 (G750L). For each visit, the target was observed for 7 hours over five consecutive HST orbits. Lastly, the Spitzer observations were taken in January and February 2017. A complete description of the data analysis and reduction is

4 While here we quote the system parameters for HAT-P-41b from the discovery paper (Hartman et al., 2012), our atmospheric retrieval uses as input parameters those revised and presented in Sheppard et al. (2021). The revised values are $R_p = 1.65\ R_J$, $M_p = 0.76\ M_J$, $T_{eq.} \approx 1960$ K, $R_s = 1.65 R_\odot$, $T_{eff} = 6480$ K.

available in Sheppard et al. (2021). Here, we present the atmospheric retrieval on their final transmission spectrum.

7.4.2 *Retrieved Atmospheric Properties*

We perform a series of atmospheric retrievals on the STIS, WFC3 and Spitzer data of HAT-P-41b to constrain the atmospheric properties at the day-night terminator of the planet. First, we consider the presence of different chemical species in the atmosphere of HAT-P-41b using its full broadband spectrum. Next, we consider the presence of possible transit depth offsets between data sets and their possible impact in the derived chemical abundances and associated metallicities.

7.4.2.1 *Evidence of H_2O and Indications of Optical-wavelength Absorbers*

We perform a full retrieval on the broadband spectrum of HAT-P-41b and present the observations and retrieved median spectrum in Figure 49. The full retrieval provides constraints on the presence of H_2O, and provides indications for the presence of Na and/or AlO in the optical. The full retrieval finds $\log_{10}(X_{H_2O}) = -1.65^{+0.39}_{-0.55}$, $\log_{10}(X_{Na}) = -3.09^{+1.03}_{-1.83}$, and $\log_{10}(X_{AlO}) = -6.44^{+0.66}_{-0.91}$. The atmospheric retrieval does not favor, by means of a model comparison described below, the presence of TiO absorption in the atmosphere of HAT-P-41b. The retrieved molecular abundance of TiO is $\log_{10}(X_{TiO}) = -9.58^{+1.37}_{-1.50}$. While the cloud/haze parameters are not tightly constrained, our retrieval indicate a cover of $\bar{\phi} = 0.25^{+0.26}_{-0.16}$ consistent with a mostly clear atmosphere. The temperature profile of the atmosphere is mostly unconstrained. We infer the temperature near the photosphere, at 100 mbar, to be $T_{100\ mbar} = 1345^{+349}_{-206}$ K. The posterior distributions for the relevant parameters are shown in Figure 64 in Appendix E.

We utilize this full retrieval as a reference model to perform a Bayesian analysis and assess the impact of not considering some of these parameters in the models. This change in model evidence is then converted to a detection significance (DS) following Benneke & Seager (2013)[5]. Table 10 shows the different models considered, their model evidence, DS, and $\bar{\chi}^2$. We find a robust detection of H_2O at a 4.89σ confidence. The presence of Na and/or AlO remain as moderate indications with confidence levels of 2.09σ and 2.58σ, respectively. The removal of TiO from the models results in an increase in the model evidence, indicating a

5 The conversion of a change in model evidence to a detection significance is explained in more detail in Chapter 4

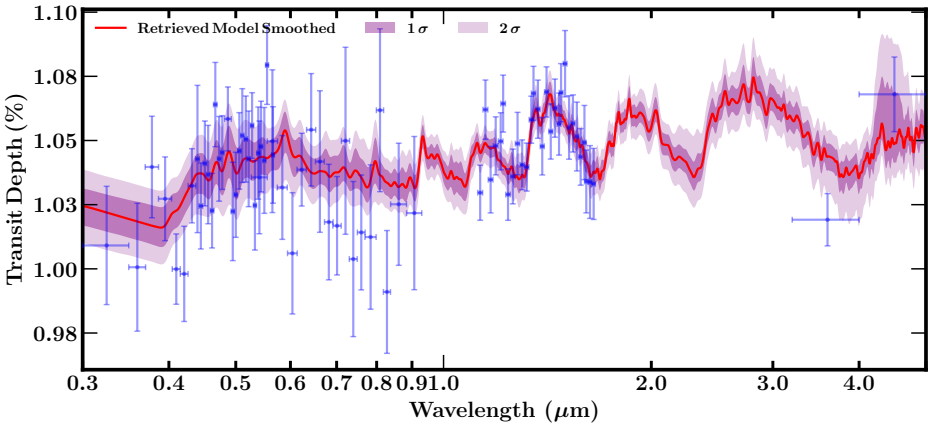

Figure 49 Retrieved spectrum of HAT-P-41b using STIS, WFC3 and Spitzer data. Observations are shown using blue markers. The retrieved median spectrum is shown in red while the 1σ and 2σ regions are shown using the shaded purple areas.

disfavor for this molecule to be present in our models. We assess the retrieved H_2O abundance relative to expectations from thermochemical equilibrium for solar elemental compositions (Asplund et al., 2009). Assuming a solar composition and that half of the available oxygen is in H_2O, the retrieved H_2O abundance corresponds to a metallicity ~ 15–131 × solar with a median of ~ 53 × solar. We also compare the retrieved H_2O abundance to the stellar metallicity of the host star ([O/H]= 0.37) to obtain a value of ~ 6–56 × stellar with a median of ~ 23 × stellar.

We consider the possibility of fitting the data using a simpler model consisting mainly of the parameters that are reasonably constrained by the full model. The simpler model considers the chemical abundances of H_2O, Na, CO, AlO, an isothermal P–T profile, and a clear atmosphere. The retrieved median fit and confidence contours are shown in Figure 50. The simplified model retrieves values consistent with the full model. The retrieved values are $\log_{10}(X_{H_2O}) = -1.65^{+0.40}_{-0.63}$, $\log_{10}(X_{Na}) = -2.60^{+0.94}_{-1.10}$ and $\log_{10}(X_{AlO}) = -5.81^{+0.51}_{-0.66}$. The retrieved isothermal temperature is $T = 1120^{+170}_{-140}$ and consistent with the inferred temperature at 100 mbar from the full retrieval. The retrieved H_2O abundance corresponds to a metallicity ~ 12–134 × solar with a median of ~ 53 × solar, or ~ 5–57 × stellar with a median of ~ 23 × stellar. The posterior distribution for the retrieved parameters is shown in Appendix E, Figure 65.

We use these retrieved parameters to generate a set of forward models to assess the spectroscopic contribution from each chemical species. Figure 50 shows that the WFC3 observations are better explained by the H_2O absorption feature at ~ 1.4 μm driving its strong detection in the

Table 10 Summary of Retrievals for HAT-P-41b.

#	Model	$\log_{10}(X_{H_2O})$	$\log_{10}(X_{Na})$	$\log_{10}(X_{AlO})$	$\log_{10}(X_{TiO})$	$STIS_{Shift}$	$WFC3_{Shift}$	$\ln(\mathcal{Z})$	$\bar{\chi}^2$	Detection of Ref.
1	Full model	$-1.65^{+0.39}_{-0.55}$	$-3.09^{+1.03}_{-1.83}$	$-6.44^{+0.66}_{-0.91}$	$-9.58^{+1.37}_{-1.50}$	N/A	N/A	559.1	0.93	Ref.
2	No H_2O	N/A	$-2.41^{+0.99}_{-2.99}$	$-5.71^{+0.99}_{-1.39}$	$-9.00^{+1.56}_{-1.76}$	N/A	N/A	548.9	1.37	4.89
3	No Na	$-1.62^{+0.42}_{-0.67}$	N/A	$-6.90^{+0.84}_{-1.05}$	$-8.32^{+0.78}_{-1.53}$	N/A	N/A	558.0	0.95	2.09
4	No AlO	$-1.49^{+0.35}_{-0.70}$	$-4.32^{+1.88}_{-4.31}$	N/A	$-8.78^{+1.07}_{-1.83}$	N/A	N/A	557.0	1.03	2.58
5	No TiO	$-1.70^{+0.41}_{-0.56}$	$-2.97^{+0.95}_{-1.25}$	$-6.39^{+0.66}_{-0.88}$	N/A	N/A	N/A	559.7	0.92	N/A
6	Simpler model	$-1.65^{+0.40}_{-0.63}$	$-2.60^{+0.94}_{-1.10}$	$-5.81^{+0.51}_{-0.66}$	N/A	N/A	N/A	560.0	0.89	N/A
7	Uniform shifts STIS & WFC_3	$-3.34^{+1.00}_{-0.86}$	$-3.43^{+1.35}_{-2.19}$	$-6.98^{+0.77}_{-0.78}$	$-9.46^{+1.38}_{-1.56}$	$89.67^{+166.90}_{-156.93}$	$-203.98^{+97.32}_{-97.53}$	560.7	0.89	N/A
8	Uniform shifts G430L, G750L, & WFC_3	$-2.96^{+0.98}_{-0.88}$	$-2.43^{+0.84}_{-1.34}$	$-7.05^{+0.75}_{-0.94}$	$-9.38^{+1.50}_{-1.68}$	G430L $1.32^{+144.08}_{-156.25}$ G750L $175.94^{+150.70}_{-160.22}$	$-189.04^{+90.72}_{-94.32}$	561.8	0.88	N/A
9	Gaussian shifts G430L, G750L, & WFC_3	$-1.91^{+0.53}_{-0.68}$	$-2.38^{+0.81}_{-1.33}$	$-6.64^{+0.70}_{-0.96}$	$-9.46^{+1.47}_{-1.58}$	G430L $-51.75^{+60.52}_{-62.71}$ G750L $79.55^{+59.32}_{-56.14}$	$-91.33^{+47.81}_{-50.06}$	562.0	0.90	N/A

Note. N/A means that the parameter was not considered in the retrieval or that it is not possible to estimate the detection significance (DS) as the model has a larger evidence than the reference model (model 1). Shifts are given in ppm.

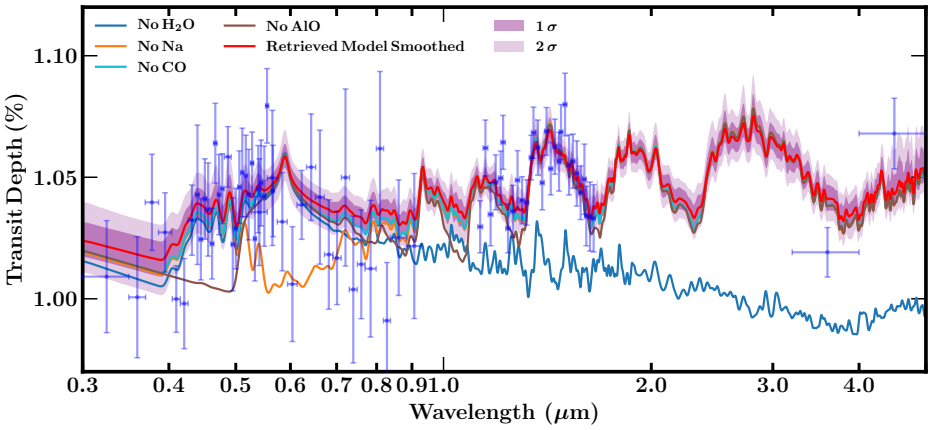

Figure 50 Retrieval of HAT-P-41b using a simplified model. Observations are shown using blue markers. The retrieved median spectrum is shown in red while the 1σ and 2σ regions are shown using the shaded purple areas. Forward models using the retrieved median parameters show the contributions to the spectra due to individual chemical species. The forward models shown exclude absorption due to H_2O (blue), Na (orange), CO (cyan), and AlO (brown).

spectrum of HAT-P-41b. On the other hand, a series of chemical species in the optical can provide some degree of fit to the STIS observations. In the optical, between ~ 0.5–0.7 μm, the broadened wings of Na along with its absorption peak provide a fit to observations. AlO provides some fit to the substructure present in the STIS observations, particularly the increased transit depth between 0.4–0.5 μm. Finally, the abundance of CO is not constrained, and its contribution to the spectrum is minimal. CO is responsible for small changes in the optical and infrared that are well within the error bar of the observations.

Our retrieval analysis of the broadband transmission spectrum of HAT-P-41b does not require additional opacity sources (e.g., H^-) to explain the data, as recently claimed by Lewis et al. (2020). Our models, with comparable or less number of free parameters which do not include H^-, provide better fits to the data with better evidence than those in Lewis et al. (2020) which were used to infer H^-. Using our fiducial model, we obtain a best-fit $\bar{\chi}^2$ of 0.93 and $\ln(\mathcal{Z}) = 559.1$. The corresponding values for our simplified model are $\bar{\chi}^2 = 0.89$ and $\ln(\mathcal{Z}) = 560.0$ (see Table 10). Their best-fit model across all considerations has $\bar{\chi}^2 = 1.50$ and $\ln(\mathcal{Z}) = 478.9$.

7.4.2.2 *Possible Offsets in the Data*

To explore the robustness of our results, we consider the presence of offsets in the data and their effect on the retrieved atmospheric properties. We consider scenarios in which the STIS observations are affected by the same offset, meaning this additional retrieved parameter is applied to both G430L and G750L STIS observations. Additionally, we consider scenarios in which a separate offset is retrieved for the G430L observations and the G750L observations. In all scenarios a shift is also allowed for the HST/WFC3 observations. We note that these retrieved offsets are relative to the atmospheric model and that the Spitzer observations remain unchanged in all scenarios. We consider both Gaussian and uniform priors. In summary, we consider three scenarios. First, two additional parameters in our retrieval account for shifts with uniform priors of [−500,500] ppm on the HST/STIS and HST/WFC3 observations. Second, we consider three possible offsets with the same uniform prior of[−500,500] ppm, one for HST/STIS G430L, one for HST/STIS G750L, and one for HST/WFC3 data. Third, three shifts with Gaussian priors are considered, one for one for HST/STIS G430L (centered on zero with a standard deviation of 105 ppm), one for HST/STIS G750L (centered on zero with a standard deviation of 85 ppm), and one for HST/WFC3 observations (centered on zero with a standard deviation of 80 ppm). These Gaussian priors are informed by the analysis of the white light transit curves of Sheppard et al. (2021).

We present the first scenario accounting for offsets in the HST/STIS and HST/WFC3 observations using a uniform prior, while keeping the Spitzer observations unshifted. The retrieval results in a shift in the STIS data of 90^{+167}_{-157} ppm and a shift in the WFC3 data of -204^{+97}_{-98} ppm. While the retrieved value for the STIS observations is consistent with no shift, the WFC3 observations preferentially retrieve a negative offset. The derived abundances, shown as model 7 in Table 10, are $\log_{10}(X_{H_2O}) = -3.34^{+1.00}_{-0.86}$, $\log_{10}(X_{Na}) = -3.43^{+1.35}_{-2.19}$, $\log_{10}(X_{AlO}) = -6.98^{+0.77}_{-0.78}$. The H_2O abundance corresponds to a metallicity $\sim$ 0.06–4.66 $\times$ stellar, an estimate lower than that of the full model without instrumental offsets.

Second, we present the results for the case with three uniform shifts between HST/STIS G430L, HST/STIS G750L, and HST/WFC3 observations. The retrieved shifts are 1^{+144}_{-156} ppm for G430L, 176^{+151}_{-160} ppm for G750L, and -189^{+91}_{-94} ppm for WFC3. The retrieved chemical abundances are shown in Table 10 as model 8 and are $\log_{10}(X_{H_2O}) = -2.96^{+0.98}_{-0.88}$, $\log_{10}(X_{Na}) = -2.43^{+0.84}_{-1.34}$, and $\log_{10}(X_{AlO}) = -7.05^{+0.75}_{-0.94}$. While the retrieved abundances for these three species are consistent within 1σ with

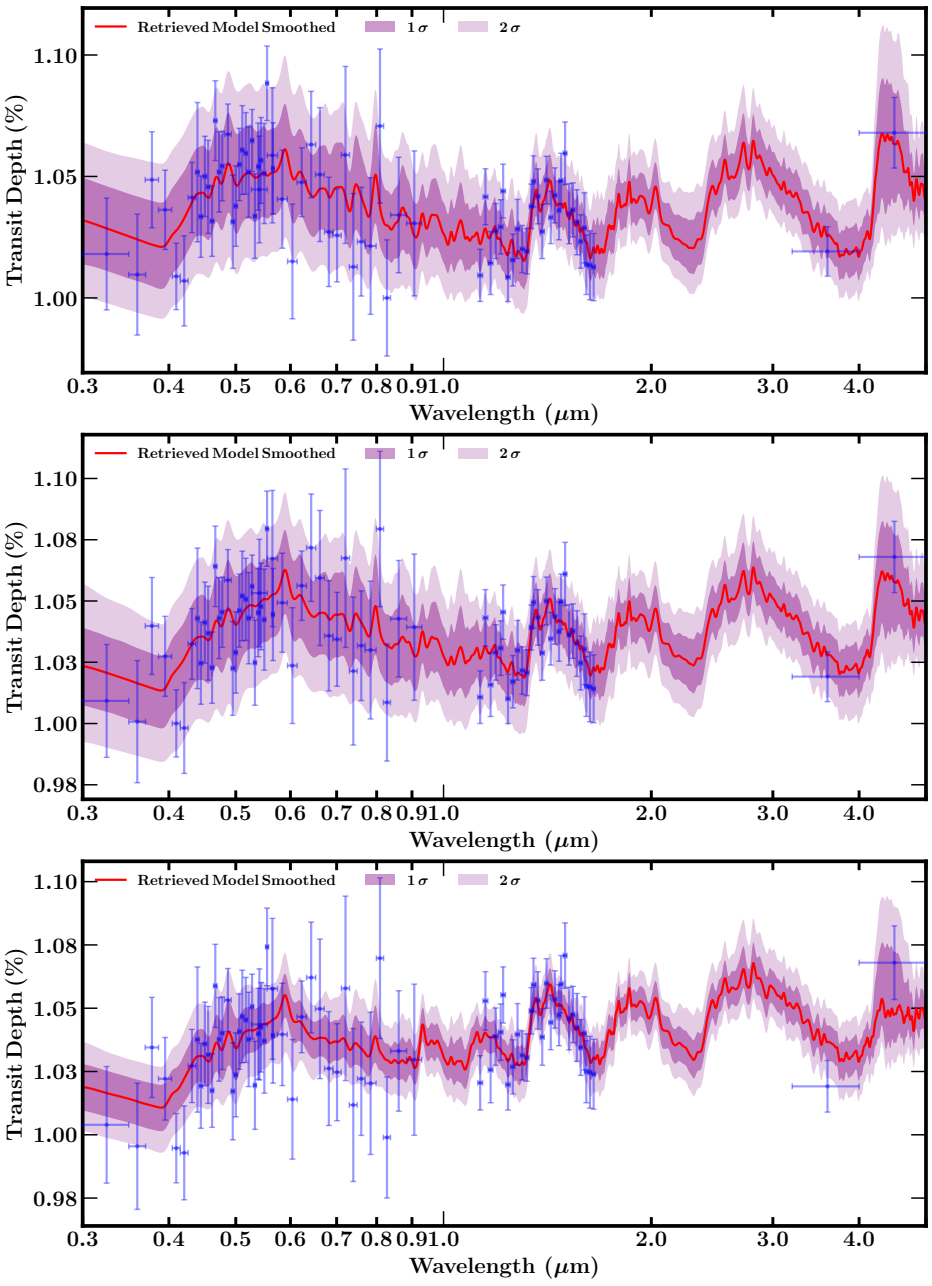

Figure 51 Retrieved spectrum of HAT-P-41b allowing for offsets in the STIS and WFC3 data sets. Observations are shown using blue markers and are shifted according to the models' retrieved median shifts. Retrieved median spectrum is shown in red, while the 1σ and 2σ regions are shown using shaded purple areas. Top: two shifts with uniform priors (model 7) and retrieved median offsets of ~ 90 ppm for STIS and ~ −204 ppm for WFC3. Middle: three shifts with uniform priors (model 8) and retrieved median offsets of ~ 1 ppm for STIS G430L, ~ 176 ppm for G750L, and ~ −189 ppm for WFC3. Bottom: three shifts with Gaussian priors (model 9) and retrieved median offsets of ~ −52 ppm for STIS G430L, ~ 80 ppm for G750L, and ~ −91 ppm for WFC3.

the full unshifted model, the retrieved H_2O abundance corresponds to a lower metallicity estimate of ~ 0.15–$10.67 \times$ stellar.

Last, we present the results of considering the presence of three offsets with Gaussian priors informed by the analysis of the white-light transit curves as explained above. The retrieved shifts are -52^{+61}_{-63} ppm for G430L, 80^{+59}_{-56} ppm for G750L, and -91^{+48}_{-50} ppm for WFC3. The retrieved abundances are $\log_{10}(X_{H_2O}) = -1.91^{+0.53}_{-0.68}$, $\log_{10}(X_{Na}) = -2.38^{+0.81}_{-1.33}$, and $\log_{10}(X_{AlO}) = -6.64^{+0.70}_{-0.96}$. Although the retrieved H_2O abundance corresponds to a lower metallicity estimate, the derived range of ~ 3–$42 \times$ stellar is consistent with that of the fiducial model. Figure 51 shows the retrieved median models and confidence contours along with their respectively shifted observations for the cases described in this section.

The models considering instrumental shifts are all preferred over the fiducial model at above the 2σ level. The model with Gaussian priors has a preference at the 2.9σ level, followed by the model with three uniform shifts at a 2.8σ level. The model with two uniform shifts is preferred over the fiducial model at 2.3σ. We note that while both models with three offsets are similarly preferred over our fiducial model, the associated metallicity ranges are different. The model with three uniform shifts retrieves an H_2O abundance corresponding to a metallicity estimate consistent with substellar and stellar values. On the other hand, the model with Gaussian priors retrieves an associated metallicity range mostly superstellar and in agreement with the fiducial model. These results highlight the sensitivity of the inferred metallicity ranges to possible large offsets between instruments. Model comparisons suggest a preference for the models considering offsets, though it is inconclusive between these models. We discuss the implications of these results in Section 7.5.

7.5 SUMMARY AND DISCUSSION

Undoubtedly, the exploration of exoplanet atmospheres has been steadily progressing over the last 20 years thanks to the many observational efforts using space-based observatories. Such observations have been constantly pushing the boundaries of what is possible, and have helped the field move from observations of transiting hot Jupiters (e.g., Charbonneau et al., 2002; Sing et al., 2016) to recognizable absorption features in the atmospheres of mini-Neptunes (e.g., Benneke et al., 2019b; Tsiaras et al., 2019; Benneke et al., 2019c). Likewise, the precision of some of these recent observations are pushing the limit of measurement preci-

sion for HST/WFC3 (e.g., Colón et al., 2020, , who obtain a median uncertainty of ~ 16 ppm), perhaps venturing the field into a new realm of instrumental systematics that need to be considered in the reduction and analysis of atmospheric data, and atmospheric retrieval models. These advancements are just a preamble for the imminent data revolution that will come with the launch of JWST and the next generation of space telescopes. Therefore, exploring the type of inferences we can derive from these observations as well as their limitations is indispensable. Here, we summarize and discuss the key atmospheric constraints we have derived in this chapter when interpreting observations obtained with space-based facilities using atmospheric retrievals.

Finding absorption features in the atmosphere of a super-Earth orbiting the habitable zone of its host star will be an important first step towards our search for life signatures in Earth-like exoplanets. This important step was recognized by Tsiaras et al. (2019) who presented the transmission spectrum of K2-18b, classified in their work as a Super-Earth, claiming the first detection of a H_2O absorption feature in a habitable zone exoplanet. The excitement of this result was later made certain by Benneke et al. (2019c), who not only confirmed the absorption feature of H_2O vapor, but additionally reported the likely presence of water clouds in the planet's atmosphere. Nonetheless, by revising the system parameters, Benneke et al. (2019c) highlight that K2-18b is not a true Earth analog and that the planet falls in the mini Neptune category with a H-rich atmosphere.

In this work we have presented our contribution to the work of Madhusudhan et al. (2020). The additional atmospheric retrieval on the latest spectrum of K2-18b presented in this chapter confirms the detection of H_2O vapor in the atmosphere of the planet. Furthermore, the retrieval constrains the atmosphere of K2-18b to be H_2-rich with a H_2O volume mixing ratio of $0.02 - 14.8\%$, consistent with previous studies, and find a depletion of CH_4 and NH_3, suggesting chemical disequilibrium. This surprising signature of chemical disequilibrium may be the result of one or many of the different atmospheric processes mentioned in Chapter 1. For instance, chemical disequilibrium may be the result of photochemical processes. However, the potential influence of biochemical processes may not be entirely ruled out with existing data. The outstanding opportunity that K2-18b presents to better understand the physical and chemical processes in exoplanetary atmospheres in the temperate regime has been recently recognized by selected General Observer Programs in Cycle 1 of JWST. Two programs (GO 2372, PI Renyu Hu; GO 2722, PI Nikku

Madhusudhan) will acquire further transmission spectra of K2-18b and promise to help us better constrain the abundances of H_2O, CH_4, NH_3, CO, and CO_2.

Future observations of K2-18b may help us better constrain the presence of clouds and/or hazes in its atmosphere. While the analysis of Benneke et al. (2019c) finds a likely presence of clouds in K2-18b, our analysis of the same observations does not conclusively detect clouds/hazes in the observable atmosphere. The disagreement between both studies may be the result of utilizing different number of parameters and priors, a pitfall of Bayesian model comparison among different studies. Alternatively, the use of different cloud parameterizations may cause this apparent disagreement (e.g., Benneke et al., 2019c, tests three configurations while we test four). Regardless, future observations in the optical wavelengths will be advantageous to reliably constrain the presence of clouds and hazes in the atmosphere of K2-18b (e.g., Welbanks & Madhusudhan, 2019, Chapter 2).

Additionally, the work presented here exemplifies an application of atmospheric retrievals and their derived atmospheric constraints. Robust atmospheric constraints, alongside planetary bulk properties, may be used to constrain the internal structure and thermodynamic conditions in the planet as performed by Madhusudhan et al. (2020). Informed by the atmospheric constraints of K2-18b derived above, they model the interior of the planet using canonical internal structure models. Their constraints on the interior composition of K2-18b result in a wide range of thermodynamic conditions at the H_2O-H/He boundary, with one of many plausible scenarios being an ocean world, with liquid water approaching STP conditions (e.g., 300 K, $\sim$ 1–10 bar) underneath a thin H/He atmosphere. Further atmospheric observations and models are needed to constrain such scenarios and discern whether the atmospheric properties, and maybe even 'surface' properties, of K2-18b feature habitable conditions. Future exoplanetary studies adopting the 'end-to-end' approach of Madhusudhan et al. (2020) will be able to investigate the atmospheric and interior properties of exoplanets when informed with by robust and reliable retrieval frameworks and their inferences.

Next in this Chapter, we presented our atmospheric retrieval on the transmission spectrum of the highly inflated sub-Saturn KELT-11b. The transmission spectrum of KELT-11b was described by Colón et al. (2020) as unusual due to the red-most part of the spectrum at $\gtrsim$ 1.5 μm (see e.g., Figure 48) which is unusually flat when compared to typical transmission spectra (e.g., Iyer et al., 2016; Tsiaras et al., 2018). Our atmo-

spheric retrieval explains this 'unusual' transmission spectrum by a combined contribution of H_2O and HCN absorption along with CIA. However, the retrieved abundances are sub-solar for H_2O and super-solar for HCN. Considering the retrieved temperature of the planet of $\sim$ 1900 K, the retrieved H_2O and HCN abundances suggest that KELT-11b has a super-solar C/O ratio (Madhusudhan, 2012). This apparent oxygen depletion and enrichment in other elements could agree with the findings presented by Welbanks et al. (2019, Chapter 3) suggesting that different elements can be differently enhanced.

The sub-solar water abundance retrieved for KELT-11b, a sub-Saturn, is in disagreement with the mass-metallicity trend for solar system giant planets using their methane abundance. Additionally, the retrieved water abundance is several orders of magnitude lower than expected from formation models which predict an atmospheric metal enrichment for sub-Saturns in the range of 10–100 $\times$ solar (Fortney et al., 2013; Mordasini et al., 2016). Likewise, the inferred water abundance for KELT-11b is in disagreement with interior structure models based on the observed masses and radii of gas giant exoplanets which suggest a metal enrichment of $\sim$ 10 $\times$ solar for planets in the sub-Saturn mass range (Thorngren et al., 2016). Our atmospheric retrieval suggests that KELT-11b is an additional member of the population of planets with subsolar H_2O abundances previously encountered (e.g., Madhusudhan et al., 2014b; Barstow et al., 2017; Pinhas & Madhusudhan, 2017; Welbanks et al., 2019, see Chapter 3).

A potential explanation for such a low metallicity could be the formation of the planet far out in the disk beyond the CO snow line where the gas is depleted of oxygen-rich volatiles (Öberg et al., 2011) and migrating inward by disk-free mechanisms, as has been proposed for some hot Jupiters (Madhusudhan et al., 2014c). Similarly, the possibility of the volatiles locked up in the core as the planet forms via pebble accretion (Madhusudhan et al., 2017) or the enhancement of other volatiles in the gas relative to oxygen through pebble drift (Öberg & Bergin, 2016; Booth et al., 2017) may also contribute to the observed abundances. Testing these different scenarios will require precise abundance measurements for other species, such as CO, which would be possible with future observations with JWST.

The high-precision spectra of KELT-11b as presented by Colón et al. (2020) has a median uncertainty of 16 ppm. Such high-precision observations exhort us to consider the possibility of unaccounted instrumental systematics in our atmospheric retrieval models. We explored this new

challenge by considering the possibility of underestimated variances in the data as part of the retrieval model. Our results indicate that a better fit to the data is possible, under some frequentist metrics, when retrieving an error-inflation factor. Nonetheless, despite the inclusion of this error-bar inflation factor, the inferred H_2O and HCN abundances were consistent with those from the fiducial uninflated model. This new realm of instrumental systematics may be a forewarning of the data challenges we will face with JWST. These and other advanced noise treatments have been implemented in the next generation retrieval framework Aurora (Welbanks et al., 2019, see Chapter 4).

Finally, in this chapter we presented our analysis of the transmission spectrum of the hot Jupiter HAT-P-41b. Our retrieval provides constraints on the presence of H_2O, and provides indications for the presence of Na and/or AlO in the optical. The retrieved H_2O abundance, when compared to the stellar metallicity of the host star, corresponds to a metallicity $\sim$ 6–56 $\times$ stellar with a median of $\sim$ 23 $\times$ stellar. This superstellar metallicity presents an exciting opportunity to find planets that do not agree with the sub-solar/sub-stellar trend seen in other hot Jupiters (e.g., Madhusudhan et al., 2014b; Barstow et al., 2017; Pinhas et al., 2019; Welbanks et al., 2019, see Chapter 3). Additionally, if confirmed, the retrieved atmospheric metallicity for HAT-P-41b further suggests that there is a diversity in the formation and migration histories of exoplanets.

The potentially high atmospheric metallicity, specifically O/H, inferred for HAT-P-41b may be the result of formation outside the H_2O snowline and migration inward while accreting substantial mass in planetesimals. If confirmed, this would be a departure from other hot Jupiters observed hitherto which have generally shown low H_2O abundances, indicative of low accretion of H_2O-rich ices that is possible for disk-free migration mechanisms (Madhusudhan et al., 2014c; Pinhas et al., 2019; Welbanks et al., 2019). Such an abundance is also a substantial departure from expectations based on solar system giant planets. The metallicity of Jupiter in multiple elements is $\sim$ 1–5$\times$ solar (Atreya et al., 2018; Li et al., 2020). With the mass of HAT-P-41 b being similar to that of Jupiter its higher metallicity would indicate an even higher amount of solids accreted than that of Jupiter in the solar system.

Nonetheless, in order to confirm the apparent high metallicity of HAT-P-41b we must address the possible instrumental offsets in the observations of the planet and their impact on the retrieved atmospheric properties. Our retrieval analysis finds a preference for models that consider

instrumental offsets in the observations. When offsets are considered, the retrieved atmospheric metallicity for HAT-P-41b is consistent with sub-stellar and stellar values. If these stellar or sub-stellar abundances are confirmed, HAT-P-41b would join the population of observed hot Jupiters with atmospheric H_2O depletion (e.g., Madhusudhan et al., 2014b; Barstow et al., 2017; Pinhas et al., 2019; Welbanks et al., 2019, see Chapter 3). Solving this conundrum will require agnostic retrieval frameworks that account for possible instrumental systematics such as Aurora, and future complementary observations.

In summary, in this chapter we have explored the challenges and opportunities presented by the latest transmission spectra obtained with space-based facilities and their interpretation with atmospheric retrieval frameworks. Our key findings are outlined below:

- Transmission spectra obtained with space-based facilities provide us with key observations in the optical and infrared to constrain the chemical composition of exoplanets. Particularly, these observations are instrumental to detect the presence and constrain the abundance of important molecules such as H_2O. The inferred atmospheric properties provide important constraints on the formation and migration history of exoplanets.

- In recent years, the field has achieved the milestone of detecting an absorption feature in the atmosphere of an exoplanet in the habitable zone of its host star. Our analysis confirms the detection of H_2O in the atmosphere of the mini-Neptune K2-18b and finds a surprising depletion of CH_4 and NH_3. These may be the signs of chemical disequilibrium in the atmosphere of the exoplanet.

- We characterize the unusual spectrum of the highly inflated sub-Saturn KELT-11b. We detect signatures of H_2O absorption and indications of HCN. The retrieved H_2O abundance is sub-solar while the HCN abundance is super-solar. Our findings suggest that KELT-11b may have a super-solar C/O ratio.

- Our retrieval on the transmission spectrum of HAT-P-41b finds a potentially high atmospheric metallicity, specifically O/H. If confirmed, this high abundance would be a departure from previous hot Jupiters with low H_2O abundances and from expectations based on the solar system giant planets.

- Recent spectra obtained with space-based facilities have highlighted challenges due to instrumental systematics and high-precision ob-

servations. These observations require advanced modeling frameworks that can be agnostic and consider different noise treatments in pursuance of reliable atmospheric inferences. These challenges are an opportunity to better prepare for upcoming observations with JWST and future facilities.

As we look towards the future, the continued use of multiple complementary high-precision exoplanet atmosphere spectra obtained with ground and space-based facilities will update our findings. Revisiting our models and their findings will be paramount, especially in the coming era of JWST and as the exoplanet community pushes towards the atmospheric characterization of high-profile, potentially rocky planets in the habitable zones of their stars. We continue our discussion of the future of exoplanet atmospheric characterization in Chapter 8.

8

CONCLUSIONS

The last 30 years have witnessed a transformation in the field of exoplanets, maturing from an era of detection to one of characterization. More than 4000 exoplanets have been discovered and over 40 of them have been observed with transmission spectroscopy. The work in this dissertation has focused on (1) determining the chemical composition of exoplanet atmospheres, (2) providing plausible abundance estimates of these chemicals species, (3) exploring trends in these compositions to inform our understanding of planet formation, and (4) devising next-generation Bayesian frameworks to maximize the information we derive from transmission spectra in a physically plausible way.

During the four years of research that our work spans, the field of exoplanet sciences has significantly changed. Together, we have moved from using semi-analytic, isothermal, and isobaric atmospheric models (e.g., Heng & Kitzmann, 2017; Fisher & Heng, 2018) to numerical models with full pressure–temperature profiles, inhomogeneous cloud and haze coverage, and multiple molecular species (e.g., Welbanks & Madhusudhan, 2019, Chapter 2). Our population studies have evolved from being limited to studying the mass-metallicity relationship for hot Jupiters using H_2O abundances (e.g., Barstow et al., 2017; Pinhas et al., 2019), to a more diverse sample considering mini Neptunes as well as hot Jupiters and multiple metallicity tracers such as Na, K, and H_2O (e.g., Welbanks et al., 2019, Chapter 3). Our retrieval frameworks have relaxed previous assumptions applicable to H-rich atmospheres only (e.g., MacDonald & Madhusudhan, 2017a; Al-Refaie et al., 2019; Pinhas et al., 2019; Zhang et al., 2019, 2020) and have expanded their considerations to become more agnostic and applicable to any type of exoplanet atmosphere, both H-rich and H-poor (e.g., Welbanks & Madhusudhan, 2021, Chapter 4). The work in this dissertation has been a participant and contributor to the growth of the field over the last few years.

Below, we recapitulate some of the contributions of this thesis to the field of atmospheric characterization of exoplanets with transmission spectroscopy. We revisit the outstanding questions presented in Chapter 1 and offer answers based on the research presented in this dissertation. Then, we offer some insights into future directions our work may take. We conclude by presenting the final remarks for our work.

8.1 UNDERSTANDING THE LIMITATIONS OF RETRIEVALS OF EXOPLANETARY TRANSMISSION SPECTRA

Certainly, transmission spectroscopy of transiting exoplanets offers a powerful probe to study their atmospheres. The interpretation of such observations is routinely performed using Bayesian inference tools known as retrievals. At its core, a retrieval framework is composed of an atmospheric forward model that computes a synthetic spectrum and an optimization algorithm that extracts atmospheric constraints from the observables (see e.g., Madhusudhan, 2018). While the retrieval approach is a powerful means to derive atmospheric properties of exoplanets, their applicability is inherently limited by the quality (e.g., resolution, wavelength coverage, signal-to-noise) of the data being interpreted and the inherent model assumptions. Indeed, the use of different model assumptions and different data sets have led to contrasting results in the literature (e.g., Kreidberg et al. 2015 vs. Heng & Kitzmann 2017, Sing et al. 2016 vs. Barstow et al. 2017 vs. Pinhas & Madhusudhan 2017, Sheppard et al. 2017 vs. Arcangeli et al. 2018).

To address this problem, we have performed in Chapter 2 a systematic exploration of the degeneracies between different model considerations and the observations that can resolve them. This study used a combination of Bayesian atmospheric retrievals and a range of common model assumptions, focusing on H_2-rich atmospheres. The models considered increased in complexity and completeness, starting with simple isothermal and isobaric atmospheres (known to be unphysical) to those with full pressure–temperature profiles, inhomogeneous cloud and haze coverage, multiple molecular species (more physically plausible), and data in the optical–infrared wavelengths obtained with HST/STIS and HST/WFC3. This exploration of model considerations demonstrates that inferences derived from observations are strongly influenced by model assumptions.

Our work demonstrates that it is possible to overcome the aforementioned limitations by using a combination of physically motivated models with minimal assumptions and broadband transmission spectra with current facilities. We robustly demonstrate that precise estimates of chemical abundances are possible with current transmission spectra when using high-precision optical and infrared spectra, along with models including variable cloud coverage and prominent opacity sources. This work's key contribution to the field was demonstrating the shortcomings of semi-analytic models employed in previous studies (e.g., Heng

& Kitzmann, 2017; Fisher & Heng, 2018). Furthermore, we demonstrate that the degeneracy between planetary radius and its reference pressure, previously considered a fundamental hindrance for transmission spectra, is well characterized, and has little effect on the derived abundance estimates.

8.1.1 *Revisiting Outstanding Questions*

In Chapter 1 we presented the outstanding questions our work aimed to provide insights into. We revisit these questions and recapitulate the insights obtained from Chapter 2.

Q1: What are the data and model combinations that allow for precise estimates of chemical abundances using transmission spectra?

A1: Transmission spectra obtained with current facilities such as the Hubble Space Telescope (HST) and the Very Large Telescope (VLT) can provide strong constraints on atmospheric abundances of exoplanets if we use physically motivated models with minimal assumptions. High-precision optical and infrared spectra are paramount to provide highly constrained chemical abundances while helping constrain the range of possible planetary radii (R_p) and their associated reference pressures (P_{ref}).

Q2: Are there any inherent model degeneracies that fundamentally hinder parameter inferences?

A2: In transmission spectra, a strong degeneracy exists between R_p and P_{ref}. However, this degeneracy is well characterized and has little effect on parameter inferences.

Q3: What are the minimum model considerations required to adequately interpret current spectroscopic observations?

A3: For current spectroscopic observations, the atmospheric models must consider variable cloud coverage; prominent opacity sources, with Na and K being important in the optical; collision-induced absorption due to H_2-H_2 and H_2-He interactions; and full pressure-temperature profiles that may deviate from isothermal assumptions.

8.1.2 *Future Considerations*

While our work demonstrates that low resolution spectro-photometric observations with current facilities such as HST and VLT can provide strong constraints on atmospheric abundances of exoplanets, these considerations will continue to be explored in the context of upcoming facilities such as the James Webb Space Telescope (JWST) and the Extremely Large Telescopes (ELTs). The current modeling paradigm (e.g., 1-dimensional, simplistic clouds, minimal chemical assumptions) will undoubtedly need revision when confronted with observations comprised of higher resolution, longer spectral coverage, and better signal-to-noise anticipated over the next decade. Therefore, in order to maximize the scientific return of tomorrow's high fidelity observations, we must systematically examine the strengths and weaknesses of the current modeling paradigms in order to develop a foundation for the next-generation of atmospheric retrieval models.

8.2 HOMOGENEOUS STUDIES TO DETERMINE POPULATION LEVEL TRENDS

As explained in Chapter 1, an objective of extra-solar planetary science is to address population level hypotheses regarding the origin and evolution of planets. Previous studies (e.g., Madhusudhan et al., 2014b; Kreidberg et al., 2014b, 2015; Barstow et al., 2017; Pinhas et al., 2019), have attempted to determine H_2O abundances relative to solar system expectations. However, in order to break important degeneracies between the atmospheric metal content and the elemental carbon-to-oxygen ratios (Madhusudhan et al., 2014c), constraints on more species beyond H_2O were desperately needed.

In Chapter 3, and building upon the findings of Chapter 2, we investigate population level composition trends leveraging the most recent data spanning the optical-to-near-infrared, covering not only H_2O, but Na and K. The work shown in Chapter 3 constitutes the largest (i.e., broad wavelength coverage, multiple chemical species, mini Neptunes to Jupiter sized planets) homogeneous chemical abundance survey for transiting exoplanets to date. In total, we retrieved and analyze the atmospheric properties of 19 exoplanets ranging from cool mini Neptunes with temperatures close to 300 K to ultra-hot Jupiters with temperatures above 2700 K.

The novel contribution of our work was extending the analysis of the so-called mass-metallicity relationship to species beyond H_2O. We found a mass-metallicity trend for H_2O abundances significantly below that anticipated from the solar system gas giant planets (e.g., Atreya et al., 2018) and from core-accretion predictions (e.g., Fortney et al., 2013; Mordasini et al., 2016). Conversely, we found abundances of alkali species (Na and K) consistent with or higher than solar system derived metallicities. These results are suggestive of superstellar C/O, Na/O, and K/O ratios, meaning stellar or superstellar metallicities but depleted oxygen relative to other species. By acknowledging that different chemical species provide different insights into the atmospheric properties of an exoplanet, this approach was able to break the important degeneracy between C/O ratios and atmospheric metallicity prevalent up to then in the field.

The consistent depletion of H_2O, relative to solar expectations, suggests planet formation pathways that differ from the standard solar system paradigm for longer period planets. Furthermore, the differing trends among the various species (H_2O, Na, K) argue against the use of more constrained retrieval models that rely upon scaled solar elemental abundances – an additional indication that modeling assumptions have a strong influence on atmospheric compositional inferences. Below we revisit the outstanding questions presented in Chapter 1.

8.2.1 *Revisiting Outstanding Questions*

We presented the following questions in Chapter 1; here we provide some answers.

Q1: Is there a mass-metallicity trend for transiting exoplanets from atmospheric abundances of H_2O, Na, and K?

A1: Our work finds a mass-metallicity trend of increasing H_2O abundances with decreasing mass, spanning generally substellar values for gas giants and stellar/superstellar for Neptunes and mini Neptunes. On the other hand, the gas giants exhibit Na and K abundances consistent with or higher than those of their host stars.

Q2: If any mass-metallicity trends are observed, are they consistent with solar system expectations? are they consistent within themselves?

A2: The overall trend in H_2O abundances, from mini Neptunes to hot Jupiters, is significantly lower than the mass-metallicity relation

for carbon in the solar system giant planets and similar predictions for exoplanets. The Na and K abundances are consistent the solar system trend. Additionally, the Na and K elemental ratios are consistent with each other.

Q3: Are there any constraints we can place on planetary formation mechanisms from the derived chemical atmospheric abundances?

A3: The inferred low H_2O abundances in hot gas giants are unlikely to be due to low O/H or low overall metallicities, considering the higher alkali enrichments in some planets. Instead, the H_2O underabundance and alkali enrichment are likely due to an overall stellar or superstellar metallicity but oxygen depleted relative to other species. Future studies could further investigate the avenues to explain the observed trends and place constraints on planetary formation mechanisms.

8.2.2 *Future Considerations*

Upcoming spectroscopic observations, especially those with JWST at longer wavelengths, will inform whether these observed trends are statistically significant and whether they exist for other chemical species. Additionally, expanding the above sample may help identify outliers to the observed trend. For instance, resolving the possible instrumental systematics in the transmission spectrum of HAT-P-41b, as conducted in Chapter 7, could help us determine whether this hot Jupiter has a metal-rich atmosphere. Likewise, resolving the prior dependency of WASP-39b uncovered in Chapter 3 will help us better inform the trend of inferred low H_2O abundances. For the case of WASP-39b, resolving this problem may be a possibility in the short term when the Transiting Exoplanet Community Early Release Science Program with JWST (Program ERS 1366) obtains its first observations of the planet's atmosphere with JWST NIRISS, NIRCam, and NIRSpec.

8.3 DEVELOPMENT OF NEXT-GENERATION AGNOSTIC EXO-ATMOSPHERE BAYESIAN INFERENCE FRAMEWORKS

The lessons derived from Chapter 2 and Chapter 3, alongside our contributions to the interpretation of recent transmission spectra presented in Chapter 6 and Chapter 7, highlight that the inferences derived from observations are strongly influenced by model assumptions. As a result,

part of the journey in this dissertation has been to build the tools that can take us towards the generalized characterization of exoplanet atmospheres with transit spectroscopy. Such tools ought to be agnostic, meaning flexible and applicable to a wide range of systems. These agnostic tools have minimal assumptions, and are cognizant of their limitations. Furthermore, these retrieval frameworks are highly adaptive and modular to address the needs of current and upcoming observations. This has been the goal of Chapter 4 and Chapter 5; to develop next-generation agnostic Bayesian modeling frameworks.

In Chapter 4 we have presented the methods for developing Aurora, a next-generation retrieval framework for the characterization of H-rich and H-poor atmospheres. Then, in Chapter 5 we have demonstrated the capabilities of our framework. Currently, Aurora is the only retrieval framework that relaxes the assumption of a H-rich atmosphere to retrieve the atmospheric composition of any type of exoplanet atmosphere, while considering the presence of inhomogeneous clouds and hazes. This new framework considerably expands the model flexibility required for explaining higher fidelity observations. Focused on transmission spectra, which, due to their geometry, require more complex forward models, Aurora incorporates several optimization and data analysis tools like Gaussian processes to treat correlated noise and next-generation Bayesian samplers.

Aurora provides key contributions to the development of retrieval frameworks. First, we have updated the methods of compositional data analysis to reparameterize the volume mixing ratios, used in traditional retrievals of exoplanet atmospheres, into compositional parameters for the nested sampling algorithm. This advancement allows for agnostic retrievals where the bulk composition of the atmosphere is inferred from the data instead of being assumed a priori. Aurora has expanded the scope of previous atmospheric retrievals beyond their assumptions of H-rich atmospheres. Second, we have introduced a new generalized treatment for inhomogeneous clouds and hazes. This new treatment mitigates biases and limitations in previous prescriptions. Then, Aurora incorporates the next generation of nested sampling algorithms. These enable our framework to handle highly degenerate problems and problems of higher dimensionality. Finally, the modular structure of Aurora is designed to evolve with the needs of future spectroscopic observations. We have incorporated several new modules to expand our noise modeling capabilities beyond the traditional assumed independently distributed Gaussian errors, and to compute forward models considering the effects

of light refraction, forward scattering, and Mie scattering due to condensates.

In Chapter 5 we contribute to the field of exoplanetary atmospheric characterization by applying this new framework to current and/or synthetic observations of the hot Jupiter HD 209458 b, mini Neptune K2-18b, and rocky exoplanet TRAPPIST-1 d, and providing an estimate of the constraints we may obtain when using agnostic retrieval tools. On current observations of HD 209458 b, we find that the cloud and haze prescription introduced in this dissertation results in a higher model evidence than previous inhomogeneous cloud and haze prescriptions. Additionally, we find that our more conservative abundance estimates for current observations of HD 209458 b result in a median H_2O abundance that is still subsolar based on expectations of thermochemical equilibrium, but consistent with a solar value to within 1σ. Nonetheless, while the H_2O abundance is largely subsolar, both Na and K abundances are significantly super-solar, implying a relative depletion in H_2O compared to Na and K as found in Chapter 3.

Our results for the mini Neptune K2-18b find that for current observations, different nested sampling algorithms are consistent with each other. Using synthetic observations, we find that future observations of K2-18b with JWST will make it possible to unequivocally retrieve the bulk gas composition in the atmosphere, improving on present-day estimates derived using current K2, HST/WFC3, and Spitzer observations. Additionally, future abundance estimates of mini Neptunes could result in precisions of ~ 0.5 dex or better. Then, through our results for future observations of rocky exoplanets, we contribute to the growing efforts to assess the potential to characterize the TRAPPIST-1 system. We find that 10 JWST transits of TRAPPIST-1 d could enable clear detections and abundance constraints of H_2O in a cloud-free, N_2-rich or CO_2-rich atmosphere. Furthermore, 10 JWST transits could enable initial indications of O_3 if present at enhanced levels ($\sim 10\times$–$100\times$ Earth levels) in a cloud-free N_2-rich atmosphere.

8.3.1 *Revisiting Outstanding Questions*

We presented the following questions in Chapter 1:

Q1: What are the modeling advancements required to model H-rich and H-poor atmospheres using atmospheric retrieval frameworks?

A1: We have presented those methods in Chapter 4 and applied them in Chapter 5. Generally speaking, when retrieving the chemical abundances of H-poor atmospheres, we must allow for all chemical species to have the same prior probability density in a permutation-invariant prescription. The tools developed by the subfield of statistics called compositional data analysis can be useful (e.g., Pearson, 1897; Tanner, 1949; Chayes, 1960; Aitchison, 1986; Aitchison & Egozcue, 2005; Benneke & Seager, 2013). Correctly implementing such methods will allow a retrieval framework to be applicable to both H-rich and H-poor atmospheres.

Q2: Do existing Bayesian inference algorithms provide consistent parameter estimates for exoplanet atmospheres using existing data?

A2: We have demonstrated that different implementations of the nested sampling algorithm provide consistent parameter estimates for exoplanet atmospheres using existing data. Future studies may explore the impact of different nested sampling algorithms on data previously considered problematic (e.g., WASP-39b).

Q3: Can we perform agnostic retrievals on existing and upcoming spectroscopic observations of exoplanetary atmospheres to constrain their bulk composition?

A3: Our results suggest that we can constrain the bulk atmospheric composition of exoplanets using agnostic retrievals on existing and upcoming observations. Nonetheless, our inferences for upcoming observations are based on synthetic data. Assessing agnostic retrievals on actual JWST or ELTs data will be enlightening.

Q4: How many transits using the upcoming JWST are required to characterize a rocky exoplanet?

A4: The number of transits with JWST required for the chemical characterization of rocky exoplanets can vary depending on the system parameters, the instrument of choice, and the desired precision on the retrieved atmospheric properties. Our results, using synthetic spectra for TRAPPIST-1 d, suggest that 10 JWST-NIRSpec transits can enable identification of the main atmospheric component for cloud-free, CO_2-rich, and N_2-rich atmospheres. However, this number of transits may be significantly higher in the presence of clouds and hazes. Our suggestion of of 10 JWST-NIRSpec transits is specific to the cases considered in this dissertation.

8.3.2 *Future Considerations*

Aurora incorporates key developments fundamental for the future of atmospheric characterization with transmission spectroscopy. For instance, this framework incorporates new optimization algorithms designed to ease the computational burden when performing parameter estimation in multidimensional atmospheric models. Furthermore, important considerations in the interpretation of transmission spectra such as the impact of stellar heterogeneity, correlated noise, instrumental shifts, and underestimated variances in the data are included within Aurora's framework. This more advanced modeling framework will be essential to reliably extracting atmospheric properties from the data of today and tomorrow.

Nonetheless, additional modeling advancements will be important for the next generation of observations. As explained in Section 5.5 in Chapter 5, additional considerations about the presence of clouds and hazes in these mini Neptunes remain to be explored. Future studies could investigate the need for more complex cloud and haze models in retrievals when interpreting observations of mini Neptunes. Likewise, future studies could expand our current retrieval framework to incorporate multidimensional P–T profiles and nonuniform mixing ratios, just as we have done for clouds and hazes. Lastly, when assessing the potential for characterizing rocky exoplanets, considering more complex atmospheric compositions with multiple absorbers and different atmospheric processes could better inform our estimates.

8.4 INTERPRETING SPACE-BASED AND GROUND-BASED TRANSMISSION SPECTRA OF TRANSITING EXOPLANETS

In Chapter 6 and Chapter 7 we have shown our contribution to recent studies obtaining and interpreting transmission spectra of exoplanets obtained with ground and space-based facilities. Our retrieval models have helped obtain constraints on the atmospheric properties of hot Jupiters, hot sub-Saturns, and even temperate mini Neptunes. In Chapter 1 we suggest that our work aims to answer the question 'What are the achievable atmospheric constraints using the latest spectroscopic data obtained with ground- and space-based facilities?'. While the answer to that question is planet and spectra specific, we can assert that current facilities allow for abundance constraints with precisions close to 0.5 dex. Additionally, high-precision observations coupled with Bayesian atmospheric

retrievals can provide us indications for the presence of multiple chemical species in these exoplanet atmospheres.

These works have contributed to the field by demonstrating the capabilities of ground-based facilities to detect, and quantify the abundances of, alkali species with absorption signatures in the optical. Likewise, these works have demonstrated that space-based observatories, particularly HST, are essential to provide constraints on the presence and abundance of H_2O and other volatiles. Some of the previously unidentified chemical species uncovered by our retrieval analyses (e.g., Li in WASP-127b and AlO in WASP-33b), if confirmed by future observations and subsequent retrieval studies, will contribute to the field by illustrating the broad diversity in planetary atmospheric composition. If, on the other hand, these suggestions are later disproved, our results highlight the importance of interpreting Bayesian detection significances as a model preference and not as the unequivocal detection of new physics (see also Chapter 4).

Our work has unveiled the atmospheric properties of several intriguing exoplanets. Two cases of particular interest to our understanding of mass-metallicity relations in exoplanets are KELT-11b and HAT-P-41b. Their retrieved abundances are suggestive of a subsolar metallicity for KELT-11b, and a metal rich atmosphere for HAT-P-41b. However, these inferences are based on spectra of limited wavelength coverage (e.g., KELT-11b) and with possible instrumental systematics (e.g., HAT-P-41b). As a result, the need for developing and implementing advanced retrieval frameworks that can take into account these data limitations is one of the main outcomes of these works. Additionally, the high-precision and instrumental systematics of these data sets are a prelude for future observations with JWST and the ELTs.

Our contribution to the analysis of K2-18b and WASP-21b highlight two important future directions for the field of exoplanetary characterization. On the one hand, our retrieval analysis of the transmission spectrum of K2-18b confirms the presence of H_2O in the atmosphere of a planet in the habitable zone of its host star. Additionally, we find a suprising depletion of CH_4 and NH_3 which may indicate chemical disequilibrium in the atmosphere of the planet. Our retrieved atmospheric properties were then used by Madhusudhan et al. (2020) to model the interior of the planet. This new 'end-to-end' approach for characterizing exoplanets, may be an important avenue for future studies looking to simultaneously constrain the atmosphere and interior of an exoplanet. On the other hand, our analysis of the transmission spectrum of WASP-

21b suggested the presence of Na in the atmosphere of the planet. This suggestion was then confirmed with high-resolution spectroscopic observations in the same study by Chen et al. (2020). Characterizing exoplanet atmospheres with complementary techniques both at high- and low-resolution will most likely be advantageous as we look into the future. Such combined approach would enable robust and reliable constraints for the atmospheric properties of exoplanets.

8.5 FUTURE DIRECTIONS

Although we are about to reach the end of this dissertation, we are far from done with the many research avenues still to investigate. The methods and concepts introduced in this work will continue to be developed over the upcoming years to answer outstanding questions in the field. Additionally, over the next decade we will have dramatically transcended as a field from having very limited data and, often conflicting, knowledge of exoplanet atmospheres to having credible and exquisite observations. This data revolution will undoubtedly invite us to revise our assumed ability to reliably extract physical parameters, such as atmospheric pressure-temperature and abundances, and our understanding of the limits of the data. Here we present some of the many outstanding questions and considerations still to be pursued and which may be a starting point for future research endeavors:

- In Chapter 2 we have revised the modeling paradigm for current spectro-photometric observations. However, what are the minimum model assumptions that our atmospheric models should have when interpreting observations with JWST and the ELTs?
- How will the mass-metallicity trends presented in Chapter 3 change with upcoming observations with JWST and the ELTs? Could we provide constraints based on other chemical species? How could we combine the atmospheric constraints obtained from other characterization methods (e.g., high-resolution spectroscopy)?
- In Chapter 4 we have introduced a new generalized prescription for the presence of inhomogenous clouds and hazes. However, a full exploration of the different degeneracies and biases in different cloud and haze prescriptions will be key in refining future parametric prescriptions. Therefore, we could ask ourselves, what are the model improvements required to constrain the physical properties of clouds and hazes with future observations?

- In Chapter 7 we found a planet with a potentially high atmospheric metallicity? Can we confirm this? Are there any outliers to the mass-metallicity trend presented in Chapter 3?
- Several considerations for the treatment of instrumental systematics and unaccounted noise sources remain to be explored. Future studied may explore the impact of these noise sources in the inferred atmospheric properties.

These questions highlight that we are at the beginning of an extraordinary growth in the field of exoplanetary atmospheric characterization. The improvements in observational facilities over the upcoming decades invite us to perform a corresponding examination of the core modeling assumptions inevitably employed to infer basic planetary conditions. Only by performing a comprehensive analysis of our existing model assumptions can we ensure that the inferences derived from these revolutionary data sets are believable. These joint efforts will help us maximize the scientific output of our shared endeavors.

8.6 FINAL REMARKS

We stand at the dawn of a new day for exoplanetary sciences. The most recent estimates suggest that by mid 2022 JWST will start its cycle 1 of science observations. If true, as early as next year we will start obtaining data at wavelengths never probed before. The secrets that these observations will uncover are bound to transform the landscape of the field. Then by sometime in 2025, the Extremely Large Telescope with its enormous 39-meter primary will receive its first light. With both JWST and ELT potentially operational within 5 years of this dissertation, the precision, wavelength coverage, and resolution of future spectroscopic observations will be unlike anything we have ever seen before.

Then, the next generation of survey missions will arrive. PLATO, the PLAnetary Transits and Oscillations of stars mission, promises to find and study a large number of exoplanets, with emphasis on the properties of terrestrial planets in the habitable zone around solar-like stars (Rauer et al., 2014). This mission, currently under development, and scheduled to launch in 2026, will provide us with attractive targets for atmospheric characterization followup. Then, ARIEL, the Atmospheric Remote-sensing Infrared Exoplanet Large-survey will pursue a chemical census of a large ($\gtrsim 1000$) and diverse sample of warm and hot exoplanets (Puig et al., 2018). This mission, currently scheduled for 2029, will

provide us for the first time with a much larger sample of exoplanet transit spectra to perform chemical surveys and further address population level hypotheses. We could almost expect that by this point, the outlook of exoplanetary sciences may be completely unrecognizable from today's point of view.

Finally, with such a rapid progress, we can only hypothesize what may happen in the next decade. We will most likely be preparing and talking about the subsequent generation of multi-wavelength space telescopes. At the time of writing this dissertation, we eagerly await the 2020 decadal survey report. Such document will help us understand which will be the next large mission through which we will explore the universe. Will it be HabEx (Gaudi et al., 2020), LUVOIR (The LUVOIR Team, 2019), the Origins Space Telescope (The OST mission concept study team, 2018), or Lynx (Gaskin et al., 2018)? Whichever the selected mission, finding and characterizing an Earth analogue may be possible in the not too distant future. Likewise the Thirty Meter Telescope (expected first light in 2027) and the Giant Magellan Telescope (expected commissioning in 2029) will collect more light than any telescope ever built. The joint efforts from ground and space-based facilities in the 2030s open up the possibility for detecting biosignatures within our lifetime.

In a nutshell, we can only expect to continue to be surprised by Nature. Theoretical and observational efforts will open our minds to the vastness of the Universe and the worlds within it. Characterization of exoplanets at both high- and low-resolution may very well uncover whether there is life somewhere else in our galaxy. Furthermore, with time we will learn about what currently are unknown unknowns. Together, past and future generations, we will continue to find our place in this Universe – our home.

Part II

APPENDIX

A

SUPPLEMENTARY INFORMATION FOR CHAPTER 2

Here we report additional figures and tables for the retrievals performed in Chapter 2. Figures 52 to 54 show the posterior distributions for X_{H_2O}, P_{ref}, and R_p and the correlations between them for cases 0 to 12. In Figure 55 we show the full posterior distributions for all parameters for the full retrieval case, case 12, discussed in Section 2.3.13. Tables 11 and 12 show the parameters retrieved for all the 12 cases along with the prior ranges and retrieved values.

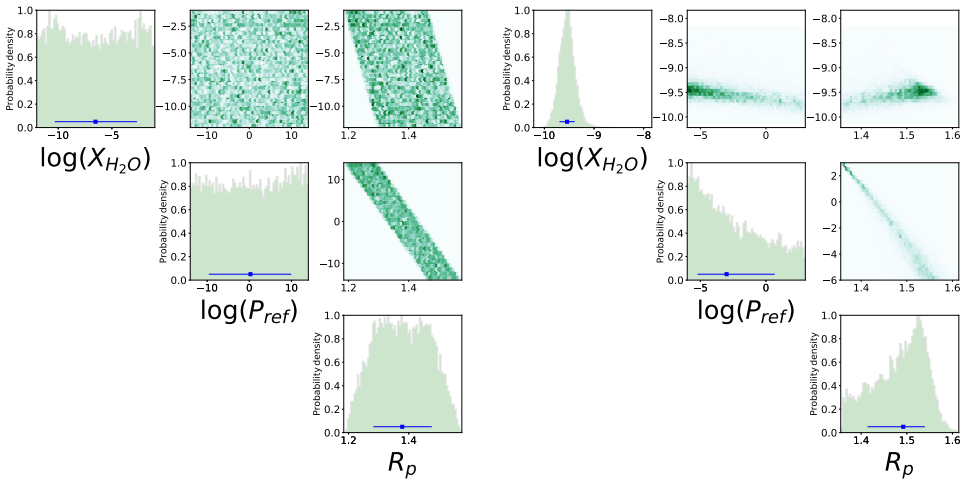

(Case 0) (Case 1)

Figure 52 Posterior distributions for cases 0 and 1 from Section 2.3.

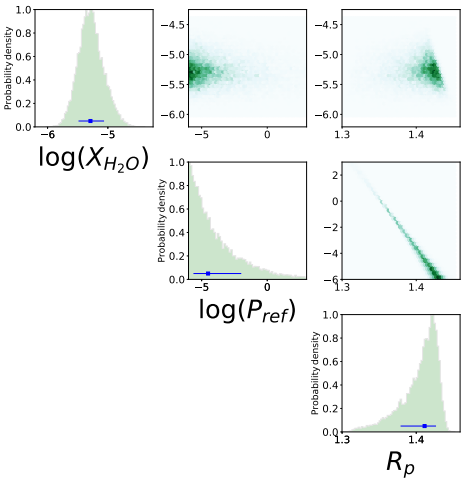

(Case 2)

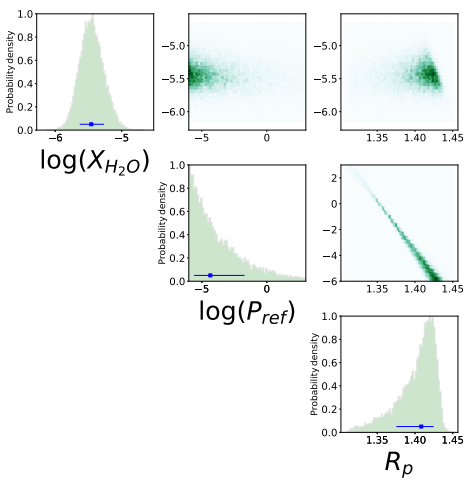

(Case 3)

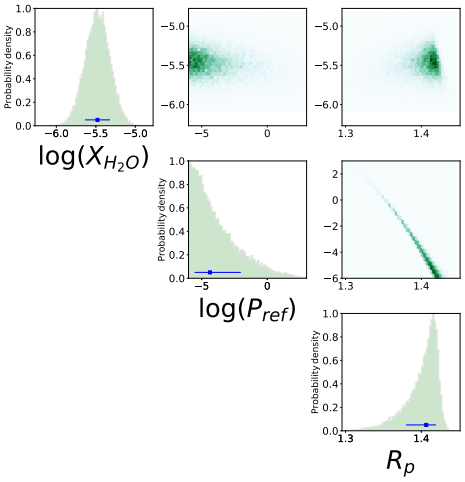

(Case 4)

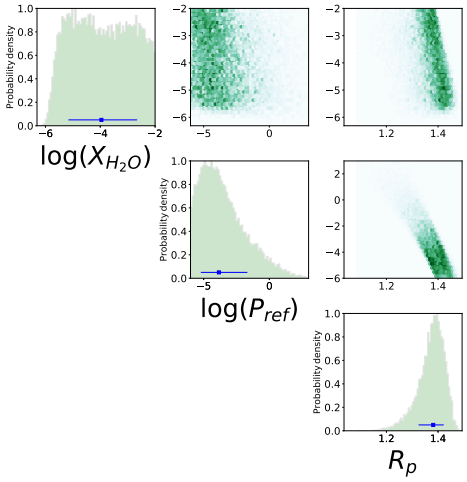

(Case 5)

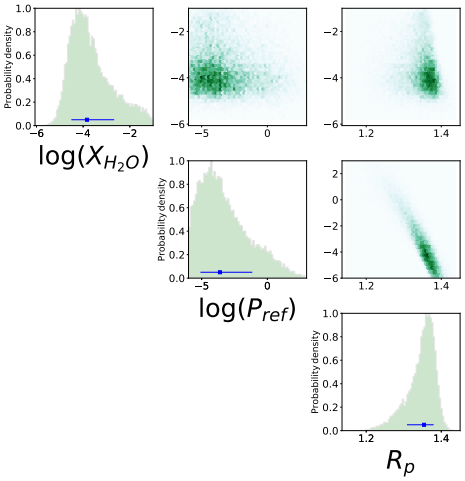

(Case 6)

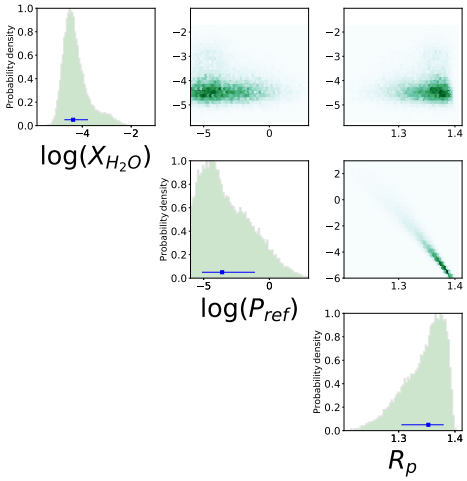

(Case 7)

Figure 53 Posterior distributions for cases 2-7 from Section 2.3.

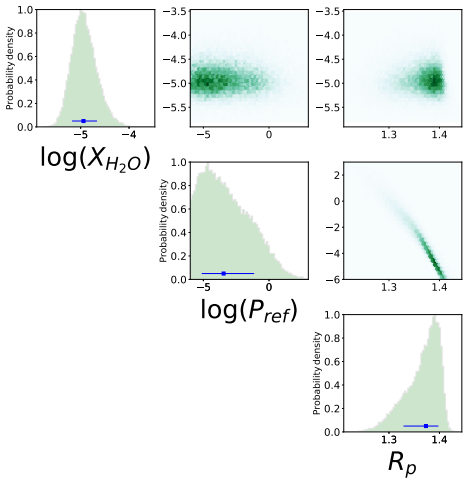

(Case 8)

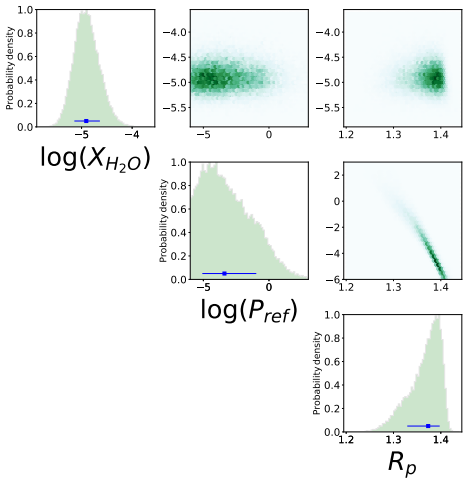

(Case 9)

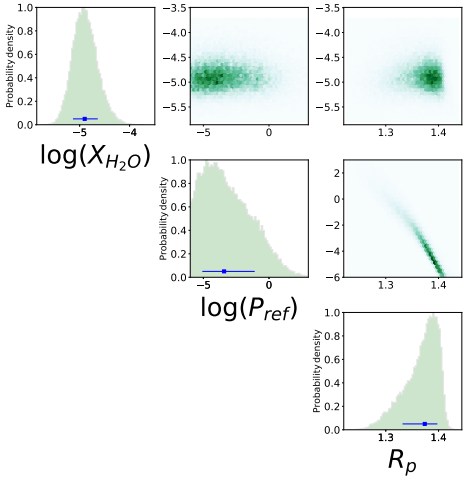

(Case 10)

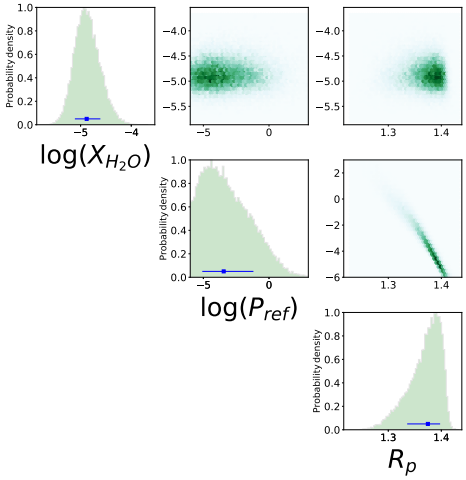

(Case 11)

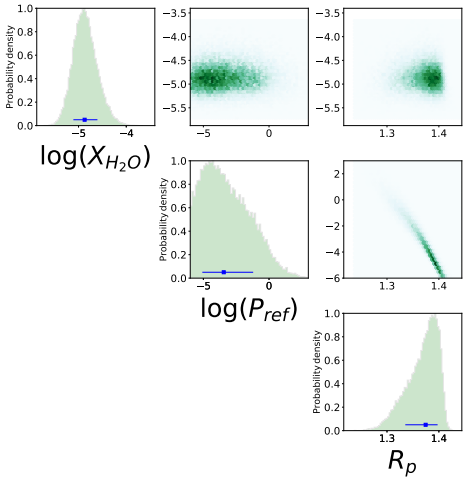

(Case 12)

Figure 54 Posterior distributions for cases 8-12 from Section 2.3.

Table 11 Results from Retrievals of Cases 1-6 as Discussed in Section 2.3.

	PARAMETER	PRIORS	CASE 1	CASE 2	CASE 3	CASE 4*	CASE 5*	CASE 6
	R_p (R_J)	0.1, 3.0	$1.49^{+0.05}_{-0.08}$	$1.41^{+0.02}_{-0.03}$	$1.41^{+0.02}_{-0.03}$	$1.41^{+0.01}_{-0.03}$	$1.38^{+0.04}_{-0.06}$	$1.35^{+0.03}_{-0.05}$
	$\log_{10}(P_{ref})$ (bar)	−6, 3	$-3.00^{+3.67}_{-2.21}$	$-4.51^{+2.53}_{-1.11}$	$-4.35^{+2.63}_{-1.25}$	$-4.36^{+2.35}_{-1.18}$	$-3.84^{+2.17}_{-1.37}$	$-3.61^{+2.46}_{-1.48}$
	$\log_{10}(X_{H_2O})$	−12, −1	$-9.54^{+0.15}_{-0.15}$	$-5.29^{+0.23}_{-0.20}$	$-5.46^{+0.19}_{-0.17}$	$-5.48^{+0.16}_{-0.16}$	$-3.96^{+1.30}_{-1.21}$	$-3.83^{+1.17}_{-0.67}$
P–T Parameters	T_0 (K)	800, 2710	$2003.65^{+248.72}_{-247.72}$	$1070.21^{+87.56}_{-92.10}$	$1046.02^{+89.50}_{-95.51}$	$870.11^{+82.12}_{-49.12}$	$1940.56^{+251.87}_{-305.81}$	$1262.74^{+225.05}_{-230.98}$
	α_1	0.02, 1.00				$0.85^{+0.11}_{-0.14}$	$0.68^{+0.20}_{-0.23}$	$0.65^{+0.21}_{-0.21}$
	α_2	0.02, 1.00				$0.67^{+0.22}_{-0.32}$	$0.60^{+0.24}_{-0.25}$	$0.60^{+0.25}_{-0.25}$
	$\log_{10}(P_1)$ (bar)	−6, 3				$-0.77^{+1.88}_{-2.35}$	$-1.30^{+1.88}_{-1.78}$	$-1.22^{+1.86}_{-1.84}$
	$\log_{10}(P_2)$ (bar)	−6, 3				$-3.61^{+2.40}_{-1.62}$	$-3.86^{+1.88}_{-1.39}$	$-3.90^{+2.00}_{-1.34}$
	$\log_{10}(P_3)$ (bar)	−2, 3				$1.45^{+1.10}_{-1.76}$	$1.19^{+1.16}_{-1.66}$	$1.27^{+1.13}_{-1.65}$
Cloud Parameters	$\log_{10}(a)$	−4, 8					$0.39^{+3.81}_{-2.73}$	$2.09^{+3.93}_{-3.88}$
	γ	−20, 2					$-12.14^{+7.38}_{-4.97}$	$-8.60^{+7.87}_{-7.40}$
	$\log_{10}(P_{cloud})$ (bar)	−6, 2					$-2.74^{+1.24}_{-1.27}$	$-4.70^{+1.33}_{-0.85}$
	$\bar{\phi}$	0, 1						$0.68^{+0.05}_{-0.06}$

Note. The uniform priors and the parameter estimates are shown for cases 1-6; the remaining cases are shown in Table 12. *The $\log_{10}(X_{H_2O})$ prior for cases 4 and 5 is −12, −2.

Table 12 Results from Retrievals of Cases 7-12 as Discussed in Section 2.3.

	PARAMETER	PRIORS	CASE 7	CASE 8	CASE 9	CASE 10	CASE 11	CASE 12
	R_p (R_J)	0.1, 3.0	$1.35^{+0.03}_{-0.05}$	$1.37^{+0.02}_{-0.04}$	$1.37^{+0.02}_{-0.04}$	$1.37^{+0.02}_{-0.04}$	$1.37^{+0.02}_{-0.04}$	$1.37^{+0.02}_{-0.04}$
	$\log_{10}(P_{ref})$ (bar)	−6, 3	$-3.59^{+2.49}_{-1.54}$	$-3.46^{+2.33}_{-1.67}$	$-3.39^{+2.43}_{-1.69}$	$-3.42^{+2.33}_{-1.66}$	$-3.45^{+2.26}_{-1.63}$	$-3.45^{+2.24}_{-1.63}$
	$\log_{10}(X_{H_2O})$	−12, −1	$-4.37^{+0.61}_{-0.36}$	$-4.94^{+0.28}_{-0.24}$	$-4.91^{+0.27}_{-0.24}$	$-4.90^{+0.26}_{-0.23}$	$-4.88^{+0.27}_{-0.23}$	$-4.87^{+0.27}_{-0.24}$
P–T Parameters	T_0 (K)	800, 2710	$1306.40^{+225.24}_{-257.81}$	$1064.75^{+283.29}_{-185.88}$	$1026.44^{+276.52}_{-161.11}$	$1026.72^{+262.72}_{-157.60}$	$1013.53^{+248.73}_{-149.27}$	$1022.15^{+246.41}_{-153.72}$
	α_1	0.02, 1.00	$0.71^{+0.19}_{-0.22}$	$0.59^{+0.25}_{-0.17}$	$0.62^{+0.24}_{-0.18}$	$0.61^{+0.23}_{-0.18}$	$0.62^{+0.23}_{-0.18}$	$0.60^{+0.23}_{-0.17}$
	α_2	0.02, 1.00	$0.67^{+0.21}_{-0.26}$	$0.47^{+0.33}_{-0.21}$	$0.49^{+0.32}_{-0.22}$	$0.49^{+0.32}_{-0.22}$	$0.49^{+0.31}_{-0.22}$	$0.50^{+0.31}_{-0.23}$
	$\log_{10}(P_1)$ (bar)	−6, 3	$-1.34^{+2.02}_{-1.84}$	$-1.16^{+1.98}_{-1.79}$	$-1.18^{+1.97}_{-1.77}$	$-1.14^{+1.94}_{-1.77}$	$-1.15^{+1.93}_{-1.78}$	$-1.03^{+1.88}_{-1.79}$
	$\log_{10}(P_2)$ (bar)	−6, 3	$-3.79^{+1.99}_{-1.45}$	$-3.89^{+2.24}_{-1.43}$	$-3.95^{+2.19}_{-1.39}$	$-3.87^{+2.15}_{-1.44}$	$-3.90^{+2.14}_{-1.42}$	$-3.86^{+2.16}_{-1.42}$
	$\log_{10}(P_3)$ (bar)	−2, 3	$1.23^{+1.20}_{-1.91}$	$1.22^{+1.21}_{-1.60}$	$1.25^{+1.18}_{-1.59}$	$1.29^{+1.15}_{-1.55}$	$1.26^{+1.16}_{-1.55}$	$1.33^{+1.13}_{-1.54}$
Cloud Parameters	$\log_{10}(a)$	−4, 8	$7.65^{+0.24}_{-0.43}$	$4.42^{+0.71}_{-1.26}$	$4.38^{+0.70}_{-1.16}$	$4.38^{+0.69}_{-1.14}$	$4.34^{+0.69}_{-1.11}$	$4.37^{+0.68}_{-1.08}$
	γ	−20, 2	$-8.97^{+1.07}_{-0.88}$	$-14.42^{+5.59}_{-3.76}$	$-14.67^{+5.19}_{-3.57}$	$-14.70^{+5.17}_{-3.55}$	$-14.63^{+4.99}_{-3.59}$	$-14.61^{+4.93}_{-3.58}$
	$\log_{10}(P_{cloud})$ (bar)	−6, 2	$-5.29^{+0.25}_{-0.16}$	$-4.69^{+0.77}_{-0.50}$	$-4.57^{+0.77}_{-0.56}$	$-4.57^{+0.76}_{-0.54}$	$-4.52^{+0.73}_{-0.54}$	$-4.52^{+0.72}_{-0.55}$
	$\bar{\phi}$	0, 1	$0.69^{+0.04}_{-0.05}$	$0.49^{+0.06}_{-0.06}$	$0.47^{+0.06}_{-0.08}$	$0.47^{+0.06}_{-0.08}$	$0.46^{+0.06}_{-0.08}$	$0.46^{+0.06}_{-0.08}$
Chemical Species	$\log_{10}(X_{Na})$	−12, −2		$-5.55^{+0.53}_{-0.44}$	$-5.53^{+0.51}_{-0.43}$	$-5.52^{+0.52}_{-0.43}$	$-5.50^{+0.51}_{-0.42}$	$-5.48^{+0.52}_{-0.43}$
	$\log_{10}(X_K)$	−12, −2		$-7.17^{+0.55}_{-0.52}$	$-7.13^{+0.54}_{-0.51}$	$-7.11^{+0.54}_{-0.49}$	$-7.09^{+0.54}_{-0.50}$	$-7.07^{+0.54}_{-0.51}$
	$\log_{10}(X_{NH_3})$	−12, −2			$-8.02^{+1.86}_{-2.64}$	$-8.14^{+1.95}_{-2.56}$	$-8.11^{+1.90}_{-2.52}$	$-8.09^{+1.89}_{-2.54}$
	$\log_{10}(X_{CO})$	−12, −2				$-7.74^{+2.85}_{-2.72}$	$-7.75^{+2.82}_{-2.73}$	$-7.73^{+2.79}_{-2.75}$
	$\log_{10}(X_{HCN})$	−12, −2					$-8.60^{+2.26}_{-2.17}$	$-8.57^{+2.24}_{-2.22}$
	$\log_{10}(X_{CO_2})$	−12, −2						$-8.46^{+2.43}_{-2.30}$

Note. The uniform priors and the parameter estimates are shown for cases 7-12; the remaining cases are shown in Table 11.

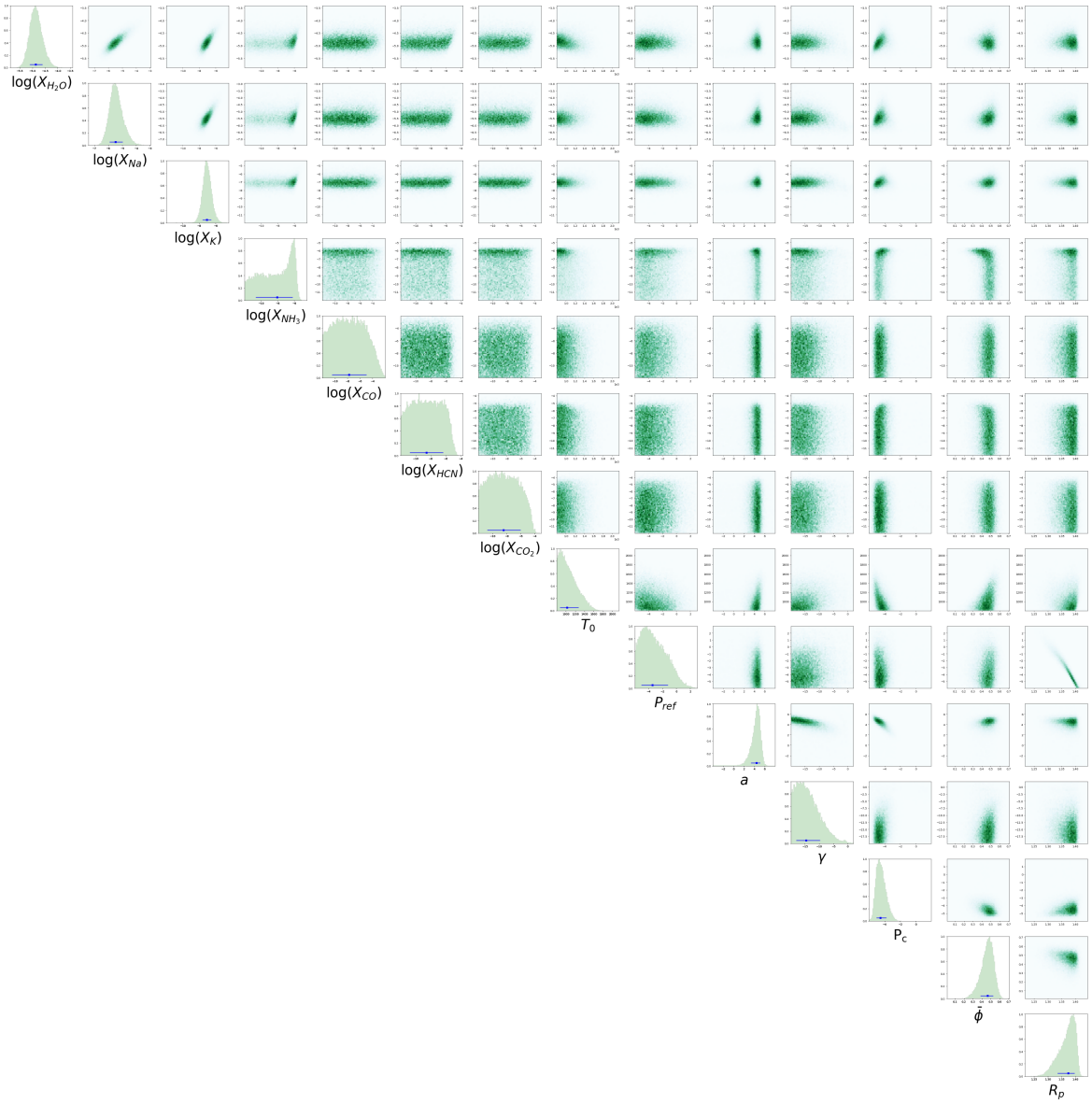

Figure 55 Posterior distribution for the parameters of interest for case 12 as explained in Sections 2.3 and 2.3.13. The parameter T_0, the temperature at the top of the atmosphere (10^{-6} bar), is shown as a subset of the P-T parameters used in the model. This is a full retrieval of HD 209458 b using data in the near-infrared and optical wavelengths from Sing et al. (2016). The model includes the effects H_2-H_2 and H_2-He CIA opacity; absorption from H_2O, Na, K, NH_3, CO, HCN, and CO_2; a parametric P–T profile; and the presence of clouds/hazes. Both R_p and P_{ref} are simultaneously retrieved.

B

SUPPLEMENTARY INFORMATION FOR CHAPTER 3

Here we report additional information for the retrievals performed in Chapter 3. Table 13 shows the assumed exoplanetary masses for the mass-metallicity trends shown in Chapter 3. Then Table 14 reports the parameters and priors used in Chapter 3. Lastly, Table 15 shows the host star metallicities used for comparing the retrieved planetary abundances to stellar expectations.

Table 13 Planetary Masses

#	PLANET NAME	$M_P(M_J)$	REFERENCE
1	K2-18b	0.03	Cloutier et al. (2019)
2	GJ3470b	0.04	Biddle et al. (2014)
3	HAT-P-26b	0.06	Hartman et al. (2011)
4	HAT-P-11b	0.07	Yee et al. (2018)
5	WASP-107b	0.12	Anderson et al. (2017)
6	WASP-127b	0.18	Lam et al. (2017)
7	HAT-P-12b	0.21	Sing et al. (2016)
8	WASP-39b	0.28	Sing et al. (2016)
9	WASP-31b	0.48	Sing et al. (2016)
10	WASP-96b	0.48	Hellier et al. (2014)
11	WASP-6b	0.50	Sing et al. (2016)
12	WASP-17b	0.51	Sing et al. (2016)
13	HAT-P-1b	0.53	Sing et al. (2016)
14	HD 209458b	0.69	Sing et al. (2016)
15	HD 189733b	1.14	Sing et al. (2016)
16	WASP-19b	1.14	Sing et al. (2016)
17	WASP-12b	1.40	Sing et al. (2016)
18	WASP-43b	2.03	Gillon et al. (2012)
19	WASP-33b	2.10	Lehmann et al. (2015)

Note. Planet mass quoted as nominal value; uncertainties are not considered. Values were rounded to two decimal places.

Table 14 Parameters and Priors for the Homogeneous Retrievals in Chapter 3.

PARAMETER	PRIOR DISTRIBUTION	PRIOR RANGE
X_i	Log-uniform	$10^{-12} - 10^{-1}$ for M> $0.3M_J$ $10^{-12} - 10^{-0.3}$ for M < $0.3M_J$
T_0	Uniform	$0 - T_{eq.} + 100$ K for $T_{eq.} < 900$ K $400 - T_{eq.} + 100$ K for $900 < T_{eq.} < 1200$ K $800 - T_{eq.} + 100$ K for $T_{eq.} > 1200$ K
$\alpha_{1,2}$	Uniform	$0.02 - 2.00$ $K^{-1/2}$
$P_{1,2}$	Log-uniform	$10^{-6} - 10^{2}$ bar
P_3	Log-uniform	$10^{-2} - 10^{2}$ bar
a	Log-uniform	$10^{-4} - 10^{10}$
γ	Uniform	-20 – 2
P_{cloud}	Log-uniform	$10^{-6} - 10^{2}$ bar
$\bar{\phi}$	Uniform	$0 - 1$
$\lambda_{shift}{}^*$	Uniform	-0.1 – 0.1 μm

Note. The wavelength shift $\lambda_{shift}{}^*$ was employed in the retrieval of WASP-19b only, as performed by Sedaghati et al. (2017). Similarly γ had a uniform prior between −60 and 2 for WASP-19b. Two different retrievals were performed for WASP-39b with different prior ranges for X_i: $10^{-12} - 10^{-0.3}$ and $10^{-12} - 10^{-1}$.

Table 15 Host Star Metallicities for the Sample of 19 Exoplanets

#	STAR NAME	[O/H]	[C/H]	[NA/H]	[K/H]	[FE/H]	OTHER	REFERENCE
1	K2-18	-	-	-	-	0.123	-	Benneke et al. (2017)
2	GJ-3470	-	-	-	-	0.18	-	Biddle et al. (2014)
3	HAT-P-26	-	-	-	-	−0.04	-	Hartman et al. (2011)
4	HAT-P-11	-	-	-	-	0.31	-	Yee et al. (2018)
5	WASP-107	-	-	-	-	0.02	-	Anderson et al. (2017)
6	WASP-127	-	-	-	-	−0.18	-	Lam et al. (2017)
7	HAT-P-12	-	-	-	-	−0.29	-	Hartman et al. (2009)
8	WASP-39	-	-	−0.04	-	−0.12	-	Faedi et al. (2011)
9	WASP-31	0.07	−0.08	−0.16	-	−0.06	-	Brewer et al. (2016)
10	WASP-96	-	-	-	-	0.14	-	Hellier et al. (2014)
11	WASP-6	-	-	−0.17	-	−0.20	-	Gillon et al. (2009)
12	WASP-17	0.09	−0.44	−0.2	-	0.01	-	Brewer et al. (2016)
13	HAT-P-1	-	-	-	-	0.13	-	Torres et al. (2008)
14	HD209458	0.09	0.03	−0.01	-	0.06	-	Brewer et al. (2016)
15	HD189733	0.07	0.04	0.05	-	0.07	-	Brewer et al. (2016)
16	WASP-19	0.18	0.13	0.17	-	0.22	-	Brewer et al. (2016)
17	WASP-12	0.33	0.09	0.19	-	0.22	-	Brewer et al. (2016)
18	WASP-43	-	-	-	-	−0.01	-	Gillon et al. (2012)
19	WASP-33	-	-	-	-	-	[M/H]= 0.1	Collier Cameron et al. (2010)

Note. For stars without [Na/H], [O/H] or [K/H] estimates we adopt the [Fe/H] or [M/H] values.

C

SUPPLEMENTARY INFORMATION FOR CHAPTERS 4 AND 5

Here we report additional information for the retrievals and models in Chapters 4 and 5.

C.1 ADDITIONAL FORWARD-SCATTERING AND REFRACTION MODELS FOR A ROCKY EXOPLANET

For completion, we consider the effects of wavelength-dependent refraction and forward scattering presented in Chapter 4, Section 4.6.3, on the rocky exoplanet TRAPPIST-1 d. We consider the same N_2-rich atmospheric model used in Chapter 5, Section 5.4. Namely, we consider an atmosphere composed of 77.51% N_2, 21.38% O_2, 1% H_2O, 0.1% CO_2, and 0.01% O_3. The model spectra are generated at a constant resolution of $R = 5000$ between 0.3 and 5.5 μm, and smoothed for the purposes of Figure 56.

When considering the effects of wavelength-dependent refraction, we specifically include N_2 refraction as our atmospheric model is N_2-rich. The forward model considering the effects of forward scattering uses the same assumptions as in Chapter 4, Section 4.6.3 (i.e., $g = 0.95$ and $\tilde{\omega}_o = 1$) and the planet-star orbital separation reported by Agol et al. (2021). Figure 56 shows these forward models and their respective model residuals.

These model considerations have a stronger effect in this rocky exoplanet test case than in the mini Neptune test case presented in Chapter 4, Section 4.6.3. The impact of N_2 refraction results in a model difference of ~ 12 ppm. On the other hand, forward scattering results in a model difference $\lesssim 2$ ppm. The impact of these considerations is $\sim 3\times$ stronger in this TRAPPIST-1 d case than in the K2-18b case presented in the main text. Nonetheless, these results are dependent on the assumed synthetic model considerations and should not be generalized to other test cases beyond the ones considered here.

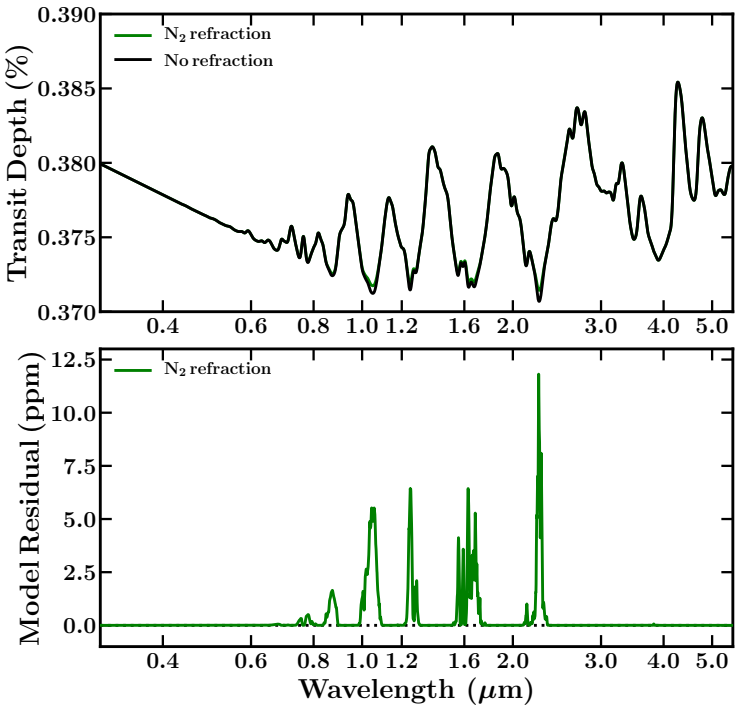

(a) Wavelength-dependent refraction

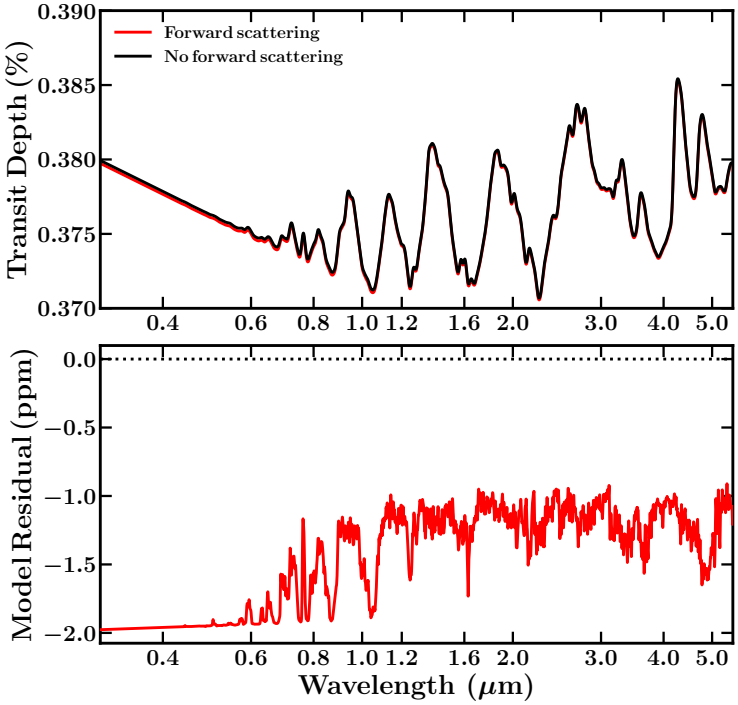

(b) Forward scattering

Figure 56 (a) Effects of wavelength-dependent refraction and (b) forward scattering for a TRAPPIST-1 d-like rocky exoplanet. The top panels show the forward model without these effects considered (black), the model with N_2 refraction (green), and the model considering forward scattering (red). The bottom panels show the model residuals.

C.2 PROCEDURE FOR SIMULATING JWST OBSERVATIONS

Here we report additional information for simulating the synthetic JWST observations in Chapter 5.

C.2.1 *PANDEXO Input for K2-18b*

The assumed stellar spectrum for K2-18 is interpolated from the Phoenix Stellar Atlas (Husser et al., 2013) by PANDEXO assuming $T_{eff} = 3457$ K (Benneke et al., 2019c), [Fe/H]$= 0.12$ (Sarkis et al., 2018), $\log_{10}(g) = 4.858$ cgs (Crossfield et al., 2016), $R_{star} = 0.4445\ R_{\odot}$ (Benneke et al., 2019c), and a K-band magnitude of 8.899. We assume a transit duration of 2.663 hr (Benneke et al., 2017). The in-transit and out-of-transit fluxes are computed using this stellar spectrum and a constant transit-depth model assuming a planet radius of 2.61 $R_{\oplus}$ (Benneke et al., 2019c).

Our simulated observations assume a saturation limit of 80% full well and an extremely optimistic noise floor of 5 ppm. Our assumed noise floor is much smaller than expectations from Greene et al. (2016) and Beichman & Greene (2018). The upcoming JWST Cycle 1 will better inform the existence of a possible systematic noise floor. Nonetheless, given that the noise in our synthetic observations at the native resolution of the gratings is much higher than noise floor expectations, our choice of 5 ppm has little impact on our results. We generate these synthetic observations for one transit and the number of groups per integration suggested by PANDEXO following the *optimize* option. The number of groups per integration is 13, 14, and 25 for G140H, G235H, and G395H respectively. Once the observations are simulated using PANDEXO, we proceed bin every two pixels to obtain individual spectral resolution elements. Subsequently, we remove any resolution elements that fall within the gaps in the spectral configurations chosen; namely 1.31–1.35 μm for G140H/F100LP, 2.20–2.27 μm for G235H/F170LP and 3.72–3.82 μm for G395H/F290LP. After this, we remove any outlier elements with noise levels above 500 ppm for G140H and G235H, and 400 ppm for G395H. We proceed to bin the observations every 40 resolution elements, remove any binned elements that fall within the gaps in the spectral configurations chosen, and obtain an average resolution of $R \sim 70$. The synthetic observations have a mean precision of ~ 26 ppm, ~ 30 ppm, and ~ 39 ppm, for G140H, G235H, and G395H, respectively.

C.2.2 *PANDEXO Input for TRAPPIST-1 d*

The assumed stellar spectrum is interpolated from the Phoenix Stellar Atlas assuming T_{eff} = 2566 K (Agol et al., 2021), [Fe/H]= 0.04, R_{star} = 0.1170 $R_{\odot}$ (Gillon et al., 2017), $\log_{10}(g)$ = 5.2396 cgs (Agol et al., 2021), and a K-band magnitude of 10.296. We assume a transit duration of 48.87 minutes (Agol et al., 2021). The in-transit and out-of-transit fluxes are computed using this stellar spectrum and a a constant transit-depth model assuming a planet radius of 0.788 $R_{\oplus}$ (Agol et al., 2021).

We maintain the assumption of a saturation limit of 80% full well and an optimistic noise floor of 5 ppm. We generate the observations for 10 NIRSpec prism transits and 2 groups per integration. The instrument configuration for PANDEXO uses aperture S1600A1 and subarray SUB512. We bin every two pixels to obtain individual resolution elements. We remove any elements with precisions larger than 300 ppm, leaving elements $\gtrsim$ 0.7 and $\lesssim$ 5.3 μm.

C.3 PRIORS USED IN CHAPTER 5

As explained in Chapter 4, Section 4.5, the priors for the parameters in Chapter 5 are mostly standard prescriptions and adopted from previous studies (e.g., Pinhas et al., 2019; Welbanks et al., 2019, see also Appendix B). Table 16 presents the parameters and priors used in Chapter 5.

C.4 VALIDATION OF AURORA ON HD 209458 B

In Chapter 5, Section 5.1, we validate Aurora's retrieval capabilities on the transmission spectrum of HD 209458 b from Sing et al. (2016). Table 17 presents the retrieved parameters for this spectrum under different model considerations explained in Chapter 5, Section 5.1.

Table 16 Parameters and Priors Used in Chapter 5.

PARAMETER	PRIOR DISTRIBUTION	PRIOR RANGE
X_i	Log-uniform	10^{-12}-10^{0} for H-rich retrievals of HD 209485b (Section 5.1) 10^{-12}-$10^{-0.3}$ for H-rich retrievals of K2-18b (Section 5.2 and 5.3.1)
z_i	Uniform	−4.61-23.03 for non-H-rich retrievals with 6 chemical components (Section 5.4) −3.45-24.18 for non-H-rich retrievals with 8 chemical components (Section 5.3.1) −3.07-24.56 for non-H-rich retrievals with 9 chemical components (Section 5.1) −2.76-24.87 for non-H-rich retrievals with 10 chemical components (Section 5.3.1)
T_0	Uniform	0-300 K for retrievals of K2-18b 0-400 K for retrievals of TRAPPIST-1 d 800-1550 K for retrievals of HD 209458 b
$\alpha_{1,2}$	Uniform	0.02-2.00 $K^{-1/2}$
$P_{1,2,cloud,ref}$	Log-uniform	10^{-6}-10^{2} bar
P_3	Log-uniform	10^{-2}-10^{2} bar
a	Log-uniform	10^{-4}-10^{10}
γ	Uniform	-20-2
ϕ_{clouds} ϕ_{hazes} $\phi_{clouds+hazes}$	Uniform	0-1

Note. The priors for the compositional parameters (z_i) are reported here to two decimal places and calculated for the purposes of this table. The compositional parameter priors are automatically calculated by Aurora given the condition that they must span the range 10^{-12}-10^{0} in the X_i space and that they must satisfy the conditions explained in Section 4.4.

Table 17 Retrieved Parameters for the Spectrum of HD 209458 b Using Different Cloud and Haze Models, as well as Assuming a H-rich Atmosphere or Not as Explained in Section 5.1.

PARAMETER	Model 0 H-rich	Model 0 no H-rich	Model 1 H-rich	Model 1 no H-rich	Model 2 H-rich	Model 2 no H-rich	Model 3 H-rich	Model 3 no H-rich
$\log_{10}(X_{H_2+He})$	N/A	$-6.03^{+1.38}_{-2.18} \times 10^{-06}$	N/A	$-1.99^{+0.97}_{-2.84} \times 10^{-05}$	N/A	$-9.52^{+7.49}_{-120.49} \times 10^{-05}$	N/A	$-1.94^{+1.68}_{-34.22} \times 10^{-04}$
$\log_{10}(X_{H_2O})$	$-4.98^{+0.13}_{-0.14}$	$-4.99^{+0.13}_{-0.14}$	$-4.53^{+0.34}_{-0.28}$	$-4.48^{+0.29}_{-0.27}$	$-4.06^{+0.73}_{-0.51}$	$-4.00^{+0.68}_{-0.51}$	$-3.89^{+0.78}_{-0.62}$	$-3.81^{+0.73}_{-0.63}$
$\log_{10}(X_{Na})$	$-6.75^{+0.20}_{-0.21}$	$-6.74^{+0.20}_{-0.22}$	$-5.43^{+0.62}_{-0.49}$	$-5.35^{+0.54}_{-0.43}$	$-4.34^{+1.55}_{-0.99}$	$-4.23^{+1.45}_{-0.99}$	$-3.95^{+1.71}_{-1.27}$	$-3.80^{+1.57}_{-1.27}$
$\log_{10}(X_{K})$	$-7.94^{+0.24}_{-0.25}$	$-7.92^{+0.23}_{-0.26}$	$-6.96^{+0.63}_{-0.51}$	$-6.90^{+0.54}_{-0.45}$	$-6.04^{+1.44}_{-0.96}$	$-5.96^{+1.40}_{-0.93}$	$-5.73^{+1.65}_{-1.15}$	$-5.58^{+1.51}_{-1.18}$
$\log_{10}(X_{CH_4})$	$-6.25^{+0.58}_{-3.44}$	$-6.13^{+0.47}_{-2.45}$	$-8.62^{+2.11}_{-2.23}$	$-8.09^{+1.62}_{-1.84}$	$-8.28^{+2.28}_{-2.44}$	$-7.71^{+1.83}_{-2.14}$	$-8.19^{+2.33}_{-2.52}$	$-7.56^{+1.88}_{-2.23}$
$\log_{10}(X_{NH_3})$	$-5.93^{+0.11}_{-0.13}$	$-5.92^{+0.11}_{-0.13}$	$-6.57^{+0.80}_{-3.48}$	$-6.42^{+0.67}_{-2.80}$	$-6.40^{+1.10}_{-3.59}$	$-6.18^{+0.96}_{-2.93}$	$-6.77^{+1.50}_{-3.48}$	$-6.33^{+1.17}_{-2.95}$
$\log_{10}(X_{HCN})$	$-9.83^{+1.97}_{-1.47}$	$-9.02^{+1.64}_{-1.46}$	$-9.44^{+2.26}_{-1.74}$	$-8.76^{+1.71}_{-1.50}$	$-9.37^{+2.37}_{-1.76}$	$-8.50^{+2.00}_{-1.75}$	$-9.25^{+2.44}_{-1.87}$	$-8.39^{+2.12}_{-1.79}$
$\log_{10}(X_{CO})$	$-7.08^{+1.43}_{-1.65}$	$-6.76^{+1.26}_{-1.43}$	$-6.33^{+1.62}_{-1.85}$	$-6.16^{+1.42}_{-1.49}$	$-5.93^{+1.79}_{-1.98}$	$-5.62^{+1.66}_{-1.76}$	$-5.76^{+1.90}_{-2.02}$	$-5.38^{+1.70}_{-1.87}$
$\log_{10}(X_{CO_2})$	$-10.19^{+1.47}_{-1.22}$	$-9.42^{+1.17}_{-1.21}$	$-9.94^{+1.64}_{-1.40}$	$-9.22^{+1.23}_{-1.22}$	$-9.69^{+1.80}_{-1.55}$	$-9.02^{+1.51}_{-1.40}$	$-9.65^{+1.85}_{-1.61}$	$-8.89^{+1.60}_{-1.49}$
T_0 (K)	$810.55^{+14.87}_{-7.71}$	$810.36^{+14.43}_{-7.51}$	$972.42^{+265.03}_{-126.67}$	$984.32^{+225.59}_{-125.41}$	$1064.53^{+283.25}_{-195.12}$	$1062.14^{+282.43}_{-192.28}$	$1081.01^{+277.22}_{-202.50}$	$1076.33^{+267.44}_{-197.43}$
α_1	$1.74^{+0.19}_{-0.32}$	$1.74^{+0.18}_{-0.32}$	$1.17^{+0.54}_{-0.52}$	$1.17^{+0.49}_{-0.46}$	$1.10^{+0.59}_{-0.53}$	$1.11^{+0.58}_{-0.53}$	$1.04^{+0.62}_{-0.54}$	$1.06^{+0.61}_{-0.54}$
α_2	$1.48^{+0.37}_{-0.65}$	$1.47^{+0.37}_{-0.63}$	$0.97^{+0.68}_{-0.58}$	$1.03^{+0.57}_{-0.54}$	$1.00^{+0.65}_{-0.59}$	$1.01^{+0.64}_{-0.59}$	$0.99^{+0.67}_{-0.59}$	$0.99^{+0.65}_{-0.59}$
$\log_{10}(P_1)$ (bar)	$-1.78^{+1.93}_{-1.94}$	$-1.78^{+1.96}_{-1.88}$	$-1.61^{+1.68}_{-1.72}$	$-1.51^{+1.46}_{-1.51}$	$-1.56^{+1.66}_{-1.76}$	$-1.57^{+1.66}_{-1.74}$	$-1.61^{+1.67}_{-1.77}$	$-1.62^{+1.68}_{-1.73}$
$\log_{10}(P_2)$ (bar)	$-3.89^{+1.83}_{-1.40}$	$-3.90^{+1.85}_{-1.35}$	$-4.13^{+1.92}_{-1.29}$	$-4.01^{+1.60}_{-1.26}$	$-4.07^{+1.92}_{-1.34}$	$-4.11^{+1.91}_{-1.28}$	$-4.14^{+1.92}_{-1.30}$	$-4.09^{+1.84}_{-1.31}$
$\log_{10}(P_3)$ (bar)	$0.52^{+1.06}_{-1.67}$	$0.46^{+1.09}_{-1.66}$	$0.62^{+0.96}_{-1.32}$	$0.67^{+0.84}_{-1.11}$	$0.64^{+0.95}_{-1.37}$	$0.62^{+0.94}_{-1.33}$	$0.59^{+0.97}_{-1.34}$	$0.60^{+0.95}_{-1.34}$
$\log_{10}(P_{ref})$ (bar)	$-0.71^{+0.06}_{-0.06}$	$-0.72^{+0.06}_{-0.05}$	$-2.64^{+0.66}_{-0.63}$	$-2.70^{+0.55}_{-0.56}$	$-3.15^{+0.79}_{-0.73}$	$-3.18^{+0.76}_{-0.71}$	$-3.33^{+0.79}_{-0.64}$	$-3.37^{+0.80}_{-0.63}$
$\log_{10}(a)$	N/A	N/A	$4.35^{+0.71}_{-1.01}$	$4.49^{+0.56}_{-0.65}$	$2.88^{+0.91}_{-0.85}$	$2.96^{+0.85}_{-0.85}$	$3.28^{+1.01}_{-1.13}$	$3.34^{+0.92}_{-1.07}$
γ	N/A	N/A	$-14.04^{+4.53}_{-3.94}$	$-14.54^{+3.85}_{-3.31}$	$-16.57^{+3.15}_{-2.37}$	$-16.60^{+2.93}_{-2.29}$	$-16.15^{+3.36}_{-2.60}$	$-16.27^{+3.25}_{-2.50}$
$\log_{10}(P_{cloud})$ (bar)	N/A	N/A	$-4.41^{+0.80}_{-0.57}$	$-4.47^{+0.56}_{-0.50}$	$-4.60^{+0.99}_{-0.91}$	$-4.65^{+0.97}_{-0.86}$	$-4.72^{+0.99}_{-0.84}$	$-4.74^{+0.99}_{-0.82}$
ϕ_{clouds}	N/A	N/A	N/A	N/A	$0.60^{+0.07}_{-0.11}$	$0.59^{+0.07}_{-0.11}$	$0.34^{+0.18}_{-0.20}$	$0.35^{+0.17}_{-0.20}$
ϕ_{hazes}	N/A	N/A	N/A	N/A	$0.30^{+0.09}_{-0.07}$	$0.30^{+0.08}_{-0.07}$	$0.27^{+0.09}_{-0.10}$	$0.27^{+0.09}_{-0.09}$
$\phi_{cloud+hazes}$	N/A	N/A	$0.54^{+0.09}_{-0.12}$	$0.53^{+0.08}_{-0.10}$	N/A	N/A	$0.24^{+0.19}_{-0.16}$	$0.24^{+0.19}_{-0.15}$
$\log(\mathcal{Z})$	949.74	946.68	957.70	951.35	958.14	955.38	958.40	955.74

Note. N/A means that the parameter not considered in the model by construction.

C.5 POSTERIOR DISTRIBUTIONS FOR K2-18B USING SYNTHETIC OBSERVATIONS

We present in Figure 57 the posterior distribution from the retrieval on synthetic observations of K2-18b as performed in Chapter 5, Section 5.3.2.

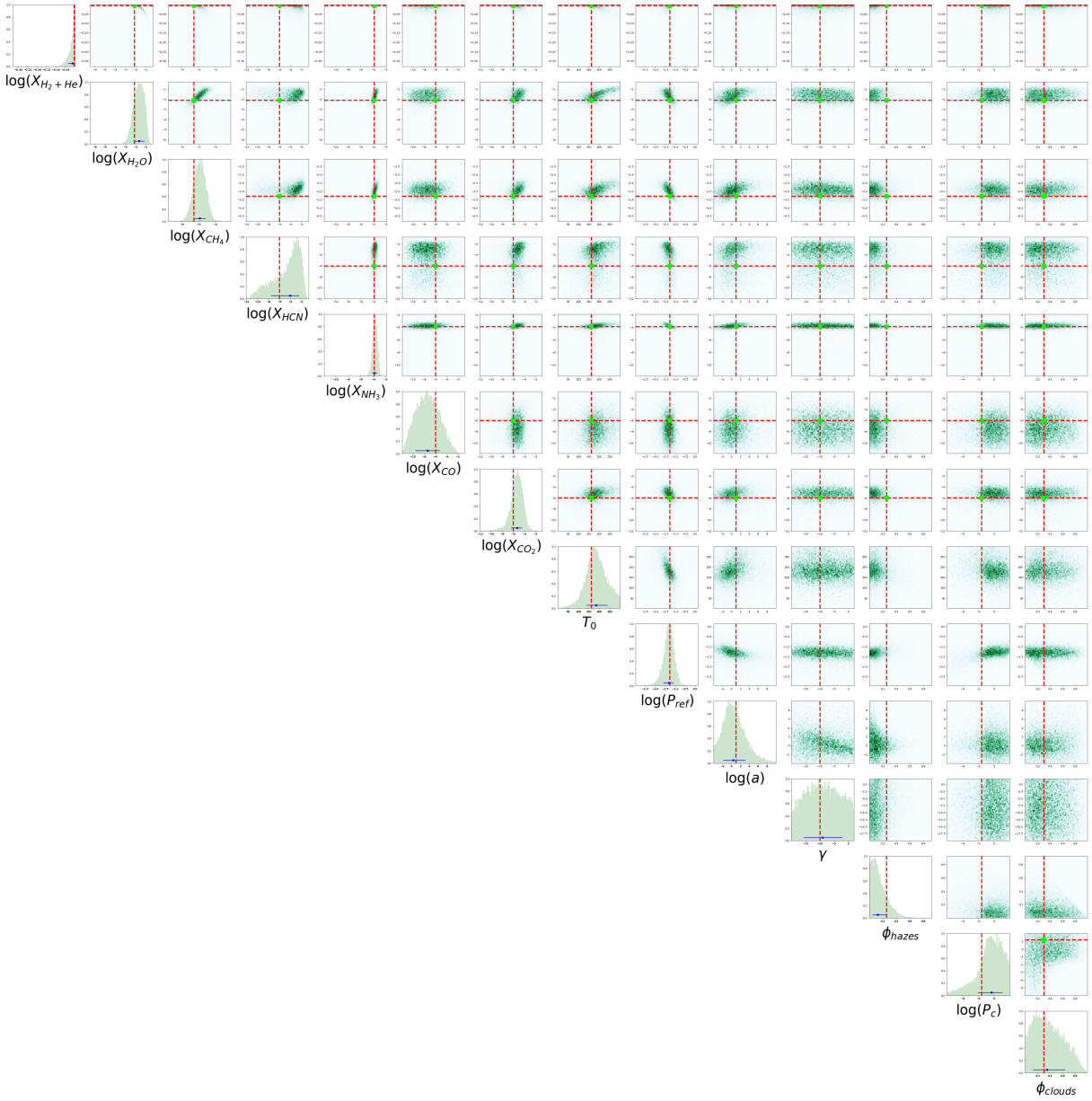

Figure 57 Posterior distributions of the relevant parameters for the retrieval of synthetic HST-STIS and JWST-NIRSpec observations of K2-18b (see Section 5.3.2). The retrieval does not assume a H-rich atmosphere. The input parameters for the true model are shown using vertical dashed red lines.

D

SUPPLEMENTARY INFORMATION FOR CHAPTER 6

Here we report additional information for the retrievals performed in Chapter 6. Figures 58, 59, and 60 show the retrieved posterior distributions for the atmospheric retrievals discussed in Chapter 6.

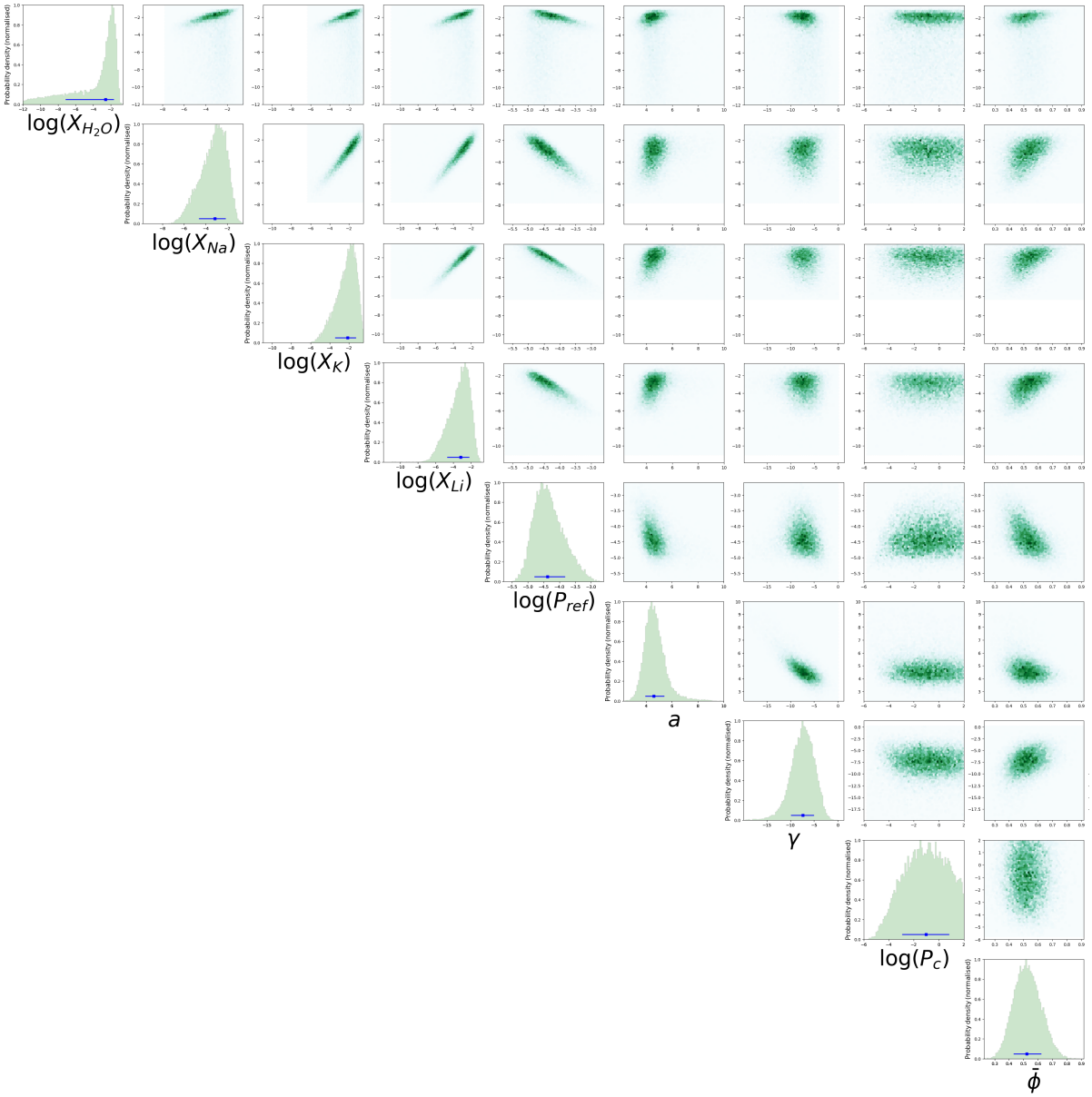

Figure 58 WASP-127b: Marginalized posterior probability densities for the retrieved species and haze parameters with the reference planet radius fixed at $R_p = 1.37\ R_{Jup}$.

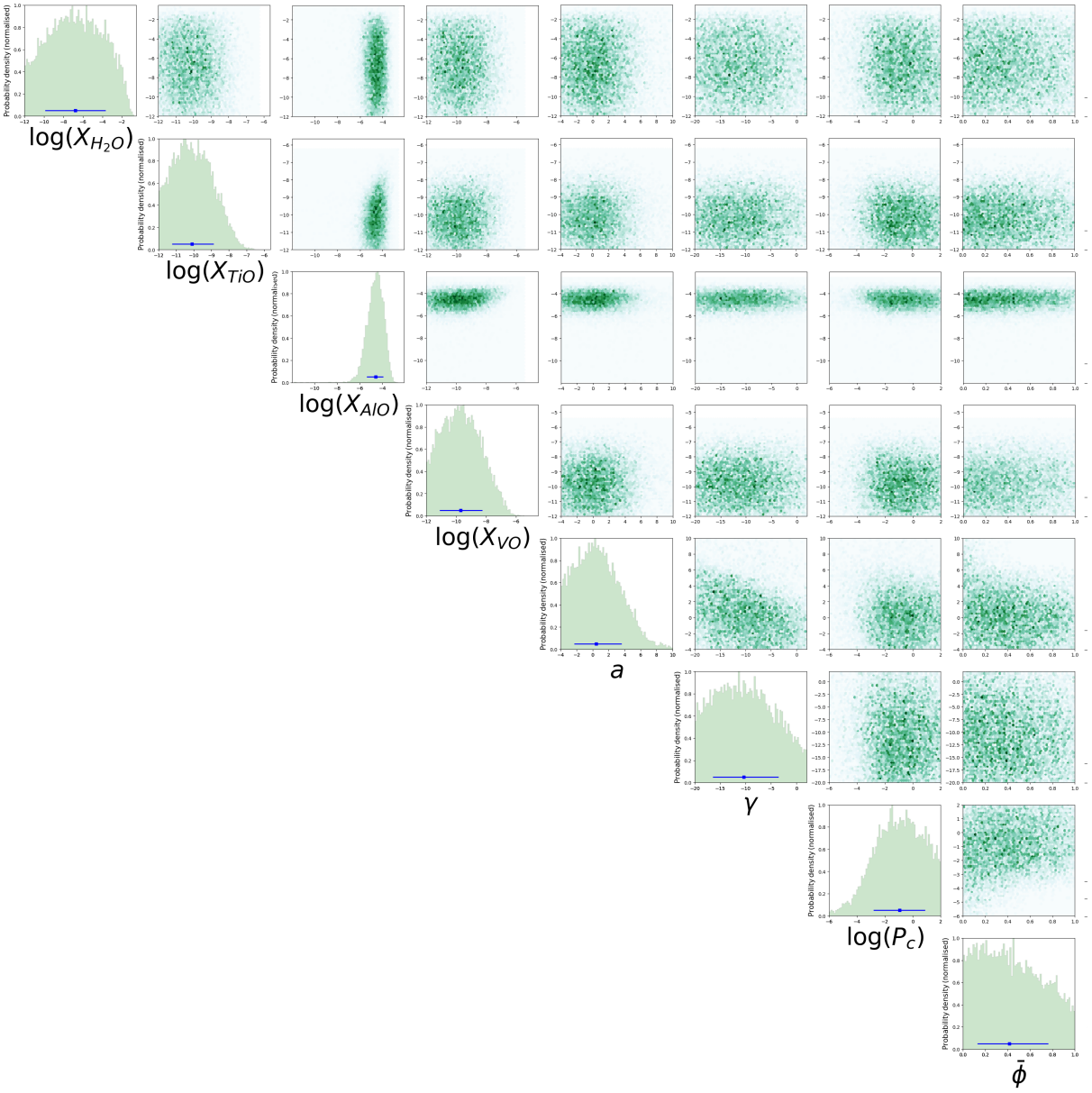

Figure 59 WASP-33b: Marginalized posterior probability densities for the detected molecule (AlO) and the molecules for which upper bounds have been determined (TiO and VO), along with the cloud/haze parameters. The posterior distribution for water is included for reference.

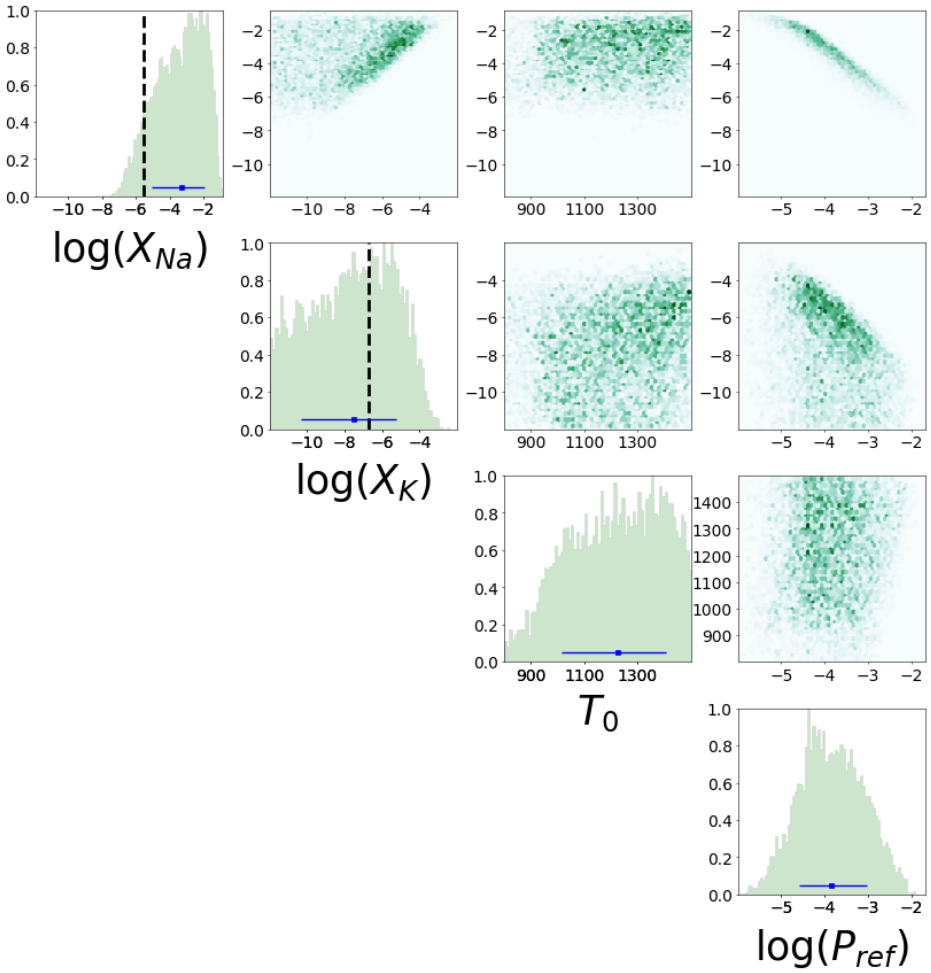

Figure 60 Posterior distribution for the simplified model retrieval of WASP-21b's transmission spectrum. This four parameter model is the highest evidence model and considers absorption due to Na and K only in a clear isothermal atmosphere. Na and K solar abundance expectations are shown using black dashed lines.

E

SUPPLEMENTARY INFORMATION FOR CHAPTER 7

Here we report additional information for the retrievals performed in Chapter 7. Figures 61, 62, 63 show the posterior probability densities for the different model and data considerations in the retrieval of KELT-11b. Additional information on the retrieved atmospheric properties of KELT-11b using models considering instrumental offsets is shown in Table 18. Then, Figures 64 and 65 show the posterior probability densities for the retrieval of HAT-P-41b using a fiducial and simplified model, respectively.

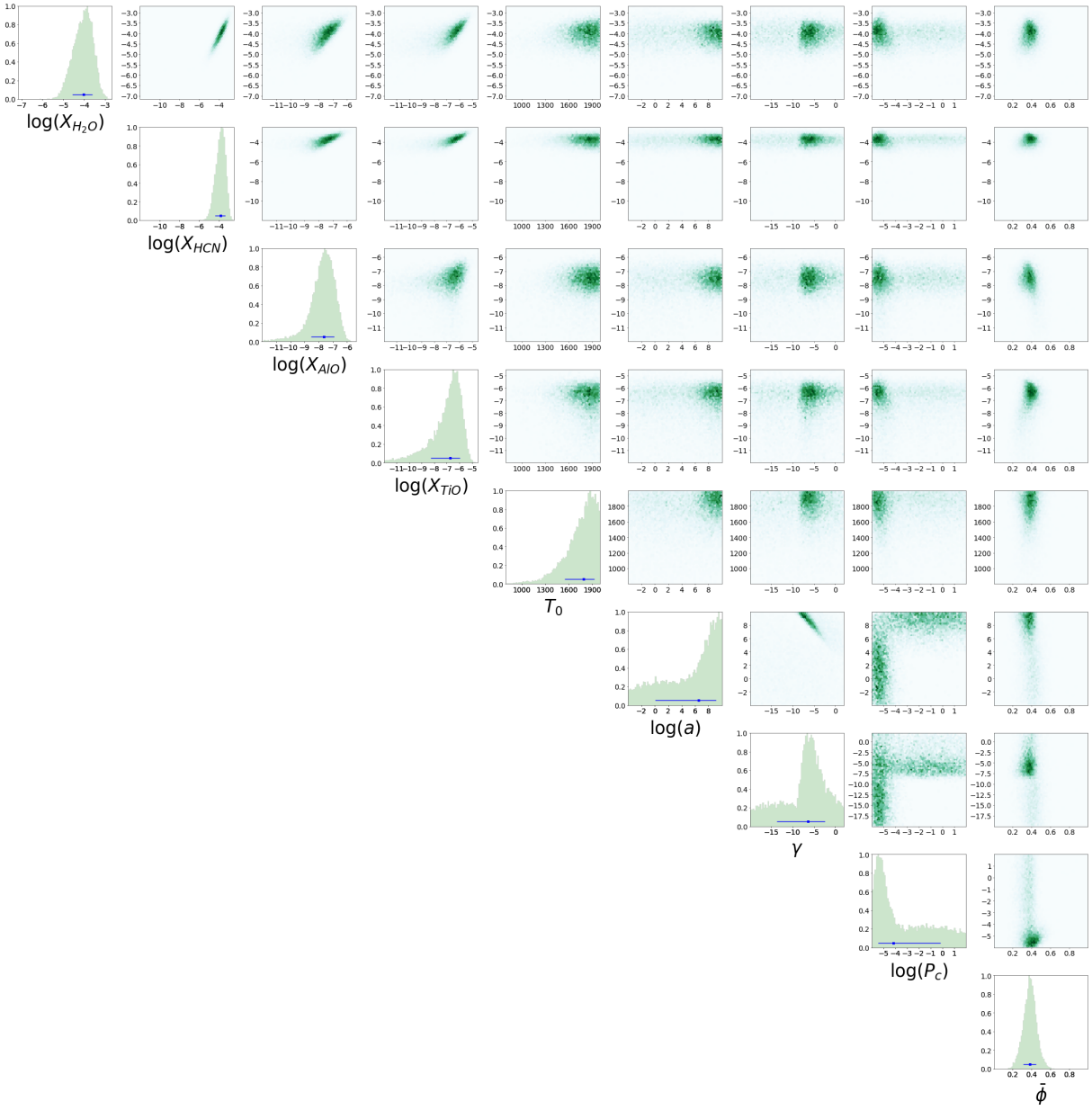

Figure 61 Posterior distributions for the constrained chemical species in the fiducial model retrieval of KELT-11b. Temperature at the top of the atmosphere T_0 from the P-T profile and cloud/hazes parameters are also shown.

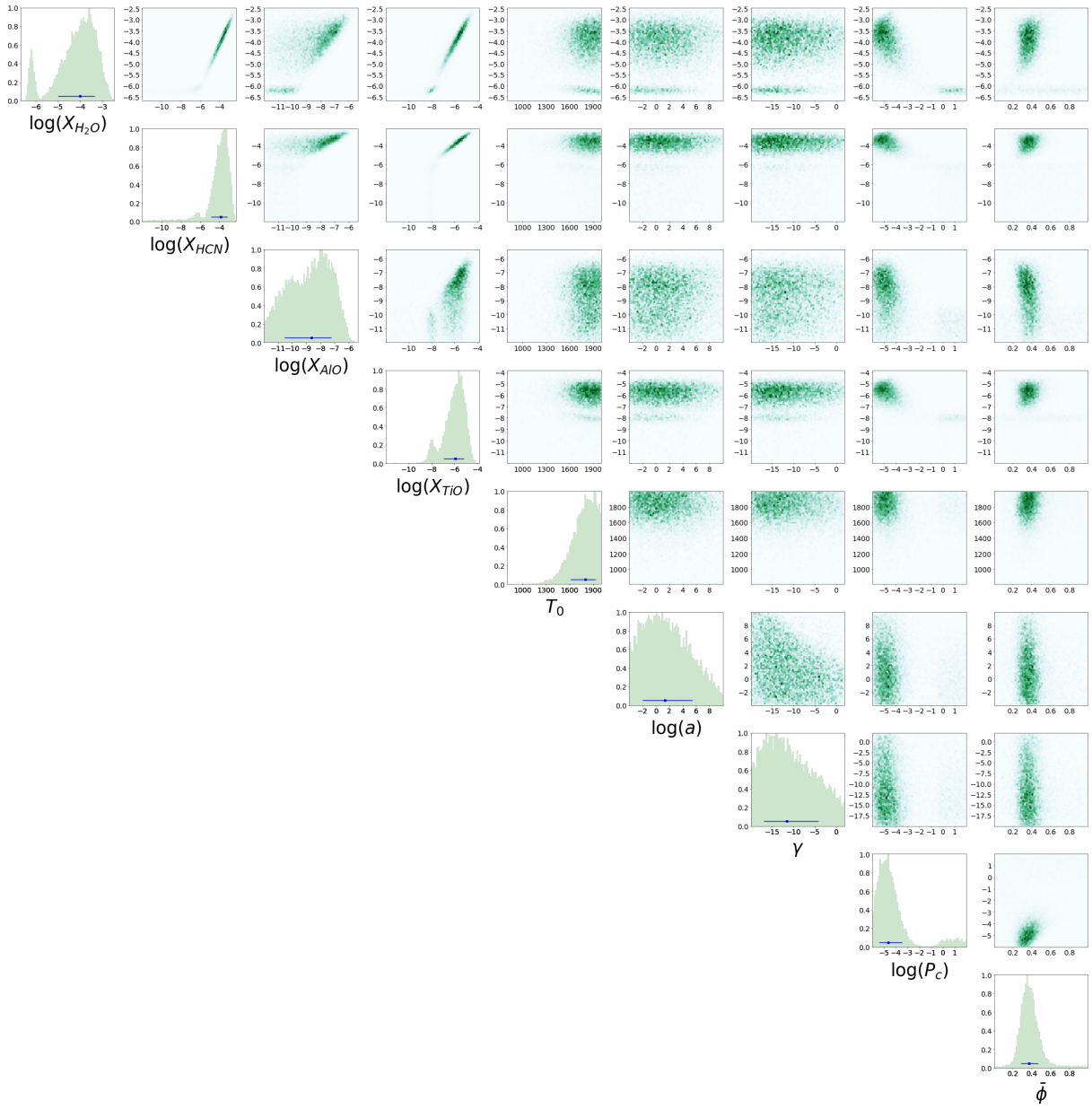

Figure 62 Posterior distributions for the retrieval of KELT-11b using HST/WFC3 observations only. The constrained chemical species are shown. Posterior distributions for the temperature at the top of the atmosphere T_0 and cloud/hazes parameters are included.

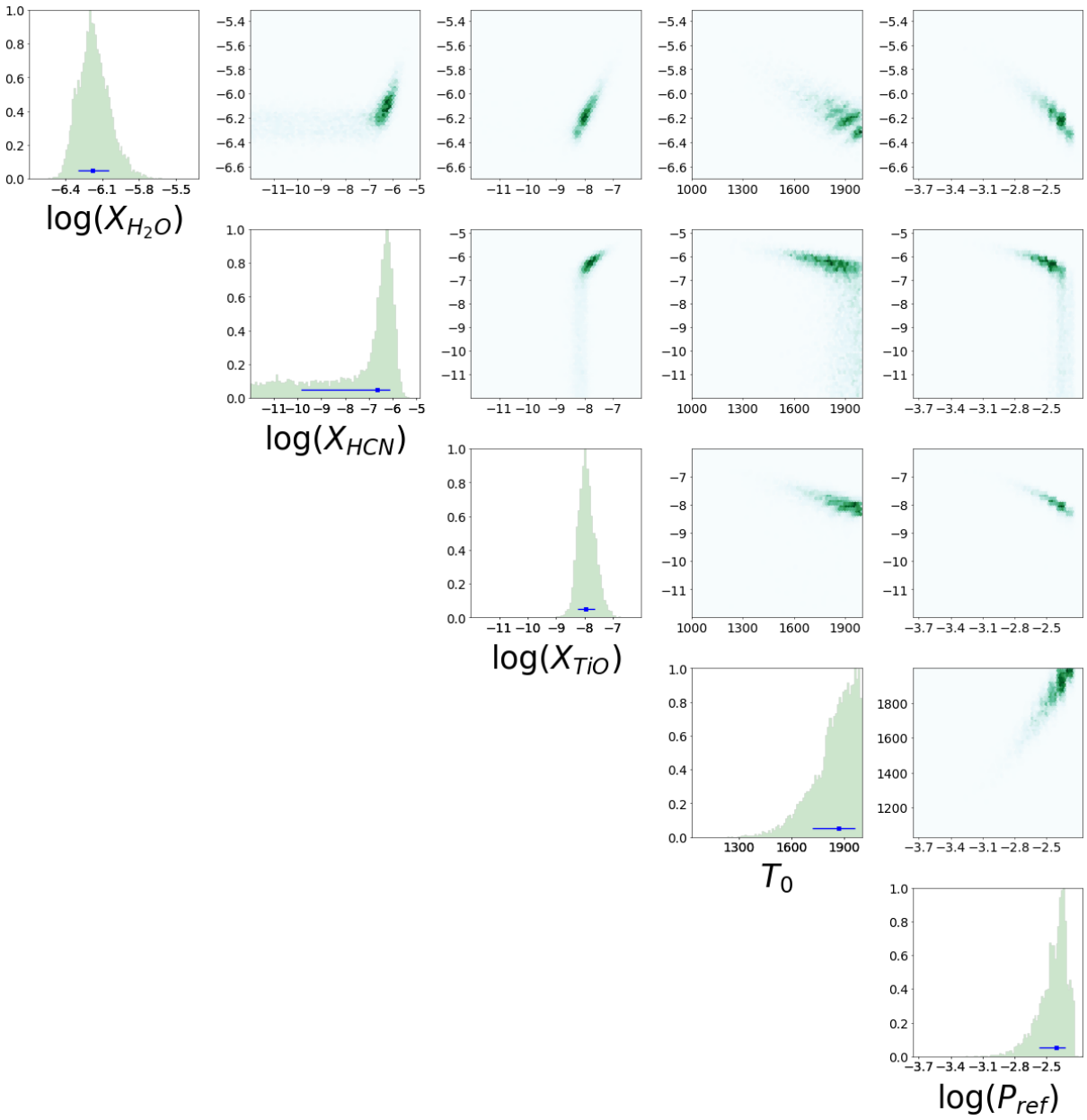

Figure 63 Posterior distributions for the retrieval of KELT-11b using HST/WFC3 observations only and assuming a clear and isothermal atmosphere.

Table 18 Summary of Retrievals for KELT-11b Considering Instrumental Offsets.

Scenario	Abundance Constraint	D.O.F.	χ^2	p value	BIC
Full Model All Data Gaussian prior vertical offset	$\log_{10}(X_{H_2O}) = -4.08^{+0.46}_{-0.53}$ $\log_{10}(X_{HCN}) = -3.99^{+0.51}_{-0.81}$ $\log_{10}(X_{TiO}) = -6.07^{+0.54}_{-0.64}$ $\log_{10}(X_{AlO}) = -7.95^{+0.86}_{-1.42}$ $\text{Shift}_{TESS} = 67.98^{+54.68}_{-52.00}$ ppm $\text{Shift}_{HST} = -110.83^{+48.58}_{-46.61}$ ppm	4	27.66	1.46×10^{-5}	87.23
Full Model All Data uniform prior vertical offset	$\log_{10}(X_{H_2O}) = -3.98^{+0.44}_{-0.54}$ $\log_{10}(X_{HCN}) = -3.82^{+0.45}_{-0.58}$ $\log_{10}(X_{TiO}) = -6.17^{+0.56}_{-0.76}$ $\log_{10}(X_{AlO}) = -7.87^{+0.87}_{-1.51}$ $\text{Shift}_{TESS} = 45.49^{+23.84}_{-40.94}$ ppm $\text{Shift}_{HST} = -58.93^{+27.36}_{-15.02}$ ppm	4	31.66	2.24×10^{-6}	91.23

Note. There are 23 data-points in the complete transmission spectrum (TESS+HST+Spitzer) and 21 in the HST transmission spectrum. For reference, solar abundances at 12 mbar and 1730 K from self-consistent models in Colón et al. (2020) are: $\log_{10}(X_{H_2O}) = -3.44$, $\log_{10}(X_{HCN}) = -9.62$, $\log_{10}(X_{TiO}) = -11.63$, $\log_{10}(X_{AlO}) < -14$. Additional retrieved values for the remaining models for KELT-11b considered in Chapter 7 are shown in Table 9 in Appendix E.

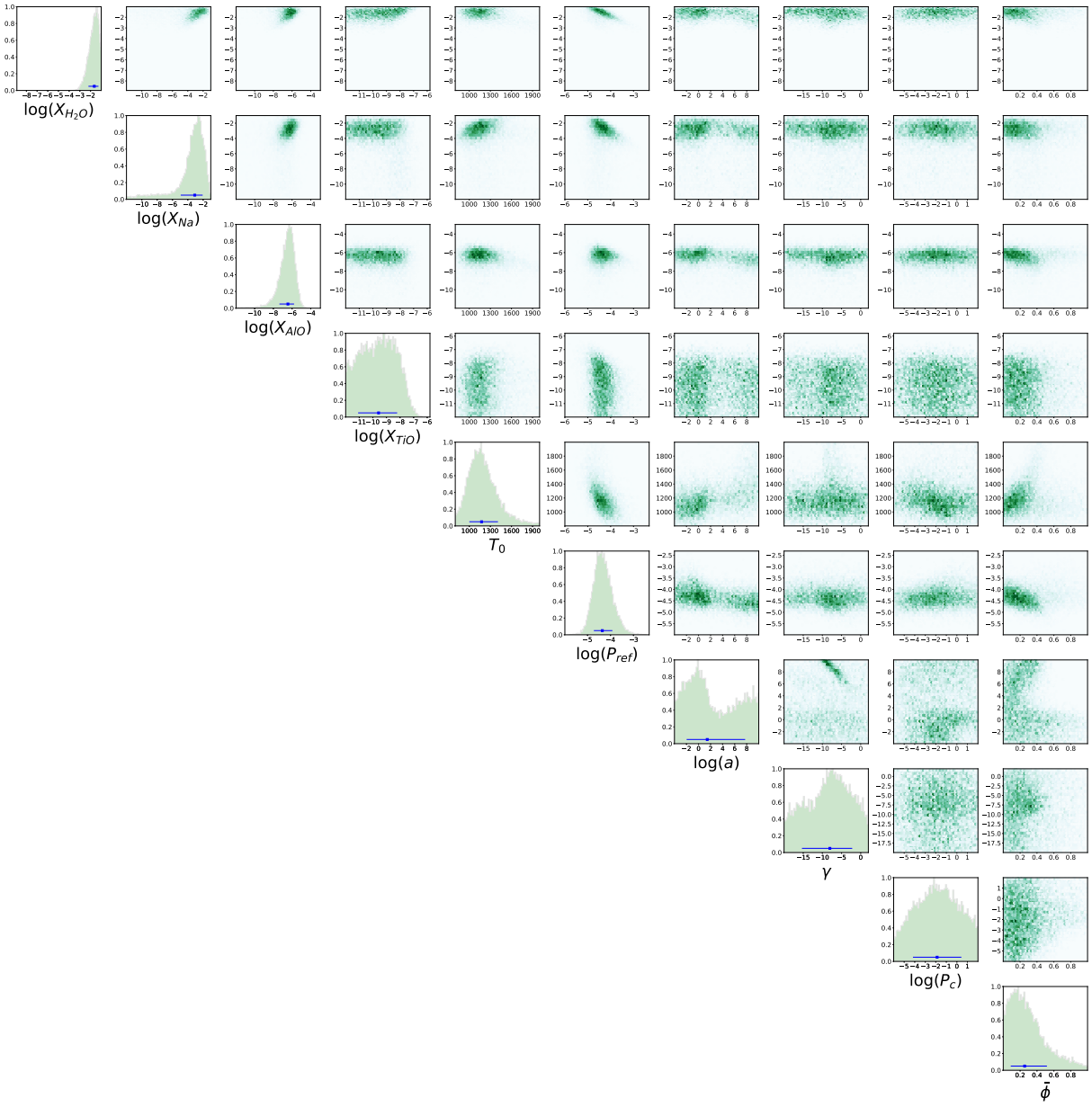

Figure 64 Posterior distributions of the relevant parameters for the full retrieval of HAT-P-41b (Model 1 in Table 10, Chapter 7) using STIS, WFC3 and Spitzer data. The abundances of H_2O, Na and AlO are constrained, while the cloud and haze parameters are not constrained. The parameter T_0, the temperature at the top of the atmosphere (10^{-6} bar), is shown as a subset of the P-T parameters used in the model.

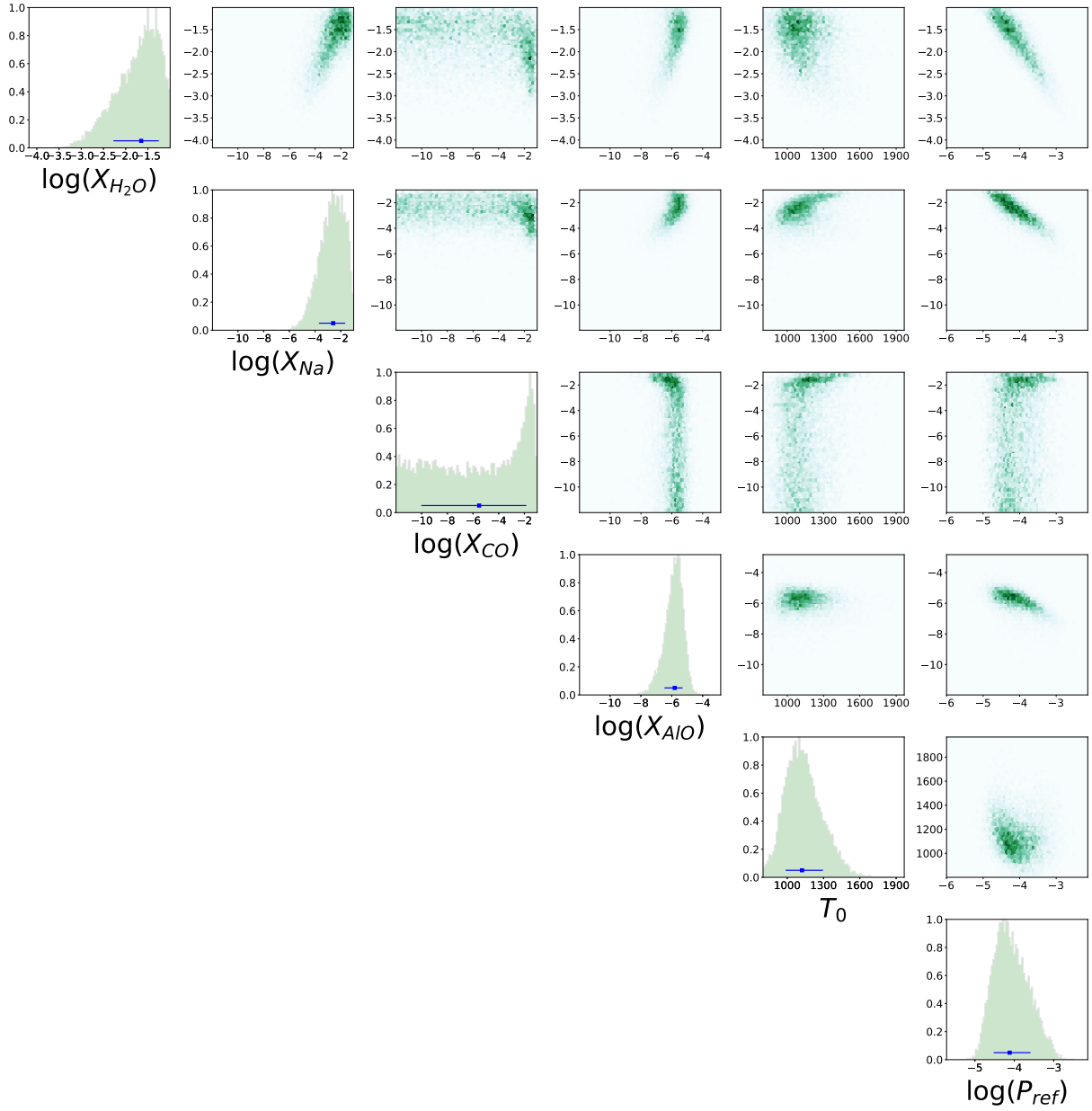

Figure 65 Full posterior distributions for the retrieval of HAT-P-41b using a simpler model, Model 6 in Table 10, Chapter 7.

Part III

BIBLIOGRAPHY

BIBLIOGRAPHY

Ackerman A. S., Marley M. S., 2001, ApJ, 556, 872

Adams D., Gao P., de Pater I., Morley C. V., 2019, ApJ, 874, 61

Agol E., Steffen J., Sari R., Clarkson W., 2005, MNRAS, 359, 567

Agol E., et al., 2021, PSJ, 2, 1

Aitchison J., 1986, The Statistical Analysis of Compositional Data. Monographs on Statistics and Applied Probability, Springer Netherlands

Aitchison J., Egozcue J. J., 2005, MatG, 37, 829

Akeson R. L., et al., 2013, PASP, 125, 989

Al-Refaie A. F., Changeat Q., Waldmann I. P., Tinetti G., 2019, arXiv e-prints, p. arXiv:1912.07759

Ali-Dib M., 2017, MNRAS, 467, 2845

Allard N. F., Royer A., Kielkopf J. F., Feautrier N., 1999, PhRvA, 60, 1021

Allard N. F., Spiegelman F., Kielkopf J. F., 2016, A&A, 589, A21

Allard N. F., Spiegelman F., Leininger T., Molliere P., 2019, A&A, 628, A120

Allart R., et al., 2018, Sci, 362, 1384

Ambikasaran S., Foreman-Mackey D., Greengard L., Hogg D. W., O'Neil M., 2015, ITPAM, 38, 252

Anderson J. G., 1987, ARPC, 38, 489

Anderson D. R., et al., 2017, A&A, 604, A110

Anglada-Escudé G., et al., 2016, Natur, 536, 437

Arcangeli J., et al., 2018, ApJL, 855, L30

Asplund M., Grevesse N., Sauval A. J., Scott P., 2009, ARA&A, 47, 481

Atreya S. K., Crida A., Guillot T., Lunine J. I., Madhusudhan N., Mousis O., 2018, The Origin and Evolution of Saturn, with Exoplanet Perspective. Cambridge University Press, p. 5–43, doi:10.1017/9781316227220.002

Baraffe I., Chabrier G., 2010, A&A, 521, A44

Barbary K., 2015, Nestle sampling library, https://github.com/kbarbary/nestle

Barber R. J., Strange J. K., Hill C., Polyansky O. L., Mellau G. C., Yurchenko S. N., Tennyson J., 2014, MNRAS, 437, 1828

Barman T. S., Hauschildt P. H., Schweitzer A., Stancil P. C., Baron E., Allard F., 2002, ApJL, 569, L51

Barstow J. K., 2020, MNRAS, 497, 4183

Barstow J. K., Irwin P. G. J., 2016, MNRAS, 461, L92

Barstow J. K., Aigrain S., Irwin P. G. J., Hackler T., Fletcher L. N., Lee J. M., Gibson N. P., 2014, ApJ, 786, 154

Barstow J. K., Aigrain S., Irwin P. G. J., Kendrew S., Fletcher L. N., 2015, MNRAS, 448, 2546

Barstow J. K., Irwin P. G. J., Fletcher L. N., Giles R. S., Merlet C., 2016a, Icar, 271, 400

Barstow J. K., Aigrain S., Irwin P. G. J., Kendrew S., Fletcher L. N., 2016b, MNRAS, 458, 2657

Barstow J. K., Aigrain S., Irwin P. G. J., Sing D. K., 2017, ApJ, 834, 50

Batalha N. E., Line M. R., 2017, AJ, 153, 151

Batalha N. E., et al., 2017a, PASP, 129, 064501

Batalha N. E., Kempton E. M.-R., Mbarek R., 2017b, ApJL, 836, L5

Batalha N. E., Lewis N. K., Line M. R., Valenti J., Stevenson K., 2018, ApJL, 856, L34

Batalha N. E., Lewis T., Fortney J. J., Batalha N. M., Kempton E., Lewis N. K., Line M. R., 2019, ApJL, 885, L25

Bauschlicher C. W., Ram R. S., Bernath P. F., Parsons C. G., Galehouse D., 2001, JChPh, 115, 1312

Baxter C., et al., 2020, A&A, 639, A36

Baxter C., et al., 2021, A&A, 648, A127

Bean J. L., Miller-Ricci Kempton E., Homeier D., 2010, Natur, 468, 669

Beatty T. G., et al., 2017, AJ, 154, 25

Beaulieu J. P., Carey S., Ribas I., Tinetti G., 2008, ApJ, 677, 1343

Beichman C. A., Greene T. P., 2018, in Deeg H. J., Belmonte J. A., eds, Handbook of Exoplanets. Springer, p. 85, doi:10.1007/978-3-319-55333-7_85

Bell T. J., et al., 2021, MNRAS, 504, 3316

Benneke B., Seager S., 2012, ApJ, 753, 100

Benneke B., Seager S., 2013, ApJ, 778, 153

Benneke B., et al., 2017, ApJ, 834, 187

Benneke B., et al., 2019a, arXiv e-prints, p. arXiv:1909.04642

Benneke B., et al., 2019b, NatAs, 3, 813

Benneke B., et al., 2019c, ApJL, 887, L14

Bétrémieux Y., 2016, MNRAS, 456, 4051

Bétrémieux Y., Swain M. R., 2017, MNRAS, 467, 2834

Bétrémieux Y., Swain M. R., 2018, ApJ, 865, 12

Biddle L. I., et al., 2014, MNRAS, 443, 1810

Biller B. A., Bonnefoy M., 2018, in Deeg H. J., Belmonte J. A., eds, Handbook of Exoplanets. Springer, p. 101, doi:10.1007/978-3-319-55333-7_101

Birkby J. L., 2018, in Deeg H. J., Belmonte J. A., eds, Handbook of Exoplanets. Springer, p. 16, doi:10.1007/978-3-319-55333-7_16

Birkby J. L., de Kok R. J., Brogi M., Schwarz H., Snellen I. A. G., 2017, AJ, 153, 138

Blecic J., 2016, arXiv e-prints, p. arXiv:1604.02692

Blecic J., et al., 2014, ApJ, 781, 116

Blecic J., Dobbs-Dixon I., Greene T., 2017, ApJ, 848, 127

Bond I. A., et al., 2004, ApJL, 606, L155

Booth R. A., Clarke C. J., Madhusudhan N., Ilee J. D., 2017, MNRAS, 469, 3994

Borucki W. J., 2018, in Deeg H. J., Belmonte J. A., eds, Handbook of Exoplanets. Springer, p. 80, doi:10.1007/978-3-319-55333-7_80

Borucki W. J., et al., 2011, ApJ, 736, 19

Boss A. P., 1997, Sci, 276, 1836

Boss A. P., 2000, ApJL, 536, L101

Bouchy F., et al., 2010, A&A, 519, A98

Bourrier V., et al., 2013, A&A, 551, A63

Bourrier V., et al., 2018, A&A, 620, A147

Bouvier J., 2008, A&A, 489, L53

Breiman L., Friedman J., Stone C. J., Olshen R. A., 1984, Classification and Regression Trees. Taylor & Francis

Brewer J. M., Fischer D. A., Valenti J. A., Piskunov N., 2016, ApJS, 225, 32

Brogi M., Line M. R., 2019, AJ, 157, 114

Brogi M., Snellen I. A. G., de Kok R. J., Albrecht S., Birkby J., de Mooij E. J. W., 2012, Natur, 486, 502

Brogi M., de Kok R. J., Birkby J. L., Schwarz H., Snellen I. A. G., 2014, A&A, 565, A124

Brown T. M., 2001, ApJ, 553, 1006

Bruno G., et al., 2020, MNRAS, 491, 5361

Buchner J., et al., 2014, A&A, 564, A125

Burningham B., Marley M. S., Line M. R., Lupu R., Visscher C., Morley C. V., Saumon D., Freedman R., 2017, MNRAS, 470, 1177

Burrows A., Sharp C. M., 1999, ApJ, 512, 843

Burrows A., Dulick M., Bauschlicher C. W. J., Bernath P. F., Ram R. S., Sharp C. M., Milsom J. A., 2005, ApJ, 624, 988

Burrows A., Budaj J., Hubeny I., 2008, ApJ, 678, 1436

Caldas A., Leconte J., Selsis F., Waldmann I. P., Bordé P., Rocchetto M., Charnay B., 2019, A&A, 623, A161

Carter A. L., et al., 2020, MNRAS, 494, 5449

Catling D. C., et al., 2018, AsBio, 18, 709

Chachan Y., et al., 2019, AJ, 158, 244

Chachan Y., et al., 2020, AJ, 160, 201

Changeat Q., Al-Refaie A., 2020, ApJ, 898, 155

Changeat Q., Edwards B., Waldmann I. P., Tinetti G., 2019, ApJ, 886, 39

Changeat Q., Keyte L., Waldmann I. P., Tinetti G., 2020, ApJ, 896, 107

Charbonneau D., Deming D., 2007, arXiv e-prints, p. arXiv:0706.1047

Charbonneau D., Brown T. M., Latham D. W., Mayor M., 2000, ApJL, 529, L45

Charbonneau D., Brown T. M., Noyes R. W., Gilliland R. L., 2002, ApJ, 568, 377

Chayes F., 1960, JGR, 65, 4185

Checlair J. H., et al., 2021, AJ, 161, 150

Chen G., Guenther E. W., Pallé E., Nortmann L., Nowak G., Kunz S., Parviainen H., Murgas F., 2017, A&A, 600, A138

Chen G., et al., 2018, A&A, 616, A145

Chen G., Casasayas-Barris N., Pallé E., Welbanks L., Madhusudhan N., Luque R., Murgas F., 2020, A&A, 642, A54

Cho J. Y. K., Menou K., Hansen B. M. S., Seager S., 2003, ApJL, 587, L117

Clark B. J. M., Anderson D. R., Madhusudhan N., Hellier C., Smith A. M. S., Collier Cameron A., 2018, A&A, 615, A86

Cloutier R., et al., 2019, A&A, 621, A49

Cobb A. D., et al., 2019, AJ, 158, 33

Collier Cameron A., et al., 2010, MNRAS, 407, 507

Colón K. D., et al., 2020, AJ, 160, 280

Cont D., et al., 2021, arXiv e-prints, p. arXiv:2105.10230

Cowan N. B., Agol E., 2008, ApJL, 678, L129

Cowan N. B., Agol E., 2011, ApJ, 729, 54

Cridland A. J., Pudritz R. E., Alessi M., 2016, MNRAS, 461, 3274

Crossfield I. J. M., Hansen B. M. S., Harrington J., Cho J. Y. K., Deming D., Menou K., Seager S., 2010, ApJ, 723, 1436

Crossfield I. J. M., et al., 2016, ApJS, 226, 7

Cubillos P. E., 2016, arXiv e-prints, p. arXiv:1604.01320

D'Angelo G., Lissauer J. J., 2018, in Deeg H. J., Belmonte J. A., eds, Handbook of Exoplanets. Springer, p. 140, doi:10.1007/978-3-319-55333-7_140

Dalgarno A., Williams D. A., 1962, ApJ, 136, 690

Damiano M., Hu R., 2020, AJ, 159, 175

Daylan T., et al., 2021, AJ, 161, 85

Deming D., et al., 2013, ApJ, 774, 95

Demory B.-O., et al., 2013, ApJL, 776, L25

Désert J. M., Vidal-Madjar A., Lecavelier Des Etangs A., Sing D., Ehrenreich D., Hébrard G., Ferlet R., 2008, A&A, 492, 585

Désert J.-M., Lecavelier des Etangs A., Hébrard G., Sing D. K., Ehrenreich D., Ferlet R., Vidal-Madjar A., 2009, ApJ, 699, 478

Désert J. M., et al., 2011a, A&A, 526, A12

Désert J.-M., et al., 2011b, ApJL, 731, L40

Désert J.-M., et al., 2015, ApJ, 804, 59

Dobbs-Dixon I., Lin D. N. C., 2008, ApJ, 673, 513

Dressing C. D., Charbonneau D., 2015, ApJ, 807, 45

Dulick M., Bauschlicher C. W. J., Burrows A., Sharp C. M., Ram R. S., Bernath P., 2003, ApJ, 594, 651

Ehrenreich D., et al., 2015, Natur, 522, 459

Eistrup C., Walsh C., van Dishoeck E. F., 2018, A&A, 613, A14

Espinoza N., et al., 2019, MNRAS, 482, 2065

Evans T. M., et al., 2016, ApJL, 822, L4

Evans T. M., et al., 2017, Natur, 548, 58

Faedi F., et al., 2011, A&A, 531, A40

Feng Y. K., Line M. R., Fortney J. J., 2020, AJ, 160, 137

Feroz F., Hobson M. P., Bridges M., 2009, MNRAS, 398, 1601

Feroz F., Hobson M. P., Cameron E., Pettitt A. N., 2019, OJAp, 2, 10

Fischer D. A., Howard A. W., Laughlin G. P., Macintosh B., Mahadevan S., Sahlmann J., Yee J. C., 2014, in Beuther H., Klessen R. S., Dullemond C. P., Henning T., eds, Protostars and Planets VI. University of Arizona Press, p. 715, doi:10.2458/azu_uapress_9780816531240-ch031

Fischer D. A., et al., 2016, PASP, 128, 066001

Fisher C., Heng K., 2018, MNRAS, 481, 4698

Fisher C., Heng K., 2019, ApJ, 881, 25

Fisher C., Hoeijmakers H. J., Kitzmann D., Márquez-Neila P., Grimm S. L., Sznitman R., Heng K., 2020, AJ, 159, 192

Foreman-Mackey D., Hogg D. W., Lang D., Goodman J., 2013, PASP, 125, 306

Foreman-Mackey D., Montet B. T., Hogg D. W., Morton T. D., Wang D., Schölkopf B., 2015, ApJ, 806, 215

Foreman-Mackey D., Agol E., Angus R., Ambikasaran S., 2017, AJ, 154, 220

Fortney J. J., 2005, MNRAS, 364, 649

Fortney J. J., 2018, in Bozza V., Mancini L., Sozzetti A., eds, Astrophysics of Exoplanetary Atmospheres: 2nd Advanced School on Exoplanetary Science. Springer, https://ui.adsabs.harvard.edu/abs/2018arXiv180408149F

Fortney J. J., Sudarsky D., Hubeny I., Cooper C. S., Hubbard W. B., Burrows A., Lunine J. I., 2003, ApJ, 589, 615

Fortney J. J., Marley M. S., Lodders K., Saumon D., Freedman R., 2005, ApJL, 627, L69

Fortney J. J., Lodders K., Marley M. S., Freedman R. S., 2008, ApJ, 678, 1419

Fortney J. J., Mordasini C., Nettelmann N., Kempton E. M. R., Greene T. P., Zahnle K., 2013, ApJ, 775, 80

Fossati L., et al., 2010, ApJL, 714, L222

Fressin F., et al., 2013, ApJ, 766, 81

Fu G., Deming D., Knutson H., Madhusudhan N., Mandell A., Fraine J., 2017, ApJL, 847, L22

Fujii Y., et al., 2018, AsBio, 18, 739

Fulton B. J., et al., 2017, AJ, 154, 109

Gandhi S., Madhusudhan N., 2017, MNRAS, 472, 2334

Gandhi S., Madhusudhan N., 2018, MNRAS, 474, 271

Gandhi S., Madhusudhan N., 2019, MNRAS, 485, 5817

Gandhi S., Madhusudhan N., Hawker G., Piette A., 2019, AJ, 158, 228

Gandhi S., et al., 2020, MNRAS, 495, 224

Gaskin J. A., et al., 2018, in den Herder J.-W. A., Nikzad S., Nakazawa K., eds, Society of Photo-Optical Instrumentation Engineers (SPIE) Conference Series Vol. 10699, Space Telescopes and Instrumentation 2018: Ultraviolet to Gamma Ray. p. 106990N, doi:10.1117/12.2314149

Gaudi B. S., 2012, ARA&A, 50, 411

Gaudi B. S., et al., 2020, arXiv e-prints, p. arXiv:2001.06683

Giacobbe P., et al., 2021, Natur, 592, 205

Gillon M., et al., 2009, A&A, 501, 785

Gillon M., Jehin E., Magain P., Chantry V., Hutsemékers D., Manfroid J., Queloz D., Udry S., 2011, EPJWC, 11, 06002

Gillon M., et al., 2012, A&A, 542, A4

Gillon M., et al., 2016, Natur, 533, 221

Gillon M., et al., 2017, Natur, 542, 456

Gould A., 2001, in Menzies J. W., Sackett P. D., eds, Astronomical Society of the Pacific Conference Series Vol. 239, Microlensing 2000: A New Era of Microlensing Astrophysics. p. 3, https://ui.adsabs.harvard.edu/abs/2001ASPC..239....3G

Goyal J. M., et al., 2018, MNRAS, 474, 5158

Greenbaum A. Z., et al., 2018, AJ, 155, 226

Greene T. P., Line M. R., Montero C., Fortney J. J., Lustig-Yaeger J., Luther K., 2016, ApJ, 817, 17

Griffith C. A., 2014, RSPTA, 372, 20130086

Guo X., et al., 2020, AJ, 159, 239

Guzmán-Mesa A., et al., 2020, AJ, 160, 15

Handley W. J., Hobson M. P., Lasenby A. N., 2015a, MNRAS, 450, L61

Handley W. J., Hobson M. P., Lasenby A. N., 2015b, MNRAS, 453, 4384

Hargreaves R. J., Hinkle K. H., Bauschlicher Charles W. J., Wende S., Seifahrt A., Bernath P. F., 2010, AJ, 140, 919

Harman C. E., Schwieterman E. W., Schottelkotte J. C., Kasting J. F., 2015, ApJ, 812, 137

Harris G. J., Tennyson J., Kaminsky B. M., Pavlenko Y. V., Jones H. R. A., 2006, MNRAS, 367, 400

Harris C. R., et al., 2020, Natur, 585, 357

Hartman J. D., et al., 2009, ApJ, 706, 785

Hartman J. D., et al., 2011, ApJ, 728, 138

Hartman J. D., et al., 2012, AJ, 144, 139

Hawker G. A., Madhusudhan N., Cabot S. H. C., Gandhi S., 2018, ApJL, 863, L11

Hayes J. J. C., et al., 2020, MNRAS, 494, 4492

Haynes K., Mandell A. M., Madhusudhan N., Deming D., Knutson H., 2015, ApJ, 806, 146

Hebb L., et al., 2009, ApJ, 693, 1920

Hellier C., et al., 2014, MNRAS, 440, 1982

Helling C., 2019, AREPS, 47, 583

Helling C., Dehn M., Woitke P., Hauschildt P. H., 2008, ApJL, 675, L105

Helling C., Woitke P., Rimmer P. B., Kamp I., Thi W.-F., Meijerink R., 2014, Life, 4, 142

Heng K., 2016, ApJL, 826, L16

Heng K., Kitzmann D., 2017, MNRAS, 470, 2972

Heng K., Marley M. S., 2018, in Deeg H. J., Belmonte J. A., eds, Handbook of Exoplanets. Springer, p. 102, doi:10.1007/978-3-319-55333-7_102

Heng K., Showman A. P., 2015, AREPS, 43, 509

Heng K., Hayek W., Pont F., Sing D. K., 2012, MNRAS, 420, 20

Henry G. W., Marcy G. W., Butler R. P., Vogt S. S., 2000, ApJL, 529, L41

Henyey L. G., Greenstein J. L., 1941, ApJ, 93, 70

Herman M. K., de Mooij E. J. W., Jayawardhana R., Brogi M., 2020, AJ, 160, 93

Higson E., Handley W., Hobson M., Lasenby A., 2019, Stat. Comput., 29, 891

Hoeijmakers H. J., et al., 2018, Natur, 560, 453

Hörst S. M., et al., 2018, NatAs, 2, 303

Howard A. W., 2013, Sci, 340, 572

Howard A. W., et al., 2012, ApJS, 201, 15

Hubbard W. B., Fortney J. J., Lunine J. I., Burrows A., Sudarsky D., Pinto P., 2001, ApJ, 560, 413

Hubeny I., 2017, MNRAS, 469, 841

Hubeny I., Burrows A., Sudarsky D., 2003, ApJ, 594, 1011

Huitson C. M., et al., 2013, MNRAS, 434, 3252

Husser T. O., Wende-von Berg S., Dreizler S., Homeier D., Reiners A., Barman T., Hauschildt P. H., 2013, A&A, 553, A6

Irwin P. G. J., Dyudina U., 2002, Icar, 156, 52

Irwin P. G. J., Weir A. L., Taylor F. W., Calcutt S. B., Carlson R. W., 2001, Icar, 149, 397

Irwin P. G. J., et al., 2008, JQSRT, 109, 1136

Irwin P. G. J., Barstow J. K., Bowles N. E., Fletcher L. N., Aigrain S., Lee J. M., 2014, Icar, 242, 172

Irwin P. G. J., Parmentier V., Taylor J., Barstow J., Aigrain S., Lee G. K. H., Garland R., 2020, MNRAS, 493, 106

Israelian G., et al., 2009, Natur, 462, 189

Iyer A. R., Line M. R., 2020, ApJ, 889, 78

Iyer A. R., Swain M. R., Zellem R. T., Line M. R., Roudier G., Rocha G., Livingston J. H., 2016, ApJ, 823, 109

Jurgenson C., Fischer D., McCracken T., Sawyer D., Szymkowiak A., Davis A., Muller G., Santoro F., 2016, in Evans C. J., Simard L., Takami H., eds, Society of Photo-Optical Instrumentation Engineers (SPIE) Conference Series Vol. 9908, Ground-based and Airborne Instrumentation for Astronomy VI. p. 99086T, doi:10.1117/12.2233002

Kalas P., et al., 2008, Sci, 322, 1345

Kaltenegger L., 2017, ARA&A, 55, 433

Kaltenegger L., Traub W. A., Jucks K. W., 2007, ApJ, 658, 598

Kammer J. A., et al., 2015, ApJ, 810, 118

Karman T., et al., 2019, Icar, 328, 160

Kass R. E., Raftery A. E., 1995, J. Am. Stat. Assoc., 90, 773

Kataria T., Showman A. P., Lewis N. K., Fortney J. J., Marley M. S., Freedman R. S., 2013, ApJ, 767, 76

Kataria T., Sing D. K., Lewis N. K., Visscher C., Showman A. P., Fortney J. J., Marley M. S., 2016, ApJ, 821, 9

Kirk J., López-Morales M., Wheatley P. J., Weaver I. C., Skillen I., Louden T., McCormac J., Espinoza N., 2019, AJ, 158, 144

Kitzmann D., Heng K., 2018, MNRAS, 475, 94

Kitzmann D., Patzer A. B. C., von Paris P., Godolt M., Rauer H., 2011, A&A, 531, A62

Kitzmann D., Heng K., Oreshenko M., Grimm S. L., Apai D., Bowler B. P., Burgasser A. J., Marley M. S., 2020, ApJ, 890, 174

Knutson H. A., et al., 2007, Natur, 447, 183

Knutson H. A., Charbonneau D., Allen L. E., Burrows A., Megeath S. T., 2008, ApJ, 673, 526

Knutson H. A., et al., 2009, ApJ, 690, 822

Knutson H. A., Benneke B., Deming D., Homeier D., 2014a, Natur, 505, 66

Knutson H. A., et al., 2014b, ApJ, 794, 155

Komacek T. D., Fauchez T. J., Wolf E. T., Abbot D. S., 2020, ApJL, 888, L20

Konopacky Q. M., Barman T. S., Macintosh B. A., Marois C., 2013, Sci, 339, 1398

Kopparapu R. K., 2013, ApJL, 767, L8

Kramida A., Yu. Ralchenko Reader J., and NIST ASD Team 2018, NIST Atomic Spectra Database (ver. 5.6.1), `https://www.nist.gov/pml/atomicspectra-database`

Kreidberg L., et al., 2014a, Natur, 505, 69

Kreidberg L., et al., 2014b, ApJL, 793, L27

Kreidberg L., et al., 2015, ApJ, 814, 66

Krissansen-Totton J., Garland R., Irwin P., Catling D. C., 2018, AJ, 156, 114

Lacy B. I., Burrows A., 2020, ApJ, 905, 131

Lagrange A. M., et al., 2010, Sci, 329, 57

Lam K. W. F., et al., 2017, A&A, 599, A3

Latham D. W., Mazeh T., Stefanik R. P., Mayor M., Burki G., 1989, Natur, 339, 38

Lavie B., et al., 2017, AJ, 154, 91

Lavvas P., Koskinen T., Steinrueck M. E., García Muñoz A., Showman A. P., 2019, ApJ, 878, 118

Lecavelier Des Etangs A., Pont F., Vidal-Madjar A., Sing D., 2008, A&A, 481, L83

Lederberg J., 1965, Natur, 207, 9

Lee J. M., Fletcher L. N., Irwin P. G. J., 2012, MNRAS, 420, 170

Lee J.-M., Heng K., Irwin P. G. J., 2013, ApJ, 778, 97

Lee G., Dobbs-Dixon I., Helling C., Bognar K., Woitke P., 2016, A&A, 594, A48

Lehmann H., Guenther E., Sebastian D., Döllinger M., Hartmann M., Mkrtichian D. E., 2015, A&A, 578, L4

Lewis N. K., et al., 2020, ApJL, 902, L19

Li C., et al., 2020, NatAs,

Lincowski A. P., Meadows V. S., Crisp D., Robinson T. D., Luger R., Lustig-Yaeger J., Arney G. N., 2018, ApJ, 867, 76

Line M. R., Parmentier V., 2016, ApJ, 820, 78

Line M. R., Zhang X., Vasisht G., Natraj V., Chen P., Yung Y. L., 2012, ApJ, 749, 93

Line M. R., et al., 2013, ApJ, 775, 137

Line M. R., Knutson H., Wolf A. S., Yung Y. L., 2014a, ApJ, 783, 70

Line M. R., Fortney J. J., Marley M. S., Sorahana S., 2014b, ApJ, 793, 33

Line M. R., Teske J., Burningham B., Fortney J. J., Marley M. S., 2015, ApJ, 807, 183

Line M. R., et al., 2016, AJ, 152, 203

Lines S., et al., 2018, A&A, 615, A97

Lines S., Mayne N. J., Manners J., Boutle I. A., Drummond B., Mikal-Evans T., Kohary K., Sing D. K., 2019, MNRAS, 488, 1332

Lissauer J. J., 2004, in Beaulieu J., Lecavelier Des Etangs A., Terquem C., eds, Astronomical Society of the Pacific Conference Series Vol. 321, Extrasolar Planets: Today and Tomorrow. p. 271, https://ui.adsabs.harvard.edu/abs/2004ASPC..321..271L

Liu C.-C., Ren D.-Q., Dou J.-P., Zhu Y.-T., Zhang X., Zhao G., Wu Z., Chen R., 2015, RAA, 15, 453

Lodders K., 2002, ApJ, 577, 974

Lovelock J. E., 1965, Natur, 207, 568

Luger R., Barnes R., 2015, AsBio, 15, 119

Lupu R. E., Marley M. S., Lewis N., Line M., Traub W. A., Zahnle K., 2016, AJ, 152, 217

Lustig-Yaeger J., Meadows V. S., Lincowski A. P., 2019, AJ, 158, 27

MacDonald R. J., Madhusudhan N., 2017a, MNRAS, 469, 1979

MacDonald R. J., Madhusudhan N., 2017b, ApJL, 850, L15

MacDonald R. J., Madhusudhan N., 2019, MNRAS, 486, 1292

MacDonald R. J., Goyal J. M., Lewis N. K., 2020, ApJL, 893, L43

Madhusudhan N., 2012, ApJ, 758, 36

Madhusudhan N., 2018, in Deeg H. J., Belmonte J. A., eds, Handbook of Exoplanets. Springer, p. 104, doi:10.1007/978-3-319-55333-7_104

Madhusudhan N., 2019, ARA&A, 57, 617

Madhusudhan N., Seager S., 2009, ApJ, 707, 24

Madhusudhan N., Seager S., 2011, ApJ, 729, 41

Madhusudhan N., Knutson H., Fortney J. J., Barman T., 2014a, in Beuther H., Klessen R. S., Dullemond C. P., Henning T., eds, Protostars and Planets VI. University of Arizona Press, p. 739, doi:10.2458/azu_uapress_9780816531240-ch032

Madhusudhan N., Crouzet N., McCullough P. R., Deming D., Hedges C., 2014b, ApJL, 791, L9

Madhusudhan N., Amin M. A., Kennedy G. M., 2014c, ApJL, 794, L12

Madhusudhan N., Agúndez M., Moses J. I., Hu Y., 2016, SSRv, 205, 285

Madhusudhan N., Bitsch B., Johansen A., Eriksson L., 2017, MNRAS, 469, 4102

Madhusudhan N., Nixon M. C., Welbanks L., Piette A. A. A., Booth R. A., 2020, ApJL, 891, L7

Mai C., Line M. R., 2019, ApJ, 883, 144

Mandell A. M., Haynes K., Sinukoff E., Madhusudhan N., Burrows A., Deming D., 2013, ApJ, 779, 128

Mansfield M., et al., 2018, AJ, 156, 10

Marley M. S., Robinson T. D., 2015, ARA&A, 53, 279

Marley M. S., Gelino C., Stephens D., Lunine J. I., Freedman R., 1999, ApJ, 513, 879

Marley M. S., Ackerman A. S., Cuzzi J. N., Kitzmann D., 2013, Clouds and Hazes in Exoplanet Atmospheres. University of Arizona Press, p. 367, doi:10.2458/azu_uapress_9780816530595-ch15

Marois C., Macintosh B., Barman T., Zuckerman B., Song I., Patience J., Lafrenière D., Doyon R., 2008, Sci, 322, 1348

Marois C., Zuckerman B., Konopacky Q. M., Macintosh B., Barman T., 2010, Natur, 468, 1080

Márquez-Neila P., Fisher C., Sznitman R., Heng K., 2018, NatAs, 2, 719

Mayne N. J., et al., 2014, A&A, 561, A1

Mayor M., Queloz D., 1995, Natur, 378, 355

Mayor M., et al., 2003, Msngr, 114, 20

Mazeh T., Holczer T., Faigler S., 2016, A&A, 589, A75

McCullough P. R., Crouzet N., Deming D., Madhusudhan N., 2014, ApJ, 791, 55

McKemmish L. K., Yurchenko S. N., Tennyson J., 2016, MNRAS, 463, 771

Meadows V. S., Barnes R. K., 2018, in Deeg H. J., Belmonte J. A., eds, Handbook of Exoplanets. Springer, p. 57, doi:10.1007/978-3-319-55333-7_57

Min M., Ormel C. W., Chubb K., Helling C., Kawashima Y., 2020, A&A, 642, A28

Mollière P., van Boekel R., Dullemond C., Henning T., Mordasini C., 2015, ApJ, 813, 47

Mollière P., Wardenier J. P., van Boekel R., Henning T., Molaverdikhani K., Snellen I. A. G., 2019, A&A, 627, A67

Montet B. T., et al., 2015, ApJ, 809, 25

Moran S. E., et al., 2020, PSJ, 1, 17

Mordasini C., 2018, in Deeg H. J., Belmonte J. A., eds, Handbook of Exoplanets. Springer, p. 143, doi:10.1007/978-3-319-55333-7_143

Mordasini C., van Boekel R., Mollière P., Henning T., Benneke B., 2016, ApJ, 832, 41

Morley C. V., Fortney J. J., Marley M. S., Visscher C., Saumon D., Leggett S. K., 2012, ApJ, 756, 172

Morley C. V., Kreidberg L., Rustamkulov Z., Robinson T., Fortney J. J., 2017, ApJ, 850, 121

Moses J. I., et al., 2013, ApJ, 777, 34

Mousis O., Lunine J. I., Madhusudhan N., Johnson T. V., 2012, ApJL, 751, L7

Mulders G. D., Pascucci I., Apai D., 2015, ApJ, 814, 130

Murgas F., Chen G., Nortmann L., Palle E., Nowak G., 2020, A&A, 641, A158

Nayak M., Lupu R., Marley M. S., Fortney J. J., Robinson T., Lewis N., 2017, PASP, 129, 034401

Nikolov N., et al., 2014, MNRAS, 437, 46

Nikolov N., Sing D. K., Gibson N. P., Fortney J. J., Evans T. M., Barstow J. K., Kataria T., Wilson P. A., 2016, ApJ, 832, 191

Nikolov N., et al., 2018, Natur, 557, 526

Nixon M. C., Madhusudhan N., 2020, MNRAS, 496, 269

Nugroho S. K., Kawahara H., Masuda K., Hirano T., Kotani T., Tajitsu A., 2017, AJ, 154, 221

O'Rourke J. G., et al., 2014, ApJ, 781, 109

Öberg K. I., Bergin E. A., 2016, ApJL, 831, L19

Öberg K. I., Murray-Clay R., Bergin E. A., 2011, ApJL, 743, L16

Ohno K., Kawashima Y., 2020, ApJL, 895, L47

Palle E., et al., 2017, A&A, 602, L15

Parmentier V., Crossfield I. J. M., 2018, in Deeg H. J., Belmonte J. A., eds, Handbook of Exoplanets. Springer, p. 116, doi:10.1007/978-3-319-55333-7_116

Parmentier V., Showman A. P., Lian Y., 2013, A&A, 558, A91

Parmentier V., Fortney J. J., Showman A. P., Morley C., Marley M. S., 2016, ApJ, 828, 22

Parmentier V., et al., 2018, A&A, 617, A110

Patrascu A. T., Yurchenko S. N., Tennyson J., 2015, MNRAS, 449, 3613

Pawlowsky-Glahn V., Buccianti A., 2011, Compositional data analysis. Wiley, doi:10.1002/9781119976462

Pearson K., 1897, RSPS, 60, 489

Pepper J., et al., 2017, AJ, 153, 215

Petigura E. A., Marcy G. W., Howard A. W., 2013, ApJ, 770, 69

Piette A. A. A., Madhusudhan N., 2020, MNRAS, 497, 5136

Pinhas A., Madhusudhan N., 2017, MNRAS, 471, 4355

Pinhas A., Rackham B. V., Madhusudhan N., Apai D., 2018, MNRAS, 480, 5314

Pinhas A., Madhusudhan N., Gandhi S., MacDonald R., 2019, MNRAS, 482, 1485

Plavchan P., et al., 2015, arXiv e-prints, p. arXiv:1503.01770

Pluriel W., Zingales T., Leconte J., Parmentier V., 2020, A&A, 636, A66

Pollacco D. L., et al., 2006, PASP, 118, 1407

Pollack J. B., Hubickyj O., Bodenheimer P., Lissauer J. J., Podolak M., Greenzweig Y., 1996, Icar, 124, 62

Pont F., Knutson H., Gilliland R. L., Moutou C., Charbonneau D., 2008, MNRAS, 385, 109

Pont F., Sing D. K., Gibson N. P., Aigrain S., Henry G., Husnoo N., 2013, MNRAS, 432, 2917

Powell D., Zhang X., Gao P., Parmentier V., 2018, ApJ, 860, 18

Puig L., et al., 2018, ExA, 46, 211

Rackham B., et al., 2017, ApJ, 834, 151

Rackham B. V., Apai D., Giampapa M. S., 2018, ApJ, 853, 122

Rajan A., et al., 2017, AJ, 154, 10

Rasmussen C. E., Williams C. K. I., 2006, Gaussian Processes for Machine Learning. MIT press Cambridge, MA, http://www.gaussianprocess.org/gpml/chapters/

Rauer H., et al., 2014, ExA, 38, 249

Redfield S., Endl M., Cochran W. D., Koesterke L., 2008, ApJL, 673, L87

Ren D., Dong B., Zhu Y., Christian D. J., 2012, PASP, 124, 247

Richard C., et al., 2012, JQSRT, 113, 1276

Robinson T. D., Fortney J. J., Hubbard W. B., 2017, ApJ, 850, 128

Rodgers C. D., 1976, RvGSP, 14, 609

Rodgers C. D., 2000, Inverse Methods for Atmospheric Sounding: Theory and Practice. WORLD SCIENTIFIC, doi:10.1142/3171

Rodler F., López-Morales M., 2014, ApJ, 781, 54

Roman M., Rauscher E., 2019, ApJ, 872, 1

Rothman L. S., et al., 2010, JQSRT, 111, 2139

Sánchez B., et al., 2012, in Society of Photo-Optical Instrumentation Engineers (SPIE) Conference Series. p. 4, doi:10.1117/12.926676

Sarkis P., et al., 2018, AJ, 155, 257

Scalo J., et al., 2007, AsBio, 7, 85

Schindler T. L., Kasting J. F., 2000, Icar, 145, 262

Schlichting H. E., 2018, in Deeg H. J., Belmonte J. A., eds, Handbook of Exoplanets. Springer, p. 141, doi:10.1007/978-3-319-55333-7_141

Schneider G., et al., 2014, AJ, 148, 59

Schwenke D. W., 1998, FaDi, 109, 321

Seager S., 2010, Exoplanet Atmospheres: Physical Processes. Princeton University Press

Seager S., 2018, IJAsB, 17, 294

Seager S., Deming D., 2010, ARA&A, 48, 631

Seager S., Sasselov D. D., 1998, ApJL, 502, L157

Seager S., Sasselov D. D., 2000, ApJ, 537, 916

Seager S., Bains W., Petkowski J. J., 2016, AsBio, 16, 465

Sedaghati E., et al., 2017, Natur, 549, 238

Sedaghati E., et al., 2021, MNRAS,

Segura A., Krelove K., Kasting J. F., Sommerlatt D., Meadows V., Crisp D., Cohen M., Mlawer E., 2003, AsBio, 3, 689

Segura A., Walkowicz L. M., Meadows V., Kasting J., Hawley S., 2010, AsBio, 10, 751

Seidel J. V., Ehrenreich D., Pino L., Bourrier V., Lavie B., Allart R., Wyttenbach A., Lovis C., 2020, A&A, 633, A86

Serindag D. B., Nugroho S. K., Mollière P., de Mooij E. J. W., Gibson N. P., Snellen I. A. G., 2021, A&A, 645, A90

Shardanand ., Prasad Rao A. D., 1977, Absolute Rayleigh scattering cross sections of gases and freons of stratospheric interest in the visible and ultraviolet regions. NASA technical note, National Aeronautics and Space Administration, https://ui.adsabs.harvard.edu/abs/1977arsc.book.....S

Sheppard K. B., Mandell A. M., Tamburo P., Gandhi S., Pinhas A., Madhusudhan N., Deming D., 2017, ApJL, 850, L32

Sheppard K. B., et al., 2021, AJ, 161, 51

Showman A. P., Guillot T., 2002, A&A, 385, 166

Showman A. P., Cooper C. S., Fortney J. J., Marley M. S., 2008, ApJ, 682, 559

Showman A. P., Fortney J. J., Lian Y., Marley M. S., Freedman R. S., Knutson H. A., Charbonneau D., 2009, ApJ, 699, 564

Showman A. P., Fortney J. J., Lewis N. K., Shabram M., 2013, ApJ, 762, 24

Sing D. K., 2018, in Bozza V., Mancini L., Sozzetti A., eds, Astrophysics of Exoplanetary Atmospheres: 2nd Advanced School on Exoplanetary Science. Springer, https://ui.adsabs.harvard.edu/abs/2018arXiv180407357S

Sing D. K., López-Morales M., 2009, A&A, 493, L31

Sing D. K., et al., 2016, Natur, 529, 59

Sivia D., Skilling J., 2006, Data analysis: a Bayesian tutorial. Oxford University Press

Skilling J., 2004, in Fischer R., Preuss R., Toussaint U. V., eds, American Institute of Physics Conference Series Vol. 735, American Institute of Physics Conference Series. pp 395–405, doi:10.1063/1.1835238

Skilling J., 2006, BayAn, 1, 833

Smith A. M. S., Anderson D. R., Skillen I., Collier Cameron A., Smalley B., 2011, MNRAS, 416, 2096

Sneep M., Ubachs W., 2005, JQSRT, 92, 293

Snellen I. A. G., Albrecht S., de Mooij E. J. W., Le Poole R. S., 2008, A&A, 487, 357

Snellen I. A. G., de Kok R. J., de Mooij E. J. W., Albrecht S., 2010, Natur, 465, 1049

Snellen I. A. G., de Kok R. J., le Poole R., Brogi M., Birkby J., 2013, ApJ, 764, 182

Soboczenski F., et al., 2018, arXiv e-prints, p. arXiv:1811.03390

Spake J. J., et al., 2018, Natur, 557, 68

Spake J. J., et al., 2021, MNRAS, 500, 4042

Speagle J. S., 2020, MNRAS, 493, 3132

Spiegel D. S., Silverio K., Burrows A., 2009, ApJ, 699, 1487

Steinrueck M. E., Showman A. P., Lavvas P., Koskinen T., Tan X., Zhang X., 2021, MNRAS, 504, 2783

Stevenson K. B., 2016, ApJL, 817, L16

Stevenson K. B., et al., 2014, Sci, 346, 838

Stevenson K. B., Bean J. L., Seifahrt A., Gilbert G. J., Line M. R., Désert J.-M., Fortney J. J., 2016, ApJ, 817, 141

Stevenson K. B., et al., 2017, AJ, 153, 68

Sudarsky D., Burrows A., Hubeny I., 2003, ApJ, 588, 1121

Tanner J. M., 1949, JAPh, 2, 1

Tegmark M., et al., 2004, PhRvD, 69, 103501

Thalman R., Zarzana K. J., Tolbert M. A., Volkamer R., 2014, JQSRT, 147, 171

The LUVOIR Team 2019, arXiv e-prints, p. arXiv:1912.06219

The OST mission concept study team 2018, arXiv e-prints, p. arXiv:1809.09702

Thorngren D. P., Fortney J. J., Murray-Clay R. A., Lopez E. D., 2016, ApJ, 831, 64

Torres G., Winn J. N., Holman M. J., 2008, ApJ, 677, 1324

Trotta R., 2008, ConPh, 49, 71

Trotta R., 2017, arXiv e-prints, p. arXiv:1701.01467

Tsiaras A., et al., 2018, AJ, 155, 156

Tsiaras A., Waldmann I. P., Tinetti G., Tennyson J., Yurchenko S. N., 2019, NatAs, 3, 1086

Vahidinia S., Cuzzi J. N., Marley M., Fortney J., 2014, ApJL, 789, L11

Valencia D., Guillot T., Parmentier V., Freedman R. S., 2013, ApJ, 775, 10

Vidal-Madjar A., Lecavelier des Etangs A., Désert J. M., Ballester G. E., Ferlet R., Hébrard G., Mayor M., 2003, Natur, 422, 143

Vidal-Madjar A., et al., 2004, ApJL, 604, L69

Wagner K., et al., 2021, NatCo, 12, 922

Wakeford H. R., Sing D. K., 2015, A&A, 573, A122

Wakeford H. R., et al., 2017a, Sci, 356, 628

Wakeford H. R., Visscher C., Lewis N. K., Kataria T., Marley M. S., Fortney J. J., Mandell A. M., 2017b, MNRAS, 464, 4247

Wakeford H. R., et al., 2018, AJ, 155, 29

Wakeford H. R., et al., 2019, AJ, 157, 11

Wakeford H. R., et al., 2020, AJ, 159, 204

Waldmann I. P., 2016, ApJ, 820, 107

Waldmann I. P., Tinetti G., Rocchetto M., Barton E. J., Yurchenko S. N., Tennyson J., 2015a, ApJ, 802, 107

Waldmann I. P., Rocchetto M., Tinetti G., Barton E. J., Yurchenko S. N., Tennyson J., 2015b, ApJ, 813, 13

Wang W., van Boekel R., Madhusudhan N., Chen G., Zhao G., Henning T., 2013, ApJ, 770, 70

Welbanks L., Madhusudhan N., 2019, AJ, 157, 206

Welbanks L., Madhusudhan N., 2021, ApJ, 913, 114

Welbanks L., Madhusudhan N., Allard N. F., Hubeny I., Spiegelman F., Leininger T., 2019, ApJL, 887, L20

Wende S., Reiners A., Seifahrt A., Bernath P. F., 2010, A&A, 523, A58

Winn J. N., 2018, in Deeg H. J., Belmonte J. A., eds, Handbook of Exoplanets. Springer, p. 195, doi:10.1007/978-3-319-55333-7_195

Winn J. N., Fabrycky D. C., 2015, ARA&A, 53, 409

Woitke P., Helling C., Hunter G. H., Millard J. D., Turner G. E., Worters M., Blecic J., Stock J. W., 2018, A&A, 614, A1

Wolszczan A., Frail D. A., 1992, Natur, 355, 145

Wordsworth R., Pierrehumbert R., 2014, ApJL, 785, L20

Wright J. T., Gaudi B. S., 2013, Exoplanet Detection Methods. Springer, p. 489, doi:10.1007/978-94-007-5606-9_10

Wunderlich F., et al., 2019, A&A, 624, A49

Wyttenbach A., Ehrenreich D., Lovis C., Udry S., Pepe F., 2015, A&A, 577, A62

Yee S. W., et al., 2018, AJ, 155, 255

Yurchenko S. N., Tennyson J., 2014, MNRAS, 440, 1649

Yurchenko S. N., Barber R. J., Tennyson J., 2011, MNRAS, 413, 1828

Zalesky J. A., Line M. R., Schneider A. C., Patience J., 2019, ApJ, 877, 24

Zhang X., 2020, RAA, 20, 099

Zhang J., Kempton E. M. R., Rauscher E., 2017, ApJ, 851, 84

Zhang M., et al., 2018, AJ, 155, 83

Zhang M., Chachan Y., Kempton E. M. R., Knutson H. A., 2019, PASP, 131, 034501

Zhang M., Chachan Y., Kempton E. M. R., Knutson H. A., Chang W. H., 2020, ApJ, 899, 27

Zhu W., Petrovich C., Wu Y., Dong S., Xie J., 2018, ApJ, 860, 101

Zingales T., Waldmann I. P., 2018, AJ, 156, 268

de Wit J., Seager S., 2013, Sci, 342, 1473

de Wit J., et al., 2016, Natur, 537, 69

de Wit J., et al., 2018, NatAs, 2, 214

von Essen C., Mallonn M., Albrecht S., Antoci V., Smith A. M. S., Dreizler S., Strassmeier K. G., 2015, A&A, 584, A75

von Essen C., Mallonn M., Welbanks L., Madhusudhan N., Pinhas A., Bouy H., Weis Hansen P., 2019, A&A, 622, A71

When I Heard the Learn'd Astronomer

When I heard the learn'd astronomer;
When the proofs, the figures, were ranged in columns
before me;
When I was shown the charts and diagrams, to add,
divide, and measure them;
When I, sitting, heard the astronomer, where he
lectured with much applause in the lecture-room,
How soon, unaccountable, I became tired and sick;
Till rising and gliding out, I wander'd off by myself,
In the mystical moist night-air, and from time to time,
Look'd up in perfect silence at the stars.

Walt Whitman (1819–1892)